Phase Transformations in Drop-Tube Processed Rapidly Solidified $CoCrCuFeNi_{0.8}$ High Entropy Alloy

Liam Sami Ellis Teggin

Submitted in accordance with the requirements for the degree of

Doctor of Philosophy

The University of Leeds

School of Chemical and Process Engineering

March, 2025

The candidate confirms that the work submitted is his/her own, except where work which has formed part of jointly-authored publications has been included. The contribution of the candidate and the other authors to this work has been explicitly indicated below. The candidate confirms that appropriate credit has been given within the thesis where reference has been made to the work of others.

1. Teggin, L.S.E., Cochrane, R.F. and Mullis, A.M., 2024. Characterisation of Phase Separation in Drop-Tube-Processed Rapidly Solidified CoCrCuFeNi0. 8 High-Entropy Alloy. *High Entropy Alloys & Materials*, ***2***(2), pp.258-276.
2. Teggin, L.S.E., Cochrane, R.F., Micklethwaite, S.L., Aslam, Z.P., Nassar, A.E. and Mullis, A.M., 2025. Solid-state decomposition following partitionless solidification in dendrite arms of rapidly solidified CoCrCuFeNi0.8 high-entropy alloy. *Acta Materialia* **289**.

Acknowledgements

First and foremost, I would like to thank my supervisors, Professor Andrew Mullis and Dr. Robert Cochrane, for their unwavering support and vital insight throughout the course of this project. I am forever indebted to them for their continued investment in the work we have undertaken.

My deepest gratitude goes to Robert Simpson and Diane Cochrane, who were not only instrumental in training me on equipment and in procedures essential to the completion of this work, but who also never failed to make me feel like I had family in the lab.

I would also like to thank supporting academics and staff from SCAPE, LEMAS and the Bragg Centre at the University of Leeds, Stuart Micklethwaite, Mac Hough, Zabeada Aslam, John Harrington, Mohammed Javed and Adrian Cunliffe for their help with the investigation.

Further, I would like to thank my colleagues Ahmed Nassar, Huamao Rao, Mehmet Abul and Osama al-Jenabi for the laughs, motivation and advice throughout my study. Thank you, as well, to my family and friends from other parts of my life, who continue to help me believe in myself.

I would like to extend my gratitude to the Engineering and Physical Sciences Research Council for supporting me financially through this research and allowing me to fulfil a lifelong goal of contributing to the scientific community.

Finally, I would like to thank my parents, John and Souhila Teggin, for everything. Maman & Papa, I love you.

Abstract

Despite the rapidly growing volume of research conducted on high-entropy alloys, only a small subset discusses the effect of non-equilibrium solidification processing on the possible phase transformations in such alloys and the resultant obtainable microstructures. Non-equilibrium processing techniques such as rapid cooling allow the study of phase transformations and other phenomena which require substantial undercooling of the alloy liquid and are often inaccessible to conventional solidification techniques like casting.

This work treats the experimental results obtained after arc-melting and drop-tube processing of $CoCrCuFeNi_{0.8}$, a dual-phase, face-centred cubic high-entropy alloy. Drop-tube processing allows the containerless rapid cooling of liquid alloy droplets in free-fall. Such an environment allows significant liquid undercooling (via reduction in heterogenous nucleation sites) while reducing the sometimes confounding effect of gravity induced flow. The experiment yielded alloy droplets of diameters between 1000 μm and 38 μm divided into 9 sieve size fractions (e.g. > 850 μm, 850 – 500 μm, …53 – 38 μm). The range of yielded droplet sizes following melt division allowed solidification at a range of cooling rates between 600 K s^{-1} and 60000 K s^{-1} in the liquid state.

The possible structures obtainable in drop-tube processed $CoCrCuFeNi_{0.8}$ were classified visually. Statistical analysis of variation between arbitrarily chosen population samples was conducted. This allowed the conclusion that a sample of 250 droplets from each size fraction was enough to provide a statistically representative sample of each particular sieve size fraction. As a result, around 2500 droplets across the complete size range were catalogued in terms of structure. The occurrence rate of each structure was then calculated for each droplet size to determine the impact of cooling rate on microstructural formation with statistical backing.

The alloy composition was initially selected to study liquid phase separation in the metastable regime. To this end, the composition was tailored based on a review of the behaviour of similar alloys in past literature to reduce the predicted undercooling required for the transformation. Surprisingly, this alloy does not undergo liquid phase separation to a statistically significant extent after drop-tube processing. Instead, a myriad of other phase transformations occurs, which, separately or in combination, cause the formation of unusual and novel microstructures in the solidified droplets. The most statistically prominent and notable structures include copper-rich dispersions in the dendrite cores of some droplets and spontaneously grain-refined microstructures.

Copper-rich dispersoids in dendrite cores were found to be the result of partitionless solidification followed by a decomposition reaction in the solid state. The average composition of the regions featuring the dispersoids were found to be the same as that of the original alloy. Interestingly, the composition of the equivalent non-decomposed regions (i.e. the regions which solidify via solute partitioning) also do not show substantial change in composition with cooling rate. Partitionless solidification was therefore found to be the result of undercooling of the alloy below the characteristic T_0 temperature, rather than the result of severe kinetic solute trapping phenomena. Subsequent solid-state decomposition is thought, on balance, to have been the result of a spinodal decomposition mechanism.

Extensive spontaneous grain-refinement was noted across the droplet size-range. Microstructural analysis has allowed the mechanism for grain-refinement in this alloy to be established. The morphology of the grain-refined structures indicated that dendritic fragmentation and remelting was the most likely cause of refinement in $CoCrCuFeNi_{0.8}$. The observation of hybrid structures consisting of grain-refined grains with copper-rich solid state dispersoids indicated that a subset of dendrites had solidified in a partitionless manner and then subsequently grain-refined. This bifurcation in refined grains allowed separate analysis of the refined grain diameter with cooling rate. The refined grains originating from partitionlessly solidified dendrites were consistently larger than grains which had undergone parititoning, even if they were solidified at the same cooling rates. This step change in grain-refined grain diameter with cooling rate corresponds well qualitatively to commonly utilised dendrite fragmentation models which describe grain-refinement in undercooled alloys. At the same time, the grain-refinement model based on superheating [Li et al., *J. Cryst. Growth*. **192** (1998) 462-470] appears to have been disproved for this alloy. Once grain-refinement is initiated, the extent to which such refinement can occur is dependent on the droplet cooling rate. Droplets which solidify at higher cooling rates only have enough time to partially refine.

Liquid phase separation was deemed to have been hindered by the low volume fraction of the separating copper-rich phase as well as the inhibition of nucleation and growth of minority phase droplets due to the high cooling rates achieved in drop-tube processing. Liquid phase separation microstructures were observed only at the highest cooling rates and were deemed, based on the likely inhibition of nucleation and growth, to be the result of a spinodal mechanism. This finding was compared to previous studies on similar alloys to illustrate the impact of solidification technique on obtainable microstructures in high-entropy alloys.

Table of Contents

List of Tables

List of Figures

Abbreviations

AED	Area equivalent diameter
BCC	Body-centred cubic
BFTEM	Bright-field transmission electron microscopy
BSE	Back-scattered electron
CALPHAD	Calculation of Phase Diagrams
CGM	Continuous growth model
DP	Dendritic phase
DSC	Differential scanning calorimetry
EBSD	Electron back-scatter diffraction
EDX	Energy dispersive X-Ray spectroscopy
EML	Electromagnetic levitation
ESL	Electrostatic levitation
FCC	Face-centred cubic
FIB	Focused ion beam
FIBSEM	Focused ion beam scanning electron microscope
HCP	Hexagonal close-packed
HEA	High-entropy alloy
H-R	Hume-Rothery
IDP	Interdendritic phase
LNDM	Local non-equilibrium diffusion model
LPS	Liquid phase separation
RK	Redlich-Kister
SAED	Selective area electron diffraction

SE	Secondary electron
SEM	Scanning electron microscope
STEM	Scanning-transmission electron microscopy
TEM	Transmission electron microscope
TTT	Time-temperature-transformation
XRD	X-Ray diffraction

Chapter 1 – Introduction

High-entropy alloys (HEA) constitute a relatively new class of metal alloy in which a large number of metallic elements, usually five or above [1], is alloyed together in equiatomic (or near-equiatomic) proportions [2]. They represent a new trend in alloy design directly opposed to conventional techniques, where small amounts of alloying elements are added to one majority element, or two elements are alloyed together in large proportions [2, 3]. HEAs have become the subject of an exponentially increasing volume of study in the decades since the first experimental work involving these alloys was published in 2004 [4, 5]. This is largely due to the postulated enormous potential of HEAs as structural and functional materials.

Such potential is based on various hypothesized effects intrinsic to HEAs. Central to their behaviour is the high-entropy effect. The mixing of a large number of elements in near equiatomic proportions is thought to increase configurational entropy and stabilise the formation of solid solutions in lieu of the expected mess of brittle intermetallic compounds [2]. Other effects such as distortion of the atomic lattice and sluggish diffusion are thought to increase HEA phase stability, which, in turn, increases damage tolerance [3]. Finally, unpredictable properties often arise from this new alloying methodology, which may be favourable for various applications [3, 6]. HEAs of varying phase structures and compositions have since been created and tested to solve some of the key problems in metallurgical engineering. These include overcoming the strength-ductility trade-off in alloys [7, 8], providing high-temperature or radiation resistance [9-12], and enhancing reaction catalysis [13, 14].

Non-equilibrium solidification techniques have been used for alloy development for decades. They primarily work by enhance the undercooling (the extent to which the alloy is cooled below the liquidus temperature) prior to solidification. This allows for access to non-equilibrium phase transformations, retainment of metastable phases, enhanced solubility, and variation of microstructural spatial morphology [15-17].

Currently, research regarding the behaviour of HEAs during solidification far from equilibrium is still in its infancy. Because of the novel properties and behaviours intrinsic to some HEAs, it is important to broaden our understanding of how non-equilibrium solidification affects HEA microstructures. Furthermore, is also important to compare HEA behaviour to our established knowledge of more compositionally simple alloys.

The way in which undercooling is achieved (e.g. via rapid cooling and/or inhibition of heterogenous nucleation) is also just as important to the final microstructural morphology as the magnitude of said undercooling [16]. Drop-tube processing involves the rapid solidification of liquid alloy droplets in free-fall through an inert atmosphere. The process achieves high undercoolings through the phenomena of melt-subdivision and inhibiting heterogenous nucleation through the removal of container walls [16, 18]. In the drop-tube, droplets of different sizes will experience drastically different cooling rates. This influences other aspects of microstructural change which depend on cooling rate, such as the growth scale of microstructural features like dendrites [19] and eutectic lamellae [20]. In general drop-tube processing is thought to provide a snapshot of the potential behaviour of alloys during industrial gas atomisation processing [19], where the small scale and batch process of alloy production renders the process variables easier to control.

Transition metal HEAs in the Co-Cr-Cu-Fe-Ni compositional family were seen as prime candidates through which to analyse the impact of rapid solidification on phase transformations in HEAs. The equiatomic alloy and some of its compositional variants have previously been observed to undergo liquid phase separation (LPS) in the metastable regime (i.e. if they are undercooled by a critical amount before solidification) [21]. Furthermore, similar alloys have been observed to undergo various transformations when solidified far from equilibrium including significant solute-trapping [22-24] and spontaneous grain refinement [24, 25].

The work presented below therefore encompasses the study of one particular alloy – $CoCrCuFeNi_{0.8}$. The alloy has been subjected to arc-melting and drop-tube processing solidification techniques. The main aim of this work is determining the impact of non-equilibrium solidification and rapid cooling on phase transformations and the final microstructure of a dual-phase solid solution HEA. $CoCrCuFeNi_{0.8}$ was initially chosen with the aim of studying metastable LPS in HEAs. The study was subsequently broadened to catalogue and explain the numerous unexpected phase transformations that were found to have occurred both during arc-melting and drop-tube processing. These phase transformations were explained in the context of both materials thermodynamics and reaction kinetics. Furthermore, the behaviour of this alloy was compared to the conventional understanding of more simple binary and ternary alloys solidified at conditions far from equilibrium.

Following on from this introduction, Chapter 2 provides the scientific background for this study and may serve as a primer for the reader on subjects regarding selected non-equilibrium phase transformations in pure metals,

simple alloys and HEAs. It also introduces the reader to the experimental techniques employed to study non-equilibrium solidification processes in metals and alloys, with particular attention focused on the drop-tube apparatus used in subsequent experimental work. Furthermore, a deeper background regarding HEAs, their unique properties and potential applications is established. In Chapter 3, past literature, encompassing previous work on non-equilibrium solidification of both simple binary and ternary alloys, and HEAs, is reviewed. A particular focus is placed on three solidification phenomena: liquid phase separation (LPS), solute-trapping/partitionless solidification, and spontaneous grain refinement. This informs the experimental objectives and the choice of alloy studied, which are both defined at the end of the chapter. Chapter 4 describes the various experimental methods used to manufacture, process and analyse the alloy selected for this work, $CoCrCuFeNi_{0.8}$. The descriptions of, and usage rationales for, selected thermodynamic modelling and statistical analysis techniques are also provided. Chapter 5 provides the results of the aforementioned theoretical and experimental analysis regarding $CoCrCuFeNi_{0.8}$. Chapter 6 brings these results together in a discussion aimed at synthesizing the gathered information to satisfy the initial investigation aims. Chapter 7 presents the key conclusions obtained as a result of the theoretical and experimental investigation. Chapter 8 suggests potential future work to begin to answer some of the questions raised by the study as well as enhance the strength of conclusions made based on the findings.

Chapter 2 – Background Science

2.1 Non-equilibrium processing: an introduction

In metallurgy, a system (a metal or alloy) is said to be in thermodynamic equilibrium when the phases present are in their most stable states. Due to this, the free energy of the system is at its lowest. In discussing phase transformations, we often assume thermodynamic equilibrium between the initial and product phase as the transformation occurs, often via consultation of an equilibrium phase diagram [26]. In the context of solidification, non-equilibrium processing defines a type of solidification processing where thermodynamic equilibrium can no longer be assumed, largely due to the rapid progression of the solidification front. The two key conditions that can be used to influence the movement of the solidification front are cooling rate and undercooling (the difference between the melting/liquidus temperature and the temperature at which solidification is initiated) [27].

A high cooling rate can be attained through use of rapid quenching processes [27]. These processes typically induce prevailing cooling rates above 10^3 – 10^4 K s^{-1}, removing thermal energy contained in a liquid melt very quickly [16].

Another method of non-equilibrium processing involves use of particular experimental apparatus to induce very high undercooling [27]. Undercooling a liquid melt by hundreds of degrees Kelvin can yield solidification microstructures drastically different from those obtained through conventional casting methods [16].

Non-equilibrium and far-from-equilibrium processing have become increasingly important in the search for alloys with novel or desirable properties, especially because the solidification kinetics at play often have more influence on the final solidified microstructure than the predicted equilibrium phases [28].

2.1.1 Microstructural refinement

Non-equilibrium solidification processes have resulted in the production of alloys with refined features compared to those solidified through conventional methods such as casting. Along with many other phenomena associated with rapid solidification, such refinement may increase gradually in severity with cooling rate, but can also occur suddenly once undercooling reaches a critical value.

2.1.1.1 Continuous refinement with cooling rate

In alloys, high cooling rates reduce the time interval between initial solidification and the point where further solute diffusion-based growth and coarsening processes become inhibited kinetically by low temperatures [26]. The distance over which solute diffusion can occur is effectively reduced as cooling rate increases. Because of this, increasing the alloy cooling rate often results in significant refinement of microstructural features in the final solidified alloy compared to near-equilibrium processing. This refinement can be continuous with increasing cooling rate and is often observed through a reduction in grain size and primary/secondary dendrite arm spacing [29]. Continuous dendritic refinement with cooling rate has been shown in steels [30], aluminium alloys [31] and nickel-based superalloys [32]. During eutectic solidification, lowering of the diffusion distance at high cooling rates also results in a refinement of eutectic lamellae [33, 34] or a decrease in the size of eutectic particles and a change in eutectic particle morphology [35].

2.1.1.2 Spontaneous Grain Refinement with Undercooling

In contrast to a continuous refinement with cooling rate, some pure metals and alloys may undergo an abrupt transformation dubbed spontaneous grain refinement. This is thought to be an undercooling controlled process. A decrease in grain size by orders of magnitude, and a change in morphology from columnar to equiaxed grains, occurs when an alloy is undercooled below a specific value ΔT_{GR}^{*} [29, 36]. Spontaneous grain refinement was first described following experiments on the solidification of pure Ni by Walker in 1959 [37] and has since been observed to occur in numerous pure metals, alloys and intermetallic compounds. This process is spontaneous in that it occurs as a result of the changing intrinsic properties of the material itself, rather than through refinement-inducing materials or processes such as stirring or addition of inoculant particles [38].

While only one such transition from columnar to fine equiaxed grains has been observed in pure metals, two separate transitions are thought to exist in many alloys. In this scenario, an alloy will solidify with a conventional columnar morphology at low undercoolings. At a critical undercooling $\Delta T_{GR}^{(1)}$, grain size decreases substantially and grains become more equiaxed. As undercooling continues to rise, the grains regain the columnar character found at the lowest undercoolings. Finally, at a higher undercooling $\Delta T_{GR}^{(2)}$, a second transition to a fine equiaxed microstructure occurs [36]. Figure 2.1 shows the variation in dendrite tip radius with undercooling as described in [39]. This is used by Mullis [36] as a base on which to superimpose the regions where columnar grains and

refined grains would constitute the prevailing microstructure. The placement of these regions is based on the reduction of dendrite tip radius below a critical value r_{tip}^{*}(shown as ρ^{*} in Figure 2.1). Below this value, dendrites are thought to be able to fragment to create the refined structure present. The model on which this is based [40, 41] is one of the models created to explain the spontaneous grain-refinement phenomenon. It is described in more detail in Chapter 2. An experimental example of the two grain refinement transitions is shown in Figure 2.2 from the work of Li et al. [42] on an undercooled Ni-Cu alloy. Figure 2.2a shows the initial dendritic structure at low undercooling which gives way to spherodized refined grains above $\Delta T_{GR}^{(1)}$ in Figure 2.2b. Columnar dendrite grains are then observed in Figure 2.2c before a second instance of grain-refinement yields equiaxed microstructures shown above critical undercooling $\Delta T_{GR}^{(2)}$ in Figure 2.2d.

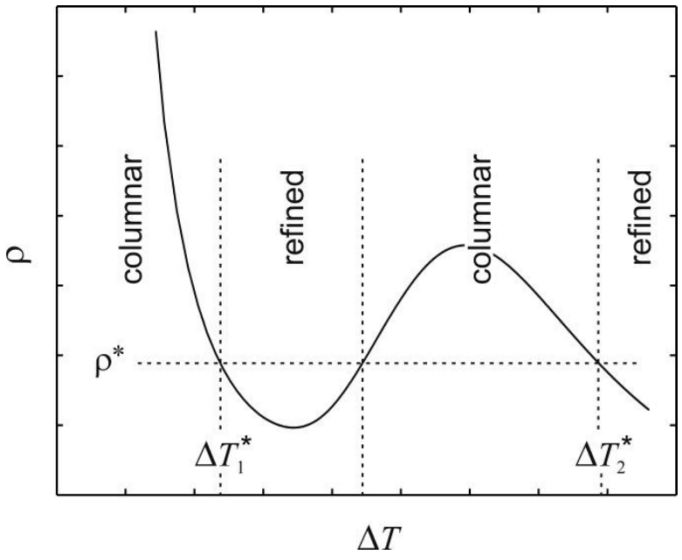

Figure 2.1 Variation in grain morphology with undercooling in alloys exhibiting spontaneous grain refinement [36] adapted from the model in [39] exhibiting variation of dendrite tip radius with undercooling. There are two specific values for undercooling where dendrite tip radius decreases below a critical value which allows fragmentation and formation of a refined structure.

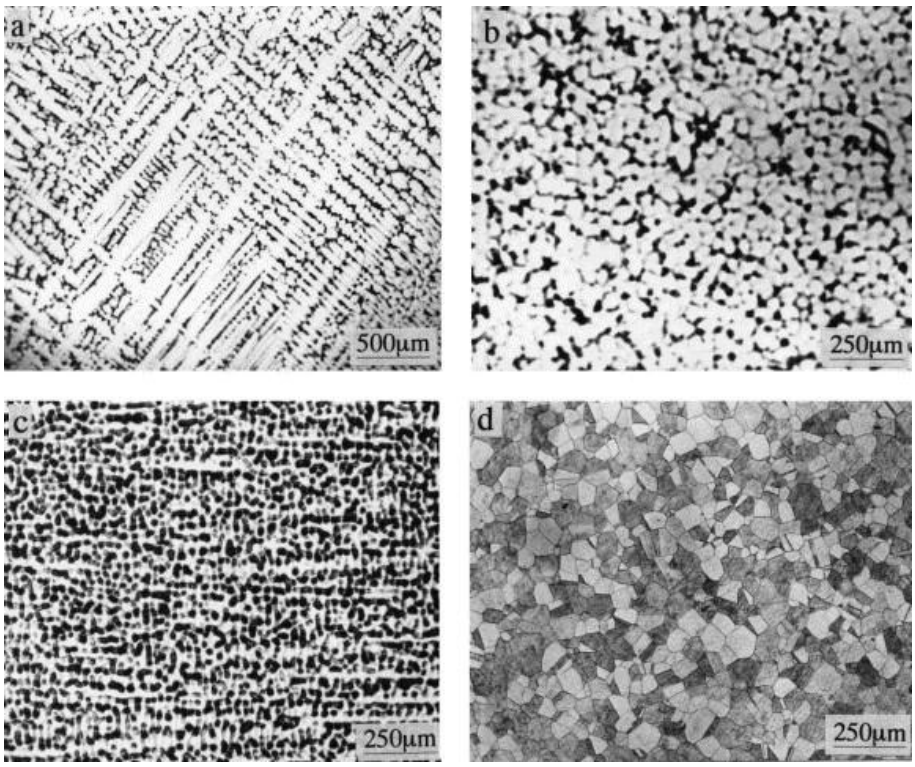

Figure 2.2 Example of grain refinement transitions at low and high undercoolings in $Ni_{75}Cu_{25}$ alloys from the work of Li et al. [42]. (a) Columnar dendrites found a low undercooling. (b) Spherodized grains after first episode of grain refinement above first characteristic undercooling. (c) Resuming of columnar dendritic solidification at higher undercoolings. (d) Second episode of grain refinement above second characteristic undercooling.

2.1.2 Accessing metastable phases and phase selection

Non-equilibrium processing can also undercool a metal/alloy to a point where metastable phases can be accessed that are unavailable to conventional solidification processes. Rapid solidification processing can also allow these phases to be retained down to room temperature. The rapid lowering in temperature kinetically inhibits the metastable phases from transforming into the stable phases predicted at equilibrium conditions. The most common example of this is the formation and retention of FCC (Face Centred Cubic) austenitic phases during the rapid quenching of steels. These phases are supersaturated with carbon which cannot be rejected during solidification due to the high cooling rate. The supersaturated austenite then transforms into tetragonal martensite when cooled to room temperature, drastically altering the properties of the solidified steel [26]. Other rapid cooling experiments on steels have allowed tailored phase configurations to be accessed. Vitek et al. [43] observed that rapid cooling techniques can be used to retain ferrite or austenite phases in stainless steels, avoiding the equilibrium transformation from one to the other. Pryds et al. [44] show that at very high cooling rates, the transformation of

austenite to martensite can even be inhibited in gas atomized steels, with austenite instead being retained to room temperature. Retention of metastable phases is also possible in non-ferrous alloys [45].

Extension of solid solubility can also occur during non-equilibrium processing, where a solid solution contains a higher atomic percentage of solute at a specific temperature than is predicted by the equilibrium phase diagram. The solid-solution field on such a diagram is therefore extended. Hehmann et al. [46] have observed such behaviour in Mg alloys. The solubility of a large array of alloying elements in the magnesium was found to increase substantially in splat cooled alloys subjected to cooling rates of 10^5 – 10^8 K s^{-1}. Zhou et al. [47] and Ning and Zhou [48] came to similar conclusions in Cu and Ag alloys. As a result of the metastable extension of solid-solubility, phase diagrams can be drawn which account for the changes in the prevailing phase during non-equilibrium processing. One such example is provided by Fecht and Perepezko [49], who undercooled Pb-Sn alloy droplets via a droplet emulsification technique. Upon analysis of the prevailing phases at various undercoolings via X-Ray Diffraction (XRD), they were able to extrapolate the liquidus and solidus lines on the equilibrium phase diagram to factor in the metastable phases that were retained below the equilibrium transformation temperatures. Such extrapolations are shown by dot-dashed lines superimposed onto the equilibrium Pb-Sn phase diagram in Figure 2.3. Here, the extended solidus has caused an increase in maximum solid solubility of Sn in the α solid-solution phase. Furthermore, a metastable peritectic phase transformation $L + \alpha \rightarrow \alpha_1$ has also been revealed when the alloy liquid of a specific composition (about 65 at% Sn) is undercooled to below the metastable peritectic temperature (about 125 °C).

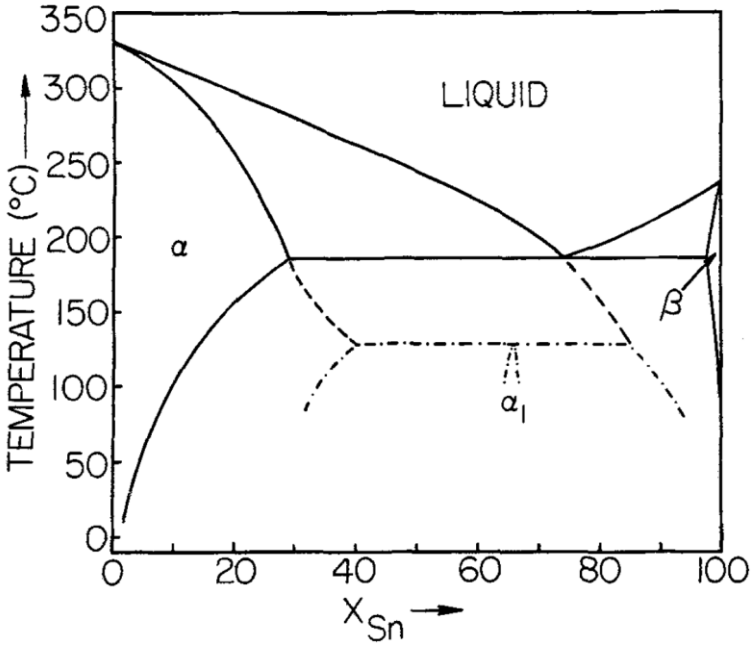

Figure 2.3 Extended solid solubility and formation of metastable phases in undercooled Pb-Sn alloys following non-equilibrium processing [49]. An extended solidus line increases maximum solid solubility of Sn in the α phase. A metastable peritectic transformation is also revealed for an alloy of composition 65 at% Sn undercooled to 125 °C.

The primary explanation for the solid-solubility extension is based on solidification kinetics and cannot be easily predicted by the thermodynamic techniques commonly used based on the relevant equilibrium phase diagram [46]. At low solute concentrations, capillarity is suggested by Boettinger et al. [50] to stabilise growth of a planar solidification front at high velocities. The speed of this advancing front then controls the extent to which an excess of solute may remain in the solid during solidification. At higher solute concentrations, however, a key factor in solid-solubility extension is kinetic solute trapping during dendritic growth [46, 50]. This is elaborated on in section 2.1.3 below.

2.1.3 Solute trapping and partitionless solidification

It is well established that the degree of undercooling of an alloy increases the dendritic growth velocity during solidification. Such a phenomenon has been described in experiments in pure metals [51-54], alloys [52, 53, 55] and intermetallic compounds [56]. As undercooling increases during a solidification reaction, the speed of the advancing solidification front may increase to the point where it approaches the rate of diffusion of solute across the solid-liquid interface. In this event, diffusion of the solute is inhibited and kinetic solute trapping may result. Any solid phase formed under such conditions would therefore become enriched in solute compared to the composition defined by an

equilibrium phase diagram. Such a solute trapping effect was discovered through rapid solidification experiments in the 1960s [57, 58]. In addition to experimental work, numerous models have been proposed to describe the kinetic solute trapping phenomenon. The extent of solute trapping in a particular phase transformation has come to be represented mathematically by a partition coefficient k where $0 \leq k \leq 1$. During equilibrium processing, a value of $k = k_e$ may be assigned, defining the equilibrium partition coefficient. Initiation of solute trapping causes the partition coefficient to deviate from k_e towards unity [59]. A partition coefficient of $k = 1$ indicates a theoretical limit where no partitioning of solute has occurred. In other words, a new phase has formed at the same composition as the parent phase.

Early models regarding kinetic solute trapping in alloys [59, 60] tend to break down as the partition coefficient approaches $k = 1$. In such models, the calculated partition coefficient may only tend asymptotically to 1 as the velocity of the solidification front tends to infinity (this is discussed at greater length in Chapter 2). Experimentation has shown this not to be the case. Willnecker et al. [61] conducted solidification experiments on Cu-Ni and propose that such kinetic models are only valid when an alloy is undercooled by an undercooling below a critical value ΔT^*. Above this undercooling, growth of solid is no longer controlled by solute diffusion. This is because above ΔT^*, the velocity of the solidification front has reached and even exceeded the velocity of solute diffusion across the interface. Instead, the growth of solid is controlled by heat diffusion (in a similar manner to pure metals). The relationship between undercooling and growth velocity transitions from exponential to linear. Eckler et al. [62], in similar experiments on Ni-B, also found such a growth transition at a critical undercooling. They further note that small changes in alloy composition can have a large impact on the value of ΔT^*. Such experiments have resulted in works which model this transition from an exponential to a linear relationship in the growth velocity-undercooling curve [63].

Baker and Cahn argued in the 1970s that this partitionless solidification is, thermodynamically, theoretically possible [64]. For such a process to occur, two conditions must be satisfied. First, the rate of advancement of the solidification front must be high enough that the compositions of the solid and liquid at the interface can be assumed to converge [27, 60]. Second, the Gibb's free energy of the product solid phase must be less than that of the liquid from which it forms. Therefore, the temperature for partitionless solidification must be below that at which the free energy of the solid and liquid phase is equal. On a conventional phase diagram, the temperatures at which $\Delta G^{l \to s} \leq 0$ for each composition is shown via the T_0 line [50]. As shown in Figure 2.4, if an alloy

liquid of composition $c_l^*$is undercooled below T_0, it is possible for a solid of equivalent composition to form from the liquid while satisfying the requirement for a reduction in free energy. This critical undercooling is ΔT_{PS} the difference between the alloy liquidus temperature T_l and the T_0 temperature at a given composition.

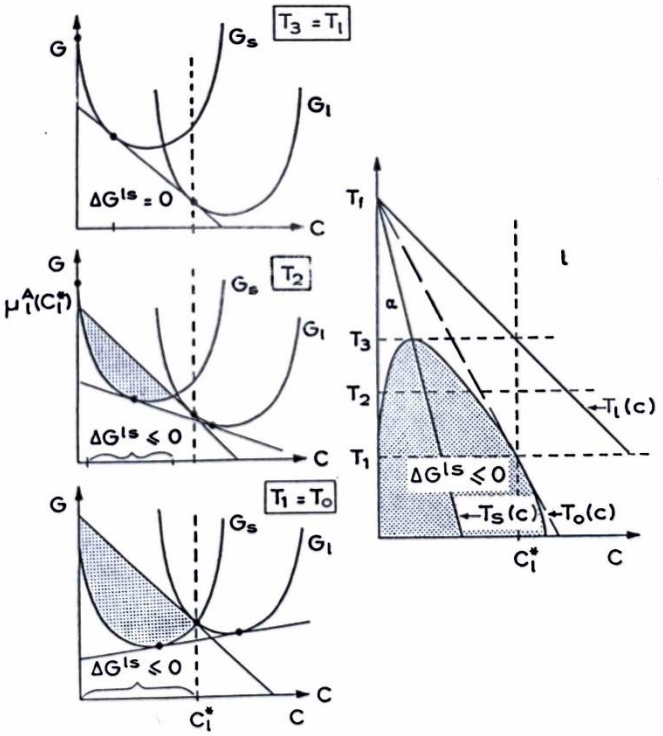

Figure 2.4 Determination of partitionless solidification region in a binary alloy phase diagram [27]. At T_3 and T_2, the composition at which a reduction in free energy upon solidification is satisfied (i.e. $\Delta G^{l\to s} \leq 0$) is below the alloy composition c_l^*. Once the alloy is cooled to temperature T_1, the composition falls on the T_0 line at this specific temperature. The condition for a reduction in free energy during solidification is now satisfied, and partitionless solidification becomes thermodynamically possible.

2.2 Phase separation in solidification

Given the large breadth of phase transformations possible during solidification, it is wise to train focus on specific reactions pertinent to this investigation. With this in mind, this work focuses on simple homogenous decomposition reactions. These include liquid phase separation (LPS), where one liquid separates into two liquids of different compositions prior to solidification, and solid-state decomposition, where a new phase precipitates in the parent solid phase leaving two distinct solid phases as the products.

2.2.1 Thermodynamics of decomposition reactions

The Gibbs free energy of a material can be represented through Equation 2.1

$$G = H - TS \tag{2.1}$$

where G is the Gibbs free energy, H is the enthalpy, T is the temperature, and S is the entropy. The available free energy, and whether it is negative or positive, is therefore governed by the balance between the enthalpy and entropy associated with the phase in question [65]. Using a binary alloy for simplicity, we may represent the change in Gibbs free energy inherent in formation of a binary alloy solid-solution phase ΔG_{mix}^{Alloy} from pure species A and B in Equation 2.2 [66].

$$\Delta G_{mix}^{Alloy} = \Delta H_{mix}^{Alloy} - T\Delta S_{mix}^{Alloy} \tag{2.2}$$

From this, it is shown that enthalpy of mixing $\Delta H_{mix}^{Alloy}$and entropy of mixing ΔS_{mix}^{Alloy} determine the Gibbs free energy of the alloy at a specific composition and temperature T. These key terms are defined in Equation 2.3 and Equation 2.4 for a regular solution and an ideal solution respectively [66-68] in a binary alloy.

$$\Delta H_{mix}^{Alloy} = \Omega X_A X_B \tag{2.3}$$

$$\Delta S_{mix}^{Alloy} = -R[X_A \ln X_A + (X_B \ln X_B)] \tag{2.4}$$

where Ω is an interaction parameter. X_A is the atomic fraction of species A and X_A is the atomic fraction of species B. The entropy term assumes a random organisation of atoms of constituent elements in the phase [66]. The regular solution enthalpy of mixing defines how the atoms in a mixture interact with each other. A negative interaction means atoms of each element will preferentially be surrounded by other elements. A very strong negative interaction means the constituent elements will form ordered solid solutions, or potentially even react to cause the formation of intermetallic compounds. Conversely, a strong positive interaction indicates preferential separation of the different constituent elements to form regions of like atoms [68]. Appropriate

mixing to form a random solid solution is therefore often achieved at values of ΔH_{mix}^{Alloy} which are close to 0 (i.e. slightly positive or slightly negative). Such a concept is applied to HEAs later in section 2.4.

Based on Equation 2.2, a positive enthalpy of mixing can introduce a critical temperature T_c, below which Gibbs free energy is minimised at two separate compositions rather than only one [65].

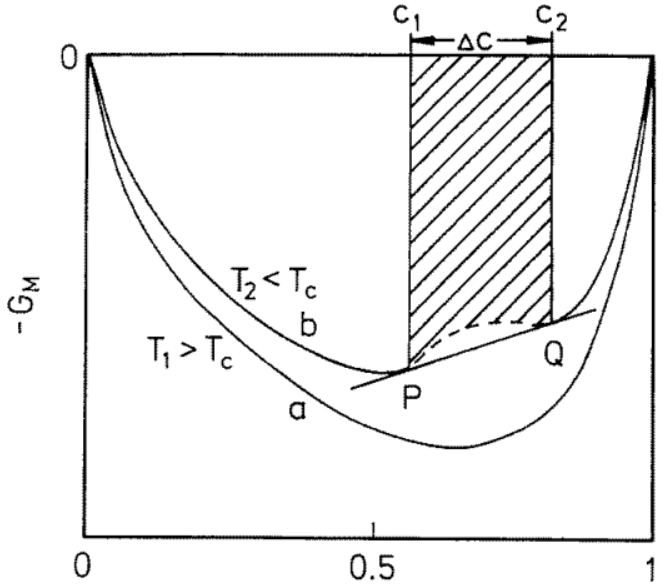

Figure 2.5 Gibbs free energy - composition plot for binary alloy showing change in shape above and below critical temperature T_c [68]. When temperature is reduced to below the critical temperature $T_2 < T_c$, local minima points P and Q are now present, and bookend a compositional interval Δc which is convex. Within this compositional interval, a reduction in free energy can occur if two distinct compositions are formed in lieu of the original one.

Figure 2.5 shows the molar Gibbs free energy curve for an alloy solid solution at two different temperatures T_1 and T_2. Because $T_1 > T_c$, the Gibbs free energy curve has one minimum which defines the unique stable alloy composition. However, at $T_2 < T_c$, the shape of the free energy curve changes and local minima points P and Q are now present. These two points bookend a composition interval Δc on the curve that is convex rather than concave. The free energy of the system is therefore minimised at two distinct compositions rather than one [65, 68]. To fulfil these thermodynamic requirements, a new phase forms in the original, most commonly via a diffusion based transformation. Alloys with positive enthalpies of mixing at specific temperatures are therefore prerequisites for decomposition reactions during cooling and solidification (where temperature is constantly changing).

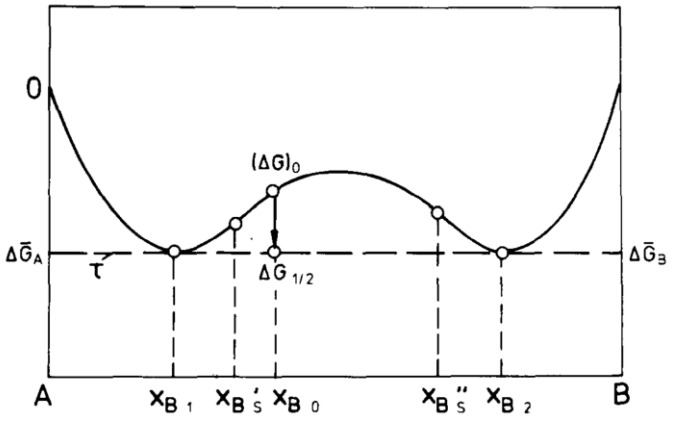

Figure 2.6 Plot of Gibbs free energy curve for alloy A-B at a specific temperature with local minima, common tangent and inflection points due to positive enthalpy of mixing [67]. Common tangent points $X_{B1}$and X_{B2} at each temperature define the binode while inflection points $X_{Bs}^{i}$and X_{Bs}^{ii} at each temperature define the spinode.

Figure 2.6 shows a more detailed potted Gibbs free energy curve for a binary alloy A-B. The presence of two local minima rather than one means that this solid solution is at a temperature below the critical temperature T_c. This curve is made symmetrical for simplicity. In real solutions, this will not always be the case. Two sets of points are important in a curve such as this, the first set includes the points that can be joined by a common tangent. These are represented by the atomic percentages of element B as $X_{B1}$and X_{B2}.The second set includes the inflection points in the curve, which define the compositions at which the second derivative of the Gibbs free energy with composition is zero. These points are located at compositions $X_{Bs}^{i}$and X_{Bs}^{ii}. At each temperature, the points intercepted by the common tangent construction define the binode in the phase diagram. The inflection points at each corresponding temperature define the spinode. Such lines define the type of transformation that governs the decomposition reaction and therefore, are of primary importance to the subsequent solidified morphology [69]. Furthermore, the thermodynamic driving force for the transformation ΔG_{drv} is defined by the difference in free energies between that at the current alloy composition ΔG_0 and the free energy of the most stable phases $\Delta G_{1/2}$. In this case this is represented through Equation 2.5.

$$\Delta G_{drv} = \Delta G_0 - \Delta G_{1/2} \qquad 2.5$$

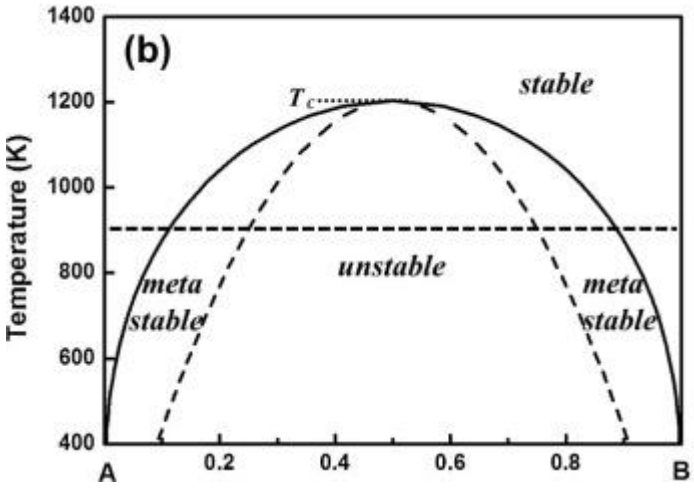

Figure 2.7 Plotted binode and spinode lines defining miscibility gap in alloy A-B, adapted from [69]. Above the binode, a single phase is thermodynamically stable. Between the binode and spinode, a single phase is metastable, with an energy barrier to the decomposition reaction. Once below the spinode, the single phase is unstable and will decompose spontaneously.

The manner in which the new phase forms from the parent phase is governed by whether the thermodynamic driving force for the transformation has rendered the original single phase unstable or metastable at a specific temperature. The regions of metastability in the miscibility gap are shown in Figure 2.7. Between the binode and spinode, the homogenous single phase is metastable, and within the spinodal region, it is unstable. The mechanism of decomposition therefore differs depending on the binodal and spinodal lines. Above the binodal line, a single mixed liquid phase is stable at all temperatures. In the region between the binode (solid line) and spinode (dashed line), the single mixed liquid phase has now become metastable. This means that phase separation can occur, but only if local compositional fluctuations overcome the associated energy barrier for transformation. This results in a nucleation and growth mechanism, where the new distinct phase nucleates in the parent phase. Below the spinode, the single phase is thermodynamically unstable. No energy barrier is required for decomposition, and the decomposition reaction is instantaneous once a local fluctuation in composition occurs [66, 67]. These are dubbed homophase composition fluctuations, and have a characteristic wavelength. Formation of a nucleus of a critical size is described as a heterophase fluctuation, given that this is reliant on an embryonic cluster of a new phase forming in the parent phase and reaching a critical size to progress the reaction. Figure 2.8 compares the nature of the change in composition during binodal and spinodal reactions [65].

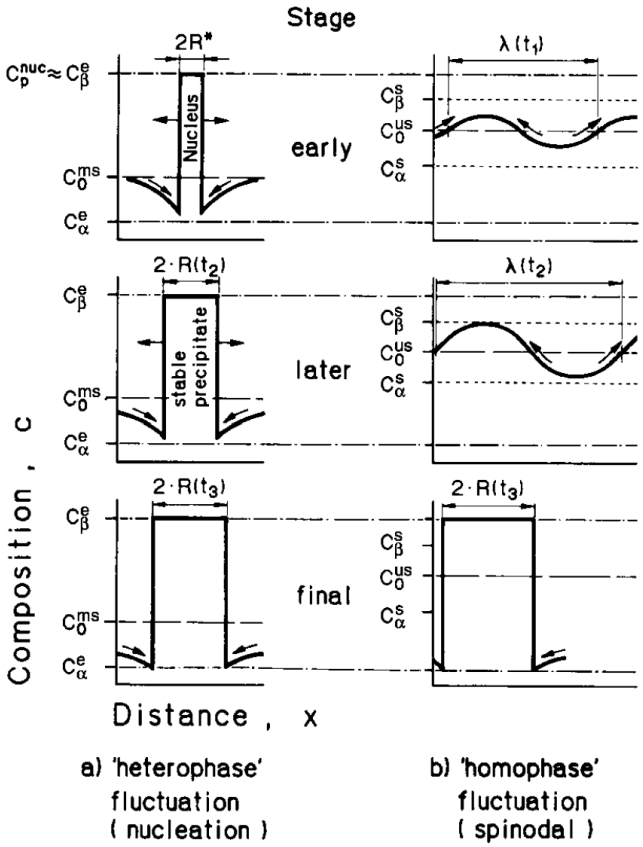

Figure 2.8 2-D description of composition change inherent in metastable (binodal nucleation and growth) and unstable (spinodal decomposition) phase separation [65]. Nucleation and growth is a heterophase fluctuation, governed by the requirement for a cluster of sufficient size of a new phase to form for the transformation to progress. A spinodal decomposition is a homophase fluctuation. No energy barrier need be overcome and a compositional fluctuation will occur spontaneously with a characteristic wavelength.

Microstructures that generally result are shown in Figure 2.9, with a globule or droplet microstructure in binodal separation and a dual-phase network structure in the case of spinodal decomposition [70].

In spinodal decomposition, the morphology of this network structure is dependent on the composition and relative volume fraction of the phases formed after separation. Above a certain volume fraction of the minority phase (depending on the alloy system), a percolation threshold is reached, at which a finely dispersed structure changes to the network structure more commonly associated with a spinodal structure [65]. Such a distinction is shown based on simulated results in Figure 2.10. It is important to distinguish the microstructure in Figure 2.10a from the resultant decomposition structure in a nucleation and growth reaction (spinodal decomposition is commonly identified visually by observation of the network structure in Figure 2.10b).

In the case of solid-state decomposition, the morphology of the spinodally decomposed solid solution (i.e. the shape of the dispersoids or percolated network that results), is also dependent on local elastic anisotropy. This impacts the eventual shape of the final network [26, 65].

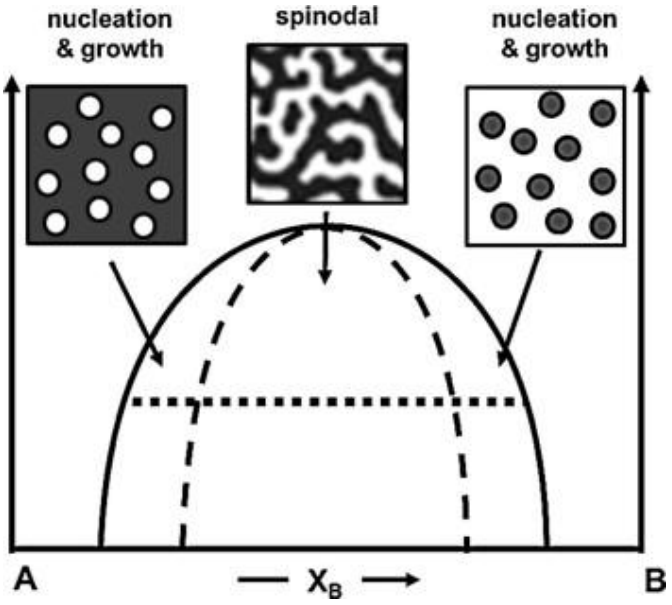

Figure 2.9 Diagram of binode and spinode in alloy miscibility gap, showing general solidification microstructures upon initiation of different forms of phase separation [69]. Nucleation and growth occurs if a single phase is cooled to within the metastable region of the miscibility gap, resulting in discrete regions of one phase in another. If a single phase is cooled into the unstable region, spinodal decomposition occurs, traditionally forming a network structure.

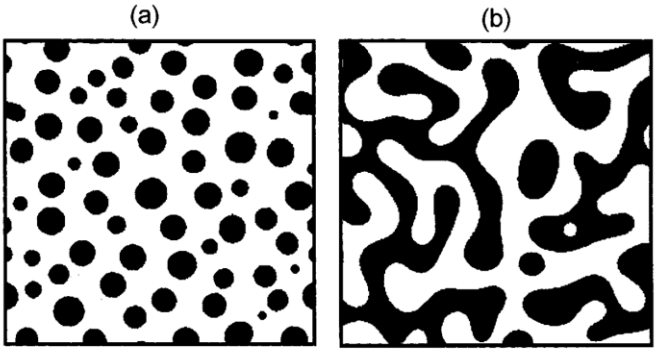

Figure 2.10 Comparison between spinodally decomposed microstructure with minority phase volume fractions (a) below and (b) above the percolation threshold [65]. The network structure may give way to a dispersion of discrete pockets of one phase in another if the volume fraction of the minority phase is low enough, similar to the result of a nucleation and growth reaction.

2.2.2 Phase separation pre-solidification – liquid phase separation

Liquid phase separation (LPS) in alloy systems defines a phenomenon where an alloy melt will de-mix into two immiscible liquids with differing compositions. This reaction is defined by Equation 2.6 below [66, 67].

$$L \rightarrow L_1 + L_2 \qquad 2.6$$

In the liquid state, the location of this miscibility gap (i.e. whether is located above or below the liquidus temperature) is particularly important. The first case is more common, and is referred to as a stable miscibility gap. The second case is dubbed a metastable miscibility gap.

2.2.2.1 Stable liquid phase separation

On a simple binary alloy phase diagram in an alloy system exhibiting stable LPS, the region of temperatures and pressures in which LPS occurs is a dome-like shape above the liquidus line and below the binodal line [66]. In order to initiate this phase separation, the liquid L must be cooled to a temperature below the binodal line, which will change depending on the composition and the nature of the alloy itself [70]. A stable miscibility gap is shown in the phase diagram in Figure 2.11.

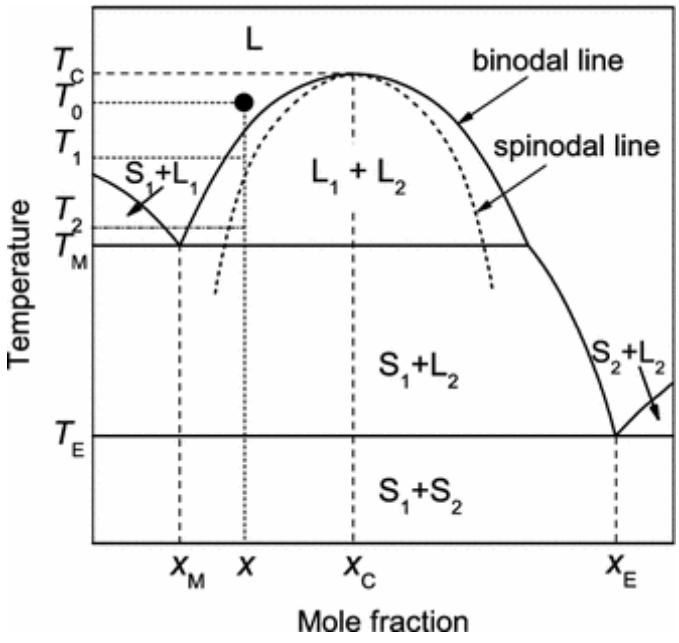

Figure 2.11 Stable miscibility gap in binary phase diagram showing critical temperature T_c, critical composition X_c, binodal and spinodal lines as well as monotectic temperature T_m [70].

After LPS, the composition of liquids L_1 and L_2 at equilibrium can be found using the lever rule along the binodal line. The two immiscible liquids coexist until the temperature drops below the monotectic temperature T_{mo} and the following reaction occurs as described in Equation 2.7 [67].

$$L_1 \rightarrow S_1 + L_2 \qquad 2.7$$

Derimow and Abbaschian [21] list numerous binary and ternary systems which contain a stable miscibility gap. These include, Al-Bi, Al-In, Cu-V, Ag-Ni, Co-Cu-Fe, Co-Cr-Fe, Al-Bi-Sn and dozens more.

2.2.2.2 Metastable liquid phase separation

Metastable LPS occurs during the presence of a metastable miscibility gap in an alloy phase diagram. In this case, the binode and spinode are located below the liquidus line, meaning that under equilibrium cooling conditions, solidification will occur before LPS [66]. The only way that LPS can be accessed in these alloys is to undercool the alloy below the metastable miscibility gap before solidification begins. Once sufficient undercooling has been achieved, the thermodynamic stability of the undercooled liquid (i.e. whether it has been undercooled into the metastable binodal region or the unstable spinodal regions) dictates the way in which the LPS reaction will proceed. Metastable miscibility gaps are often discernible because of a noticeably flatter liquidus line than that in other diagrams [71]. The first alloy systems found to contain a metastable miscibility gap were Co-Cu and Cu-Fe systems by Nakagawa et al. [72]. Since then, a larger volume of alloys exhibiting this behaviour have been discovered. A comparison of the phase diagrams of systems with a stable and metastable miscibility gap respectively is shown in Figure 2.12.

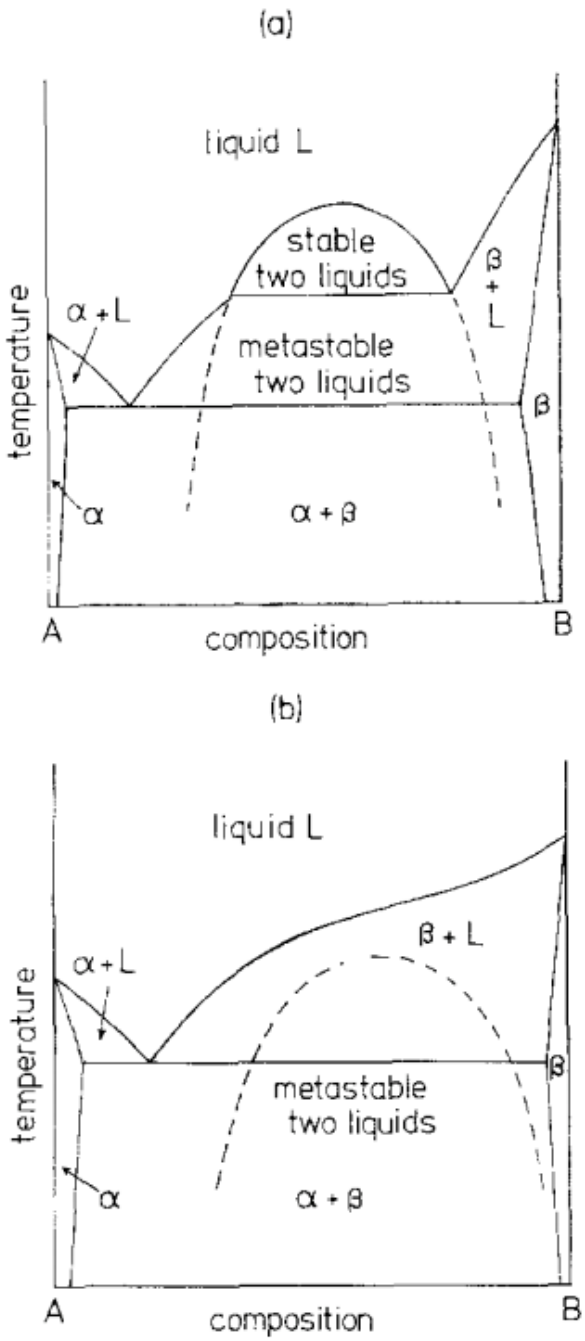

Figure 2.12 Diagram showing (a) stable miscibility gap with characteristic domed region above the monotectic temperature and (b) metastable miscibility gap with dashed binodal line below the liquidus line [73].

2.2.2.3 Factors determining final LPS solid microstructure

Given that binodal LPS proceeds through a nucleation and growth mechanism, effects of different physical forces and conditions on the final solidification morphology must be considered. Once droplets of L_2 have nucleated, growth is generally controlled by a diffusion mechanism where the supersaturated liquid L_1 rejects solute into the nucleated liquid. The growth rate of the droplets decreases with increasing cooling rate [67]. Ostwald ripening occurs in which

diffusion of solute from smaller dispersed particles to larger ones lowers overall interfacial energy between the two separated phases, and coalescence can also occur where colliding particles will merge to form a single larger one [67, 74]. Ratke and Deifenbach further describe some of the most important forces in altering the solidification microstructure [67]:

- Stokes sedimentation due to gravity occurs, with its importance increasing as the density difference between the two separated liquids increases. Stokes sedimentation is governed by Stokes equation [67, 75, 76].
- Temperature gradients can cause thermal convection to be established [67]
- Marangoni convection is established due to tension at the interface between the two separated liquids. The severity of this interfacial tension is influenced by gradients in solute concentration and temperature. This interfacial tension causes change in pressures in different areas of the liquid, leading to motion completely unrelated to gravitational forces [66, 67, 75, 77, 78].
- Preferential wetting of container walls or liquid-gas interface in the case of solidification without a container [67]
- Brownian motion [70]

2.2.3 Phase separation post-solidification – solid state decomposition

Miscibility gaps can also occur in the solid state. An example in the Ti-Cr phase diagram is shown in Figure 2.13 [79, 80]. The binode and chemical spinode are defined as they would be in a liquid. However, in the solid state, a coherent spinode is also defined, which constitutes the position of the spinode if elastic strain energy is included in the overall calculation of the system free energy [81]. In the solid state, spinodal decomposition can cause significant coherency stresses to develop if the decomposition product phases differ in crystal structure [82]. If the strain energy caused by these stresses is substantial, the position of the coherent spinodal curve may differ drastically from the position of the chemical spinodal [81]. Separation is therefore more difficult to initiate and a much higher undercooling is required for the spinodal decomposition to proceed [82]. As discussed in 2.1.2 and 2.1.3, techniques such as rapid solidification and high undercooling induce departures from equilibrium. Phases formed can often have substantially different compositions compared to those estimated by an equilibrium phase diagram. For example, a solid solution may form from the liquid with a higher concentration of solute than it would have at equilibrium (often due to high undercooling upon solidification). The solid solution is said to be supersaturated [26, 83]. After solidification, continual cooling below the

critical temperature at a specific composition will cause a solid solution to become supersaturated and thus, unstable. A decomposition reaction will follow through Equation 2.8, where a supersaturated solid solution α' decomposes into compositionally distinct solid solution phases α and β.

$$\alpha' \rightarrow \alpha + \beta \qquad 2.8$$

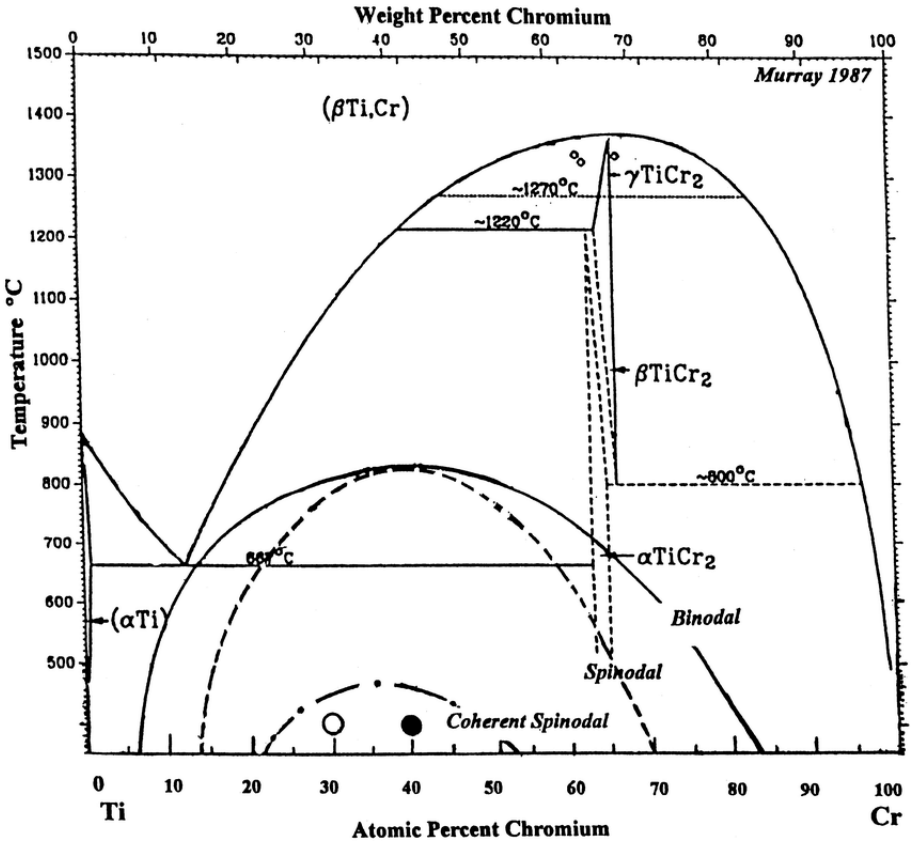

Figure 2.13 Ti-Cr phase diagram showing a miscibility gap in the solid state with the boundaries for binodal (nucleation and growth) and spinodal phase decomposition reactions [79, 80].

Because there is no fluid flow during solid state decomposition reactions, the factors which influence the morphology of the final decomposed microstructure are slightly different. As with LPS, the volume fraction of the two phases can be important. However, other factors previously discussed such as Marangoni convection, are no longer relevant. Instead, the nature of the interface between the new precipitating solid phase and the parent phase becomes a defining factor, as it is in defining the coherent spinodal curve.

2.2.3.1 Coherent, semi-coherent and incoherent interfaces

In many cases, the shape of precipitates created during solid state decomposition depends on interface coherency. In highly simplified terms, a

fully coherent interface is characterised by the two crystal structures matching perfectly at the interface. The crystal structures of both phases at the interface must be the same. Additionally, the lattice parameters (spacings between unit cells in a crystal structure) must be very near identical. When there is a slight difference in lattice parameter (lattice mismatch) the lattice will deform slightly to maintain matching crystalline planes at the interface. This are termed coherency strains. The degree of lattice mismatch δ_{lm} can be defined as a percentage through Equation 2.9.

$$\delta_{lm} = \left| \frac{d_{ip(B)} - d_{ip(A)}}{d_{ip(B)}} \right| \times 100 \qquad 2.9$$

where $d_{ip(A)}$ and $d_{ip(B)}$ represent lattice parameters of phases A and B respectively which are separated by an interface. Above a certain degree of lattice mismatch, misfit dislocations are required to lower the interface energy. The presence of these dislocations defines a semi-coherent interface. Finally, if the lattice mismatch exceeds 25%, the interface becomes fully incoherent. The crystal structures of the phases at the interface are now very different structurally and form high-energy boundaries [26]. This, along with other factors such as anisotropies in interfacial energy and the mechanical properties of the two phases, influence the final precipitate shape as it forms in the original material [84]. If the precipitated phase is fully coherent with the parent phase, and the lattice parameters are near equal, interface energy can be minimised if the precipitate forms in a spherical shape [26]. For example, a sphere is also more likely if the atoms of the precipitated phase are of similar size to those of the parent phase. If the atoms in the precipitated phase differ significantly in size, a plate-like precipitate is more likely to form due to a higher lattice misfit [83].

2.2.3.2 Kinetics in solid-state diffusion reactions

Finally, after solidification is complete and phase transformations have been initiated, diffusion based transformations such the coarsening that occurs after decomposition reactions, are considered significant only while the alloy in question has a temperature above a minimum of $0.5T_l - 0.7T_l$ [85, 86]. Below such temperatures, diffusion processes are kinetically hindered and cease to change the microstructure further. This is the case regardless of whether the initial reaction occurred via a binodal or spinodal mechanism.

2.3 Experimental methods for non-equilibrium processing

The final prevailing microstructure after solidification is primarily dependent on two key factors. These are the ease of nucleation (i.e. the conditions in the material which promote nucleation in the liquid phase) and the rate of heat extraction which dictates the progression of the solidification front [87]. Techniques have been devised to influence both of these conditions. Five are briefly introduced here. These include rapid-quenching methods such as splat-quenching and melt-spinning as well as techniques which inhibit heterogenous nucleation, including glass-fluxing, electromagnetic levitation (EML), and drop-tube processing.

2.3.1 Rapid-quenching techniques

The most simple example of a rapid-quenching technique is splat-quenching, where a small volume of liquid metal is propelled against a chilled landing surface. The liquid spreads upon impact at speeds which exceed the rate of heat transfer from the sample. Solidification starts at the meeting point between the liquid and the chosen landing surface [16]. A continuous process similar to this is melt-spinning. A liquid metal is poured onto a quickly rotating surface, often a spinning wheel. A high cooling rate, and a large temperature gradient may be achieved the contact point between the wheel surface and the melt [87]. The melt spreads across the wheel as well, thinning the liquid layer and increasing the overall cooling rate [16]. An example schematic of a melt-spinning apparatus is shown in Figure 2.14.

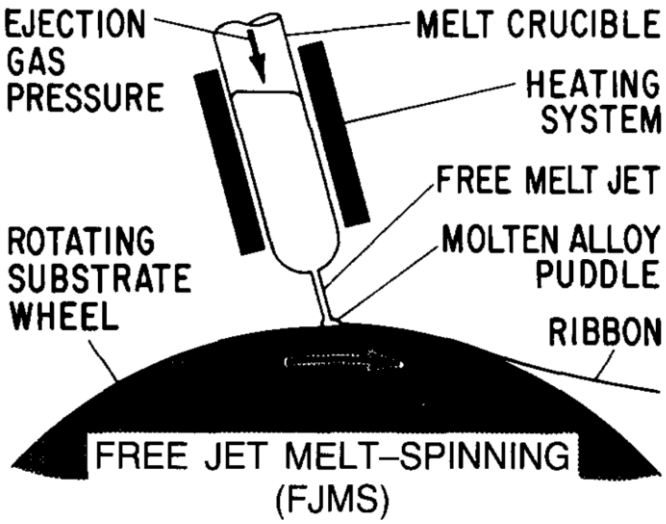

Figure 2.14 Schematic of one possible configuration of the melt-spinning rapid solidification process [87].

Importantly though, the removal of thermal energy in the rapid manner described often causes the inhibition of kinetic processes and therefore, gives less time for phase transformations to occur. Such a restriction can cause substantial morphology differences, particularly in the solid state where diffusion of solute is much slower than in the liquid.

2.3.2 Inhibition of heterogenous nucleation

While techniques such as melt-spinning and splat-quenching can ensure high cooling rates, the interface between the liquid metal and chill surface provides a high volume of heterogenous nucleation sites [87]. Heterogenous nucleation tends to occur more readily than homogenous nucleation due to a lower energy barrier [28], which lowers the undercooling attainable in the liquid before nucleation. Inhibition of heterogenous nucleation therefore often enhances the undercooling achieved before solidification which directly determines the solid phase that forms from the liquid. Furthermore, higher undercooling promotes the rapid growth of dendrites, causing phenomena such as solute trapping described above (see section 2.1.3) [88]. Many techniques have hence been devised to diminish the possibility of heterogenous nucleation.

Glass-fluxing involves the melting of a metal alloy in tandem with a fluxing agent. Simple borosilicate glass or even commonly available soda-lime glass have been used as fluxing agents for undercooling experiments, along with more complicated mixtures. Inclusion of the glass contains the melt and keeps it separated from potential heterogenous nucleation sites, which increases the obtainable undercooling [18]. Because of this, high cooling rates are not necessary to raise undercooling and access metastable solidification microstructures and cooling can be restricted to very slow rates if desired [89]. Furthermore, oxide impurities in the melt, which have been shown to cause heterogenous nucleation [90], can dissolve in the molten flux and no longer provide heterogenous nucleation sites [91].

Electromagnetic levitation (EML) techniques involve containerless solidification of a metallic melt through suspension of an alloy droplet in an electromagnetic field. In this way, nothing is required to contain the melt and heterogenous nucleation sites on the container walls are eliminated. Furthermore, the apparatus can be kept under high vacuum or an inert gas atmosphere to prevent oxidation, and temperature is directly measurable through methods such as pyrometry [18]. Similarly to glass-fluxing, the alloy sample can be cooled very slowly during the experiment. Unfortunately however, a key downside regarding EML is the strong stirring induced by the magnetic field in the liquid metal. This can have a dramatic effect on the eventual solidified

microstructure. For example, Cao et al. [92] found drastic differences between structures formed in EML processed liquid phase separating Co-Cu alloys compared to conventional solidification without such stirring. The shear rate has also been found to increase the nucleation rate in some alloys during solidification [93]. Finally, growth velocities in solidifying Ni_2B alloys were found to increase more rapidly during EML processing than other methods such as electrostatic levitation (ESL), which does not apply a magnetic field and, therefore does not induce stirring. This is due to the convection induced in the liquid droplets during EML [94]. Such forces are important to consider when considering the final microstructures achieved using various solidification techniques. A basic schematic describing the key components of the aforementioned undercooling experiments is provided in Figure 2.15.

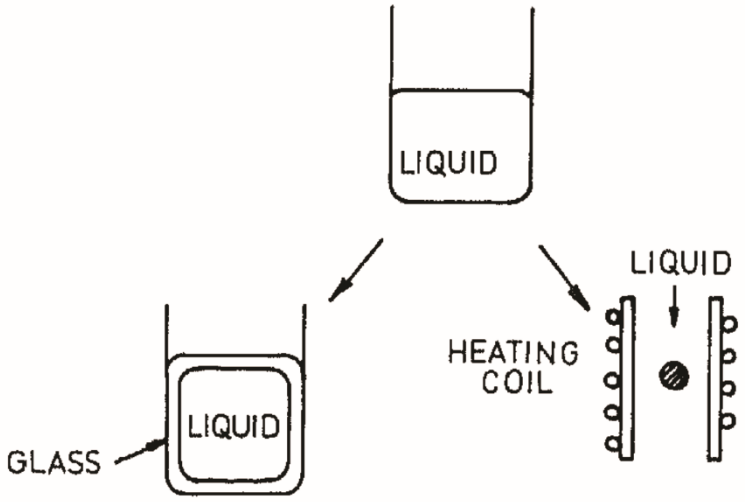

Figure 2.15 Summary of key components of glass-fluxing (left) and electromagnetic levitation (right) undercooling experiments for solidification of liquid alloys adapted from [18].

2.3.3 Drop-tube processing

Drop-tube processing and other similar techniques like gas-atomisation can combine rapid solidification with a containerless environment to further enhance undercooling achievable in metallic melts. The system operates by forcing a liquid melt through a nozzle or small orifices. This disperses the melt into approximately spherical droplets of varying diameters, which solidify in free-fall through either a vacuum (such an apparatus is usually referred to as a long drop-tube) or an inert gas atmosphere [18]. In the gas atmosphere, the drag forces on the droplet mean that it attains terminal velocity very rapidly and does not require a long time to solidify due to the gas acting as a heat transfer fluid. This means such an apparatus may be shorter in length that in the case of

solidification in vacuo. It is therefore often referred to as a short drop-tube. In both cases, the solidification occurs into a negative temperature gradient. Such a method has key advantages. Drop-tube processing allows research into solidification in microgravity without the need for expensive space-based research [71]. Because the droplet solidifies in freefall, heterogenous nucleation sites on container walls are removed. The apparatus also provides more control of experimental variables during the solidification process than similar methods such as gas atomisation [19], and can therefore be used to study, on a smaller scale, possible products of industrial atomisation processes. Some disadvantages of this method include the minimal ability to log the cooling profile or history of specific droplets, or to measure the instantaneous temperature of the droplets in-situ as one can in EML or glass-fluxing experiments. Figure 2.16 shows an example of a fully realised short drop-tube apparatus.

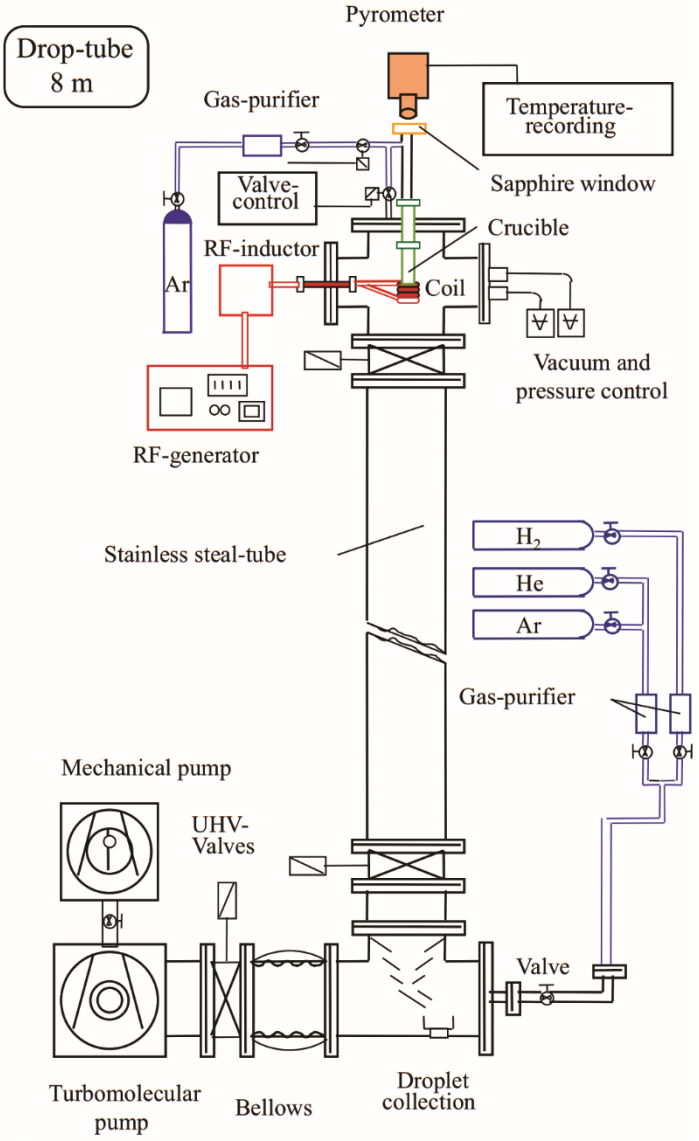

Figure 2.16 Example schematic of short drop-tube apparatus [95].

2.4 Introduction to high-entropy alloys

The first published research on HEAs was conducted separately by the research groups of Brian Cantor [4] and Jien-Wei Yeh [5] in 2004. Cantor et al. [4] began by creating 20-element and 16-element alloys with each element at 5 at% and 6.25 at% respectively. They later investigated the microstructures of quintenary and senary equiatomic alloys based on the CoCrFeMnNi equiatomic alloy. Additions of Nb, Ge, Cu, Ti and V in equiatomic proportions were made to investigate the impact of additional alloying elements. The 20-element and 16-element alloys were found to consist of a large number of solid solution and intermetallic phases and were, as a result, very brittle. However, a large proportion of the microstructure was taken up by a single FCC phase with high occurrence of Co, Cr, Fe, Mn, and Ni. Many of the subsequent alloys based off of CoCrFeMnNi consisted primarily of FCC and BCC (Body Centred Cubic)

solid solutions, and the number of phases present was much lower than that allowed thermodynamically [4]. This runs counter to the common assumption that the use of large amounts of principal metals in an alloy results in a microstructure saturated with intermetallic compounds [5, 96]. Yeh at al. [5] concurrently proved this phenomenon, casting alloys such as AlCoCrCuFeNi and finding only simple FCC and BCC structures. The team suggested that configurational entropy was the cause of microstructural simplification. Configurational entropy ΔS_{conf} of an equiatomic alloy can be defined in Equation 2.10 assuming a random solid solution.

$$\Delta S_{conf} = Rln(n) \qquad 2.10$$

where R is the molar gas constant. The equation indicates that as the number of elements (n) in the alloy increases, configurational entropy increases. It is thought that solid solutions are stabilised when the entropy increases to a point whereby the formation of a random solid solution competes with the enthalpy of formation of easily formed intermetallic compounds like AlTi and AlNi divided by their respective melting points. This hypothesis was proposed by Yeh et al. and forms the basis of one of the four core effects of HEAs. It is also one of the reasons the term HEA is used as a name for alloys of the kind described [5].

2.4.1 Definition of HEAs

The definition of a HEA is difficult to pin down. In their seminal paper, Yeh et al. [5] initially define HEAs compositionally as alloys possessing five or more principal elements each with compositions of 5-35 at%. In later work [97, 98], they further their definition to include a minimum configurational entropy in the alloy of about $1.5R - 1.61R$, allowing solid solution formation to compete with the growth of easily forming intermetallics. Alloys with configuration entropy lower than this are dubbed medium and low entropy alloys. Furthermore, the increase in configurational entropy continues to be significant for each further element addition (each increase in n) only until the 13th element. Therefore, Yeh et al. [5, 97] suggest a maximum limit of 13 elements for use in developing HEAs. Miracle and Senkov [99] note, however, that this definition is difficult to utilise due to the fact that configurational entropy can change with temperature.

For the purposes of this investigation, the definition of HEAs was narrowed to include alloys with 5-8 principal elements (composition of each principal element above 5 at%) which form a solid solution or multiple solid solutions upon solidification without intermetallics present.

2.4.2 Four core effects of HEAs

Four core effects have been hypothesised to attempt to explain the physical metallurgy of HEAs compared to conventional alloys. They are the high entropy effect, the severe lattice distortion effect, the sluggish diffusion effect and the cocktail effect [3].

2.4.2.1 High entropy effect

During metal solidification under equilibrium conditions, possible states compete for formation, with the state with the lowest (most negative or least positive) Gibbs free energy being formed preferentially. These equilibrium states are solid solutions (ordered or disordered), intermetallic compounds, and elemental phases, a solid solution of one element [3, 97]. Using a more complex analysis than that presented in 2.4, it can be shown that the high configuration entropy in HEAs avoids the formation of intermetallic compounds in favour of ordered or disordered solid solutions [3, 99]. Following the reasoning outlined by George et al. [2] the Gibbs free energy of solid solutions ΔG_{mix}^{ss} and intermetallic compounds ΔG_f^{IM} can be represented by Equation 2.11 and Equation 2.12.

$$\Delta G_{mix}^{ss} = \Delta H_{mix}^{ss} - T\Delta S_{mix}^{ss} = \Delta H_{mix}^{ss} - T\Delta S_{conf} = \Delta H_{mix}^{ss} - RTln(n) \qquad 2.11$$

$$\Delta G_f^{IM} = \Delta H_f^{IM} - T\Delta S_f^{IM} \qquad 2.12$$

where ΔH_{mix}^{ss} is the enthalpy of mixing of the solid solution phase, ΔS_{mix}^{ss} is the entropy of mixing of the solid solution phase ΔS_{conf} is the change in configurational entropy inherent in the formation of a solid solution, ΔH_f^{IM} is the enthalpy of formation of the intermetallic compound and ΔS_f^{IM} is the change in entropy inherent in the formation of the intermetallic compound. If the intermetallic is assumed to be perfectly ordered, $-T\Delta S_f^{IM} = 0$. Hence, to stabilise the solid solution phase (i.e. make $\Delta G_{mix}^{ss} < \Delta G_f^{IM}$), the $-T\Delta S_{mix}^{ss}$ value must be close to or higher (more negative) than ΔH_f^{IM}. Following Equation 2.10 and Equation 2.11, $-T\Delta S_{mix}^{ss}$ is assumed to be equal to $-RTln(n)$, so increasing the number of elements, and/or increasing the temperature, lowers ΔG_{mix}^{ss} [2, 5]. Murty et al. [3] note that the smaller the difference between enthalpies of mixing of the different binary element combinations, the simpler the microstructure that can form (one solid solution as opposed to two or more phases).

It is important to take into account that this argument does not fully describe the behaviour of all quintenary alloys. Indeed, it is not the case that all alloys with five or more principal elements form only simple solid solutions. The resultant phases formed after solidification can also depend heavily on solidification kinetics, diffusion rates, and temperature [2]. Other entropic (vibrational, magnetic etc…) contributions rather than simply configuration entropy must also be considered [3]. Moreover, based on Equation 2.11 lowering the enthalpy of mixing can be just as important as raising the entropy for the reduction of Gibbs free energy and production of a solid solution [2].

2.4.2.2 Severe lattice distortion effect

Due to the fact that HEAs are made up of numerous atoms, each with its own characteristic bonding and atomic size, the crystal lattices formed in HEAs tends to be heavily distorted compared to those of binary alloys. Because of this, HEAs have generally been found to possess low conductivity of electricity and heat as well as a low sensitivity of these properties to rises or falls in temperature [3, 99]. This phenomenon also has the added effect of making XRD diffraction peaks more diffuse as the amount of added elements increases, because the distorted crystal planes cannot be resolved as accurately [100]. A representation of lattice distortion in a HEA as opposed to an elemental crystal is shown in Figure 2.17.

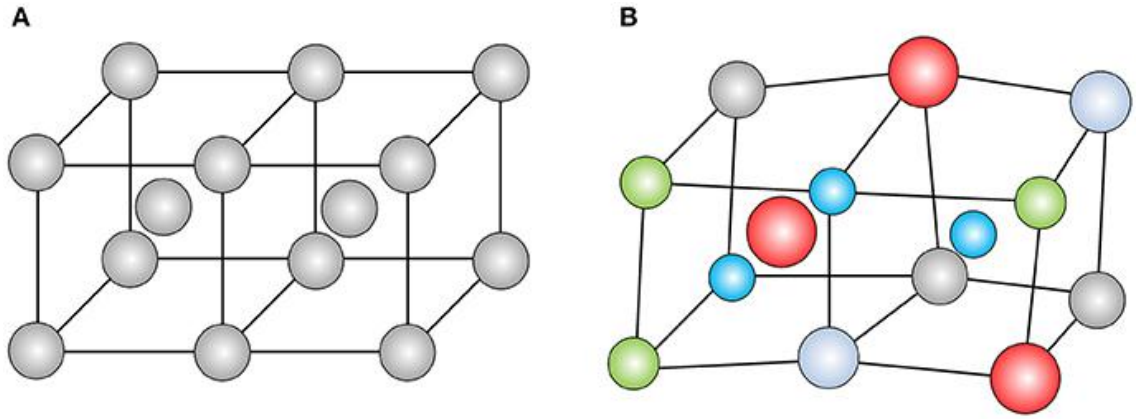

Figure 2.17 Graphic representation of crystal lattice in (a) pure element and (b) HEA with lattice distortion as a result of different element additions [101].

2.4.2.3 Sluggish diffusion effect

It was first hypothesised by Tsai et al. [102] that diffusion required for phase transformations in HEAs would generally occur more slowly than in binary alloys because of the difference in atoms occupying lattice sites adjacent to vacancies. The authors used a pseudo-binary diffusion couple technique to determine the rate of diffusion of each element in CoCrFeMnNi. These results

were compared to the diffusion of these elements in conventional alloys. The team concluded that the HEA diffusion required higher activation energy and also possessed a lower normalised diffusion coefficient, pointing to sluggish diffusion being a phenomenon in HEAs. Calculated diffusion data from this investigation is shown in Figure 2.18. This conclusion was strengthened in part, by Beke et al. [103], who reanalysed the diffusion data provided by Tsai et al. [102] and confirmed that diffusion coefficients were noticeably lower for self-diffusion of elements in the HEA as opposed to simpler alloys. However, they argue that the data are not as clear when it comes to activation energies being higher than those in conventional alloys. Other studies such as the bulk tracer diffusion experiments of Vaidya et al. [104] conclude that sluggish diffusion in HEAs cannot be assumed to be purely a result of how many elements are added to the alloy. Instead, it may often be based on the specific element added to the alloy, and how this affects the overall thermodynamic properties of the alloy.

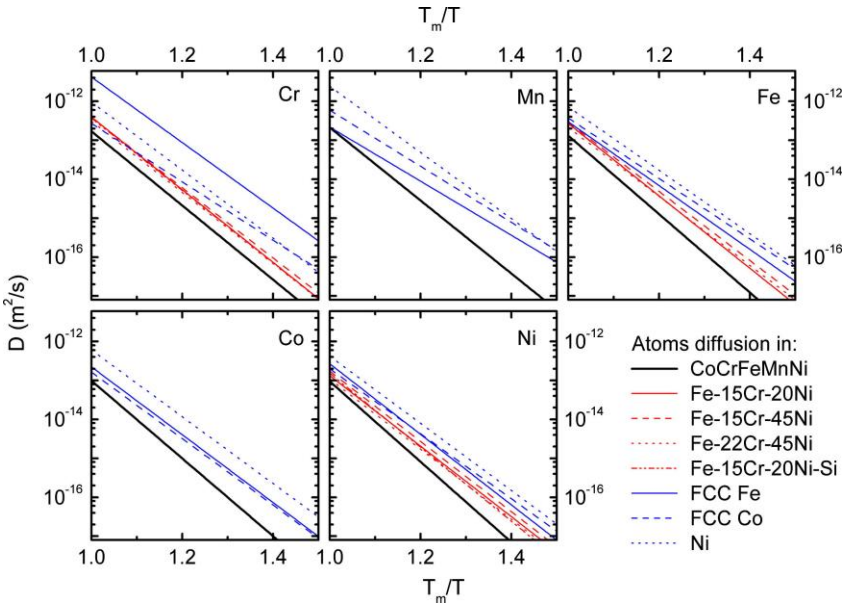

Figure 2.18 Diffusion coefficients of Co, Cr, Fe, Mn and Ni in different alloys at varying temperatures. The diffusion coefficient of each element is lower at all temperatures for diffusion in CoCrFeMnNi compared to all other alloys, demonstrating sluggish diffusion in HEAs [102].

2.4.2.4 Cocktail effect

The cocktail effect describes changes in alloy properties of HEAs and other multicomponent alloys that are unexpected and occur based on the interactions between the numerous alloying elements that make up these alloys. The term was coined by Ranganathan [3, 6] in a 2003 paper to describe these effects. These properties can be unexpected and are often unpredictable through

extrapolation and other forms of logical reasoning. However, they are also sometimes highly desirable in alloy design [99].

2.4.3 Solid solution formation criteria Hume-Rothery parameters

The criteria for the formation of a HEA in this work is the formation of a simple solid solution phase without intermetallic compounds present. In addition to the composition definition given by Yeh et al. [5], Hume-Rothery (H-R) parameters have been routinely utilised, as they are in binary alloys, to predict the likelihood of solid solution formation in lieu of intermetallic compounds. These parameters were first proposed by Hume-Rothery in 1967. The resultant translations of each parameter for binary alloys have become a relatively simple method to predict formation ability of solid solutions [105, 106]. The criteria involve difference in atomic size, electronegativity, valence electron concentrations and other parameters [107, 108]. In binary substitutional solid solutions, the rules are defined by Smith and Hashemi [109]:

- Difference in atomic radii should not exceed 15% to ensure some solubility. If solubility across the whole range of compositions is desired, a maximum difference of less than 8% should prevail.
- Both pure elements involved must have a similar original crystal structure.
- Both solute and solvent should have the same valency.
- Both solute and solvent should have similar electronegativity.

In HEAs, other key values used in prediction of solid solution formation include thermodynamic parameters such as the enthalpy and entropy of mixing [110].

2.4.3.1 Enthalpy of mixing

The enthalpy of mixing can be estimated based on composition for each binary pairs in a HEA using a sub-regular solution model in Equation 2.13 from Miedema's scheme and fitting the enthalpy of mixing with interaction parameters (Ω_n) [111]:

$$\Delta H_{i.j}^{mix} = 4\left(\sum_{n=0}^{3} \Omega_n \left(X_i - X_j\right)^n\right) X_i X_j \qquad 2.13$$

To apply this method to multicomponent alloys. Takeuchi and Inoue [111] consider the enthalpy of mixing as the sum of all the enthalpies of mixing between each binary pair involved. This is shown in Equation 2.14.

$$\Delta H_{Alloy}^{mix} = \sum_{\substack{i=1 \\ i \neq j}}^{{}^{n}C_2} \Delta H_{i.j}^{mix} \quad 2.14$$

The term $\Delta H_{i.j}^{mix}$ is the enthalpy of mixing for each binary pair present in the multicomponent alloy. To apply Equation 2.14 to a binary pair within a multicomponent alloy, the compositions of the i'th and j'th components X_i and X_j are normalised using Equation 2.15 and 2.16. The enthalpy of mixing of the binary pair can then be calculated using Equation 2.17 [111]:

$$X_{i,nor} = \left(\frac{X_i}{X_i + X_j}\right) \quad 2.15$$

$$X_{j,nor} = \left(\frac{X_j}{X_i + X_j}\right) \quad 2.16$$

$$\Delta H_{i.j}^{mix} = 4\left(\sum_{n=0}^{3} \Omega_n \left(X_{i,nor} - X_{j,nor}\right)^n\right) X_i X_j \quad 2.17$$

2.4.3.2 Atomic size difference

Zhang et al. [110] were among the first groups to utilise atomic size difference to predict the formation of solid solutions in HEAs. The atomic size difference in a multicomponent alloy δ can be calculated from Equation 2.18 and Equation 2.19, where r_i is the atomic radius of the i'th component and $\bar{r}$ is the weighted average of the atomic radii in the alloy [112].

$$\delta = 100\sqrt{\sum_{i=1}^{n} X_i(1 - \frac{r_i}{\bar{r}})^2} \quad 2.18$$

$$\bar{r} = \sum_{i=1}^{n} X_i r_i \quad (2.19)$$

2.4.3.3 Valence electron concentration

Valence electron concentration (VEC) is the number of electrons in the valence band of an atom of a particular species. VEC is calculated through Equation 2.20, where $(VEC)_i$ is the valence electron concentration of the i'th component [112].

$$VEC = \sum_{i=1}^{n} X_i (VEC)_i \quad (2.20)$$

2.4.3.4 Electronegativity difference

The difference in Pauling electronegativity between the components in the alloy is defined by Equation 2.21 and Equation 2.22, where χ_i is the electronegativity of the i'th component and $\bar{\chi}$ is the weighted average of the electronegativity in the alloy [112].

$$\Delta\chi = \sqrt{\sum_{i=1}^{n} X_i (\chi_i - \bar{\chi})^2} \quad (2.21)$$

$$\bar{\chi} = \sum_{i=1}^{n} X_i \chi_i \quad (2.22)$$

2.4.3.5 Entropy of mixing

The entropy of mixing was also used initially by Zhang et al. to attempt to predict solid solution formation in multicomponent alloys [110]. The entropy of mixing can be represented for a mixture of n elements through Equation 2.23, a generalised form of Equation 2.4.

$$\Delta S_{Alloy}^{mix} = -R \sum_{i=1}^{n} X_i \, lnX_i \qquad 2.23$$

Numerous research groups have analysed large numbers of HEAs to try to formulate conditions for solid solution formation based on the H-R parameters, enthalpy of mixing and entropy of mixing. In terms of H-R parameters, atomic size distribution is usually of prime importance, with VEC and $\Delta\chi$ primarily used to distinguish between crystal phases (FCC and BCC) rather than intermetallic vs HEA behaviour. The results of some of these works are summarised by Murty et al. [3] and are compiled in Table 2.1.

Table 2.1 Thermodynamic and H-R parameter ranges used to produce HEA solid solution phases

Study	ΔH_{Alloy}^{mix} /kJ mol^{-1}	ΔS_{Alloy}^{mix} /J kmol^{-1}	δ /%
[112]	$-22 \leq \Delta H_{Alloy}^{mix} \leq 7$	$11 \leq \Delta S_{Alloy}^{mix} \leq 19.5$	$0 \leq \delta \leq 8.5$
[113]	$-11.6 \leq \Delta H_{Alloy}^{mix} \leq 3.2$		$\delta \leq 6.6$
[114]	$-8.8 \leq \Delta H_{Alloy}^{mix}$		$\delta \leq 2.77$
[115]	$-15 \leq \Delta H_{Alloy}^{mix} \leq 5$		$0 \leq \delta \leq 5$
[116]	$-50 \leq \Delta H_{Alloy}^{mix} \leq 40$		$6 \leq \delta \leq 10$

2.4.4 Potential applications for high-entropy alloys

Since their discovery, HEAs have been the subject of an incredible volume of research, encompassing the development of alloys for specialised structural and functional applications via careful selection of starting elements, element ratios, and thermomechanical processing [3]. Structurally, some examples include alloys that attempt to overcome the strength-ductility trade-off encountered in conventional alloys [7, 8] and alloys that function well in high temperature and high radiation environments [9-12]. Functional HEAs have been developed with enhanced magnetic [117] and catalytic properties [13, 14]. Such applications make HEAs prime candidates for further study. Before the full extent of their utility in various applications can be understood, the fundamentals of their behaviour in different environments must be elucidated. Particularly, more research is required to understand how such alloys behave during the non-equilibrium solidification processing discussed in this chapter. An understanding of any differences in solidification and phase transformation of

HEAs compared to more compositionally simple binary and ternary alloys is also important to explore. In Chapter 3, we will begin to review some of the previous literature regarding non-equilibrium processing of HEAs, the phase transformations that result, and similarities and differences between these compositionally complex alloys and the more simple alloys currently utilised extensively in industry.

Chapter 3 – Literature Review

3.1 Phase transformations in rapidly solidified alloys

The exponentially increasing volume of literature involving alloys, their properties, and production methods means that a full review of the state of such research is not possible in this work. Instead, this chapter focuses on a discussion of the literature involving non-equilibrium phase transformations in some simple alloys and HEAs during solidification, and the experimental techniques that have been used to study them. The primary transformations discussed are LPS, solute trapping/partitionless solidification, and spontaneous grain refinement. To provide context regarding some of these transformations in HEAs, and for the purposes of comparison, the chapter initially discusses such transformations during solidification of more simple binary and ternary alloys. It also utilises findings from literature to select an appropriate alloy for study in accordance with the investigation aims.

3.2 Liquid phase separation

LPS is routinely observed in simple binary alloys as well as more compositionally complex alloys. At a critical temperature (or a critical undercooling for metastable LPS) the alloy melt de-mixes into two liquids of distinct composition and thermophysical properties (see section 2.2.2). The presence of two liquids of differing composition in the microstructure before solidification can yield final solidification microstructures that are not otherwise obtainable in alloys that do not undergo LPS.

3.2.1 Obtainable microstructures following LPS in alloys

Owing to the many different forces at play in the final LPS microstructure upon solidification (see section 2.2.2.3), numerous microstructures may be obtained in alloys exhibiting LPS in the stable and metastable states depending on processing conditions. For example, in a drop-tube and during other microgravity experiments such as EML processing, Stokes motion is eliminated or significantly reduced and forces such as Marangoni convection become more dominant. The interaction between these forces and changes in cooling rate and undercooling can provide conditions favourable for production of certain microstructures. Two prominent examples are core-shell structures and fine dispersions.

3.2.1.1 Core-shell structures

Core-shell structures are one of the two main microstructures obtainable via LPS in an immiscible alloy melt. The first instance of core-shell structures forming in immiscible alloys immediately raised questions about the rules governing the solidified microstructure. Of particular interest is which phase forms the core and shell respectively upon separation. In two microgravity experiments performed aboard rockets in 1979, Ahlborn and Lohberg, and Potard [66, 118, 119] solidified Al-In alloys, which feature a stable miscibility gap. A similar composition is used in both studies, and core-shell LPS structures were formed in both cases. Surprisingly however, the Al-rich phase was found to form the core in the former study, and the shell in the latter. In spite of this discrepancy, both groups agreed that wetting behaviour with the crucible containing the liquid alloy had an instrumental effect on the eventual structure. Two decades later, Wang et al. [120] solidified two Cu-Fe based alloys ($C_{0.6}Cu_{65}Fe_{31.4}Si_3$ and $C_{0.6}Cu_{45}Fe_{51.4}Si_3$) via containerless gas atomisation. Cooling rates on the order of 10^3 K s^{-1} – 10^4 K s^{-1} were achieved. In the Cu-rich alloy, most of the droplets contain a Fe-rich phase in the core and a Cu-rich shell (Figure 3.1a), while in the Fe-rich alloy, the Cu phase forms the core with a shell of Fe-rich phase and a further outside layer of Cu-rich phase (Figure 3.1c). Some droplets were found to also contain multiple cores (Figure 3.1b). The authors concluded that it was the volume fraction that determined phase placement, with the lower volume fraction phase forming the droplet core. They also concluded that the structure forms after LPS and before solidification, with the temperature gradient between the droplet centre and the outer edge causing a drop in interfacial tension near the middle. Given that Marangoni migration causes the droplets to move to the area with the lowest interfacial tension, the minority phase droplets will coalesce in the centre to form a core (visualised in Figure 3.1d). The velocity of the droplets due to Marangoni motion was calculated to be much higher than those due to Stokes motion, showing the dominance of the Marangoni migration when the material is in freefall.

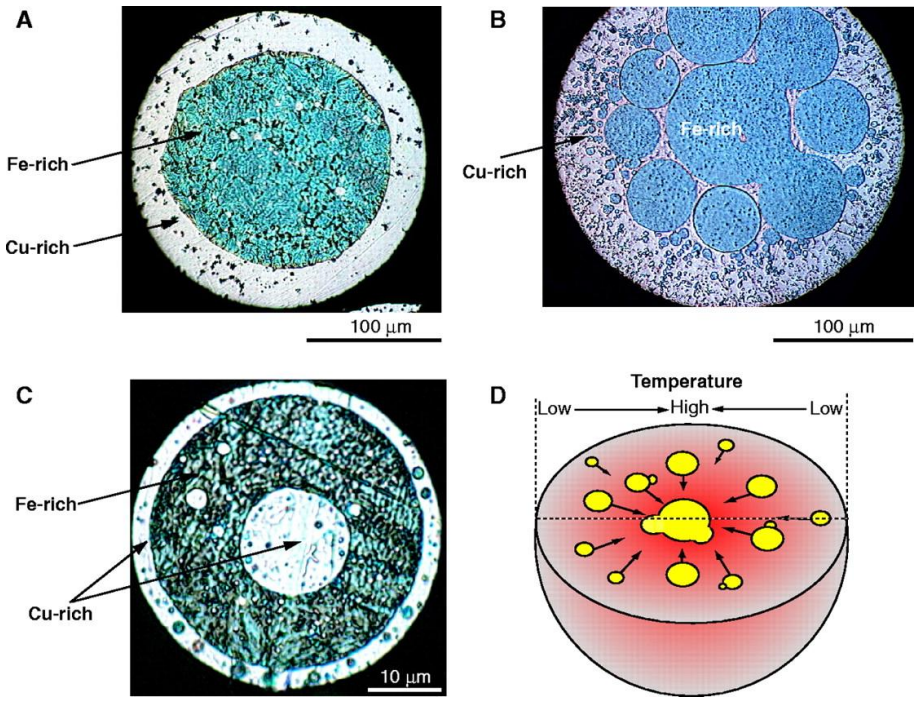

Figure 3.1 Core-shell structures obtained in gas atomisation of Cu-Fe rich alloys (a) $C_{0.6}Cu_{65}Fe_{31.4}Si_3$ fully formed core (b) $C_{0.6}Cu_{65}Fe_{31.4}Si_3$ multi-core (c) $C_{0.6}Cu_{45}Fe_{51.4}Si_3$ fully formed onion structure (d) Representation of core coalescence due to thermal gradient [120].

Core-shell structures can be used as valuable composites. Wang et al. [121] used gas atomisation to successfully create core-shell droplets of Cu-Fe-Cr-C alloys, an attempt at creating a composite microstructure in which one phase was Cu-rich (conducting) and the other was a form of stainless steel.

Dai et al. [122] conducted a study on binary Al-Bi, ejecting $Al_{90}Bi_{10}$ melt droplets through an orifice into silicon oil at room temperature. They observed Al-rich cores and Bi-rich shells. The team propose that the Bi-rich phase always forms the shell due to the high affinity Bi has for surface segregation. Core-shell structures were more perfect (annular) when high superheat and low droplet size avoided sedimentation due to gravity and increased the time for Marangoni migration. In Al-Bi-Sn ternary alloys, core-shell structures with Al-rich cores and Bi-Sn-rich shells form, and the same trend in core-shell formation with superheating and cooling rate is observed [123]. The Sn is preferentially situated in the Bi-rich phase, the authors note, due to a tendency to de-mix with Al. Multiple spheres of one liquid present in the other are described as core-shell structures where the Al-rich liquid has not had time to coalesce completely before solidification. The time allowed for coalescence depends on how large the range of immiscibility is (i.e. the range between the de-mixing temperature and the liquidus temperature at the given composition) [124].

Composition also impacts on core-shell forming ability in immiscible alloys droplets. Wang et al. [125] solidified Cu-Pb and Fe-Sn (stable miscibility gaps) alloys at varying compositions using a drop-tube. Core-shell structures were found near the critical point (the point where there is the largest time between LPS and solidification) in droplets mostly above about 150 μm in diameter. As composition shifts away from the critical point droplets must become larger (lower cooling rate) to allow core-shell structures to form. Furthermore, the switch in which liquid phase is the minority phase occurs at the critical point, with differing viscosities and other properties of the phases changing the way core-shell structures are formed, or not. The impact of composition on core-shell formation is demonstrated in Figure 3.2 for Cu-Pb alloys. Core-shell structures are readily observed in drop-tube processed droplets when the composition is at or near to the critical point. As the distance in composition from the critical point increases, a smaller droplet (i.e. a higher cooling rate) is required to initiate core shell structure formation. For example, a larger droplet of Cu-55%Pb will solidify dendritically, while core-shell structures are observed in smaller droplets at the same composition. At the extremities in composition, radial dendritic growth, or the formation of minority phase droplets (without coalescence in to a core-shell structure) occurs. In all cases, the very smallest droplets (i.e. the highest cooling rates) cause the formation of finely dispersed structures no matter the composition selected [125].

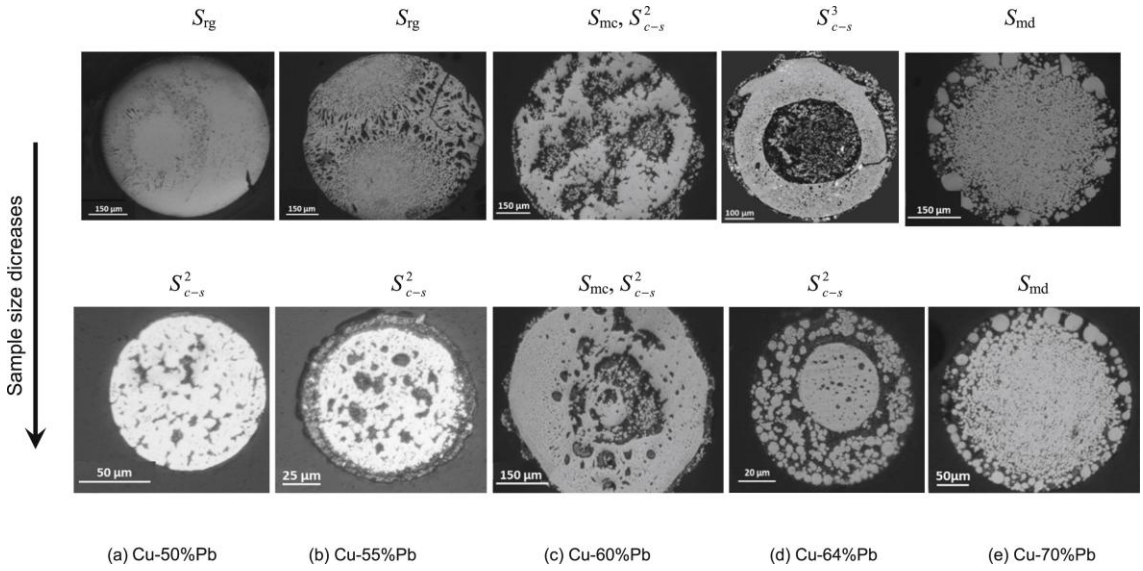

Figure 3.2 Impact of sample size and composition on structure formation in drop-tube processed Cu-Pb alloy with stable miscibility gap [125]. Core-shell structures are found at compositions near the critical composition which allows more time for coalescence before solidification.

Wang et al. [126] solidified $Fe_{47.5}Cu_{47.5}Sn_5$ in a drop tube. The results are shown in Figure 3.3. Intermediate droplet sizes between 800 μm and 100 μm displayed core-shell morphology, and finely dispersed structures were seen in smaller droplets. Simple 2-layer core-shell (see Figure 3.3b) and core-shell-corona structures (such as those in Figure 3.1c above) can only form if there is enough time for this Marangoni migration to occur before solidification. Simple two-layer core-shell structures require longer than core-shell-corona particles. The simple two-layer core-shell structure is deemed to be the most stable structure present.

This trend in structural formation with cooling rate was partly echoed by Yan et al. [127] in their study of Al-Sn-Cu alloys where the incidence of core-shell structures peaked at intermediate droplet sizes. The higher melting point Al-rich phases form the core of the simple two-layer core-shell structures.

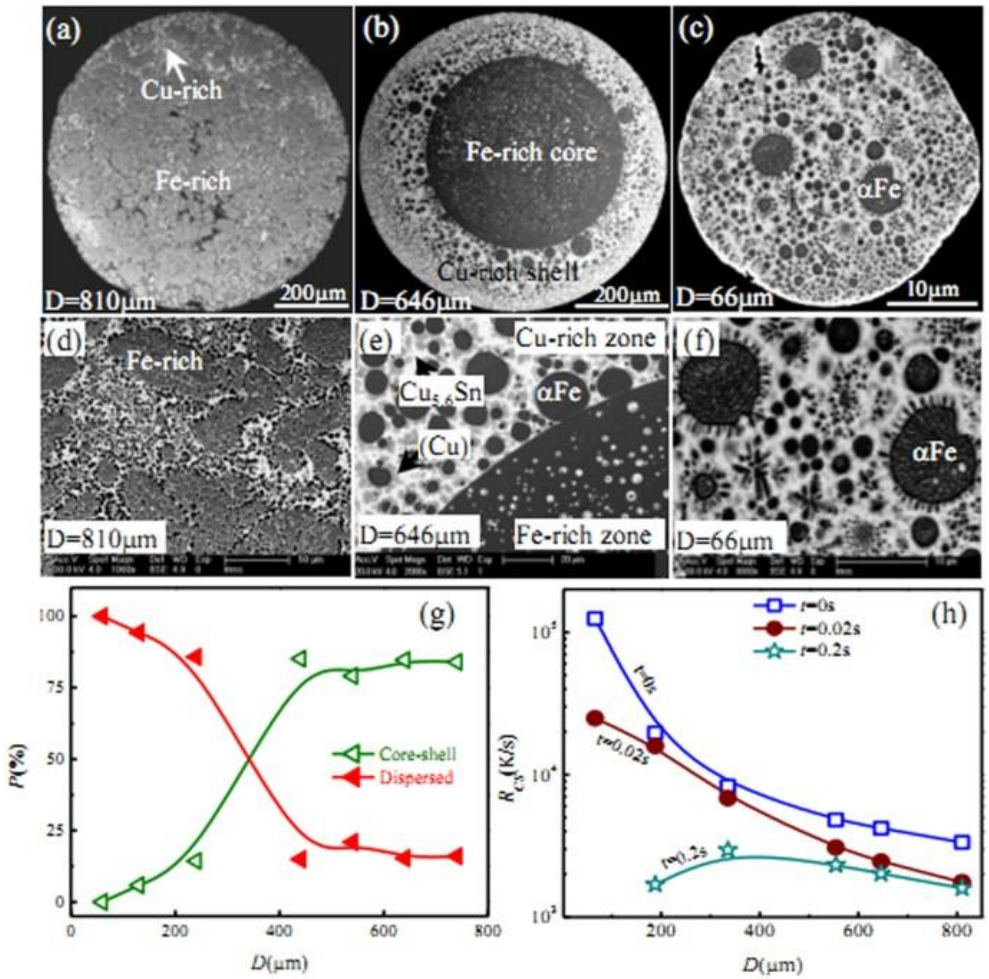

Figure 3.3 Fe-Cu-Sn alloy droplets of different sizes rapidly solidified in a drop-tube. (a) – (c) Whole droplets in large, medium, and small droplet sizes respectively. (d) – (f) Magnified structure of each droplet. (g) Structure prevalence variation with diameter. (g) Cooling rate change with diameter [126].

Jegede et al. [128] rapidly solidified two compositions of the metastable miscibility gap Co-Cu alloy ($Co_{50}Cu_{50}$ and $Co_{68.5}Cu_{31.5}$, closer to and further away from the critical point respectively) in a drop-tube. Incidence of core-shell formation peaked at intermediate particle sizes and cooling rates of about 212 μm and 1.5×10^4 K s^{-1} respectively. The higher melting point Co-rich phase forms the core in both cases as well.

3.2.1.2 Fine dispersions

Fine dispersions of one liquid phase in another have been observed in both stable and metastable liquid phase separated alloys. Wang et al. [125] observed that fine dispersions were generally found in smaller droplets in drop-tube processing of Cu-Pb and Fe-Sn alloys undergoing stable LPS. The authors attribute this to the small size and high cooling rate of these droplets removing the necessary time for Marangoni motion to facilitate coalescence of minority phase droplets into a coherent core-shell structure. These were also observed in smaller Cu-Fe alloy droplets [126]. Fine dispersions in a stable LPS Fe-55%Sn droplet processed by Wang et al. [125] are shown in Figure 3.4. As is indicated, these dispersions are found in smaller (i.e. more rapidly cooled) droplets with compositions far from the critical point (bottom left of the figure).

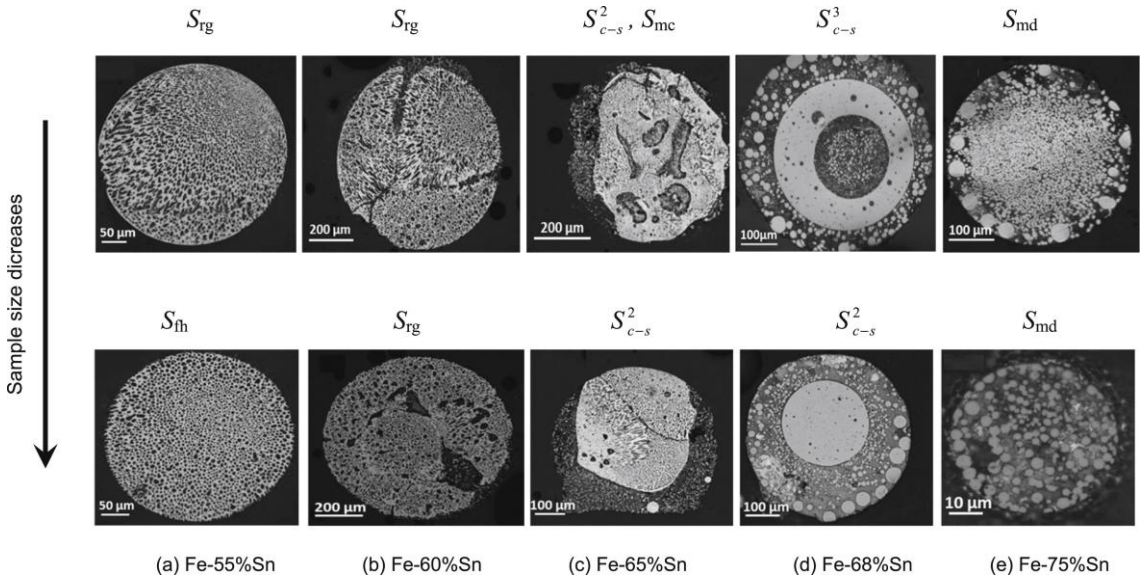

Figure 3.4 Impact of sample size and composition on structure formation in drop-tube processed Fe-Sn alloy with stable miscibility gap [125]. Fine dispersions are observed in smaller (faster cooling) droplets away from the critical composition where the time interval between LPS and solidification (i.e. the time for Marangoni motion induced core-shell formation) is drastically reduced.

Jegede et al. [128] also observe finely dispersed L_2 phase in L_1 phase in their study of rapidly solidified droplets of Co-Cu. These are shown in Figure 3.5g.

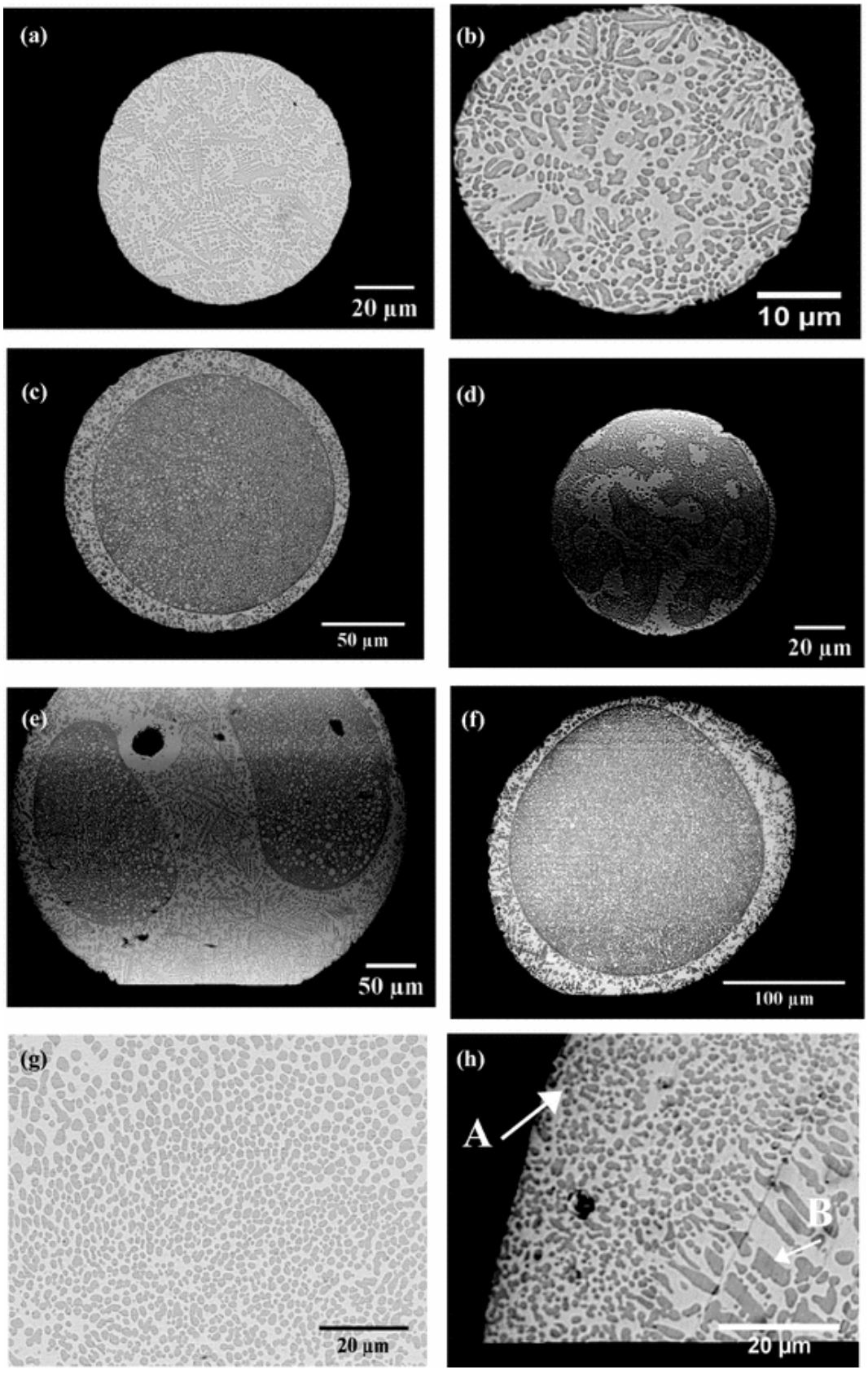

Figure 3.5 Co-Cu droplet structures obtained after metastable liquid phase separation in a drop tube. (c)-(f) show fully coalesced and evolving core-shell structures, while (g) and (h) show fine dispersion microstructures in the fastest cooling droplets [128].

Dispersed structures have been thought to have wide reaching uses. One example is as bearing materials, where a soft phase is dispersed evenly in a matrix of a hard phase. Cu-Pb and Al-Bi have been researched as candidates for this application [67, 129, 130].

3.2.2 Liquid phase separation in high-entropy alloys

Like other areas of HEA behaviour, LPS has been subject to a growing volume of research. A more extensive review of early advances in the area up to 2018 is given by Derimow et al. [21]

3.2.2.1 Stable liquid phase separation

One of the first investigations observing LPS in HEAs was in conducted 2007 by Hsu et al. [131], who solidified AlCoCrCuNi, AuAlCoCrCuNi and AgAlCoCrCuNi via arc-melting. while the base alloy and Au-alloy displayed dendritic structures, a separated layered structure was found in the Ag-alloy. The reason for separation in the Ag-alloy was attributed to the fact that in a six-element alloy, the entropy of mixing is not high enough to supress de-mixing due to the high immiscibility (positive enthalpy of mixing) between Ag and many of the other components. Au was found to mix better in general, allowing for entropy of mixing to counter the de-mixing tendency Au has with Co and Ni. In 2012, Mishra et al. [132] who found that an arc-melted CoCuFeNiTi alloy with varying molar ratios of Cu and Ti. In some of these alloys, solidification begins by dendritic growth of a Ti-rich solid solution, after which the inter-dendritic liquid separates into Co-rich and Cu-rich phases respectively. Another example is the 2013 work of Munitz et al. [133] on AgAlCoCrCuNi and AgAlCoCrCuFeNi. Where the addition of Ag to the alloys caused stable LPS into AgCu-rich and CoCrNi/CoCrFeNi-rich phases respectively. The resultant liquids stratified based on density differences and gravity driven Stokes motion. An example resultant structure is shown in Figure 3.6.

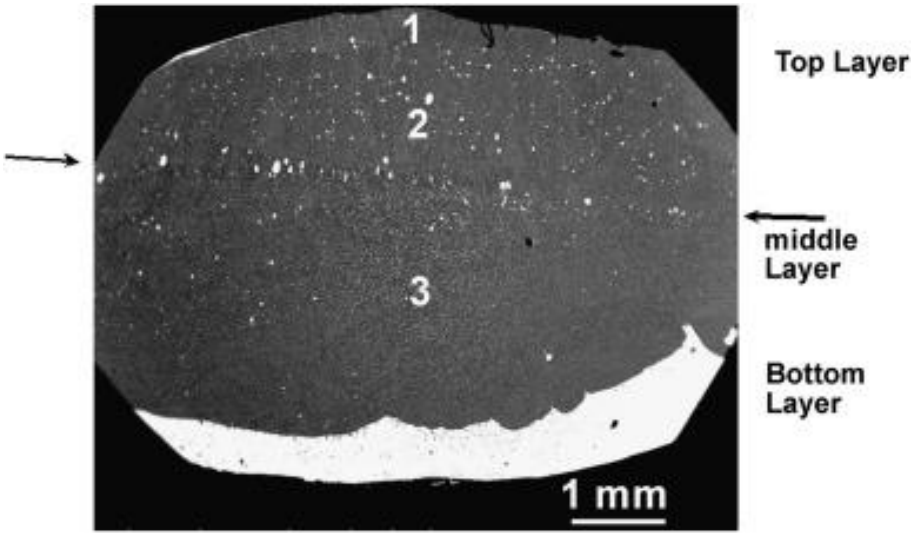

Figure 3.6 Stable LPS in arc-melted AgAlCoCrCuNi alloy showing dark AlCoCrNi-rich phase layered above denser AgCu-rich phase [133].

In the years since, stable LPS has been studied in a broader range of alloys. The bulk of work focuses primarily on elemental additions to HEAs made of common transition metals which have traditionally been used in HEAs (Co, Cr, Cu, Fe, Mn, Ni) along with Al. However, additions of other elements such as Ag, Au, B, Mo, Nb, Sn, Ti, V and W have been explored more briefly.

Derimow and Abbaschian [134] conducted a wide-ranging study on MPEAs based on the CoCrCu ternary system. Additions of Ni, Mn, Ti and V were made to form four and five-component alloys at equiatomic proportions. The alloys were arc-melted, and the microstructures analysed using Scanning Electron Microscopy (SEM) and XRD analysis. Stable LPS was found to occur in all alloys with the exception of CoCrCuNi, CoCrCuFeNi and CoCrCuMnNi which, solidified in a dendritic fashion. Another broad survey was conducted by Munitz et al. [135]. Multiple elemental additions and substitutions on a baseline alloy made of some or all of the elements in CoCrCuFeNi were investigated. The investigation of a substantial number of alloys has indicated that Co, Ti, Ni and Al lowered the miscibility gap (made immiscibility more metastable). However, Cr, V and Nb make LPS easier (de-mixing occurs at a higher temperature for a given composition). In the bulk of cases, the LPS was stable and yielded a Cu-rich and Cu-lean liquid. In some instances, secondary LPS occurred, primarily in the Cu-lean phase. Munitz et al. suggest that the appearance of this secondary LPS may be due to the lack of diffusion speed in the melt.

Other work on refractory metal additions has complemented the initial survey by Munitz et al. Separate experiments by Rahul [136] and Churyumov [137] corroborated that additions of Nb to transition metal based HEAs enhanced LPS behaviour, although the presence of intermetallic compounds in the alloy

microstructure begins to conflict with the definition of HEAs as being made exclusively of simple solid solutions. Another elemental addition that has drawn a large amount of attention is that of Mo. Wu et al. [138] investigated the alloy family $CoCrCu_xFeMoNi$ ($0 \leq x \leq 1$). Vacuum arc melted samples of these alloys were subject to microscopy and compositional investigation. Stable LPS was observed in those alloys above $x \leq 0.5$, at which point the calculated enthalpy of mixing ΔH_{Alloy}^{mix} of the alloy changes from negative to positive due to the increase of Cu content. Peng et al. [139] investigated $CrCu_xFeMo_yNi$ (x and y = 0.5 or 1 for total of 4 tested alloys). All 4 tested alloys showed stable LPS. It is again suggested that the tendency to fully liquid phase separate increases with increasing Cu content. The authors also note that the rules for determining whether or not the resultant LPS alloy is high-entropy is difficult given that the resultant liquid phases are so different in composition. Rounding out refractory metal additions, Rahul et al. [140] observed that adding a small amount of W to the alloy CoCuFeNi to form $CoCrFeNiW_{0.5}$ caused phase separation in arc melted samples as well as the undercooled (melt-fluxed) samples, indicating stable LPS.

Investigation has also begun into interstitial alloying elements and their impact on LPS. Nagase et al. [141, 142] also observed LPS in AgCoCrFeMnNi equiatomic alloy. Ag-rich and Ag-lean liquids were both formed. They subsequently [141] added the interstitial element B to a $CoCrCu_xFeMnNi$ alloy in the form $CoCrCu_xFeMnNiB_{0.2}$ (x = 1,2,3). LPS was observed in samples where x = 2,3. From this study, it seems that the Ag substitutional element and the B interstitial both stabilise LPS. The separated Cu-rich liquid is also relatively rich in Mn (and, to a certain extent, Ni) while the other elements de-mix significantly and congregate heavily in the HEA parent liquid phase.

3.2.2.2 Metastable liquid phase separation

Derimow and Abbaschian note that due to the frequency with which stable LPS occurs in Cu-based HEAs, it is conceivable that other Cu-based alloys which undergo dendritic solidification at relatively low cooling rates may possess metastable miscibility gaps only accessible by methods such as rapid cooling. In the aforementioned 2013 study on stable LPS, Munitz et al. [133] predicted that LPS was metastable in $Al_{20}Co_{11.2}Cr_{11.2}Cu_{35.2}Fe_{11.2}Ni_{11.2}$ and used the high cooling-rate method of electron beam surface melting (an electron beam melts the surface, which rapidly re-solidifies) to test this theory. They failed to observe metastable LPS, likely due to the lack of enough Cu present in the alloy to provide a strong enough de-mixing tendency. It is also important to mention that arc-melting, while prevalent in the study of stable LPS in HEAs, usually does

not usually provide high enough cooling rates to create an undercooling required for metastable LPS to occur with significant frequency. The cooling rate achievable by arc-melting is estimated to be on the order of 2000 K s^{-1} by Nagase et al. [141].

Consequently, we see that two factors are important to consider to enhance the probability of metastable LPS in HEAs, in much the same way as more simple alloys. First, the alloy composition must be such that a miscibility gap is present below the liquidus (see section 2.2.2.2). Additionally, the solidification method must be such that adequate undercooling is achieved to access such a miscibility gap and initiate LPS before solidification. The relative difficulty in achieving these conditions simultaneously means that metastable LPS has been observed in fewer alloys than stable LPS. However, the useful obtainable structures following metastable LPS, particularly in microgravity, have made it the subject of considerable study over the last few years.

CoCrCuFeNi and its compositional variants are currently the only HEAs in which a metastable miscibility gap has been extensively observed and studied. Since 2016, multiple experiments have characterised the impact of undercooling and composition on the LPS characteristics of this alloy.

Liu et al. [143] processed $CoCrCuFe_xNi$ alloys (where x = 1, 1.5 and 2) via glass-fluxing. LPS was found in all alloys and determined to be metastable, with a critical undercooling required to achieve de-mixing. The critical undercooling was found to be ΔT^*_{LPS} = 160 K for the equiatomic alloy, and increases with the increase in Fe prevalence. After LPS, Cu-rich spheres form, embedded in a Cu-lean matrix. Their prevalence increases and size decreases with further undercooling. At ΔT^*_{LPS} = 230 K, an “egg-type” microstructure is formed (Figure 3.7). This opens the door for potential core-shell structures, although the presence of Stokes sedimentation forces inhibits this. Interestingly, Cu-rich nanophases are observed in the Cu-rich region of the phase separated alloys, their formation attributed to high-entropy and sluggish diffusion effects in the alloy. Dendritic solidification occurs below the critical undercooling, with Cu-lean dendrites in a Cu-rich matrix.

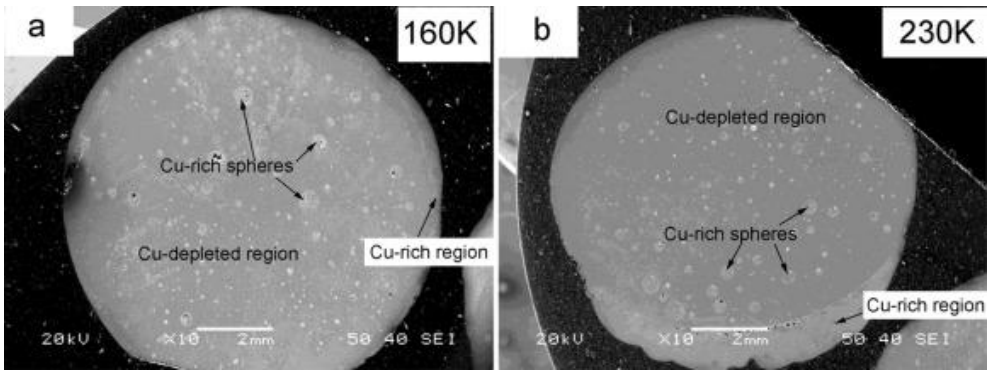

Figure 3.7 Solidified CoCrCuFeNi samples at undercoolings of (a) 160 K and (b) 230 K showing liquid phase separated spheres and an egg-type phase separated structure in the 230 K sample [143].

Wu et al. [144] conducted a similar compositional study, undercooling $CoCrCuFe_xNi$ and $CoCrCuFeNi_x$ alloys (x = 0.5, 1, 1.5, 2). Of these, $CoCrCuFe_{0.5}Ni$ and $CoCrCuFeNi_{0.5}$ were seen to undergo LPS in the stable regime. Interestingly, LPS was not observed in the equiatomic CoCrCuFeNi in this study, potentially due to the fact that the critical undercooling was not reached with the utilised cooling method of crucible casting. This is likely also the reason LPS was also not observed in the $CoCrCuFe_xNi$ alloys, in direct contrast to the work of Liu et al. [143]. The correlation between enthalpy of mixing and Fe content is surprising considering that based on theoretical calculations of mixing enthalpy from Takeuchi and Inoue [111], the enthalpy stays constant at 3.25 kJ mol^{-1} for CoCrCuFeNi and 3.26 kJ mol^{-1} for $CoCrCuFe_{1.5}Ni$, and drops to 3.12 kJ mol^{-1} for $CoCrCuFe_2Ni$. Conversely, critical undercooling increases monotonically as Fe content increases. Such a contradiction exemplifies the difficulty in engineering alloys with easily predictable LPS behaviour, particularly if they are compositionally complex.

Wang et al. [145] investigated the LPS more quantitatively, using glass-fluxing to achieve a maximum undercooling of 381 K in the equiatomic alloy. The critical undercooling required for metastable LPS was noted as 223 K. Dendritic solidification, when it occurred, proceeded faster the higher the undercooling, with a power law relationship. The liquid separated into a FCC high entropy zone and a minor Cu-rich phase (Cu with small amounts of the remaining elements at <5 at%). The volume fraction of the Cu-rich zones increased as the undercooling rose.

Guo et al. [146] have also studied, and further measured the tensile properties of, liquid phase separated CoCrCuFeNi equiatomic alloy. Undercooling of between 30 K and 300 K was achieved. In this case, critical undercooling for LPS was found to be only 100 K, although in this scenario, the undercooling itself is not far above the minimum required, given that only minor LPS was

observed. Egg-type microstructures similar to those found by Liu et al. [143] were witnessed at higher undercoolings between 140 K and 300 K. In terms of mechanical properties, hardness of the dendritic (Cu-lean) phase, was found to peak at intermediate undercoolings of 200 K before decreasing noticeably. This varies in the same way as the Cu content within the dendrites. Solid solution strengthening through Cu addition, and grain refinement via higher undercooling, are seen as the causes for the initial increase, but the depletion in Cu past undercooling of 200 K is suggested to be the reason for hardness loss later on. Finally, the elastic modulus of the dendritic alloy at ΔT_{LPS}^{*} < 100 K and the high-entropy component of the liquid phase separated alloy at ΔT_{LPS}^{*} > 100 K are compared. Elastic modulus of the liquid phase separated phase is lower than the dendritic alloy. The modulus decreases with increasing undercooling for the dendritic alloy but is relatively stable for the separated phase. However, LPS creates improvements in both elongation and tensile strength.

Focusing on the $CoCrCu_xFeNi$ alloy group, Wang and Kong [147] observe metastable LPS in glass-fluxed samples of the equiatomic alloy starting from a critical undercooling of 180 K. At this undercooling, LPS is observed in the interdendritic regions of the alloy. The structure then shifts to a globular microstructure, with Cu-rich globules present at the bottom of the melted sample. Finally LPS becomes much more apparent at the highest undercoolings achieved, with the Cu-rich phase separating to the bottom of the sample, forming a layer. This phase only contributes 1% of the volume of the entire sample. The dendrites are a found to consist of a high-entropy phase with a low Cu content. The authors point out that gravitational separation due to Stokes motion is important for the alloy as the Cu-rich and Cu-lean HEA phase have drastically different densities. Like Fe, Cu addition was found to increase critical undercooling required for LPS, which is also surprising given that addition of Cu drastically increases overall enthalpy of mixing of the alloy (i.e. makes it more positive). Dendritic growth velocity upon solidification rises exponentially with undercooling but decreases slightly as Cu content is increased at the same undercooling. Addition of Cu initially increases the microhardness of the alloy compared to CoCrFeNi, but $CoCrCu_2FeNi$ saw an initial increase followed by a drastic decrease in microhardness, attributed to phase separation in the alloy at a critical undercooling.

Most recently, Yan et al. [24] completed a comprehensive study of EML processed equiatomic CoCrCuFeNi, finding a critical undercooling of about 172 K was required to initiate metastable LPS. The reduction in Stokes motion due to the EML process provided a scenario where other forces such as Marangoni convection dominated structure formation in the levitated droplets. As a result,

core-shell structures at various stages of coalescence were created. Figure 3.8 shows some of the structures obtained by Yan et al. in their EML study of equiatomic CoCrCuFeNi. An example of a core-shell structure obtained in the heavily undercooled alloy is shown in Figure 3.8c.

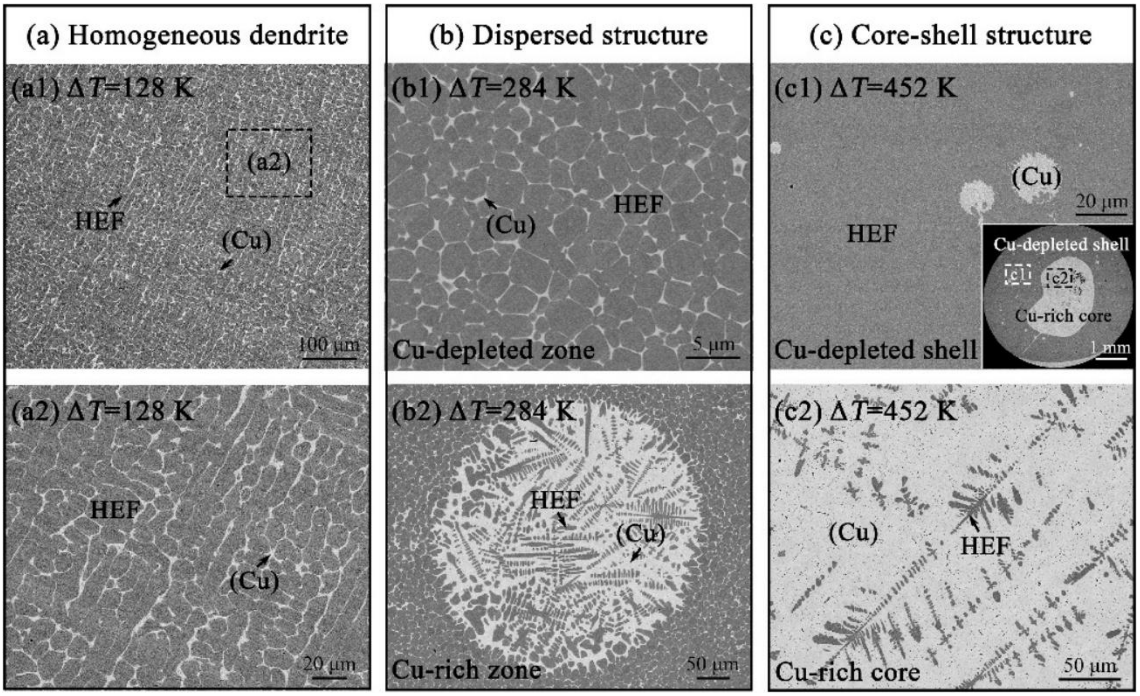

Figure 3.8 Structures obtained in EML processed CoCrCuFeNi equiatomic HEA including (a) dendritic, (b) dispersed, and (c) fully coalesced core-shell structures after metastable LPS [24].

These studies indicate that even small variations in atomic ratio between the elements in $CoCrCu_xFe_yNi_z$ can have a dramatic effect on the undercooling required to initiate LPS. Furthermore, the experimental technique used for solidification of these alloys heavily impacts the final solidified microstructure observed. As such, considerations need to be made when selecting an alloy composition for further study and an experimental technique if the study of any particular structure is desired. A summary of the undercooling required to initiate metastable LPS in $CoCrCu_xFe_yNi_z$ alloys shown below in Table 3.1.

Table 3.1 Tabulated data regarding occurrence of stable/metastable LPS in $CoCrCu_xFe_yNi_z$ alloys

Alloy	Critical Undercooling /K	Cooling Method	Study
CoCrCuFeNi	160	Glass-fluxing	[143]
	223	Glass-fluxing	[145]
	100	Glass fluxing	[146]
	180	Glass fluxing	[147]
	172	EML processing	[24]
	No LPS	Crucible casting	[144]
$CoCrCuFeNi_{0.5}$	Stable LPS	Crucible casting	[144]
$CoCrCuFe_{0.5}Ni$	Stable LPS	Crucible casting	[144]
$CoCrCuFe_{1.5}Ni$	190	Glass-fluxing	[143]
$CoCrCuFe_2Ni$	293	Glass-fluxing	[143]
$CoCrCu_2FeNi$	217	Glass-fluxing	[147]
$CoCrCuFe_{1.5}Ni_{0.5}$	43	Glass-fluxing	[148]

Apart from varying the atomic ratios between the elements, the addition of small amounts of other elements to the $CoCrCu_xFe_yNi_z$ base alloy has also been found to maintain metastable LPS behaviour while introducing other interesting properties. A study by Wang et al. [149] concerns the addition of 3 at% Sn to the equiatomic CoCrCuFeNi alloy. Here the undercooling required for separation was noted at about 150 K. The liquid separated alloy showed FCC_1 and FCC_2 phases, one being CoCrFeNi-rich and the other being CuNi-rich. XRD analysis concludes that the addition of the Sn has a negligible impact on crystal structure. Sn also has a positive enthalpy of mixing with the other constituents (including Cu) and is seen to form nanoprecipitates within the liquid phase separated alloys. The Sn is believed to facilitate the formation of three observed types of nanoprecipitates (Co-Cr-rich, Sn-rich, and Cr-Sn-rich), which in turn improve the hardness of the liquid phase separated alloy by a considerable margin compared to the equiatomic CoCrCuFeNi.

3.2.3 Other forms of liquid phase separation in high-entropy alloys

In a minority of studies, LPS in HEAs has been attributed to factors other than the enthalpy of mixing between constituent elements which come to constitute

the eventual separated phases. Two such examples are discussed briefly below.

3.2.3.1 Constitutional liquid phase separation

In their study on arc-melted $Al_{2.2}CuCrFeNi_2$ alloy, Munitz et al. [150] observe a complex solidification microstructure which they attribute, in part, to LPS driven not by cooling, but by a change in composition. Upon cooling, a B2 (ordered Body Centred Cubic) phase solidifies dendritically first, the solidification causes Cu to be rejected into the residual liquid, enriching this liquid in Cu. The change in concentration of Cu in the liquid is then thought to cause LPS into a CrFe-rich liquid and a Cu-rich liquid which then solidifies between the already solidified B2 dendrites. Hence, the typical separated structure caused by LPS such as that shown in Figure 3.3 cannot be created. This compositionally driven LPS is dubbed constitutional LPS by the authors. Microstructures of the overall alloy, the L_1 and L_2 regions are shown in Figure 3.9.

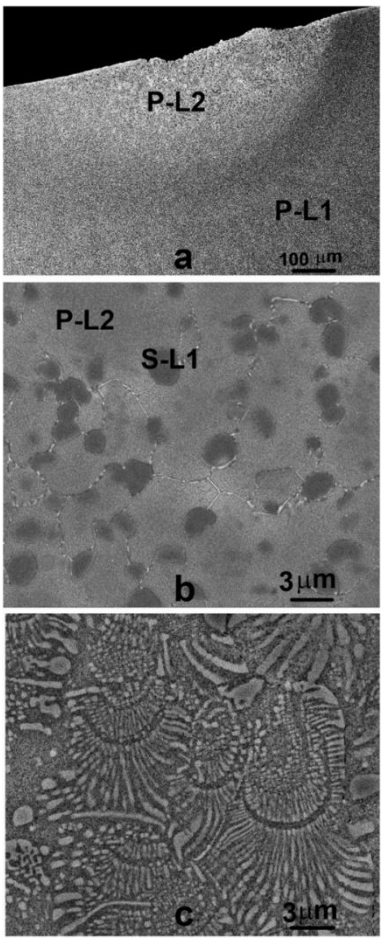

Figure 3.9 Constitutional liquid phase separated $Al_{2.2}CrCuFeNi_2$ alloy. (a) LPS microstructure. (b) L_1 phase. (c) L_2 phase.

3.2.3.2 Binary interaction liquid phase separation

In a study on $AlCrFeNiMo_{0.3}$, Munitz et al. [151] note previous studies in ternary alloys where, in the scenario where binary enthalpy of mixing between all possible binary pairs is negative, a miscibility gap can be created if one pair has negative enthalpy of mixing of a much higher magnitude than the others (that is, it is much more negative). Part of this reasoning is based on the presence of a closed miscibility gap in some thermodynamically treated multi-component (ternary) systems such as the Al-Mg-Sb system, where there are no miscibility gaps in the individual binary phase diagrams, but there is a miscibility gap present in the ternary system itself. The system also contains one binary pair with a much higher magnitude negative enthalpy of mixing than the other two possible pairs [152]. Therefore, because the Al-Ni pair in $AlCrFeNiMo_{0.3}$ has a much more negative interaction that the other possible pairs in the system, it is suggested that this is the reason for LPS occurring in the alloy. The proposed phenomenon, the authors note, is separate from the extensively studied thermally-driven and the previously discussed constitutional LPS mechanisms [151].

3.3 Solute trapping and partitionless solidification

As discussed in Chapter 1, phase separation may also occur in the solid-state, and can be termed solid-state decomposition. Such a reaction is initiated, analogous with LPS, when a single solid phase becomes thermodynamically unstable and two stable phases are preferentially formed instead. The formation mechanisms of these new phases can be through nucleation and growth or a spinodal decomposition, resulting in various microstructures.

3.3.1 Thermodynamic instability in HEAs

A defining feature of HEAs has become the preferential stabilisation of simple solid solutions over large assortments of intermetallic compounds. However, it has become apparent that many of these solid solution phases are actually metastable, and decompose into different product phases upon prolonged annealing treatments at elevated temperatures. CoCrFeMnNi, the iconic Cantor alloy, is routinely described as a single phase FCC solid solution at room temperature. However, the common casting/arc-melting methods used to produce such samples are not necessarily a representation of solidification at true thermodynamic equilibrium. Initial annealing studies [153, 154] indicated the precipitation of other phases in the alloy after hundreds of hours at elevated temperatures. In a long term study, Otto et al. [155], found that annealing the alloy at 500 °C or 700 °C for 500 days causes phase decomposition into

numerous other phases including BCC (Body Centred Cubic), B2, $L1_0$ (chemically ordered tetragonal) and σ (sigma tetragonal) phases. As the authors note, this potentially reveals a thermodynamic instability of the single FCC phase below 800 °C. However, it is likely that any decomposition reactions are kinetically inhibited at lower temperatures. Some refractory HEAs such as TiZrNbHfTa have been found to behave similarly. Schuh et al. [156] found that annealing temperatures of 800 °C to 900 °C caused a decomposition from single phase BCC to a dual-phase BCC or even HCP (Hexagonal Close-Packed) crystal structures. Theil et al. [157] found similar phase metastability in precious metal HEA AuCuNiPdPt. Yurchenko et al. [158, 159] observed similar, albeit more complex, behaviour in Al-Cr-Nb-Ti-V-Zr alloys. They key point here is that many HEAs solid-solution phases are actually thermodynamically metastable and are maintained to room temperature after casting due to the reaction kinetics which prevent decomposition or precipitation.

It is reasonable to assume, therefore, that in a parent phase which is more metastable than the alloys described above (i.e. where the driving force for transformation into more stable components is higher), a decomposition reaction can occur during the initial solidification without being kinetically suppressed. This may occur even during non-equilibrium (rapid solidification) techniques. Often, the metastable precursor state is a supersaturated solid solution. Here, rapid progression of the solidification front causes the solidified phase to hold a higher concentration of solute than it otherwise would at equilibrium. As temperature continues to fall, this solid solution in turn becomes unstable and decomposes in the solid state [160].

The literature shows this is indeed the case. In more simple alloys such as Al-Zn, a supersaturated α' solid solution causes a decomposition reaction in the form of zinc solute rejection. This rejected excess zinc forms a new η phase. This can occur during conventional casting processes as well as after heat treatment [161]. Gusakova et al. [162] showed that rapidly solidified Sn-Bi alloys also underwent a decomposition reaction due to supersaturation of the formed solid solution. Importantly, they note that the initial solid solution is supersaturated because of diffusionless solidification. This is discussed later in this section.

The story is the same in HEAs, Munitz et al. [163] solidified AlCrFeMnNi alloys by casting and found that the initially solidified dendritic and interdendritic solid solutions both underwent solid-state spinodal decomposition. Separate work done by Wang et al. [164] and Manzoni et al. [165] indicates a similar phase transformation sequence in AlCoCrFeNi alloys, although these groups do not go so far as to suggest a decomposition mechanism. Pickering et al. [166] suggest

that spinodal decomposition occurs in solidified dendrites of cast $Al_{0.5}$CoCrCuFeNi alloy. They further note that it is unlikely that this decomposition reaction can be hindered by rapid cooling, given that ageing and subsequent quenching did not hinder the formation of the decomposed structure. The equiatomic AlCoCrCuFeNi alloy had also been earlier found undergo extensive solid-state decomposition during solidification by casting [167]. However, the authors of the study, Singh et al., note that even a splat-quenched sample (which was initially thought to be a single BCC phase), featured small nanoscale domain structures of a pseudo-ordered BCC phase.

These studies show the importance of solid-state decomposition reactions during alloy solidification and, furthermore, shows that these reactions can occur even during non-equilibrium processing which kinetically suppresses such phase changes. This is an even more important conclusion in HEAs where solute diffusion has routinely been thought to be slower than in more simple alloys. Furthermore, in some cases, particularly when discussing rapid solidification, solid-state decomposition reactions and their product microstructures can be a key fingerprint used to identify the presence of solute trapping or partitionless solidification. The mechanisms of both of these phenomena are described in below.

3.3.2 Kinetic models for solute trapping

The concept of kinetic solute trapping has been introduced in section 2.1.3. In order to describe the experimental change in partition coefficient with increasing dendrite growth velocity, numerous theoretical models have been proposed. One particularly prominent description is known as the continuous growth model (CGM) proposed by Aziz [60]. A key conclusion of this model is represented in Equation 3.1 which defines the partition coefficient of solute across the solid liquid interface for a given growth velocity $k_{CGM}(V)$ [60].

$$k_{CGM}(V) = \frac{k_e + V/V_{D_i}}{1 + V/V_{D_i}} \qquad 3.1$$

Equation 3.1 tells us that when the velocity of the advancing interface V is very slow ($V \to 0$), partitioning occurs as it would at equilibrium ($k \to k_e$). Conversely, when interface speed is much faster than the velocity of solute diffusion across the interface V_{D_i} (i.e. when $V \gg V_{D_i}$), then the partition coefficient approaches unity ($k \to 1$) where the solid and liquid compositions are equal at the interface. A more general model was proposed later by Aziz and Kaplan [59]. It

constitutes a generalisation of the Aziz CGM such that any solute concentration in the liquid at the interface X_L^* may be considered (the Aziz CGM was utilized in dilute solute cases where $(1 - k_e)X_L^* = 0$). The partition coefficient is therefore calculated through Equation 3.2.

$$k_{CGM}(V) = \frac{k_e + V/V_{D_i}}{V/V_{D_i} + 1 - (1 - k_e)X_L^*} \quad 3.2$$

Such models were later substantiated by experimental data such as that on Al alloys [168] and Si-As at dilute solute concentrations [169, 170].

Solute trapping has also been observed in HEAs. In an early study of laser-cladded CoCrCuFeNi equiatomic alloy, Zhang et al. [22] observed that the very high cooling rates (above 10^4 K s^{-1}) provided by the laser-cladding method caused the dendritic and interdendritic matrices in the alloy to solidify with rather similar compositions. This is unusual given that the high entropy of mixing between Cu and the other components usually causes formation of highly Cu-rich and Cu-lean phases upon more conventional solidification processing [134]. The authors [22] suggest this is caused by the high cooling rates (which enhance kinetic solute trapping by increasing undercooling) and the comparative sluggish substitutional of partitioning elements encountered in HEAs. A similar suggestion was made by Yan et al. [24] who solidified equiatomic CoCrCuFeNi via EML processing. They postulate that the very low volume fraction of interdendritic Cu-rich phase present in the solidified shell of the core-shell LPS structure points significant kinetic solute trapping during solidification due to a high undercooling.

3.3.3 Kinetic models for partitionless solidification

As discussed in section 2.1.3, it is possible for the solidifying phase to possess the same composition as the liquid from which it solidifies. This is dubbed partitionless solidification.

The continuous growth model proposed by Aziz and Kaplan, provides an accurate description of solute trapping only at relatively low interface growth velocities, tending asymptotically towards $k = 1$ as the growth velocity exceeds the diffusion velocity of solute across the interface [171]. Therefore, it does not generally represent the transition from solute diffusion controlled growth to thermal diffusion controlled growth [61, 62]. At this point, partitionless solidification is initiated and $k = 1$. To combat this discrepancy, other models have been proposed to build upon the continuous growth model and describe

the transition from growth at equilibrium ($k = k_e$) to kinetic solute trapping ($k > k_e$) to fully partitionless solidification ($k = 1$). Two analytical models in particular, will be briefly introduced here.

One such model is that proposed by Sobolev [171-174], dubbed the local non-equilibrium diffusion model (LNDM). The key improvement on the CGM is that it factors in the diffusion velocity of solute in the bulk liquid V_{D_b} as well as that of solute across the interface (only the latter is covered in the CGM) [173]. It was initially assumed that the velocities which solute diffused across the interface and that which it diffused in the bulk was comparable ($V_{D_i} \cong V_{D_b}$). Instead Sobolev suggests [172] that this is not the case, and that V_{D_i} and V_{D_b} should instead be treated as two separate values with, generally, $V_{D_i} < V_{D_b}$. These characteristic velocities may influence the extent of solute trapping. This becomes particularly important at high interface growth rates. Significant solute trapping occurs when V approaches V_{D_i}. However, when $V \cong V_{D_b}$, the larger of the two diffusive velocities, complete solute trapping will result. The diffusion coefficient of solute in the bulk liquid reduces to zero [172], and the partition coefficient therefore rapidly increases to $k = 1$. Because of this, a critical value of growth velocity V delineates the transition from partitioning to partitionless growth. The model therefore more accurately describes solute partitioning behaviour during solidification at the full range of interface velocities. The partition coefficient of solute at a given dendrite growth velocity $k_{LNDM}(V)$ is described from this model in Equation 3.3.

$$k_{LNDM}(V) = \begin{cases} \dfrac{k_e + (1 - V^2/V_{D_b}^2) + V/V_{D_i}}{(1 - V^2/V_{D_b}^2) + V/V_{D_i}}, & V < V_{D_b} \\ 1, & V > V_{D_b} \end{cases} \quad 3.3$$

Galenko [175] and coworkers have formulated a model which unites the limit cases presented by the CGM and LNDM presented above. They calculate the partition coefficient $k_{GAL}(V, X_L^*)$ through Equation 3.4 for any specific concentration of solute in the liquid X_L^* at the interface.

$$k_{GAL}(V, X_L^*) = \begin{cases} \dfrac{k_e(1 - V^2/V_{D_b}^2) + V/V_{D_i}}{(1 - V^2/V_{D_b}^2)[1 - (1 - k_e)X_L^*] + V/V_{D_i}}, & V < V_{D_b} \\ k_{GAL}(V, X_L^* = X_0) = 1, & V \gg V_{D_b} \end{cases} \quad 3.4$$

In the first case, at the limit where the solute diffusion velocity in the liquid tends to infinity ($V_{D_b} \to \infty$), we arrive at the generalised expression posited in the CGM proposed by Aziz and Kaplan in Equation 3.2 [59]. With the additional condition for a dilute solute content in the liquid ($X_L^* \to 0$), the equation further simplifies to Equation 3.1 proposed by Aziz [60]. In the scenario where the alloy is dilute ($X_L^* \to 0$) for a specific value of solute diffusion velocity in the bulk liquid V_{D_b} the solution to the equation simplifies to that proposed by Sobolev [171] in Equation 3.3. A model therefore emerges that behaves similarly to the CGM at low solute concentrations, but yields a more substantial increase in partition coefficient (and hence, solute trapping) as growth velocity V increases. In line with the LNDM, the partition coefficient becomes 1 when the velocity of the propagating interface is equal to the velocity of solute diffusion in the bulk liquid melt V_{D_b}. Galenko [175] provides a comparison of the change in partition coefficient with increasing dimensionless velocity V/V_{D_b} for the four models discussed. A similar comparison is shown in Figure 3.10. Here, the blue dotted line represents the model by Aziz (Equation 3.1), and the green dashed line that of Aziz and Kaplan (Equation 3.2). The red dot-dashed line represents the model of Sobolev (Equation 3.3), and finally, the magenta solid line represents the unified model proposed by Galenko (Equation 3.4). Improvements in analytical models have allowed better correlations with experimental data including that of [169].

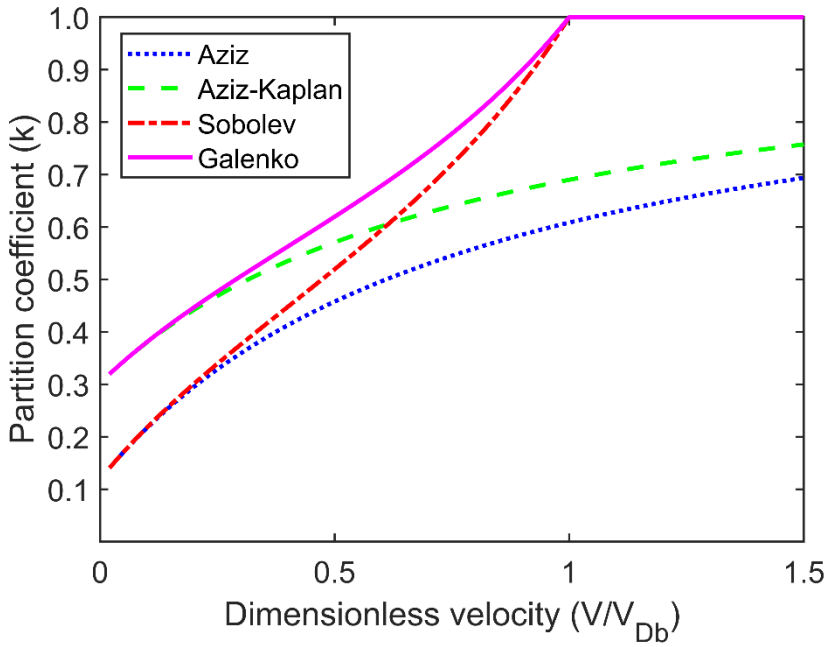

Figure 3.10 Graphical comparison of analytical models of solute trapping in growing solid as dimensionless velocity increases, based off of the comparative analysis in [175].

3.3.4 Kinetic and thermodynamic conditions for partitionless solidification

While the kinetic models described above bridge the gap between solute trapping and completely partitionless solidification due to attainment of a critical interface growth velocity, it is important to remember that the cause of partitionless solidification need not always be ascribed to kinetic phenomenon. The thermodynamic argument as described by Baker and Cahn [64] (see section 2.1.3) relies purely on undercooling the alloy to below the T_0 temperature at a particular composition. Satisfying this condition opens the possibility of partitionless solidification regardless of the reaction kinetics. Therefore, it is equally relevant to explore thermodynamic reasons for partitionless solidification. This argument has been invoked extensively to explain the occurrence of partitionless regions in both conventional alloys and HEAs.

3.3.5 Partitionless solidification in conventional alloys

Because of a complete lack of partitioning, the presence of partitionless solidification can often be identified by the presence of featureless solid regions in the microstructure that possess the same composition as the original alloy liquid. In an early study on melt spun Ni-Al alloys and 316 stainless steel, Cantor et al. [176] observed regions in the melt-spun ribbons adjacent to the wheel surface with no visible solute segregation, suggesting partitionless solidification. The thickness of this region increased with increasing cooling rate, which points to the notable conclusion that the prevailing undercooling upon nucleation is proportional to cooling rate. The release of latent heat upon continued solidification eventually causes a shift to conventional partitioning during solidification further away from the wheel surface. McKeown et al. [177, 178], used a centrifugal atomisation technique to rapidly solidify eutectic U-6wt% Nb droplets, achieving cooling rates between 10^3 and 10^8 K s^{-1}. The microstructures that result from this processing are shown in Figure 3.11.

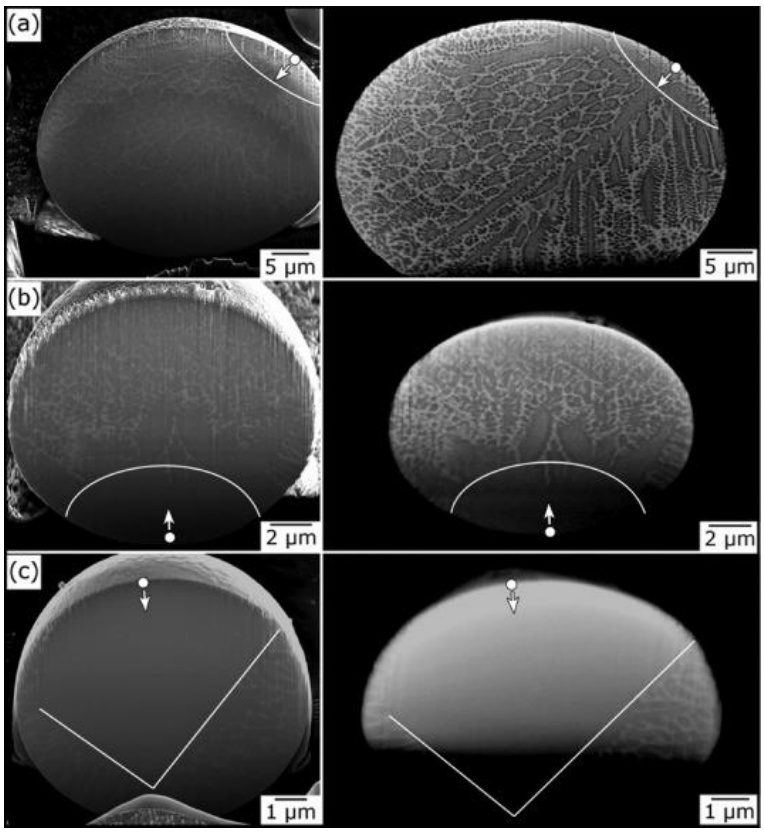

Figure 3.11 Dendritic structures and featureless regions yielded during rapid solidification of U-6wt%Nb [178]. White arrows indicate the nucleation point and growth direction of the solid. Featureless regions are bounded by white lines.

Many of the interdendritic regions in these droplets have an average composition nearly identical to the initial alloy composition. Additionally, smaller droplets (which have cooled faster), often contain large featureless regions with the initial alloy composition. It is believed that these regions have solidified in a partitionless manner via the progression of a planar solidification front. The release of latent heat then results in a reversion to solute partitioning and dendritic growth. In other scenarios, a region in the microstructure which has undergone a decomposition reaction in the solid state may have an average composition identical to that of the starting alloy, a likely indicator of partitionless solidification. Gusakova et al. [162] observed such behaviour in a Sn-57wt%Bi eutectic alloy. At the highest cooling rates, regions having undergone an apparent discontinuous decomposition were analysed based on average composition. The composition of this region was found to be that of the initial alloy melt, which suggests partitionless solidification in these regions before decomposition occurred.

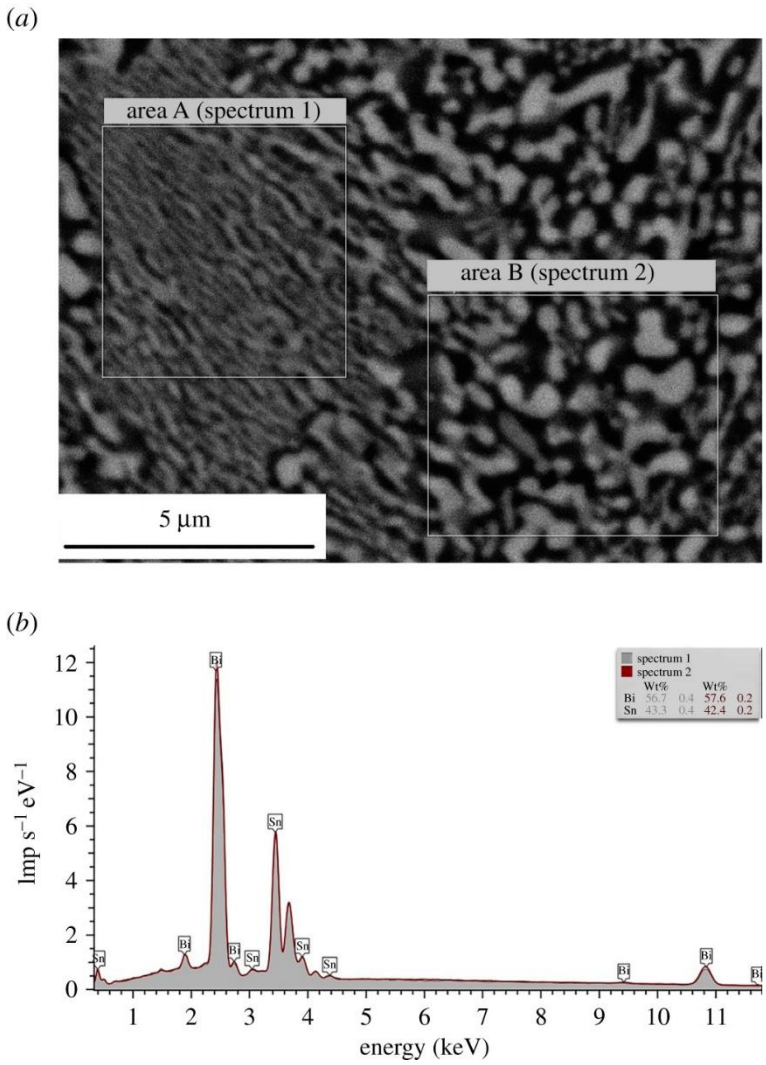

Figure 3.12 Microstructures (a) and EDX spectra (b) from selected regions of rapidly solidified Sn-57wt%Bi alloy [162]. EDX spectra of both areas of interest show average compositions very close to that of the original alloy liquid.

As can be seen from Figure 3.12, the summed spectrum of areas A and B, have a composition extremely similar to that of the original alloy Sn-57wt%Bi, meaning that these regions may have solidified in a partitionless manner and then decomposed during further cooling.

In a recent series of drop-tube experiments, Abul et al. [179] observed potential partitionless solidification of rapidly solidified Al-3.9wt%Fe alloys. A featureless region which possesses the same composition as the liquid turned out to be populated by nanosized precipitates, evidence of a decomposition reaction. Through calculation of a T_0 temperature at 42 K below the liquidus, the authors note that drop-tube processing is highly likely to be able to induce the undercooling required for partitionless solidification in the alloy. A further study by Abul et al. [180] on Al-4.1wt%Fe-1.9wt%Si also seemed to show regions solidified in a partitionless manner. In this alloy, however, the authors found that

while the Fe had not partitioned in these regions, the Si solute had still partitioned, and the atomic percentage of silicon was different from that of the starting alloy in the regions which had undergone partitionless solidification with regards to Fe. This was attributed to the diffusion speed of Si in Al being an order of magnitude higher than the diffusion speed of Fe. An additional experiment by Gusakova [181] on Al-12.6 wt%Si-0.8 wt%Mg-0.4wt%Mn-0.7wt%Fe-0.9wt%Ni-1.8wt%Cu shows that partitionless solidification is eminently possible in alloys with many minor additions. In contrast to Abul et al., they do not observe a partitioning of silicon in the homogenous region of the microstructure.

3.3.6 Partitionless solidification in high-entropy alloys

In HEAs, research focusing specifically on partitionless solidification is more sparse, but the phenomenon has been hypothesized to occur based on the same telltale signs. An early mention of the phenomenon is discussed in 2016. In suction cast ZrNbAlTiV, Vishwanandh et al. [182] observed a featureless region radiating from the contact point between the alloy and casting surface. Such a microstructure is shown in Figure 3.13. In this region, EDX data revealed a composition almost exactly the same as the original alloy, pointing to partitionless solidification. Further from the contact point between alloy and casting surface, conventional partitioning re-emerges and a dendritic structure prevails.

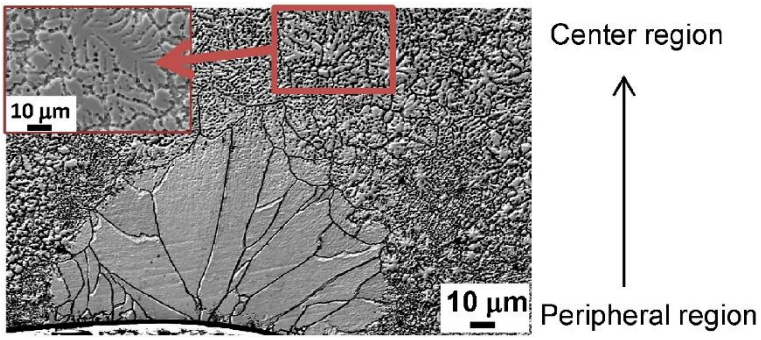

Figure 3.13 Partitionless solidification near nucleation surface (peripheral region) in rapidly solidified ZrNbAlTiV HEA [182].

In work on Al-Cr-Fe-Mn-Ni alloys of varying atomic ratio, Ananiadis et al. [183] and Mathiou et al. [184] invoked partitionless solidification followed by solid-state spinodal decomposition to describe the formation of fine microstructures within dendrites. Srimark et al. [185] subjected arc-melted $Al_{0.7}CoCrFeNi$ to various annealing heat treatments after initial solidification. The initially solidified alloy consists of a B2 phase with FCC phases originating from the grain boundaries. They demonstrate, using a CALPHAD (Calculation of Phase Diagrams) based thermodynamic model of the driving force, that partitionless

solidification for transformation between the liquid phase and a B2 phase is possible at the chosen composition. They use this to suggest that the precursor to the final annealed microstructures of this alloy is partitionless solidification of the liquid to a B2 phase. A FCC phase subsequently nucleates at the grain boundaries upon further cooling of the supersaturated B2 phase. Finally, Bai et al. [186] used CALPHAD modelling and molecular dynamics simulations to explore reasons for unusual microstructure formation in $Al_{30}Co_{10}Cr_{30}Fe_{15}Ni_{15}$ eutectic alloy. They determine that the presence of short range order in the alloy stabilises a very low eutectic temperature. It would generally be expected that cooling deep into this eutectic well would result in formation of a metallic glass. Instead, according to the authors, the short range order present in the high entropy eutectic liquid results in a structural similarity to that of a B2 crystalline phase. This causes preferential formation of a metastable B2 phase via partitionless solidification. The metastable phase then undergoes spinodal decomposition in the solid state upon further cooling.

3.4 Grain refinement

Attempts to describe and understand the grain refinement episodes in alloys has resulted in a relatively large volume of literature on pure metals, intermetallic compounds, and binary alloys. Additionally, to further simplify the transformations and gain an isolated understanding of the grain refinement process, most of these studies involve grain refinement in single-phase solid solution alloys. In a substantial portion of these studies, a primary goal has been to determine the mechanism responsible for spontaneous grain refinement. Here, studies focusing on alloys of all types will be covered in more detail, along with manipulated variables such as undercooling, alloy solute content and solidification method.

3.4.1 Dendrite re-melting and fragmentation

While many refinement mechanisms been suggested over time (and are covered more extensively elsewhere), a few have garnered particular interest. The first is the dendrite fragmentation and re-melting mechanism proposed initially by Schwarz et al. and Karma [40, 41]. The model assumes that dendrites growing during solidification fragment after recalescence. The extent of this fragmentation is based on the balance between the time required for fragmentation to occur (the break-up time Δt_{bu}) and the plateau time Δt_{pl}, which describes the time interval the remaining interdendritic liquid (that which is left over after recalescence) requires to fully solidify. This occurs at a near constant ‘plateau’ temperature. Substantial grain-refinement is thought to occur when the

breakup time is shorter than the plateau time $\Delta t_{bu} < \Delta t_{pl}$. Such a model corresponds well with findings in EML processed Cu-Ni alloys, which are summarized in Figure 3.14 below [187].

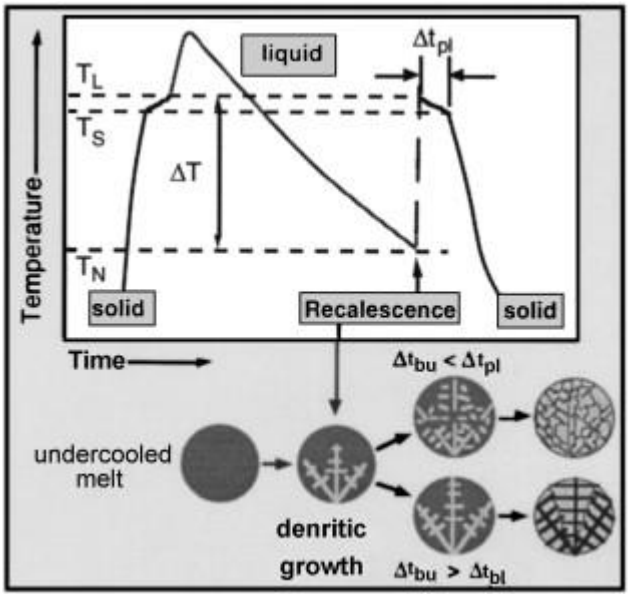

Figure 3.14 Typical alloy heating and cooling curve and summary of dendrite fragmentation and re-melting after recalescence, comparing plateau time to dendrite break-up time [187]. The interval for grain refinement (dendrite break-up) falls within the characteristic plateau time after recalescence. If the plateau time is longer than the required break-up time, grain refinement can proceed.

The model has also been invoked to explain the fragmentation and re-melting of dendrites in drop-tube processed Ni_3Ge intermetallic compounds by Mullis and Haque [188]. Fragmentation of dendrite arms was clearly observed and attributed to Rayleigh instabilities in line with the work of Schwarz et al. and Karma [40, 41]. Example micrographs are shown in Figure 3.15. Modelling of the alloy behaviour revealed that increasing cooling rates reduced the likelihood for grain refinement due to a reduction in plateau time (but only once undercooling was increased above a critical value required to initiate said refinement).

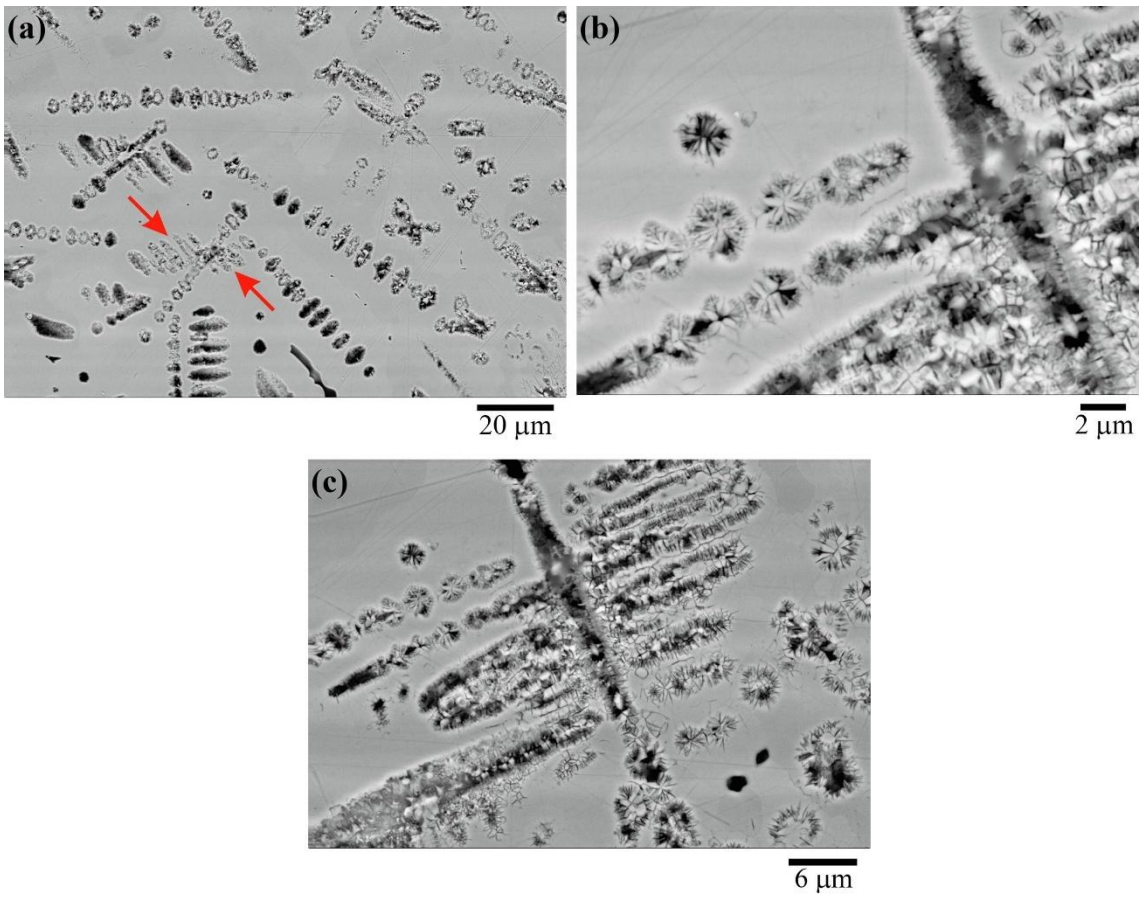

Figure 3.15 Examples of dendrite fragmentation and spheroidization from Rayleigh instabilities in drop-tube processed Ni_3Ge intermetallic compound [188].

In contrast to the fragmentation model of Schwarz et al. and Karma [40, 41], Li et al. [42] propose the re-melting of dendrites during, rather than after, recalescence. The team conducted an extensive study of grain refinement in the Ni-Cu system across the full composition range via a glass-fluxing technique. In all alloys, regardless of solute content, they find two episodes of grain refinement, one at low undercoolings and one at very high undercoolings. They also find that the undercooling required to initiate the first episode of grain refinement increases as solute content (in this case, Cu) increases. They link grain refinement at low undercooling to extensive dendrite remelting during recalescence. Data from the experiment is used to construct a mathematical model employing a dimensionless superheating $\Delta\bar{T}_s{}'$ which is a ratio between the superheating $\Delta T_s{}'$ and the crystallization temperature range of the particular alloy at equilibrium $\Delta T_0{}'$ (Equation 3.5). They then relate the tendency for dendrite disintegration (represented by the fraction of the alloy that becomes liquid f_l' during recalescence) to the superheating through the Equation 3.6.

$$\Delta\bar{T}_s{}' = \frac{\Delta T_s{}'}{\Delta T_0{}'} \quad 3.5$$

$$f_l' = k_e \Delta\bar{T}_s{}' [1 - (1 - k_e)\Delta\bar{T}_s{}'] \quad 3.6$$

The melted fraction of the alloy f_l' is found to tend towards 1 as dimensionless superheating $\Delta\bar{T}_s{}'$ tends to 1. A plot of dimensionless superheating against undercooling peaks at a low undercooling, indicating that this undercooling provides the best conditions for dendrite disintegration (i.e. remelting) regardless of solute content. An example of such a plot is shown in Figure 3.16.

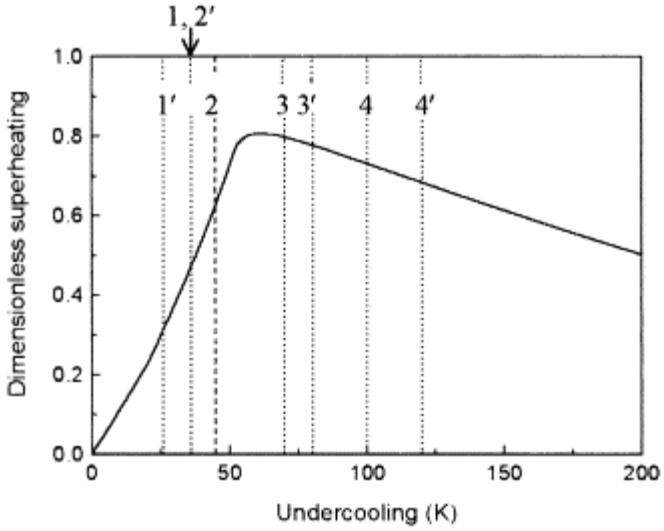

Figure 3.16 Dimensionless superheating plotted at varying undercooling for $Cu_{70}Ni_{30}$ alloy [189] showing single peak at undercooling between 50 K and 75 K.

Figure 3.16 also suggests that re-melting cannot be the likely cause of refinement at high undercooling. Li et al. [42] attribute this, instead, to stress-induced re-crystallization. During both grain refinement stages, the grain size decreased with increasing solute content, and in the case of the first grain refinement step, the size of the particles scaled with the tip radius of the dendrites from which the refined particles originated. This model was used as context for further studies by Li et al. [189] into grain refinement in Cu-Ni alloys. They studied the impact of solidification time on grain refinement transitions in $Cu_{70}Ni_{30}$, observing that as the solidification time increased, the undercooling range at which the first episode of grain refinement takes place enlarges significantly (shown by the increase in interval between undercooling 1' and 4' compared to that between 1 and 4 in Figure 3.16). In contrast, the undercooling associated with the beginning of the second grain refinement episode does not

change. Furthermore, the work notes that, at longer solidification times spanning more than a few seconds, the characteristic grain refinement undercooling ranges for the Cu-Ni alloy analysed do not correspond well to those predicted by the fragmentation model of Schwarz et al. and Karma [40, 41]. In the comparatively slow-cooled samples, grain refinement was observed at undercoolings far above what the model calculated to be impossible. The authors importantly also argue that in rapid solidification environments where solidification is treated as adiabatic, initial grain refinement due to remelting is impossible to avoid due to the inability to suppress recalescence. In an experiment on directional solidification of $Cu_{70}Ni_{30}$, Li et al [190]. found that at high undercoolings, the sharp increase in dendrite growth velocity likely occurs to the directional growth of dendrites becoming unstable, and breaking down due to stress induced by shrinkage of the solidifying structure. This can eventually cause decreases in grain size and subsequent refinement.

3.4.2 Recrystallisation

If remelting is not considered the reason for all occurrences grain refinement (especially at higher undercoolings $\Delta T_{GR}^{(2)}$) in alloys, another phenomenon might be responsible. The other set of mechanisms that is believed to yield spontaneously grain refined structures involves recrystallisation. This process involves the nucleation and growth of new grains in the material by holding the alloy above a characteristic temperature, often to relax the stresses induced by deformation of the material [191]. An early invoking of the dendrite recrystallisation argument was in the work of Powell [192] in pure Ag, and later, in Cu-Ag alloy [193]. Work by groups including that of Jones and Weston [194] on undercooled Ni-Si also seemed to indicate that residual stress increased with undercooling up to a critical value. Once this critical undercooling was surpassed, and grain refinement was initiated, the internal stress lowered, which indicated possible recrystallisation. Figure 3.17 shows an example of a recrystallisation process occurring in a previously cold-rolled titanium alloy. New grains nucleate and grow at the boundaries between the large, long, columnar shaped grains during annealing at elevated temperatures. This causes a refinement in microstructure and a shift from columnar to equiaxed morphology [195].

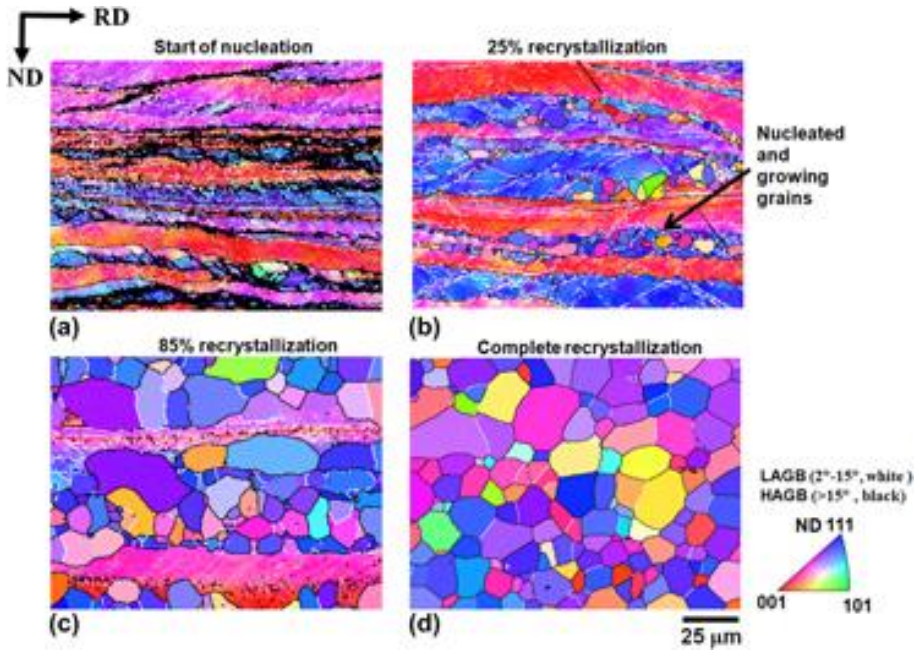

Figure 3.17 Example of recrystallisation process during annealing of cold-rolled Ti–15V–3Sn–3Cr–3Al alloy [195]. The initial structure (a) consists of defomed, elongated grains. Applied heat during annealing allows the nucleation and growth of new grains (b-c) until a nearly complete recrystallised microstructure of equiaxed grains is formed (d).

Numerous methods are available to distinguish between the occurrence of fragmentation/remelting, or recrystallisation as the grain refinement mechanism. Often the grain orientation of the resultant fine grains, and changes in the alloy microhardness pre and post-transformation can be the key. In an early comparative study on Cu-O and Cu-Sn alloys, Cochrane et al. [196] found that Cu-O seemed to undergo grain refinement through a remelting mechanism while attributing the refinement in Cu-Sn to recrystallisation. The clues which suggested a recrystallisation included the presence of annealing twins and a sharp reduction in microhardness with increasing undercooling. The authors also suggest that the random orientation of crystal grains may be due to a recrystallisation rather than a remelting process, where evidence of the former dendritic structure would likely remain. A similar drop in microhardness is found by Biswas [197] in Fe-Ge compounds. Xu et al. [198] undercooled Co-Pd alloys and observed, after the second grain refinement transition, a series of equiaxed grains with grain boundaries much straighter than might be expected had re-melting occurred. The change in microstructure as a result of this process is shown in Figure 3.18. The presence of annealing twins in the FCC microstructure and low angle grain boundaries was also suggested to confirm recrystallisation. They also calculate that the stress induced in the microstructure due to the rapid removal of heat will exceed the yield stress of the alloy at an undercooling of 250 K, a similar value to where recrystallized

microstructures are observed as in Figure 3.18b. the occurrence of dislocations suggests that internal stresses are also significant in the microstructure.

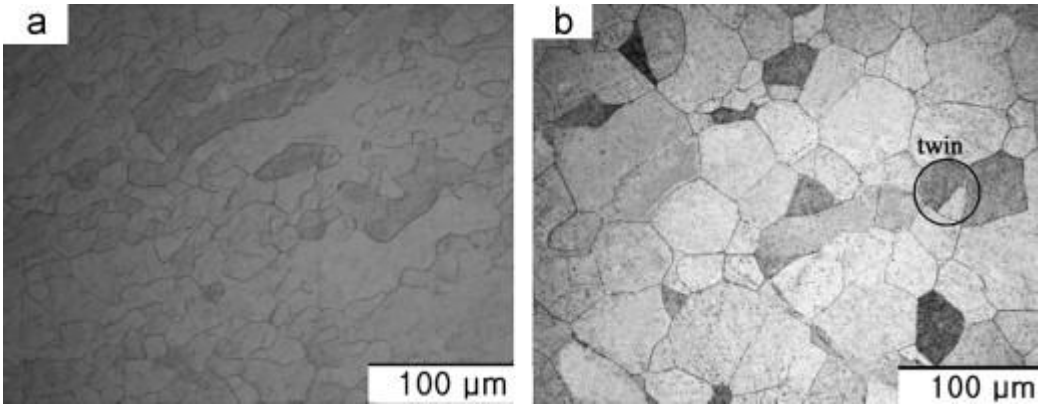

Figure 3.18 Example of alloy microstructure before (a) and after (b) spontaneous grain refinement via recrystallisation at very high undercooling, found by Xu et al. [198] in $Co_{80}Pd_{20}$ alloy.

Haque et al. [199] drop-tube processed congruently melting Ni_3Ge intermetallic compounds and suggested refinement by recrystallisation had occurred due to the presence of many low angle boundaries between grains (as opposed to a random assortment of angles) and a large grain size distribution. This reasoning surprisingly contradicts the hypothesis made by Cochrane et al. [196].

3.4.3 Selected studies on grain refinement in alloys

In a series of studies on DD3 nickel-based superalloys (Ni-9wt%Cr-5.2wt%W-5wt%Co-3.2wt%Mo-5.9wt%Al-2.2wt%Ti), Liu et al. [200] and Liu and Yang [201] argued the same sequence of grain refinement mechanisms, with a re-melting at $\Delta T_{GR}^{(1)}$ and a re-crystallization at $\Delta T_{GR}^{(2)}$. Both of these studies, in line with the work of Li et al. [42] before, invoked an argument for recrystallisation grain refinement at high undercoolings based on the arguments made initially by Powell [192]. Solidification of a highly undercooled melt is thought to encourage the formation of defects in the solid. The more defects that are present, the higher the strain energy. This provides a driving force for plastic deformation and fragmentation of dendrites. From this, recrystallisation can proceed.

Chen et al. [202] processed $Fe_{75}Ni_{25}$ alloy via fluxing and cyclic superheating methods to determine the presence, or not, of grain refinement at low undercooling $\Delta T_{GR}^{(1)}$ (a transformation at high undercooling had been determined earlier by Kattamis and Flemings [203] among others). Observing such grain refinement at between 56 K and 145 K, they used the dendrite fragmentation model by Schwarz et al. and Karma [40, 41] and the dimensionless

superheating model developed by Li et al. [42] to demonstrate that grain refinement at low undercoolings was likely caused by dendrite re-melting.

In 2010, Wang et al. [204] rapidly solidified $Ni_{85}Cu_{15}$ alloy via glass-fluxing followed by rapid quenching after recalescence was complete. They indeed observed two episodes of spontaneous grain refinement at low and high undercoolings $\Delta T_{GR}^{(1)}$ and $\Delta T_{GR}^{(2)}$ but argue that the cause of this refinement is different at each characteristic undercooling. In the sample solidified at low undercooling the consistent grain orientation points to a dendrite remelting mechanism. Conversely, random grain orientation in the highly undercooled sample, along with the presence of annealing twins, suggests that recrystallisation may be the final cause of refinement at high undercooling. Notably, the authors do not view recrystallisation as occurring in isolation. They argue that dendrite fragmentation and remelting occurs at both high and low undercoolings, but also that only at high undercoolings does this dendrite deformation and fragmentation become substantial enough to form grain boundary sites necessary for nucleation of recrystallized grains. A similar study by Yang et al. [205] calculated the dendrite break-up time and plateau time for $Cu_{70}Ni_{30}$ following the model of Schwarz et al. and Karma [40, 41]. They calculate that there are two separate temperature ranges, one at low and one at high undercooling, where the dendrite break-up time falls below the plateau time. This suggests that refinement by fragmentation and remelting is possible at low and high undercoolings. Additionally, at high undercoolings, Yang et al. propose that as undercooling increases, the maximum temperature reached during re-calescence decreases, but the degree of recalescence (i.e. the temperature rise inherent in the recalescence process) increases. This, in turn, means that the fraction of alloy solidified during recalescence increases with undercooling. Because of this, the authors argue that flow of the residual liquid is hindered, increasing residual stresses in the solidified material. This is in addition to enhanced solute trapping at high undercooling, and dislocations causing distortion of the lattice, provides the driving force required for recrystallisation.

The impact of altering solute concentration on critical undercooling was studied by An et al. [206] who found that increasing the amount of Cu present in a Ni-Cu alloy from $Ni_{82}Cu_{18}$, to $Ni_{65}Cu_{35}$ and $Ni_{55}Cu_{45}$, caused a rise in critical undercooling due to a higher recalescence degree (i.e. the difference between the temperature at nucleation and the highest temperature achieved during subsequent recalescence). All alloys displayed the same two mechanisms of grain refinement as the previous studies mentioned in this section, with a high degree of misorientation between grains and a drop in microhardness indicating

that the second grain refinement episode proceeds via recrystallisation. This was also found for $Ni_{82}Cu_{18}$ and $Ni_{50}Cu_{50}$ alloys analysed by the same group [207]. Furthermore, Transmission Electron Microscopy (TEM) analysis showed a prevalence of dislocations in the alloy microstructure at high undercooling, which are believed to provide the driving force for recrystallisation. The similarity in these studies may lead us to believe that grain refinement proceeds, in all cases, via remelting at low undercoolings and re-crystallization at high undercoolings. However, many studies have slightly (or even substantially) different explanations for grain refinement at $\Delta T_{GR}^{(1)}$ and or $\Delta T_{GR}^{(2)}$ undercoolings. This is the case even when studying alloys of similar composition.

3.4.4 Dendritic “seaweed” remelting

Although the models presented above are the most frequently discussed in grain refinement studies, some works have suggested spontaneous grain refinement, at low or high undercoolings, can proceed via entirely different mechanisms. Mullis et al. [36] argue that the simultaneous occurrence of the second grain refinement transformation at high undercooling and a discontinuity in dendrite growth velocity-undercooling curves has occurred in too many alloy systems (such as Cu-Ni [208], Fe-Ni [209] and others [196]) to be coincidental as is assumed by the dendrite fragmentation model of Schwarz et al. and Karma [40, 41]. Furthermore, Mullis and Cochrane [210] have also suggested that at the high undercooling refinement transition, re-melting is difficult or impossible in dendrite arrays given the high volume fraction of alloy solidified during recalescence. Instead, it is hypothesized that grain refinement could be caused by dendrite remelting during, rather than directly after, recalescence itself. In this vein, Mullis and Cochrane [211, 212] developed a model concluding that dendritic growth in alloys could become unstable at high undercoolings (and, potentially, also at lower undercoolings). They further [213] used phase field simulations to suggest that at high dendrite growth velocities (often obtained at high undercoolings), dendritic growth becomes unstable, resulting in tip-splitting and the formation of a “dendritic seaweed” structure. The term itself was earlier coined by [214].

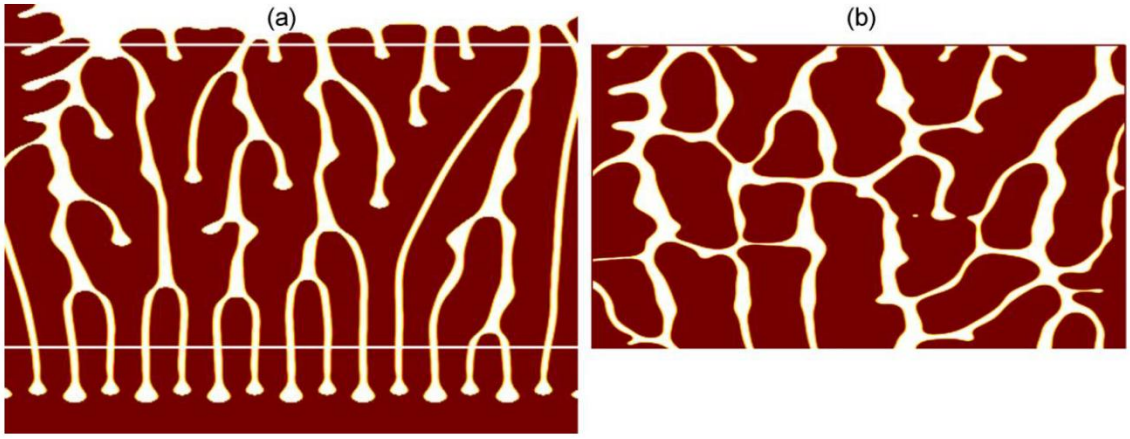

Figure 3.19 Illustration of grain refinement after partial remelting of a dendritic seaweed precursor based on the model of Mullis [36]. (a) Dendritic seaweed precursor structure. (b) Re-melted grain refined structure.

Such works culminate in a phase field model by Mullis [36] demonstrating that certain operating conditions defined by the operating point parameter σ^* cause a similar change in dendrite tip radius to that illustrated in Figure 2.1. Furthermore, at some undercoolings, σ^* may also reach 0, causing dendritic growth to break down and a seaweed structure to be formed. This structure, according to Mullis, is what may partially re-melt to produce the grain refined structure we observe in alloys. Figure 3.19 shows the result of the phase field model by Mullis showing a dendritic seaweed structure and the morphology that may result from remelting of such a structure. Such seaweed structures have been observed in studies on ultra-pure Cu by Dragnevski et al. [215], as well as in the work of Castle et al. [216, 217] on dilute Cu-Ni alloys.

The work of Castle et al. is particularly significant in that it observes no less than three separate mechanisms for grain refinement in similar alloys. In Cu-3.98wt%Ni [216], Castle et al. argue that both observed episodes of grain refinement occur via re-melting and fragmentation. However, upon increasing the Ni content to Cu-8.9wt%Ni [217], they suggest a recrystallisation mechanism is responsible for grain refinement at low undercoolings followed by the re-melting of the aforementioned dendritic seaweed at higher undercoolings. The solute content is important here as the further addition of Ni to the alloy is believed to initiate a transition, at lower undercooling, of preferred dendrite growth direction. The authors suggest that seaweed growth is also initiated at a lower undercooling due to changes in solute content. The study by Zhang et al. [218] on congruently melting CoSi intermetallic compounds, shows the presence of dendritic seaweed structures without significant grain refinement. This provides additional evidence that these structures may be a precursor to

some grain refinement transitions, but do not always result in refined structures in all alloys/compounds under all processing conditions.

3.4.5 Grain refinement transitions and processing route

As with many undercooling experiments, glass fluxing and EML processing seem to be the most widely used methods of solidification when studying grain refinement in alloys. However, each can impact structural formation in the material.

As discussed in section 2.3.2, EML studies induce significant convection in a liquid alloy during solidification. This is notably important in grain refinement studies. Yasuda et al. [219] compared the microstructure in Fe-Ni alloys solidified during EML processing with alternating and static magnetic fields. The static magnetic field reduced melt convection during solidification and hindered dendrite fragmentation and subsequent grain refinement. Instead, more conventional columnar grains were found. This informed the later work of Chen et al. [202] (see 3.4.3), who suggested that the refinement they observed in $Fe_{75}Ni_{25}$ cannot therefore be explained by melt convection as the induction coil was turned off before solidification began in their glass-fluxing experiment.

Drop-tube processing removes the magnetic field altogether and thus, removes the associated induced stirring effect. This is viewed as essential by Mullis and Haque [188] in their work on drop-tube processed Ni_3Ge. Although significant dendrite fragmentation was observed, Electron Backscatter Diffraction (EBSD) results indicate that the resultant dendrite fragments do not always present good nucleation sites for subsequent grain growth into a refined grain structure. This is potentially due to the lack of induced fluid flow during solidification in the drop-tube (as opposed to EML where the induced magnetic field causes significant stirring). This suggests that the fragmentation process does not invariably beget a consistent, refined, microstructure and that other variables need to be considered to achieve such a morphological transformation.

Drop-tubes also differ significantly from other processes due to their very rapid heat extraction rate when the metallic droplet is in freefall. As a result, this may alter the progression of other grain refinement processes like recrystallisation. For example, Cochrane et al. [220] argued that the rapid heat extraction post-solidification was a potential reason for the lack of recrystallisation observed in drop-tube processed Cu-Ni alloys. However, they did note that high dendrite growth velocities may also incorporate significant internal stress in the solid that may provide a driving force for crystallisation. Much as the other studies discussed seem to have shown, the process of remelting, which was not suppressed the alloy droplets (no matter how high the cooling rate), was

deemed to be very rapid, and likely highly dependent on solute trapping and flow of the residual liquid.

Perhaps the most extensive study of grain-refinement in drop-tube processed binary alloys was undertaken by Norman et al. [221] who have processed Cu-Ni alloys at various compositions via EML, drop-tube processing and gas atomization. They perform a semi-quantitative statistical analysis of the occurrence of grain refinement with undercooling. Initially, structures are divided into purely dendritic, fragmented, and grain-refined structures. In high purity alloys solidified under high vacuum conditions, grain refined structures are observed at droplet sizes between 800 μm and 30 μm. They tend to increase in occurrence with decreasing droplet size to peak at droplet sizes from 100 – 200 μm. A notable trend reversal is found in Cu-Ni samples drop-tube processed at lower purity and at a lower vacuum. Grain-refined droplets are instead present in the highest percentage at the largest droplet sizes, with occurrence rate decreasing monotonically as droplet size decreases. Perhaps the most intriguing conclusion discussed in this work is the occurrence of any grain-refinement at all in the drop-tube processed and atomized alloy. The group argue that based on calculated plateau times Δt_{pl}, the model proposed by Schwarz et al. and Karma [40, 41], would predict no grain refinement whatsoever in drop-tube processed or gas atomized samples [221]. The fact that this grain refinement is clearly observed reveals the potential need to adapt grain-refinement models to factor in solidification at very high cooling rates.

3.4.6 Grain refinement in ternary alloys

Grain refinement has thus far been very seldom explored in more complex alloys and HEAs. In addition to the nickel-based superalloy discussed in [200] and [201], An et al. [222] found that the single solid solution phase in binary Ni-Cu can be maintained even upon addition of a small amount of Co (to form $Ni_{65}Cu_{31}Co_4$). They then rapidly solidified the alloy and found that the grain refinement mechanisms at $\Delta T_{GR}^{(1)}$ and $\Delta T_{GR}^{(2)}$ are remelting/fragmentation and recrystallisation respectively. While the Co addition did not change the nature of the mechanisms of refinement, it altered the undercooling at which they occurred. Other work has been undertaken on the similar $Ni_{65}Cu_{33}Co_2$ alloy and $Cu_{60}Ni_{35}Co_5$ on the opposite end of the compositional spectrum by Xu et al. [223, 224]. In both cases, the minor addition of Co did not yield changes in the grain refinement mechanisms, but did influence the final mechanical properties of the alloys.

3.4.7 Grain refinement in high-entropy alloys

The first specific mention of grain refinement in HEAs seems to be from a study by Andreoli et al. [25] in 2021 on CrFeNi, CoCrNi and CoCrFeNi undercooled via EML. In the quaternary alloy, a columnar dendritic grain structure transforms into a refined equiaxed grain structure at an undercooling of about 160 K. The authors tentatively suggest that the fragmentation and re-melting mechanism is responsible for such a change, but do not definitively eliminate other possibilities. Intriguingly, no discontinuity is found in the dendrite growth velocity-undercooling curve for CoCrFeNi, although the steep rise in growth velocity at an undercooling of 160 K may have the same effect. The same group later investigated the impact of Al addition on the solidification characteristics, conducting another EML study on $Al_{0.3}$CoCrFeNi and AlCoCrCuFeNi, Andreoli et al. [225] further found that $Al_{0.3}$CoCrFeNi underwent a grain refinement transition at 70 K of undercooling. Interestingly, addition of Al also caused a reduction in dendrite growth velocity compared to quaternary CoCrFeNi at an equivalent undercooling. The grain refinement mechanism is also attributed to dendrite remelting and fragmentation. In contrast, a recent study by Zhang et al. [226] on FeCoNiPd points to the importance of the formation of subgrains to facilitate the grain refinement process in undercooled alloys. These subgrains can be formed in dendritic and inter-dendritic phases through multiple pathways, and result in a scattering of the orientation angle of the grains and even a splitting of grains into two separate orientations. This is a key reason for the formation of the equiaxed grain morphology. The experiment also works to unite the commonly discussed refinement mechanisms of dendrite re-melting/fragmentation and recrystallisation. The authors point out that while these subgrains are likely formed via recrystallisation in FeCoNiPd, it is very possible that subgrains could instead be formed by the aforementioned fragmentation and rotation could be induced by fluid flow in the still partially re-melted alloy microstructure. Whatever the final mechanism, undercooling the alloy by about 100 K caused a reduction in grain size by one order of magnitude. Finally, the previously discussed work of Yan et al. [24] on EML processed CoCrCuFeNi also observes a grain refinement transition and the shift from columnar dendrites to finer equiaxed dendrite microstructures. A grain size reduction of about one order of magnitude also occurs as with FeCoNiPd. However, the undercooling required for this reduction is higher, at about 250 K. The group seem to find indications of both recrystallisation and dendrite fragmentation in the resultant grain refined microstructure, but do not go so far as to make a choice between them in this work. There is, therefore, further experimentation to be done in this area of HEA design.

3.5 Investigation aims

Given the myriad of non-equilibrium structures obtainable in HEAs processed via rapid cooling, the initial aims of the experiment are summarised as follows:

- To gain information on obtainable microstructures in HEAs undergoing LPS in the metastable regime
- To determine criteria for metastable LPS in HEAs with regards to undercooling, cooling rate, composition etc…
- To understand the effect of cooling rate and undercooling on the structures in metastable liquid phase separated HEAs
- To compare the LPS behaviour in HEAs to that of more conventional binary and ternary immiscible alloys solidified under similar conditions

3.5.1 Alloy selection process

In accordance with the initial experimental aims of this work, it was imperative to select for study a HEA in which it is possible to initiate metastable LPS. Studies conducted in this area so far are overwhelmingly based on glass fluxing or EML experiments. As discussed in section 2.3.2, this solidification technique is very different in terms of time scale and key variables compared to drop-tube processing. Importantly, LPS structures created by glass-fluxing fall under the influence of Stokes motion. A layer of the more dense liquid will therefore settle at the bottom of the solidified sample, removing the possibility of core shell formation. By levitating the droplet, EML studies remove the effect of gravity and allow core-shell structures to be achieved. However, they are similarly focused on comparatively slow reduction in temperature and inhibition of heterogenous nucleation to enhance undercooling. Rapid cooling experiments, such as drop-tube studies, of HEAs exhibiting LPS have yet to been undertaken extensively. Furthermore, as has been discussed, only a few studies have observed and discussed core-shell formation or the formation of fine LPS dispersions, in HEAs. There therefore exists a gap in the literature regarding the impact of cooling rate on microstructure formation in HEAs capable of LPS. Such a gap is what the following investigation was undertaken to address.

Based on the above discussion, the decision was made to pursue experiments regarding a $CoCrCuFeNi_x$ alloy. As shown in Table 3.1, $CoCrCuFeNi_{0.5}$ undergoes stable LPS while CoCrCuFeNi undergoes metastable LPS. Furthermore, the study by Wu et al. [144] suggests that $CoCrCuFeNi_{1.5}$ and $CoCrCuFeNi_2$ do not undergo stable LPS, suggesting that these alloys might liquid phase separate in the metastable regime. At the same time, the enthalpy of mixing model from Takeuchi et al. [111] shows that increasing Ni content monotonically lowers enthalpy of mixing of a $CoCrCuFeNi_x$ alloy. It is therefore hypothesized that enthalpy of mixing and potentially tendency to liquid phase

separate is inversely related to Ni content. Specifically, in the compositional space where metastable LPS occurs, lowering Ni content should lower the critical undercooling required for LPS. In the $CoCrCuFeNi_x$ alloy system, it is known that equiatomic CoCrCuFeNi possesses a critical undercooling with an average of 170 K and $CoCrCuFeNi_{0.5}$ liquid phase separates in the stable regime. Therefore, the compositional envelope of $CoCrCuFeNi_x$ where $0.5 < x < 1$ should be the focus of the investigation. A value of x can be predicted where $CoCrCuFeNi_x$ undergoes metastable LPS, but at a critical undercooling lower than that of the equiatomic alloy. It was predicted that this would allow LPS to be initiated more easily via drop-tube processing, and would hopefully allow a more varied range of structures to be observed in the different powder size fractions (in particular, core-shell and finely dispersed structures). This would also likely give core-shell structures the most time to form in the rapid cooling environment of the drop-tube, before the onset of solidification. For the above reasons, $CoCrCuFeNi_{0.8}$ was selected for further study and processing in the drop-tube.

3.5.2 Modified experimental objectives

As will be discussed in Chapter 5 and Chapter 6, the extensive metastable LPS that was observed to occur in similar drop-tube experiments on binary and ternary alloys (see section 3.2), as well as in $CoCrCu_xFe_yNi_z$ HEAs (see section 3.2.2.2) was very seldom observed in drop-tube processed $CoCrCuFeNi_{0.8}$. As is often the case, however, the extensive collection of microstructures produced as a result of this processing merit analysis and discussion in their own right. Furthermore, the lack of occurrence of LPS structures (compared to the original hypothesis) is also an interesting facet of the experimental results that needs to be explained. Hence, the modified objectives for this investigation are as follows:

- To observe and catalogue the key structures formed in drop-tube processed $CoCrCuFeNi_{0.8}$
- To characterise and describe the mechanisms of structural formation in drop-tube processed $CoCrCuFeNi_{0.8}$ for the key microstructures produced
- To understand the impact of cooling rate and undercooling on microstructure formation in drop-tube processed $CoCrCuFeNi_{0.8}$
- To describe and explain the reasons for differences between microstructures formed as a result of drop-tube processing and the hypothesized structures, namely the lack of LPS

3.5.3 Initial considerations regarding $CoCrCu_xFe_yNi_z$ alloys

In general, it is known at near equilibrium conditions, $CoCrCu_xFe_yNi_z$ solidifies into a dual-phase FCC solid solution microstructure, with dendrites of a CoCrFeNi-rich phase growing into an interdendritic Cu-rich phase. In a relatively early 2015 study, Park et al. [227] observed these two distinct FCC phases in equiatomic CoCrCuFeNi after casting and calculated a 0.77 volume fraction of CoCrFeNi-rich phase and a 0.23 volume fraction of Cu-rich interdendritic phase. The lattice parameters of each phase were found to be very similar, at 0.359 nm and 0.361 nm respectively. The Cu-rich interdendritic phase contained about 86 at% Cu. This dual phase FCC structure was echoed by Derimow and Abbaschian [134], with XRD distinctly observing two separate sets of FCC peaks. The interdendritic phase was extremely Cu-rich, at above 85 at% Cu. The segregation behaviour of the Cu to the inter-dendritic phase is largely attributed to the positive enthalpy of mixing between Cu and the other elements in the alloy [134, 227]. This is also the same reasoning that is invoked to describe the high Cu content of the Cu-rich liquid following metastable LPS in the equiatomic alloy [135, 144, 146, 147] and in its compositional variants [144, 147, 148]. The alloy has drawn interest as a laser cladded coating for its low stacking fault energy and thermal stability [23], and its ability to resist corrosion and inhibit bacterial growth [228]. Early studies on the mechanical properties of as-cast CoCrCuFeNi equiatomic alloys indicate a Vickers hardness of about 130 in the as-cast condition [229].

Based on these experimental aims, Chapter 4 describes the methodology used to prepare and process the $CoCrCuFeNi_{0.8}$ alloy and the methods used to analyse the microstructures produced. Chapter 5 shows the results of this analysis. Chapter 6 discusses the nature of the results presented based on the objectives of the study described above.

Chapter 4 – Methodology

4.1 Sample preparation

Pure forms of the required elements, cobalt, copper, chromium, iron and nickel were sourced, cut and ground down to the appropriate weight for a final alloy sample of between 15 g and 20 g. The metal, purity and source of each of the starting components is shown in Table 4.1. The initial weights of the alloying elements prepared for arc-melting are noted below in Table 4.2.

Table 4.1 Information on raw metals used for alloy creation

Metal	Supplier	Form	Purity
Cobalt	Koch-Light Laboratories	Rod	99.998%
Chromium	Goodfellow	Rod	99.7+%
Copper	Alfa Aesar	Shot	99.99%
Iron	Goodfellow	Rod	99.8+%
Nickel	Goodfellow	Rod	99.0%

Table 4.2 Calculation of atomic subscript for $CoCrCuFeNi_{0.8}$ based on weights of raw materials

Material	Mass /g ± 0.001	Molar Mass	Wt%	At%	Atomic Subscript
Cobalt	4.154	58.933	21.27	20.85	1.0
Chromium	3.667	51.996	18.71	20.79	1.0
Copper	4.481	63.546	22.94	20.85	1.0
Iron	3.936	55.845	20.14	20.83	1.0
Nickel	3.311	58.693	16.94	16.68	0.8
Total	19.549				

Table 4.2 indicates that upon cutting and grinding the materials, a 19.55 g sample was created with the required atomic ratios of each of the elements.

4.1.1 Arc-melting

The method through which the master alloy is created in this investigation is through arc-melting. A schematic of a typical arc-melter is shown in Figure 4.1. The system works by passing a high current through a tungsten electrode to create an arc between the electrode and a water cooled-copper hearth [230]. At each stage, starting pure metals or alloys are placed into one of the many different shaped crucibles in the copper hearth. The chamber is evacuated and flushed between two and three times with argon gas. The vacuum reached in the arc-melter at the University of Leeds is usually around 6×10^{-2} – 8×10^{-2} bar. A small amount of argon gas is then fed in through the gas line to create an inert atmosphere in the chamber. The argon atmosphere helps to avoid excessive oxidation during melting. In addition, a titanium getter is placed into a different section of the copper hearth and melted first to scavenge any excess oxygen that remains after evacuating the chamber and flushing with argon. The metal samples were arc-melted together to form the final alloy. In order to ensure thorough mixing, the miscible alloy pairs of Cu-Ni and Co-Fe [231] were melted together first. The two pairs were then melted together to form $CoCrCuNi_{0.8}$, after which Cr was added to form the final alloy. Between each re-melting step, the sample was removed from the arc-melter and polished with SiC paper to remove the external oxide layer which had formed during melting. The alloy pairs and $CoCrCuNi_{0.8}$ were flipped over and re-melted three times to allow for proper mixing. Upon addition of the Cr, the final alloy was flipped and melted five times. The resultant metal ingot weighed between 16.45 g, with the loss in mass of about 3.10 g attributed to metal lost to oxidation or grinding. The mass loss during arc-melting and associated processing is shown in Table 4.3.

Table 4.3 Mass loss during melting and grinding process in arc-melted $CoCrCuFeNi_{0.8}$ ingot production process

Alloy	Initial Mass /g ± 0.001	No. of melt and grind cycles	Final Mass /g ± 0.001	Mass Loss /g ± 0.002
CoFe	8.090	3	8.048	0.042
$CuNi_{0.8}$	7.792	3	7.754	0.038
$CoCuFeNi_{0.8}$	15.802	3	15.744	0.058
$CoCrCuFeNi_{0.8}$	19.411	5	16.453	2.958
			TOTAL	3.096

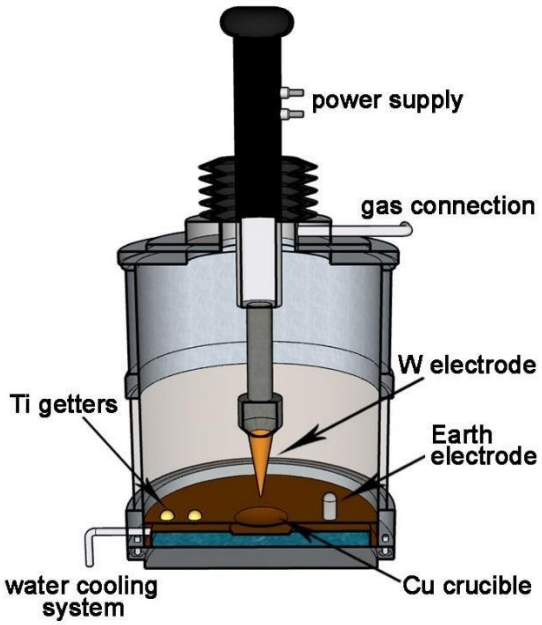

Figure 4.1 Diagram of typical arc-melting furnace [230].

4.1.2 Sectioning

After arc-melting, a dome-shaped (near hemispherical) button was formed. A small piece was sectioned off using an Accutom-5 sectioning machine with a rotating circular diamond-coated blade so that a full cross-section from the top of the dome to the flat side in contact with the copper hearth in the arc-melter, is observable. One section was kept for microstructural analysis of the alloy in arc-melted condition. The smaller portion, weighing 8.10 g, was removed and rapidly solidified via drop-tube processing.

4.1.3 Differential scanning calorimetry

A small section of the $CoCrCuFeNi_{0.8}$ arc-melted ingot was subjected to Differential Scanning Calorimetry (DSC) analysis using a Netzsch STA449 F3 Jupiter simultaneous thermal analyser fitted with a SiC high-temperature furnace. This technique slowly heats and/or cools a material and logs the heat flow between the material and the surroundings. This data output is a continuous curve of heat flow with time. Temperature of the material is logged concurrently with heat flow at each time-step. If the material is being heated, peaks represent heat flow out of the material (exothermic reactions) while troughs in the curve represent heat flow into the material (endothermic reactions). These peaks (and the phase changes they represent) occur at characteristic temperatures during heating or cooling. Characteristic phase transformations such as melting and glass-transitions in the material can therefore be logged. Furthermore, the energy transferred during these phase

changes can be estimated to determine physical properties such as the latent heat of fusion [232]. This technique was employed on $CoCrCuFeNi_{0.8}$ ingot to elucidate the thermal behaviour of any distinct phases in the alloy.

4.1.4 Drop-tube processing

The general methodology behind drop-tube processing has been introduced in section 2.3.3. A schematic of the specific experimental apparatus used at the University of Leeds is provided in Figure 4.2.

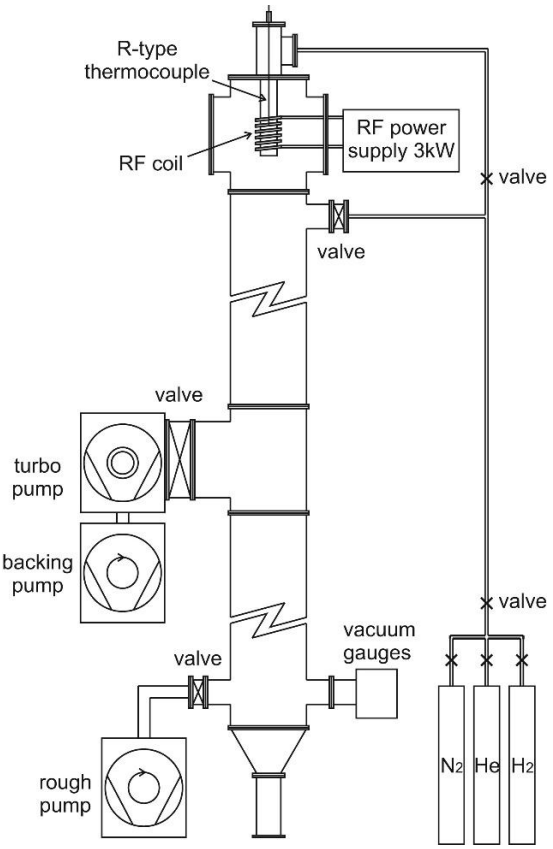

Figure 4.2 Schematic of 6.5 m drop-tube apparatus used for containerless processing at the University of Leeds.

The 8.10 g $CoCrCuFeNi_{0.8}$ sample, (with a volume of approximately 1 cm^3) is placed in an alumina crucible with a tri-hole modification (i.e. three laser-drilled holes in the crucible bottom through which the liquid alloy will be ejected). The diameter of each hole is about 300 μm. The crucible is inserted in a graphite susceptor that is, in turn, inserted into two concentric cylindrical alumina heat-shields. Graphite paper is used to cover the top of the assembly to avoid heat escaping out of the gaps between the heat shields via gas convection. This configuration is suspended at the top of the drop-tube such that the outer heat shield is situated just inside the water-cooled copper heating coil. A thermocouple is inserted into the crucible so that temperature readings can be taken as close as possible to the alloy melt. The drop-tube is sealed and made

airtight before a rough pump is used to establish a low vacuum inside. The tube is then repeatedly flushed with N_2 gas to remove as much oxygen as possible. After 3-4 flushes, the rough pump is isolated and a turbomolecular pump and its associated backing pump are used to establish a higher vacuum. The lowest pressure reached in this particular experiment was 20 Pa ($2*10^{-4}$ bar). The tube was then filled with 40 kPa (400 mbar) of N_2 gas. The N_2 creates an inert atmosphere to avoid oxidation and also acts as a heat transfer fluid when the droplets are in freefall. Power is applied to the RF heating coil to melt the alloy sample. This experiment required the RF coil to operate at full power with a maximum recorded temperature of 1500 K. In reality, the temperature is likely higher due to the fact that the thermocouple is suspended at least a couple of centimetres above the melt. This temperature was held for 30 min to allow complete melting of the alloy before ejection.

During ejection, the crucible is pressurised to 400 kPa (4 bar) creating a high pressure differential. The gas used to pressurise the crucible is the same as that used in the drop-tube atmosphere (N_2 in this case).This forces the liquid alloy through the holes in the bottom of the crucible. The liquid forms a spray of approximately spherical droplets varying diameters. These droplets solidify as they fall down the drop-tube and collect in a catch pot at the bottom. Droplets produced vary in diameter between about 20 μm and 1000 μm. These droplets are sieved into a maximum of ten size fractions, 850+ μm, 850 – 500 μm, 500 – 300 μm, 300 – 212 μm, 212 – 150 μm, 150 – 106 μm, 106 – 75 μm, 75 – 53 μm, 53 – 38 μm, and <38 μm. In this particular experiment, droplet samples in all of the size fractions, with the exception of the smallest <38 μm size fraction, were obtained in suitable numbers for study. Additional, more detailed information on the operation of the drop-tube apparatus at the University of Leeds is provided in [19].

4.1.5 Mounting, grinding, and polishing

The sectioned ingot sample was hot-mounted in transoptic resin. The droplet samples of each size fraction were cold-mounted. Each of these samples was ground and polished to ensure an appropriate finish for use in optical and electron microscopes. The determined optimal grinding and polishing route for $CoCrCuFeNi_{0.8}$ alloy is outlined in Table 4.4 below and is based on [233].

Table 4.4 Grinding and polishing procedure for $CoCrCuFeNi_{0.8}$

Process	Media	Cloth	Size (μm)	Relative Rotation	Force (N)	Time
Grinding	SiC (P400)	N/A	~35	Contra	20	30sec – 1min
Grinding	SiC (P1200)	N/A	~18.3	Contra	20	30sec – 1min
Polishing	Diamond	TexMet C	3	Contra	20	3min
Polishing	Diamond	TexMet C	1	Contra	20	2min
Polishing	Colloidal Silica	Chemomet	0.02-0.06	Contra	20	3min

After each stage, the samples were washed in weak detergent and rinsed with isopropanol alcohol to remove grinding/polishing media and other debris. The samples were then dried. After the final polishing stage, the surface of each sample was swept with a lens cleaner to mechanically remove colloidal silica particles which had adhered (likely electrostatically) to the alloy. Due to the high colour contrast between the principal phases in the solidified alloy, no etching was required before metallographic analysis via optical or electron microscopes.

4.1.6 Microscopy

4.1.6.1 Confocal microscopy survey

In similar studies involving rapid solidification of alloys in the drop-tube, authors often note a wide range of structures such as LPS structures (core-shell, evolving core-shell etc…), dendritic structures and fine dispersions, which occur in various, often differing configurations [128]. A wide range of structural occurrence is what is also, predictably, found in this work on $CoCrCuFeNi_{0.8}$. Although the structures formed in this study are just as varied as those found in other previous work, the assortment of structures observed differs significantly to those found in work on rapid solidification of binary alloys with predicted metastable miscibility gaps. Findings in this experiment include single and multi-crystalline dendritic droplets, droplets in various stages of grain refinement, and dispersions occurring in large scales within droplets or within dendrite arms. Conventional LPS structures such as core-shell are extremely rare. Because of the sheer number of droplet microstructures observed, and the colossal number of droplets produced during the experiment, it was desirable for enough droplets of each size fraction to be

photographed (and their structures, tallied) to further understand the prevalence of each structure with cooling rate.

A Carl Zeiss LSM800 Mat CLSM confocal microscope was used to view these microstructures for tallying purposes. A laser acting as the microscope light source allows sufficient resolution to delineate between structures. The time taken for this analysis is fixed by the resolution required to adequately classify microstructures and the number of droplets that can be seen in a single photograph. The laser light source uses surface topography in the z-axis to enhance picture detail, dividing the z-axis into slices, taking a photograph at each elevation and stitching the photographs together to allow enough contrast to enhance the resolution and view surface features. Figure 4.3 shows an example of a photograph taken using this method.

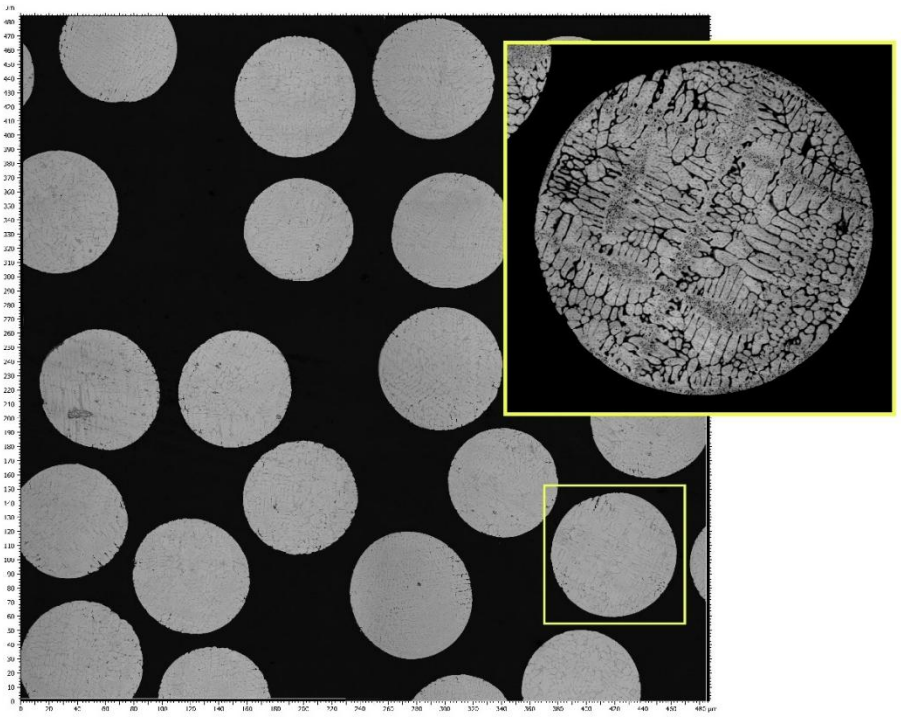

Figure 4.3 Large optical micrograph of droplets of $CoCrCuFeNi_{0.8}$ in the 106 – 75 µm size fraction taken using laser optical imaging on Carl Zeiss LSM800 Mat CLSM confocal microscope. Yellow inset shows level of microstructural detail available for each droplet via such analysis, with dendrites, dispersions and other microstructural features clearly distinguishable.

The raw images taken, which are made up of four separate “tiles”, are stitched together using Carl Zeiss accompanying software. The resolution of the raw image is much greater than is visible in the Figure 4.3. This is shown by an enhanced image of a single droplet bordered in yellow, where details including dendrites, interdendritic phases, impurities and fine dispersions are visible. In this

way, droplets are photographed in large enough numbers for analysis to be statistically relevant, but individual droplets can also be resolved in enough detail for a judgement to be made about what microstructure prevails in each droplet.

Those droplets whose cross-sections were completely or near-completely visible were analysed, and their structures tallied and categorised. Analysis was also limited to spherical or ovular droplets. Multiple photographs, each consisting of four stitched tiles, were taken at varying locations across the sample, with no overlap allowed between photographs to avoid counting the same droplet(s) twice. Photographs were taken in this manner until a sufficient number was available from which to view, analyse and classify at least 250 droplets. However, in each set of photographs pertaining to a particular size fraction, all of the sufficiently exposed droplets were taken into account, meaning that for most size fractions, more than 250 droplets ended up being counted. Over 500 droplets were counted for the 75 – 53 μm size fraction to conduct a deeper statistical analysis to determine minimum representative sample size, which is explained in section 4.3.1 below.

4.1.6.2 Scanning electron microscopy

For detailed analysis of individual droplets and the phases present within, optical microscopy is often insufficient due to limited resolution. Electron microscopy, which uses electrons rather than light to render an image of the sample can be used for this purpose. Scanning electron microscopes fire a beam of accelerated electrons at a sample surface. These electrons interact with nuclei of the atoms in the specimen. The interaction alters the path of the electrons which can be mapped to produce an image of the microstructure. Resolutions down to the hundreds of nanometres can be achieved in this way [234]. A schematic of a typical SEM setup is shown in Figure 4.4.

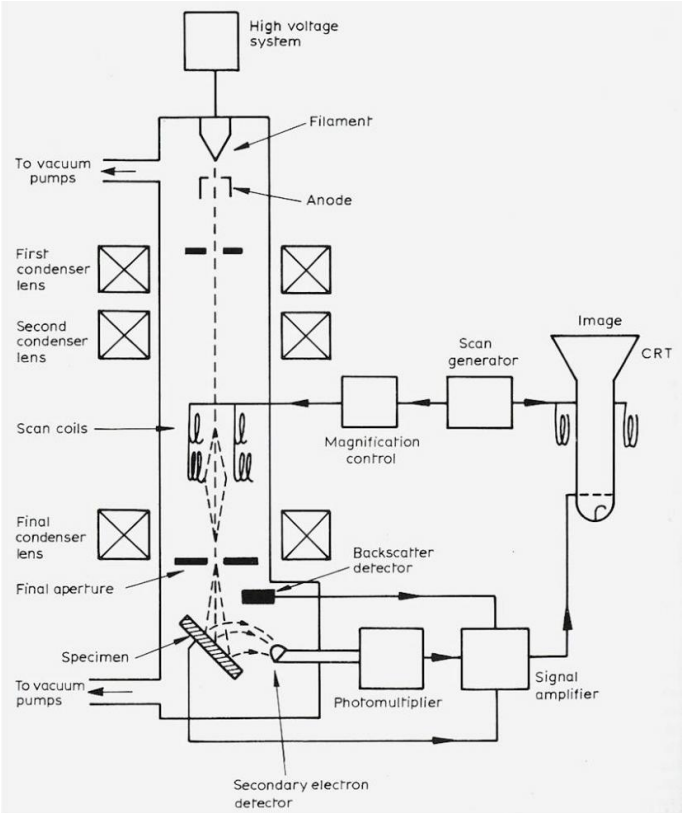

Figure 4.4 Schematic representation of scanning electron microscope showing both secondary electron and backscatter electron detectors [235].

In the SEM, two key electron signals are important. These are secondary electrons (SE) and backscattered electrons (BSE). SE are low energy electrons originating in the sample itself. The incident electron beam ionises electrons on the sample surface which can then be detected by instrumentation. Because these electrons originate from the first few nanometres of depth into the sample surface, they are extremely useful for surface topography analysis. BSE are more energetic and are scattered from their original direction by angles of more than 90 degrees. These electrons penetrate deeper into the sample and the degree of scattering they are exposed to is more dependent on the atomic number of the interacting atom. For this reason, BSE images enhance contrast between areas of the microstructure based on composition. Importantly, the accelerating voltage of the electron gun in the SEM increases the depth of BSE penetration and the interaction volume within which the electrons gather data from the sample. This often reduces the resolution of the final image [236-238].

Before microscopy, the samples were mounted on aluminium stubs and the bottom and sides were coated in carbon paint. The polished regions selected for observation were coated in a thin 20 nm layer of carbon using a sputtering technique. The carbon serves as an electron conductor to avoid the sample become charged over time by the electron beam. The ingot sample and

droplets of all size fractions were analysed in a Hitachi SU8230 SEM. Based on the data requirements of this investigation, electron backscatter images were taken using an accelerating voltage of 5 kV and a working distance of about 8 mm. This allowed enhanced contrast of the individual phases due to differences in composition (elements of higher atomic number appeared brighter in backscatter images). This was deemed more useful than secondary electron imaging, which provided higher resolution and information about surface topography (which was not a key part of this experiment), but yielded less useful compositional information.

During use of the SEM, the energy dispersive X-ray spectrometry (EDX) attachment was used to gather additional compositional information in key areas of the sample. This equipment detects the X-rays emitted from specific areas in the sample as they become ionised during electron bombardment. When an electron is removed from a lower orbital, an electron from a higher energy level drops to take its place, releasing a photon of discrete energy. The characteristic energies of the X-rays enable the particular element from which the X-ray originated to be determined. The composition of different areas of the sample can then be catalogued and processed into an image overlay [239]. Two important examples of these discrete energies are the K_α and L_α characteristic energies. An X-ray of energy K_α is emitted when an electron in the L energy level fills a vacant inner K orbital after the atom has been ionised by the electron beam. The L_α energy X-ray is emitted when an electron falls from an M energy level to the L energy level [240]. For compositional analysis, images were taken using 20 kV accelerating voltage and a working distance of 15 mm. Resolution of the image is reduced, but vital data regarding the composition of the phases present in large areas of the microstructure can be collected via this non-destructive method. The high interaction volume brought on due to the large accelerating voltage means that there is a limit to resolution of the EDX data of about 1 μm. A diagram of the escape depth of SE and BSE, in addition to the interaction volume during EDX compositional analysis is shown in Figure 4.5.

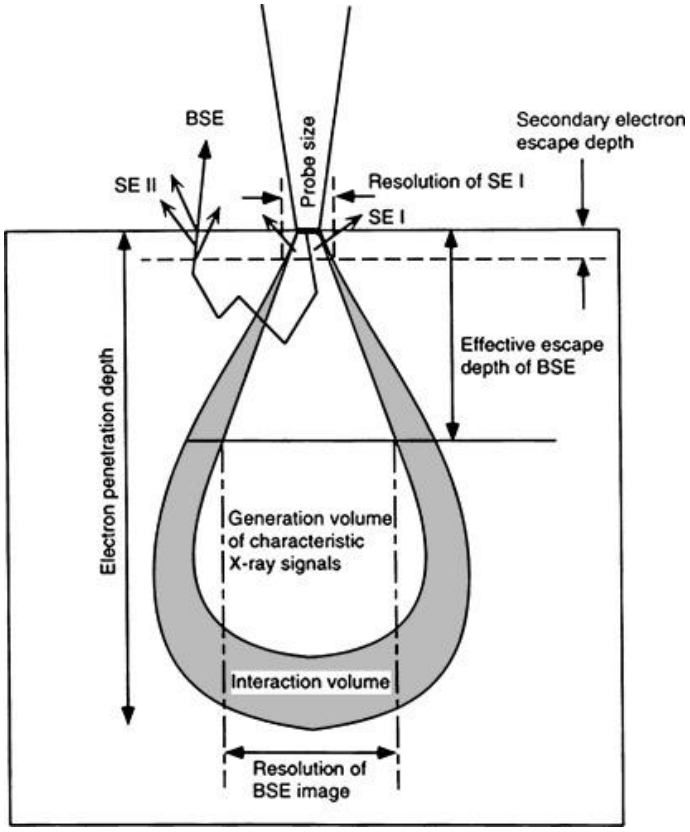

Figure 4.5 Schematic representation of escape depth of secondary and backscattered electrons, and interaction volume for generation of X-ray signals [238]

Use of the particular Hitachi SU8230 SEM requires some specific considerations when observing the $CoCrCuFeNi_{0.8}$ alloy. The presence of Cu in particular caused some discrepancies in the composition calculation with the EDX attachment. During EDX data acquisition at low magnifications, the at% of Cu was heavily overestimated. This was attributed to two primary factors. The first is the presence, in this alloy, of two solid solution phases, one which is Cu-rich and one which is Cu-lean. Such a configuration may make it more difficult for the computer program to calculate the total amount of Cu present in the sample. The other factor is the accelerating voltage. At 15 kV, the voltage conventionally used for EDX mapping, the detector only logs the presence of the Cu L_α peak, omitting the K_α. In contrast, both characteristic peaks for the other constituent elements Co, Cr, Fe and Ni, are logged. This results in an overestimation of the overall Cu content of the alloy sample compared to reality due to a significant uncertainty in the L_α peak. Such a phenomenon is likely due to the overvoltage being insufficient to excite the Cu K_α peak, which has a characteristic energy of ~8 eV. An overvoltage of up to 2-3 times this value is necessary to efficiently excite this peak for accurate composition values to be gathered. The conventional accelerating voltage of 15 kV is likely insufficient in this case. This issue was rectified by increasing the accelerating voltage to 20

kV which allowed the K_α peak of Cu to be included in the analysis as well. However this increase in voltage has the downside of increasing the interaction volume. This likely decreased the accuracy in composition data obtained at scales where dimensions of the desired acquisition area are on the same scale as the interaction volume (i.e. under 10 μm). Areas adjacent to the feature of interest may therefore fall into the surface interaction area and alter composition readings. Additionally, features within the sample underneath the surface can also be included in compositional data if they fall within the interaction volume, which may further alter results.

4.1.6.3 Focused ion beam sectioning

For phase/feature analysis at scales not easily achievable in a SEM, and to analyse the internal microstructure, analysis with a transmission electron microscope (TEM) was required. Because electrons are easily absorbed by the sample [28], a thin section must be cut with a thickness below about 100 nm for use in the TEM. A Focused Ion Beam (FIB) can be used for such preparation. An ion beam (usually comprising Ga cations) is used to cut out a section of material from the bulk and, once the section is removed, to mill and polish each side so the final sample is of the correct thickness and is electron transparent [241]. In this study, a FEI – Helios G4 CX Dual-beam FIBSEM (Focused Ion Beam Scanning Electron Microscope) was used to remove a thin section of material from two particular droplets of interest. The chosen droplets were both selected from the 212 – 150 μm size fraction. Once the desired area was chosen and mapped for section production (Figure 4.6a) the FIB was used to dig two parallel trenches on either side of it (Figure 4.6b). The sample was then lifted out and milled (Figure 4.6c) to the correct thickness (Figure 4.6d). The final FIB sections had a thickness of 50 – 90 nm. These sections were analysed microstructurally and compositionally using TEM.

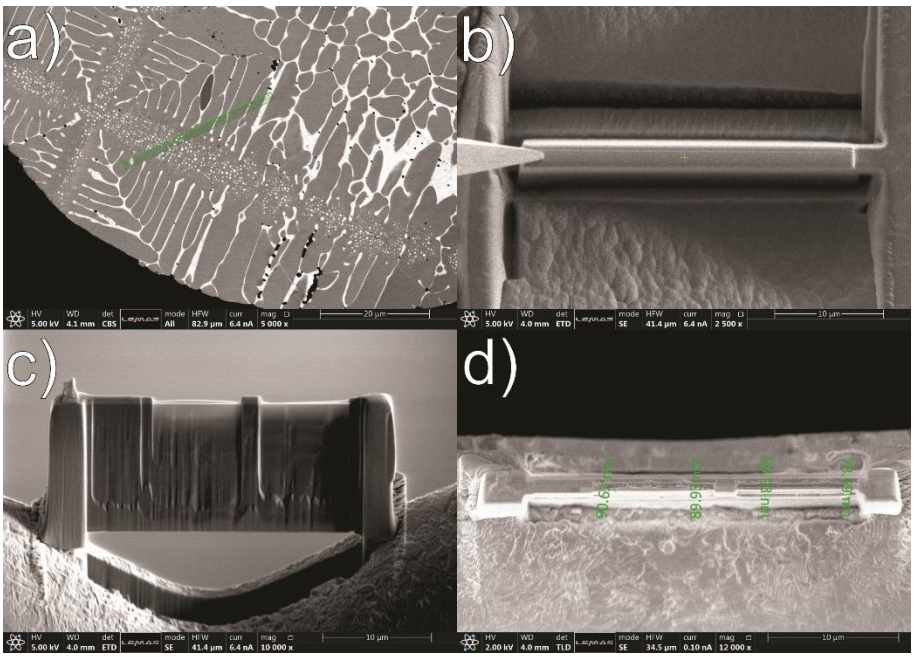

Figure 4.6 Electron micrographs of the FIB sectioning process. (a) Designation of milling area. (b) Initial milling prior to section removal from bulk. (c) Removed section prior to final milling steps to reduce thickness. (d) Overhead view of final FIB section with thickness dimensions marked along full section length.

4.1.6.4 Transmission electron microscopy

In contrast to SEM, TEM techniques create images using electrons that have been accelerated enough to pass through the sample entirely. This allows images and data involving the internal structure of the sample to be gathered [28]. An electron gun fires electrons which are focused on a sample through a condenser lens. Once the beam has passed through the sample, a further series of objective and projection lenses magnify the image, and a fluorescent screen allows the information to be converted to a photograph understandable to the human eye [242]. This form of microscopy allows resolution down to angstrom length scales [234]. Hence, where more accurate composition data was required for a particular part of the droplet microstructure, a FEI Titan Cubed Themis 300 G2 FEG S/TEM was utilised, operating at a 300 kV accelerating voltage. Initially, bright field TEM (BFTEM) images were taken using the attached GATAN OneView 16 Megapixel CMOS digital camera. The fitted windowless 4-detector Super-X EDX (0.7 srad solid angle) was also used to obtain detailed composition information in the material at the nanoscale.

In addition to the above analysis, the crystal structure and lattice parameters of each of the phases present were also subjected to selected area electron diffraction (SAED) analysis. An electron beam (less focused than in the case of bright field electron microscopy) is fired at a selected area of the thin crystalline

sample in the TEM, the electron beam is diffracted while passing through the sample crystal lattice. These diffracted beams form a pattern on the screen on which they are projected, which is then read by the TEM software. The pattern for a single crystal is a series of diffraction points with repeating spacing in between them [243]. An example is shown in Figure 4.7. The diffraction patterns are represented through reciprocal lattices, and the spacing is therefore measured as reciprocal distance in units of nm^{-1}.

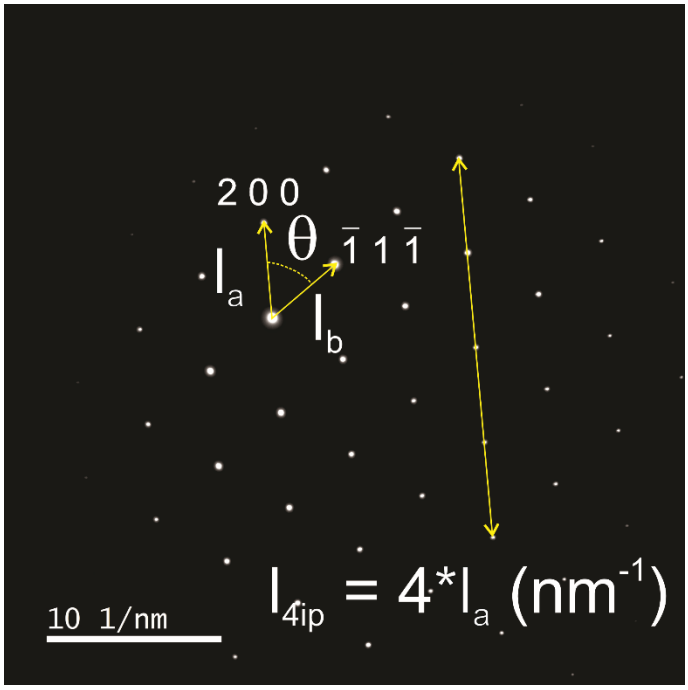

Figure 4.7 Example crystal structure and lattice spacing determination for reciprocal lattice SAED pattern of $CoCrCuFeNi_{0.8}$ phase. Key lengths l_a and l_b along with angle θ are marked along with the final determined crystallographic directions.

Because of the lattice distortion that is characteristic of many HEAs (see section 2.4.2.2), lattice spacings do not often conform exactly to those of more common structures (common alloys, compounds etc…) contained in relevant databases. It was therefore impossible to use accompanying software TEM software to automatically index the SAED patterns and determine the crystal structure. Such a task was instead performed manually. The diffraction patterns were analysed in ImageJ software for the purposes of comparison. The lengths l_a and l_b, and the angle θ from Figure 4.7 were measured using the program. The characteristic reciprocal length ratio $l_a/l_b$was used in combination with θ to predict the phase structure of the material. Given that, based on literature involving similar alloys, a dual-phase FCC structure was predicted (see section 3.5.3), these values were compared against commonly encountered metallic solid solution crystal structures (FCC and BCC) in different orientations. Some

of these common patterns are given in [244]. This same method was used to determine the zone axis along which the image was taken. Once this was done, the interplanar spacing(s) of said material were estimated directly from the diffraction pattern images using the average distance between lattice points in specific directions. For example, in a cubic system, the distance between lattice points in the $< 100 >$ set of directions (d_{100}) can be used to find the unique interplanar spacing (lattice parameter), given that the cubic crystal is symmetrical in all three dimensions. The distance between the lattice points in the $< 200 >$ set of directions (d_{200}) is therefore half of that between the d_{100} spacings. In the example in Figure 4.7, $l_a/l_b \cong 1.155$ and $\theta \cong 54.74$. This suggests a FCC crystal lattice with l_a in the $[200]$ direction and l_b in the $[\bar{1}1\bar{1}]$ direction. Based on this orientation, the zone axis was found to be $[011]$. Finally, if the distance between the (200) planes is used to estimate the lattice parameter, we calculate the lattice parameter using Equation 4.1 for a cubic crystal lattice. In this example, a length l_{4ip} incorporating four inter-plane distances is used to ensure a valid average interplanar distance is used.

$$a = b = c = 2 * \frac{4}{l_{4ip}} = 2 * \frac{4}{4l_a} \qquad 4.1$$

A key caveat regarding this measurement is the reported lack of accuracy regarding interplanar spacings (and thus, lattice parameters) measured in this way using TEM SAED patterns. This has been mentioned by Zhang et al. [245] among others, who suggest that the accuracy error in such measurements would be on the order of at least ± 0.5%. However, Mugnaioli et al. [246] have shown that with proper calibration and correction for factors such as elliptical distortion, interplanar spacings can be calculated for various crystalline materials to an accuracy of ± 0.1%. In this investigation, systematic errors may arise from lens distortions in the TEM camera or inaccuracy in the determined camera constants. Further random error is also likely in the manual measurement of the distance between diffraction points. In general therefore, measurements of interplanar spacing in this work are subject to a total error of ± 4%. However, if SAED patterns are gathered contemporaneously from adjacent regions in the sample, and are subsequently used to calculate interplanar spacings, the error inherent in these measurement can be reduced from ± 4% to around ± 1%. The magnitude of these errors has been estimated based on discrepancies in measurements of interplanar spacings of well-known crystalline materials using the TEM, and the values of these spacings available

in literature. Errors are also reduced through consistent calibration of the microscope as per the manufacturer instructions.

4.1.7 Estimation of cooling rate in drop-tube

As discussed in section 2.3.3, the drop-tube experimental method involves the near simultaneous rapid solidification of thousands of liquid alloy droplets. This makes it impossible to measure the temperature of specific droplets over time and makes the thermal history of one particular droplet unobtainable. However, given that the drop-tube presents a relatively controlled solidification environment, we can solve the relevant energy balance equation for a metal droplet in freefall through a gas atmosphere to estimate the cooling rate of a spherical droplet based on its diameter. Such a heat balance is treated extensively in [247] and applied to the specific drop-tube apparatus at the University of Leeds in [19, 128]. The heat balance factors in the heat transferred via conduction, convection and radiation and can be represented by Equation 4.2.

$$\frac{dT_d}{dt}\left[c_{p(l)}(1-f)+c_{p(s)}f-L_{f(alloy)}\frac{df}{dt}\right]=\frac{6h}{\rho_{alloy}d}\left(T_d-T_g\right)+\frac{6\varepsilon\sigma_b}{\rho_{alloy}d}\left({T_d}^4-{T_g}^4\right) \qquad 4.2$$

where $\frac{dT_d}{dt}$ is the overall droplet cooling rate, $c_{p(l)}$ is the specific heat capacity of the liquid alloy, f is the fraction of the droplet solidified, $c_{p(s)}$ is the specific heat capacity of the solid alloy, $L_{f(alloy)}$ is the alloy latent heat of fusion, ρ_{alloy} is the alloy density, T_d is the instantaneous alloy droplet temperature, T_g is the gas temperature, ε is the alloy emissivity, σ_b is the Stefan-Boltzmann constant, and d is the diameter of the alloy droplet in free-fall, also often referred to as the droplet size. Term one on the right hand side represents heat transfer via conduction and convection and term two, heat transfer via radiation. The term h represents the combination of conductive and convective heat transfer coefficients at the droplet-gas interface and can be approximated from Equation 4.3 [247, 248].

$$h=\frac{\kappa_g}{d}\left(2+0.6\sqrt{Re}\sqrt[3]{Pr}\right) \qquad 4.3$$

where κ_g is the thermal conductivity of the gas atmosphere, Re is the Reynolds number, and Pr is the Prandtl number. The Reynolds and Prandtl numbers are

used to describe the gas flow characteristics, and are defined in Equation 4.4 and Equation 4.5 respectively.

$$Re = \frac{\rho_g d}{\mu} \left| v_d - v_g \right| \tag{4.4}$$

$$Pr = \frac{c_{p(g)} \mu}{\kappa_g} \tag{4.5}$$

where ρ_g is the gas density, μ is the gas kinematic viscosity, and $c_{p(g)}$ is the gas specific heat capacity. The term $\left| v_d - v_g \right|$ is the difference between the droplet velocity v_d and the gas flow velocity v_g. Assuming the gas movement is negligible, the term can be approximated as the droplet terminal velocity v_{term} as it falls through the N_2 gas. Assuming the droplet instantaneously reaches terminal velocity, and that it maintains this velocity the entire time it is in freefall, we arrive at Equation 4.6.

$$\left| v_d - v_g \right| = v_{term} = \sqrt{\frac{4gd}{3C_d} \left(\frac{\rho_{alloy} - \rho_g}{\rho_g} \right)} \tag{4.6}$$

where g is the acceleration due to gravity, and C_d is the drag coefficient. C_d is found through Equation 4.7.

$$C_d = \frac{4mg\rho_g}{\pi \mu^2 Re^2} \tag{4.7}$$

where m is the droplet mass. From this, the cooling rate can be estimated for any spherical droplet diameter. The heat balance in Equation 4.2 calculates the average cooling rate during solidification, factoring in the phase change from liquid to solid and the consequent release of latent heat $L_{f(alloy)}$. In some cases, however, we are only concerned with the maximum cooling rate achieved in the liquid state (i.e. the cooling rate just after ejection) and the maximum cooing rate achieved in the solid state (i.e. the cooling rate just after solidification is complete). To calculate these values, we eliminate the heat capacity term of the phase that is not being considered and set the latent heat of fusion $L_{f(alloy)}$ to 0

in Equation 4.2. After reducing terms, the maximum liquid phase and solid phase cooling rates $d\,T_{d(l)}/dt$ and $d\,T_{d(s)}/dt$ respectively, are represented in Equation 4.8.

$$\frac{dT_{d(l,s)}}{dt} = \frac{1}{c_{p(l,s)}} \left\{ \frac{6h}{\rho_{alloy(l,s)} d} \left(T_d - T_g\right) + \frac{6\varepsilon\sigma_b}{\rho_{alloy(l,s)} d} \left({T_d}^4 - {T_g}^4\right) \right\} \qquad 4.8$$

4.2 Structural classification

To properly evaluate structural change with droplet size and cooling rate, we divide the structures observed into broad categories and, subsequently, indicate secondary features that further divide these categories into subsets. We note the presence of ten broad categories of structure, which can be further subdivided into eighteen subsets. A classification system was developed to better differentiate repeatedly occurring structures and their relative frequency of occurrence in each size fraction. A sample of droplets in each size fraction (n_s ≥ 250) was divided into these categories.

1) Simple dendritic microstructure
   a) Single crystal (SC) – Comprising dendrites of a higher melting point phase solidified in a matrix of the lower melting point phase
   b) Multi-crystal (MC) – Similar to SC structure, with visible grain boundaries likely caused by nucleation and growth of the dendritic phase at multiple different sites across the droplet diameter
2) Grain refined microstructure
   a) Partially grain refined (PGR) – incomplete dendrite fragmentation and refinement where prevailing structure varies between well-defined primary, secondary and tertiary dendrite arms and equiaxed grain structure, as well as intermediate structures such as partially fragmented dendrites and ‘dendritic seaweed’ [216].
   b) Fully grain refined (FGR) – complete dendrite fragmentation and refinement producing an equiaxed grain structure in the large majority of the exposed droplet cross-section
3) Grain refined and cellular structure
   a) Partially grain refined with a cellular structure (PGR+Cell) – as in 2a) but with cells of minority phase surrounded by network of majority phase making up a significant proportion of the microstructure in the otherwise partially grain refined droplet
   b) Fully grain refined with a cellular structure (FGR+Cell) – as in 2b) but with cells of minority phase surrounded by network of majority phase making up a significant proportion of the microstructure in the otherwise fully grain refined droplet
4) Dendritic dispersions
   a) Single crystal (SCDD) – Single crystal droplet as in 1a) where closer inspection shows clear two-phase dispersions within the dendrite arms

   b) Multi-crystal (MCDD) – Multi-crystal droplet as in 1b) where closer inspection shows clear two-phase dispersions within the dendrite arms
5) Grain refined microstructure with dispersions
   a) Partially grain refined (PGRDD) – as in 2a) with circular dispersions within dendrites, intermediate structures and/or equiaxed regions of partially grain refined microstructures
   b) Fully grain refined (FGRDD) – as in 2b) with circular dispersions within the equiaxed regions of a fully grain refined microstructure
6) Grain refined and cellular structure with dispersions
   a) Partially grain refined with a cellular structure (PGRDD+Cell) – as in 5a) but with cells of minority phase surrounded by network of majority phase making up a significant proportion of the microstructure in a partially grain refined droplet
   b) Fully grain refined with a cellular structure (FGRDD+Cell) – as in 5b) but with cells of minority phase surrounded by network of majority phase making up a significant proportion of the microstructure in a fully grain refined droplet
7) Large dispersions
   a) Simple large dispersions (LDOP) – large dispersions occupying a significant area fraction of the droplet surface, distinguishable from dendritic dispersions in that they occur on a much larger scale and cannot be linked to dendrite arms occurring in the droplet.
   b) Cellular dispersions (CDOP) – large dispersions occupying a significant area fraction of the droplet surface, similar to those in simple large dispersions but, with an added feature of a fine cellular network of one phase which separates pockets of the large dispersions from one another.
8) Conventional liquid phase separation microstructures
   a) Core-shell (CS) – core of one phase surrounded partially or fully by the shell of another
   b) Evolving core-shell (ECS) – LPS structure in intermediate stages of coagulation and ripening to eventually form a core and shell
9) Highly globular dendrites with dispersions (HGDD) – rounded highly globular dendrites with primary, secondary or tertiary arms almost merging and/or leaving less space than usual for the interdendritic phase.
10) Extremely fine dendrites with dispersions (ExFDD) – dendrites occurring on a much finer scale then that prevailing regularly in other droplets in the analysed size fraction (which therefore theoretically undergo the same cooling process at the same rate).

Examples of droplets displaying these structures are shown in SEM backscatter micrographs in Figure 4.8. In all photographs, the darker grey phase is Cu-lean (CoCrFeNi-rich) while the lighter phase is Cu-rich. Figure 4.8a and Figure 4.8b show single (SC) and multi-crystal (MC) dendritic structures with no dendrite dispersions. Figure 4.8c and Figure 4.8d show partially (PGR) and fully (FGR) grain-refined structures with no dendrite dispersions. Figure 4.8e shows a cell structure found in some partially and fully grain-refined structures (with and without dispersions). Figure 4.8f and Figure 4.8g show single (SCDD) and multi-

crystal (MCDD) dendritic structures with dendrite dispersions. Figure 4.8h and Figure 4.8i show partially (PGRDD) and fully (FGRDD) grain-refined structures with dispersions in the refined grains. Figure 4.8j and Figure 4.8k show large (LDOP) and cellular (CDOP) dispersions of the Cu-rich phase in the Cu-lean phase. Figure 4.8l and Figure 4.8m show conventional liquid phase separation structures including evolving (ECS) and fully formed (CS) core-shell structures respectively. Figure 4.8n shows highly globular dendrites with dispersions (HGDD). Figure 4.8o shows extra fine dendrites with dispersions (ExFDD).

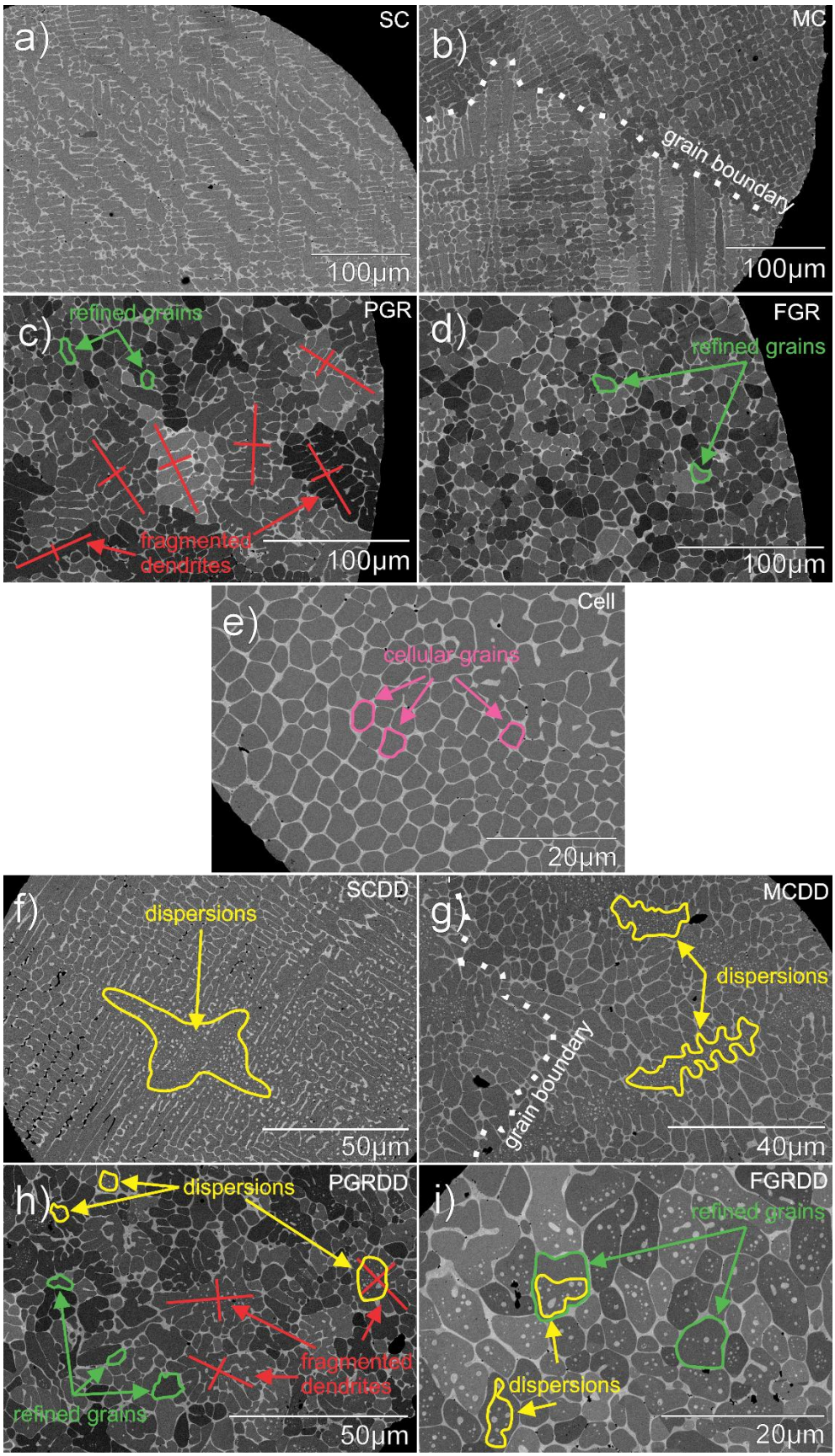
a)
SC
100μm
b)
MC
grain boundary
100μm
c)
refined grains
PGR
fragmented dendrites
100μm
d)
FGR
refined grains
100μm
e)
Cell
cellular grains
20μm
f)
dispersions
SCDD
50μm
g)
MCDD
dispersions
grain boundary
40μm
h)
dispersions
PGRDD
fragmented dendrites
refined grains
50μm
i)
FGRDD
refined grains
dispersions
20μm

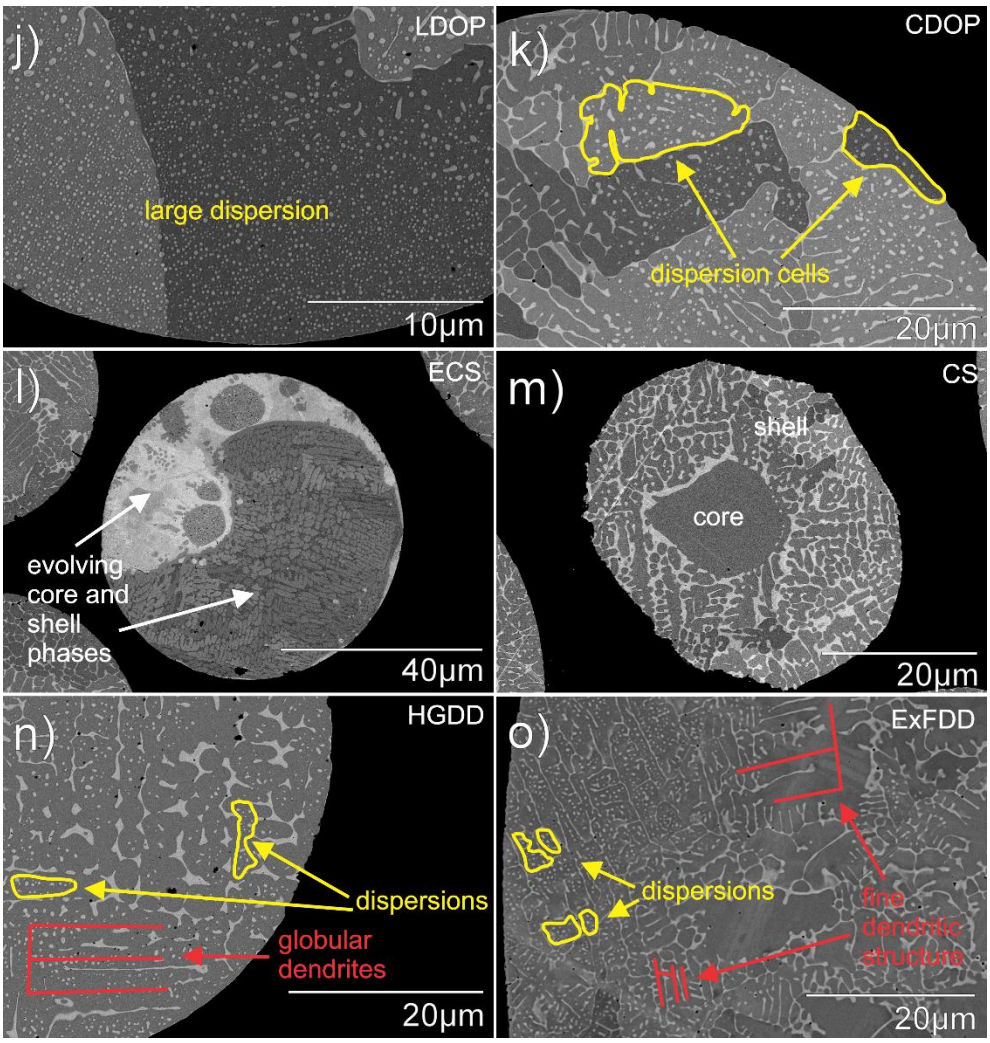

Figure 4.8 SEM BSE micrograph catalogue of microstructures formed in drop-tube processed $CoCrCuFeNi_{0.8}$ alloy. (a) SC – single crystal dendritic structure. (b) MC – multi-crystal dendritic structure. (c) PGR – partially grain refined structure with combination of refined grains and fragmented dendrites. (d) FGR – fully grain refined structure with refined grains occupying the full droplet cross section area. (e) Cell – cellular structure with network of heavily spherodized grains. (f) SCDD – single crystal dendritic structure featuring dispersions in some dendrite arm cores. (g) MCDD – multi-crystal dendritic structure featuring dispersions in some dendrite arm cores. (h) PGRDD – partially grain refined structure showing combination of refined grains and fragmented dendrites. Some dendrites and refined grains contain dispersions. (i) FGRDD – fully grain refined structure showing refined grains occupying the full droplet cross section area. Some refined grains contain dispersions. (j) LDOP – large dispersions occupying significant part of droplet cross section area. (k) CDOP – cellular dispersions occupying significant part of droplet cross section area. (l) ECS – core-shell structure at intermediate stages of formation. (m) CS – fully formed core-shell structure. (n) HGDD – highly globular dendrite structures. Some dendrites contain dispersions. (o) ExFDD – Extra-fine dendritic structures. Some dendrites contain dispersions. Grain boundaries are indicated by white dotted lines, dendrites are mapped with red lines, refined grains are outlined in green, dispersions are outlined in yellow, cells are outlined in magenta.

4.3 Droplet statistical analysis

From the large series of possible structures present in each droplet size fraction, we focus primarily on three trends. These are incidence of dendrite dispersions, large dispersions and grain refinement.

The incidence of each of these structures in all size fractions is calculated by summing together more specific classification structures in each size fraction. For example, to analyse the prevalence of large dispersions across droplet sizes, we add together all structures noted to contain these dispersions, namely the LDOP and CDOP structures. The resultant summations for each of the three trends are shown in Equation 4.9, Equation 4.10 and Equation 4.11 for each size fraction.

$$Dendrite\ Disp. = SCDD + MCDD + PGRDD + FGRDD + PGRDDcell + FGRDDcell + HGDD + ExFDD \quad 4.9$$

$$Large\ Disp. = CDOP + LDOP \quad 4.10$$

$$Grain\ Ref. = PGR + FGR + (PGR + cell) + (FGR + cell) + PGRDD + FGRDD + (PGRDD + cell) + (FGRDD + cell) \quad 4.11$$

Because a slightly different number of total droplets was counted in each size fraction during the classification, the number of each structural category present is divided by the number of total droplets analysed in each size fraction to yield a percentage value for better comparison of structural incidence across size fractions and hence, cooling rates.

4.3.1 Minimum sample size determination

Because the droplet samples were mounted in resin and prepared before microscopic analysis, the number of droplets with their internal microstructures exposed for tallying is only a small subset of the actual number of droplets of each size fraction recovered from the drop-tube. Despite this, viewable and classifiable droplets, particularly in the case of smaller size fractions, often number in the hundreds or even thousands. Statistically, a large sample size is favourable for determining trends across droplet size with any degree of certainty. Therefore, we establish a minimum sample size for droplet size

fractions in situations where it was deemed unfeasible to count all exposed droplets (i.e., all droplet size fractions other than the two largest). To determine minimum sample size, one size fraction was chosen at random (75 – 53 μm) and the structures of 514 droplets in this size fraction were catalogued to determine a minimum sample size necessary to provide a sample size that was adequately representative of the whole size fraction population in terms of structural occurrence.

To determine the degree to which the sample is representative of the whole size fraction, the sample is randomized and the total droplets within the sample (n_s) are divided into two groups of equal population (g_s) using Equation 4.12. Each group therefore comprises half of the droplets in the sample. Using the 75 – 53 μm as an example, a sample of n_s = 514 is divided into two groups of g_s = 257. The numeric incidence of each catalogued structure in group 1 and group 2 is then compared, noting the absolute value of the difference between the incidence of each structure, and summing the difference values for all of the structures. The absolute value of the differences between the samples, θ_i divided by the group size (g_s, half of the full sample size, calculated in Equation 4.12) gives us the mean absolute error (MAE), a value between 1 and 0 which represents the magnitude of difference between the samples relative to the sample size. The closer the value is to 1, the larger the differences between the two randomised groups. Subtracting this value from 1 and multiplying by 100 therefore gives the percent similarity. Equation 4.13 and Equation 4.14 calculate MAE and percent similarity below [249].

$$g_s = n_s/2 \tag{4.12}$$

$$MAE = \frac{\sum_{i=1}^{g_s} |\theta_i|}{g_s} \tag{4.13}$$

$$\%similarity = (1 - MAE) * 100 \tag{4.14}$$

Using MATLAB®, this analysis is conducted one hundred times (one hundred different randomisations) and average $\%similarity$ is calculated. The program was also used to calculate the average $\%similarity$ (from the 100 trials) for a wide range of group sizes, from as small as 15 droplets each (g_s = 15, n_s = 30) to the full size of the sample (g_s = 257, n_s = 514), the average percent similarity

is then plotted as a function of increasing sample size. Sample sizes under 30 were omitted due to the tendency of drastically different results between trials (i.e., sample sizes of n_s = 2 would either produce a 100% or 0% difference). The resultant plot is shown below in Figure 4.9 for the 75 – 53 µm size fraction for sample sizes between a minimum of n_s = 30 and a maximum of n_s = 514, which is the total sample size catalogued for the 75 – 53 µm.

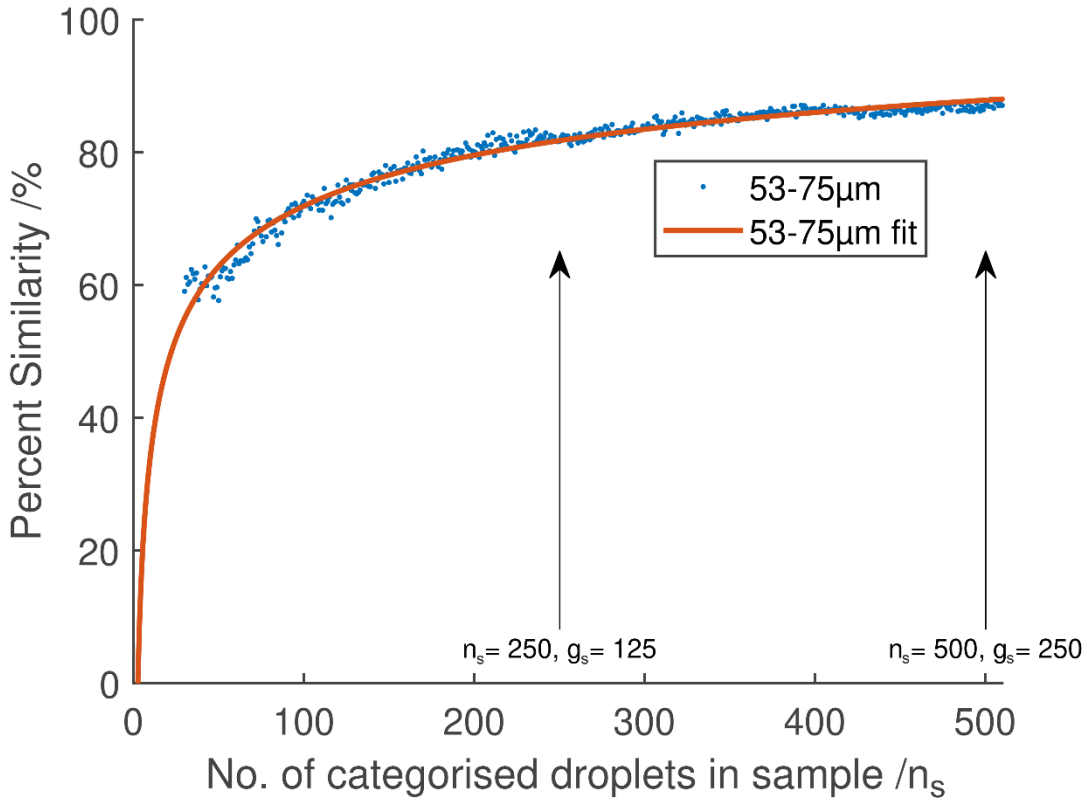

Figure 4.9 Percent similarity variation with sample size in 75 – 53 µm size fraction of $CoCrCuFeNi_{0.8}$ droplets. Percentage similarity begins to plateau as sample size continues to increase. Doubling the sample size n_s from 250 to 500 increases percentage similarity by less than 10%.

Figure 4.9 shows the variation in percent similarity with respect to sample size for the 75 – 53 µm size fraction. The raw data for percentage similarity between the minimum sample size n_s = 30 and the full sample size is used to plot a best-fit line that represents the trend in increase of percent similarity with sample size (shown by the red curve). Based on the trend (best represented here by an exponential curve), increasing sample size n_s from 250 to 500 (that is, doubling the number of droplets counted in the size fraction) is likely to only result in a 5-10% increase in percent similarity. It is therefore concluded that for the other size fractions, a count far above n_s = 250 is unnecessary given the time requirement involved in gathering such data.

Other size fractions, which present a different spread of structures than the 75 – 53 µm, can also be treated with this analysis method, and this is done below. However, as only 250 droplets have been analysed in each other size fraction, the graphical exponential fit was used to extrapolate to a sample size n_s = 500. Results are shown in Figure 3.10. Importantly, the 850+ µm and 850 – 500 µm size fractions had a total of less than 250 countable droplets, meaning that this extrapolation was not necessary for these two size fractions, as the whole exposed sample could be classified.

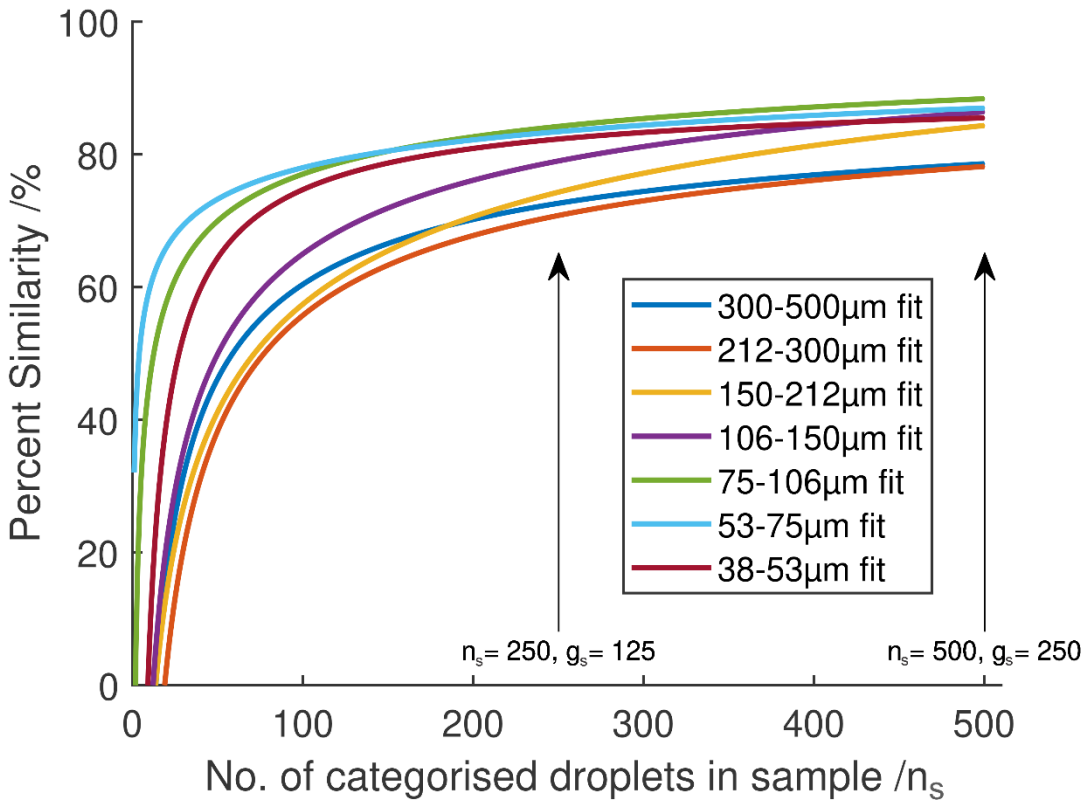

Figure 4.10 Percent similarity variation with sample size in all droplet size fractions of CoCrCuFeNi$_{0.8}$. All droplets in the 850+ µm and 850 – 500 µm populations are counted, so they are omitted from this analysis.

Figure 4.10 shows the plots of percent similarity as a function of sample size for all size fractions of CoCrCuFeNi$_{0.8}$. Exponential fits have been plotted using MATLAB® to extrapolate percent similarity to a sample size of 500, double the chosen minimum sample size. The percent similarity is then calculated using the extrapolation equation for each sample size at n_s = 250 and n_s = 500 respectively. The final similarity values are an average calculated after simulating the randomisation of the samples five times. The maximum increase in similarity yielded when doubling the sample size is lower than 10% in all size fractions. With a percent similarity at already at least 70% across all size fractions, it can be argued analysing the microstructure of a further 250 droplets

in each size fractions would not produce an increase in similarity statistically significant enough to justify the time required to do so. Subsequent analysis and conclusions surrounding structural incidence trends are therefore based on this knowledge.

4.3.2 Uncertainty quantification

Finally, the uncertainty in measurements of percentage incidence of structures across the different size fractions is quantified by assuming a binomial distribution with a 95% confidence interval. Here, we ask: "in a sample of size n_s, what is the chance of getting k_s droplets of a particular type given a specified probability (p) that a random droplet selected from the sample will be of this particular type?".

The key assumption of the binomial distribution is that each selection must be independent from the next. Here, however, the probability of a given structure occurring in the sample is estimated based upon its actual measured occurrence during categorisation of the droplets in the relevant size fraction. Hence, the probability of a structure occurring is its numeric occurrence (k_s) divided by the total number of droplets in the size fraction being treated (n_s). A modified version of the binomial equation [250] shown in Equation 4.15 is used to complete the analysis.

$$\mathrm{B}_n(k_s) = \binom{n_s}{k_s} \frac{k_s}{n_s}^{k_s} \left(1 - \frac{k_s}{n_s}\right)^{n_s - k_s} \qquad 4.15$$

This is an approximation because the probability of success (i.e., the chance of picking a droplet with the desired structure out of the main sample) is informed by the nature of the sample and thus, not independent of the sample itself. However, it is argued that its use gives sufficient indication of the likely error in the sample.

To find a confidence range and thus, delineate uncertainty for the percentage incidence of certain structures in the sample, we ask: "in a sample of n_s droplets, where k_s droplets possess the structure we desire, what are the values of k_s above and below the original value so that if it was guessed that the structure chosen was that which was desired, the guesser would be right 95% of the time?". Given the nature of the binomial distribution, there are two values of k_s for which the equation holds given the earlier assumption in Equation 4.15. Setting the value of $\mathrm{B}_n(k_s)$ to 0.95 and solving for the two possible values of k_s for each size fraction gives the confidence intervals for the

number of desired droplets. For example, if 100 droplets from a sample of 250 are found to possess the selected structure, the probability is hence 10/25 of finding this structure if we pick a droplet at random. Using 250 for n_s and 10/25 for p, assuming $\mathrm{B}_n(k_s)$ = 0.95, values straddling the 100 droplets observed are found, 107 and 94 for example. These then form the upper and lower extremities of the uncertainty in the probability and thus, percentage incidence of a particular structure. The values of these upper and lower bounds have been used to generate the error bars in percentage occurrence for the structures discussed of Figure 5.8, Figure 5.16, Figure 5.22 and Figure 5.23. This analysis allows us to appreciate whether certain trends borne out in the data are substantiated, or not, by the uncertainty in percentage incidence and are not the result of random error or noise in the data. This is particularly important when dealing with structures which have a low probability of occurrence in general.

4.3.3 Thermodynamic modelling

4.3.3.1 Theoretical binary pair enthalpies of mixing

To inform initial alloy design and gain an understanding of element partitioning during LPS, solidification, and other subsequent phase transformations, the mixing enthalpy of each constituent binary pair in $CoCrCuFeNi_{0.8}$ was calculated and plotted at each composition over the full composition interval. These values were estimated via the theoretical work of Takeuchi and Inoue [111] for a sub-regular solution model and calculated using Equation 2.17. The theoretical interaction parameter coefficients Ω_n for each binary pair are also tabulated in [111].

4.3.3.2 Modelling phase diagrams and miscibility gaps

The CALPHAD computational method was used to search for miscibility gaps (see section 2.2.2, 2.2.3) in pseudobinary phase diagrams of the $CoCrCuFeNi_{0.8}$ alloy. The methodology is described in more detail in [251, 252]. Here, assuming substitutional regular solution model to represent crystalline phases, the molar Gibbs free energy G_m for a particular phase can be described through Equation 4.16.

$$G_m = G^{srf} + G^{phys} - T * S_{conf} + G^{ex} \qquad 4.16$$

Each of these four terms merits explanation. First, G^{srf} represents the free energy inherent in a simple mechanical mixture of the components involved, factoring in their atomic ratios. The sum of all of the contributions of each individual species (represented via the atomic percentage of the i'th component X_i) is represented in Equation 4.17.

$$G^{srf} = \sum_{i=1}^{n} X_i G_i^0 \tag{4.17}$$

Even more fundamentally, the standard Gibbs free energy of each constituent element G_i^0 must be represented based on a specific reference state H_{SER} that is the same for each element. Expressions for these values are often temperature dependent polynomials such as that in Equation 4.18. Each value from h_0 to h_7 is an element-specific coefficient.

$$G_i^0 = G_i - H_{SER} = h_0 + h_1 T + h_2 * T log(T) + h_3 T^2 + h_4 T^3 + h_5/T + h_6 T^7 + h_7 T^{-9} \tag{4.18}$$

The term G^{phys}, which denotes the free energy originating from specific materials properties like magnetism, is ignored for the purposes of this study. The next term focuses on the configurational entropy of the system, describing the possible configuration of elements in the crystal lattice. Assuming, as before, a regular solution, configurational entropy can be written as in Equation 4.19.

$$S_{conf} = R \sum_{i=1}^{n} X_i \, lnX_i \tag{4.19}$$

In many cases, the regular solution model cannot adequately represent the deviations from ideal behaviour. In such cases, experimental work often allows us to quantify the deviation from such behaviour. This is mathematically represented in the term G^{ex}, the excess free energy. For a binary alloy, this can be represented through Equation 4.20.

$$G^{ex} = \sum_{i} \sum_{j>i} X_i X_j L_{ij} \tag{4.20}$$

where L_{ij} is a binary interaction parameter term that quantifies departure from ideal behaviour. These parameters are often described mathematically in the form of Redlich-Kister (RK) polynomials. Generally, they have the form described in Equation 4.21.

$$L_{ij} = \sum_{v=0}^{v_{max}} (X_i - X_j)^v * {}^vL_{ij} \qquad 4.21$$

where $v = 0,1,2 \ldots v_{max}$ and ${}^vL_{ij}$ is the vth parameter in the RK polynomial describing the interaction between binary pair $i - j$. As $CoCrCuFeNi_{0.8}$ is a 5-component HEA on which few experiments have been conducted, finding a RK polynomial describing the interaction between all five constituent elements is currently impossible. Furthermore, it continues to be difficult to represent the compositional space of a five-component alloy on a two dimensional diagram. We can solve these issues by using the binary interaction parameters for all ten possible binary pairs in the alloy and weighting them according to their prevalence in the final HEA. The relevant free energy curve is then plotted on a pseudobinary phase diagram assuming a $CoCrFeNi_{0.8}$-Cu alloy system. This division between elements can be used as a reasonable approximation given that Cu is the element which de-mixes the most readily with the other alloying components. Although a fully detailed analysis is impossible without full experimental thermodynamic derivation of the phase diagram, this serves as a valuable initial step to predict the alloy phase behaviour.

One way to determine if a miscibility gap is present in the phase diagram is by searching, mathematically, for a binode and chemical spinode. This suggests that there are temperatures for which a phase of a specific composition will be metastable or unstable respectively (and therefore, potentially undergo a decomposition reaction).

As described in section 2.2.2, the binode can be found by finding the compositions defined by a common tangent on the Gibbs free energy curve for a specific phase at each temperature. This is shown in Figure 4.11 for a solid FCC phase in the pseudobinary $CoCrFeNi_{0.8}$-Cu alloy system at 1200 K.

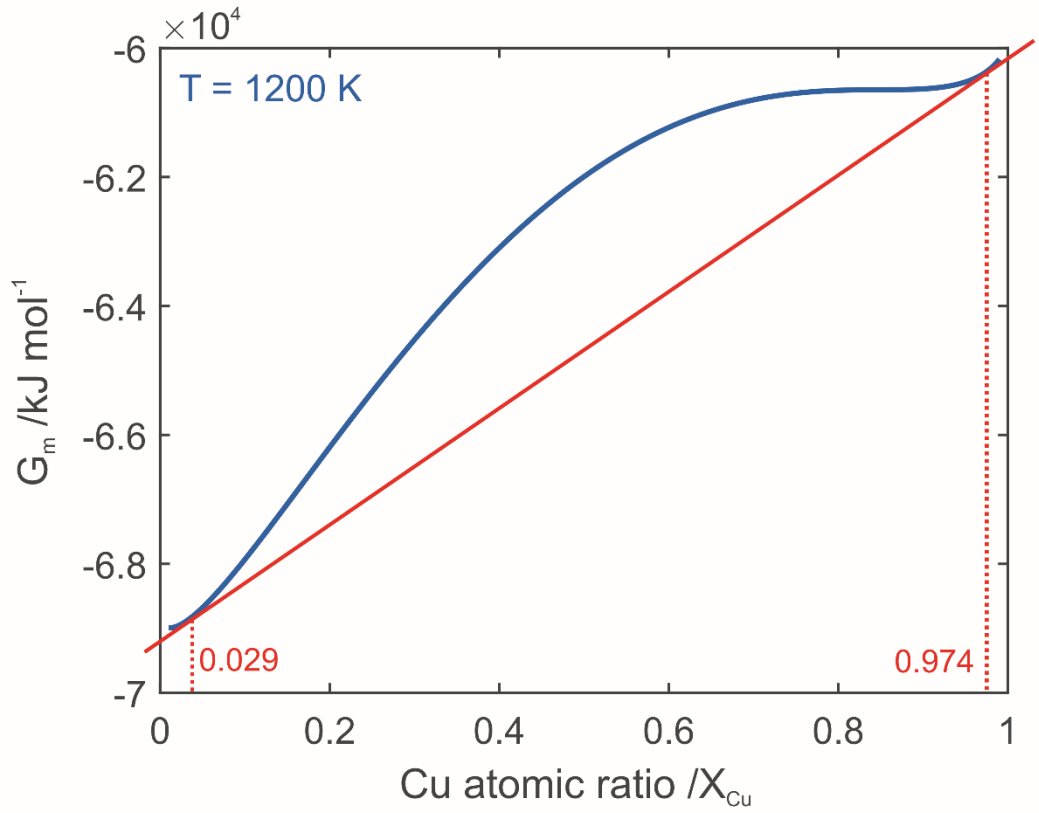

Figure 4.11 Example free energy curve for pseudobinary CoCrFeNi$_{0.8}$-Cu alloy system at 1200 K with common tangent construction. Compositions of 0.029 at% Cu and 0.974 at% Cu will form part of the estimated binode curve for the pseudobinary system.

A spinode is present at a specific temperature if there are inflection points in the phase Gibbs free energy curve at certain compositions. The inflection points are described mathematically by points where the second derivative of the molar Gibbs free energy with composition is equal to zero as in Equation 4.22.

$$\frac{d^2 G_m}{dX_{Cu}{}^2} = 0 \qquad 4.22$$

The compositions at which inflections in the free energy curve of the chosen phase occurred were logged at each temperature from room temperature to the alloy liquidus temperature T_{liq}. This allowed a binode and a chemical spinode to be estimated for specific phases. Temperature dependent expressions for the elemental free energy of each constituent, as well as the binary interaction Redlich-Kister polynomials for each binary alloy pair, were taken from the SGSOL solutions database 2024 (SGTE) and are provided in Appendix 1.

4.3.4 Image analysis

4.3.4.1 Intradendritic dispersions

The ImageJ program was initially used to determine the area fraction of phases or microstructural features occupying specific area fractions of droplet cross-sections. This analysis was particularly important for the characterisation of dispersoids found in dendrite arms of certain droplets.

In dendritically solidified droplets which feature dispersoids in the dendrite arm cores (SCDD and MCDD categories), five droplets were selected from each size fraction (with the exception of the 850+ μm size fraction, where only 3 were analysed) and manipulated using the ImageJ program. The area featuring dispersoids was manually defined and given a blue fill to distinguish it from the rest of the microstructure. Colour thresholding was then used to determine the number of pixels occupied by dispersoids, as well as the pixels occupied by the two primary phases (i.e. the dark grey dendritic phase and the light grey interdendritic phase). This process is shown in Figure 4.12.

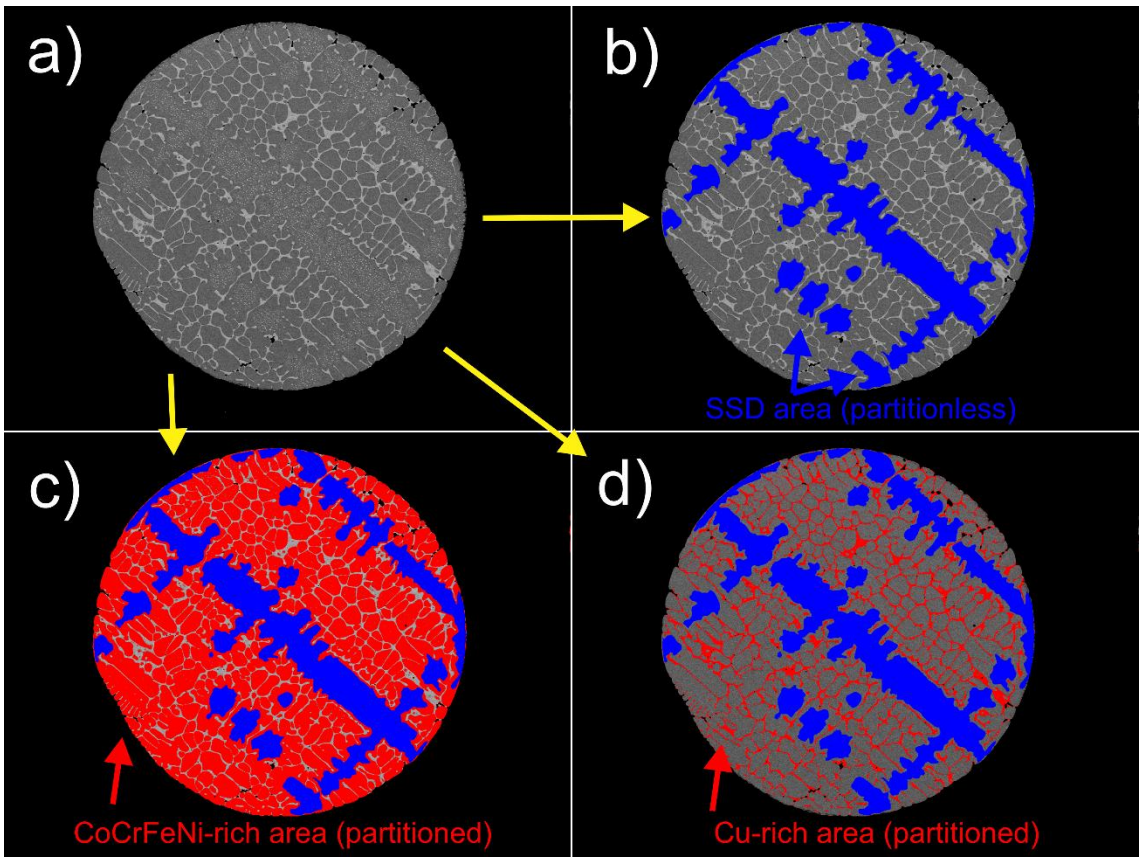

Figure 4.12 Image processing steps for determination of area fraction of primary phases present in drop-tube processed CoCrCuFeNi$_{0.8}$. (a) Initial electron micrograph. (b) Partitionless region A_{disp} (i.e. region featuring solid state dispersoids in dendrite cores) indicated in blue. (c) Dendritic phase of partitioned region A_{DP} indicated in red. (d) Interdendritic phase of partitioned region A_{IDP} indicated in red.

From this, three area percentages were determined. The first of these is the area percentage occupied by dispersoids $A\%_{disp}$. The second and third are the percentages of the remaining area (i.e. the area of the droplet that does not feature dispersions) occupied by the dark grey dendritic phase $A\%_{DP}$ and the light grey interdendritic phase $A\%_{IDP}$ respectively. These three area percentages are calculated through Equation 4.23, Equation 4.24 and Equation 4.25 respectively.

$$A\%_{disp} = \frac{A_{disp}}{A_{droplet}} * 100 \qquad 4.23$$

$$A\%_{DP} = \frac{A_{DP}}{A_{droplet} - A_{disp}} * 100 \qquad 4.24$$

$$A\%_{IDP} = \frac{A_{IDP}}{A_{droplet} - A_{disp}} * 100 \quad 4.25$$

where A_{disp} is the area of the droplet cross-section occupied by Cu-rich dispersoids in the dendrite arms of SCDD and MCDD droplets, $A_{droplet}$ is the area of the full droplet cross section, A_{DP} is the area of the droplet which is made up of the dark-grey dendritic phase, and A_{IDP} is the area of the droplet which is made up of the light-grey interdendritic phase.

4.3.4.2 Grain refinement

The ImageJ program was also used for image manipulation for particle size and analysis. This is particularly important for the portion of the study regarding grain-refined microstructures. To gather data on the grain structures for analysis, the images were binarized and manipulated to maximise the contrast between grain-refined grains and the intergranular matrix. This allowed more accurate data on quantities such as the area and roundness of each particle to be gathered. Enough droplet images were taken such that more than 900 grain-refined grains were catalogued for each size fraction (this required about 5-10 droplets to be imaged in the SEM for each size fraction). The manipulation process is outlined in Figure 4.13. Initially, the image of the droplet in question was cropped (Figure 4.13a) so that the rectangular image consisted only of the droplet microstructure (no resin). This image was manipulated in two ways separately. In the first, the ImageJ 'find edges' function was used to enhance delineation between the two phases present in the droplets. This image was then converted to a binary b/w image, and the 'despeckle' function was used to remove outlier pixels so that only an outline of the microstructure remained (Figure 4.13b-d). In the other case, the original cropped image was binarized and a threshold was applied using the 'threshold' function (Figure 4.13e). Finally, these two images are merged using the image calculator function with an 'AND' operator (Figure 4.13f). In this way, only pixels which are black in both images are black in the final combined image. Any other combination of white and black results in the particular pixel being coloured white in the final image. Due to the relatively low contrast between the phases in some areas of the microstructure images, this automatic method does not perfectly binarize the image. A further manual step is often required to colour in sections which have failed to be correctly processed by the ImageJ program. An example of a resultant change from this manual manipulation is shown in magnified sections of Figure 4.13f and Figure 4.13g.

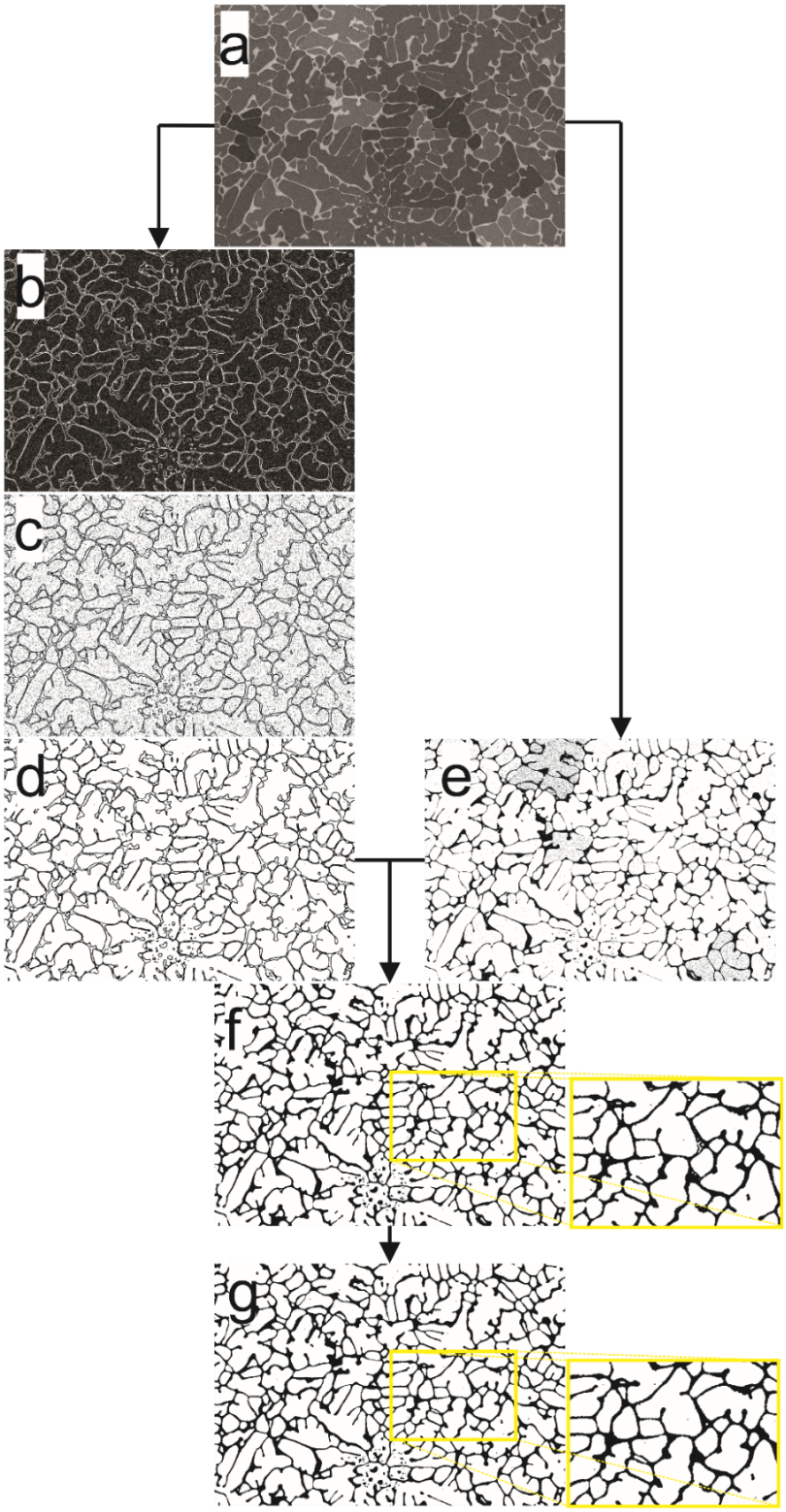

Figure 4.13 Image processing steps for grain refinement particle analysis in ImageJ. (a) Original cropped electron micrograph. (b-d) Resultant micrograph after application of 'find edges' function, binarization, and application of 'despeckle' function. (e) Separate binarization and thresholding of original electron micrograph. (f) Combination of processed images (d) and (e) using the 'AND' operator. (g) Result of minor manual colour corrections of poorly processed regions of final image.

4.3.5 Particle analysis

Each of these images was then analysed using the 'analyse particles' function in ImageJ. Numerical data regarding properties of each of the grain-refined grains was taken for all imaged droplets. These values of most importance were the area of the refined grains (A_{RG}) and roundness values. From the area value, the area equivalent diameter (AED), which gives an idea of grain size of irregularly shaped grains, can be calculated using Equation 4.26. the roundness values are calculated directly in the ImageJ program through Equation 4.27.

$$AED = 2\sqrt{A_{RG}/\pi} \tag{4.26}$$

$$roundness = 4A_{RG}/(\pi l_{MA}^2) \tag{4.27}$$

where A_{RG} is the area of the refined grain, and l_{MA} is the length of the major axis of the refined grain. These values were calculated for each grain refined grain and the average was logged for each droplet size fraction/cooling rate.

The AED value of an irregular 2-D shape is essentially the diameter of a circle with an area equivalent to the cross section area of the shape. Importantly, because of sectioning effects brought on by grinding and polishing of the drop-tube processed powders, refined grains within the droplet microstructure are not necessarily all polished to the largest cross section (e.g. for a set of spherical particles, not all are polished exactly down to the equator). This results in errors in the estimated dimensions of the 3-D shape compared to those experimentally measured.

To increase the accuracy of particle size measurements, correction factors have often been introduced to allow more accurate estimates of the dimensions of 3-D shapes using measured dimensions of the 2-D cross section after sample preparation. Some examples of these corrections are compared in the work of Gallagher et al. [253] with regards to mounted additively manufactured Ti-6Al-4V powders. However, as the authors note, such methods rely on the assumption that the all of the particles are spherical when determining correction factors. While this is generally the case for the drop-tube processed droplets themselves, it is not so for the refined grains within each droplet, which are often irregularly shaped and therefore deviate significantly from a reference spherical volume. It is also important to mention that mean grain refined grain

AED value calculated for each droplet size fraction is compared only to the AED of refined grains in other droplets of the same material.

These arguments mean that it is difficult to conclude that the application of a stereological correction factor would actually increase the accuracy of the AED values calculated. Therefore, it was decided that the correction factor remain at 1, allowing an understanding of the relative change in refined grain AED as droplet size decreases.

The sample standard deviation s of each value was also calculated. Given the large spread of the samples, an estimate of the error in average area equivalent diameter and average roundness was found using the standard error (SE) rather than the standard deviation. The formula for SE is given in Equation 4.28:

$$SE = s/\sqrt{n_g} \tag{4.28}$$

where s is the standard deviation and n_g is the total number of grain-refined grains analysed in all of the droplets in a given size fraction. The sample skew and sample kurtosis of the roundness data were also found using Equation 4.29 and Equation 4.30 respectively, where $roundness_i$ is the roundness value of the i'th refined grain in the sample, and $\overline{roundness}$ is the mean roundness for the entire sample. MATLAB® was used to plot histograms of the roundness values for all of the grain refined grains in each size fraction for visual analysis of the spread of the data. Additionally, a normal distribution with the same mean and standard deviation values was overlaid over each histograph for the purposes of visual comparison.

$$skew = \frac{n\sum_{i=1}^{n}(roundness_i - \overline{roundness})^3}{(n-1)(n-2)s^3} \tag{4.29}$$

$$kurtosis = \frac{n(n+1)\sum_{i=1}^{n}(roundness_i - \overline{roundness})^4}{(n-1)(n-2)(n-3)s^4} - \frac{3(n-1)^2}{(n-2)(n-3)} \tag{4.30}$$

4.3.6 Hardness testing

Indentation hardness testing was used to gain knowledge of the mechanical behaviour of drop-tube processed CoCrCuFeNi$_{0.8}$, particularly in regards to the grain-refined material discovered. The Vickers hardness testing method was

used which involves the application of a known force to a sample of the chosen material. This applied load will result in displacement of the material via plastic deformation, and an indent will be formed when the test is complete. The load required to displace the material over a specific distance is then logged, and the hardness can be calculated. Because the displacement calculation is determined via the measurement of specific indent dimensions, the indenter must have a well-defined geometry and a consistent shape [254].

The Vickers Hardness of dendritic and grain-refined grains was estimated using a Struers Duramin A/S DK-2750 hardness testing machine. For these tests, a $HV_{0.01}$ (0.09807 N) load was applied via a square-pyramidal diamond indenter. Where possible in each size fraction tested, average hardness values were gathered for five droplets with a grain-refined structure (PGR or FGR structures) and five droplets showing dendritic characteristics (SC or MC structures). For each droplet, at least three indents were taken and an average hardness value was obtained. These hardness values, which give an idea of the overall hardness of the $CoCrCuFeNi_{0.8}$ alloy (as opposed to the individual phases) was then tabulated across droplet sizes according to microstructure type to allow analysis of the alloy hardness in the dendritic and grain-refined state across cooling rates. This testing was conducted only for the four largest size fractions to isolate any potential impact of grain-refinement transformation and cooling rate on alloy hardness. The prevalence of intradendritic dispersoids and other transformed microstructures in smaller grains competes with the grain-refinement transformation with regards to the final alloy hardness. Figure 4.14a and Figure 4.14b show examples of the Vickers hardness tests undertaken on dendritic and grain-refined droplets respectively in the 300 – 212 μm size fraction. A distance between indents of at least three times the indent size was defined to avoid the deformation of material in one test affecting subsequent tests on the same droplet.

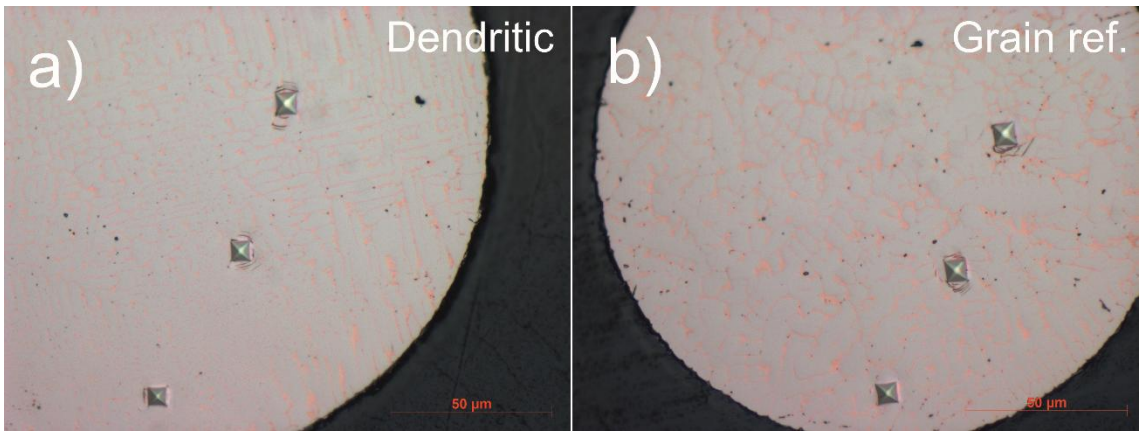

Figure 4.14 Optical micrographs of Vickers hardness pyramidal indents in (a) dendritic and (b) grain-refined droplets in 300 – 212 µm size fraction in drop-tube processed $CoCrCuFeNi_{0.8}$

Chapter 5 – Results

5.1 Determination of HEA H-R parameters

While the change in composition from the more studied equiatomic CoCrCuFeNi alloy to the $CoCrCuFeNi_{0.8}$ alloy selected is not drastic (and thus, would not be predicted to change alloy properties, solid solution stability, and crystal structure in a severe manner), it is important to establish as clear a rationale as possible in alloy selection. Three primary goals were considered.

1. An alloy which solidifies in the form of one, or multiple, stable solid solutions was the primary goal of the HEA study.
2. A positive (or comparatively mildly negative) enthalpy of mixing was desired to indicate significant potential of the alloy to de-mix and thus undergo LPS in the metastable regime.
3. An alloy composition was desired such that LPS might be predicted to initiate at an undercooling lower than that of commonly studied HEAs that undergo metastable LPS (namely equiatomic CoCrCuFeNi).

Tabulated data regarding key H-R parameters of previously studied $CoCrCu_xFe_yNi_z$ alloys is presented in Table 5.1 for the purposes of comparison, along with the properties of the alloy $CoCrCuFeNi_{0.8}$ selected for this work. The relevant parameters δ, ΔH_{mix}^{Alloy}, ΔS_{mix}^{Alloy} , VEC and $\Delta\chi$ were calculated using Equation 2.14 – 2.23. Theoretical data regarding enthalpy of mixing for each binary pair $\Delta H_{i.j}^{mix}$ is sourced from the work of Takeuchi and Inoue [111]. Data regarding atomic radii r_i, valence electron concentration $(VEC)_i$, and electronegativity χ_i values for each specific alloy component was gathered from [112].

Table 5.1 Calculated Hume-Rothery parameters and undercooling required for liquid phase separation in $CoCrCu_xFe_yNi_z$ high-entropy alloys

Alloy	Source	ΔT^*_{LPS} /K	δ /%	ΔH^{Alloy}_{mix} /kJ mol^{-1}	ΔS^{Alloy}_{mix} /J kmol^{-1}	VEC	$\Delta\chi$
CoCrCuFeNi	[24, 143, 145-147]	~180	1.03	3.25	13.38	8.80	0.09
$CoCrCu_2FeNi$	[147]	217	1.20	6.24	12.98	9.17	0.09
$CoCrCuFe_{0.5}Ni$	[144]	Stable	1.03	3.11	13.15	8.89	0.10
$CoCrCuFe_{1.5}Ni$	[143]	190	1.02	3.28	13.25	8.73	0.09
$CoCrCuFe_2Ni$	[143]	293	1.01	3.26	12.98	8.67	0.08
$CoCrCuFeNi_{0.5}$	[144]	Stable	1.07	4.50	13.15	8.67	0.09
$CoCrCuFeNi_{0.8}$	This work		1.05	3.70	13.35	8.75	0.09
$CoCrCuFe_{1.5}Ni_{0.5}$	[148]	43	1.06	4.43	12.95	8.60	0.09

Based on the data in Table 5.1, the prediction can be made that $CoCrCuFeNi_{0.8}$ will maintain a solid solution based microstructure similar to that of the equiatomic alloy and other compositional variants. With an atomic size difference of 1.05 %, ΔH^{Alloy}_{mix} of 3.70 kJ mol^{-1} and ΔS^{Alloy}_{mix} of 13.35 J kmol^{-1}, values of H-R properties fall into nearly all of the ideal ranges for solid solution formation (see Table 2.1). The notable exception is the more narrow ideal range of $-11.6 \leq \Delta H^{mix}_{Alloy} \leq 3.2$ kJ mol^{-1} suggested by Guo et al. [113] from which the calculated enthalpy of mixing is not markedly different. Furthermore, the dataset presented by Guo et al. [113] does not seem to include alloys with a mixing enthalpy greater than 3.2 kJ mol^{-1} in the study, meaning that this stated maximum does not preclude the occurrence of solid solutions above this value (provided other relevant criteria are satisfied). Based on this comparison, the first condition for alloy selection is satisfied.

$\Delta\chi$ changes very little when small changes to the atomic ratio are made and no new elements are added to the alloy or used to replace one of the current constituents. VEC was suggested by Guo et al. [255] to be highly important in determining the crystal structure of the solid solution (i.e. if it is FCC or BCC). A VEC greater than 8, in all the alloys discussed, suggests that the solid-solution that forms in $CoCrCuFeNi_{0.8}$, as with the equiatomic alloy, will likely consist of FCC solid solutions.

The second and third goals alloy selection are also satisfied given that the reduction in Ni content has raised enthalpy of mixing to a more positive value than that of the equiatomic alloy. It is predicted that an alloy with a more positive enthalpy of mixing will reduce the critical undercooling ΔT^*_{LPS} required to initiate such LPS, but will allow LPS to remain metastable.

5.2 Binary enthalpies of mixing

Figure 5.1 shows the theoretical estimation of enthalpies of mixing with atomic percentage for each binary pair present in $CoCrCuFeNi_{0.8}$. These are calculated for the sub-regular solution model presented in Equation 2.17. Coefficients for the interaction parameter Ω_n for each pair were gathered from [111].

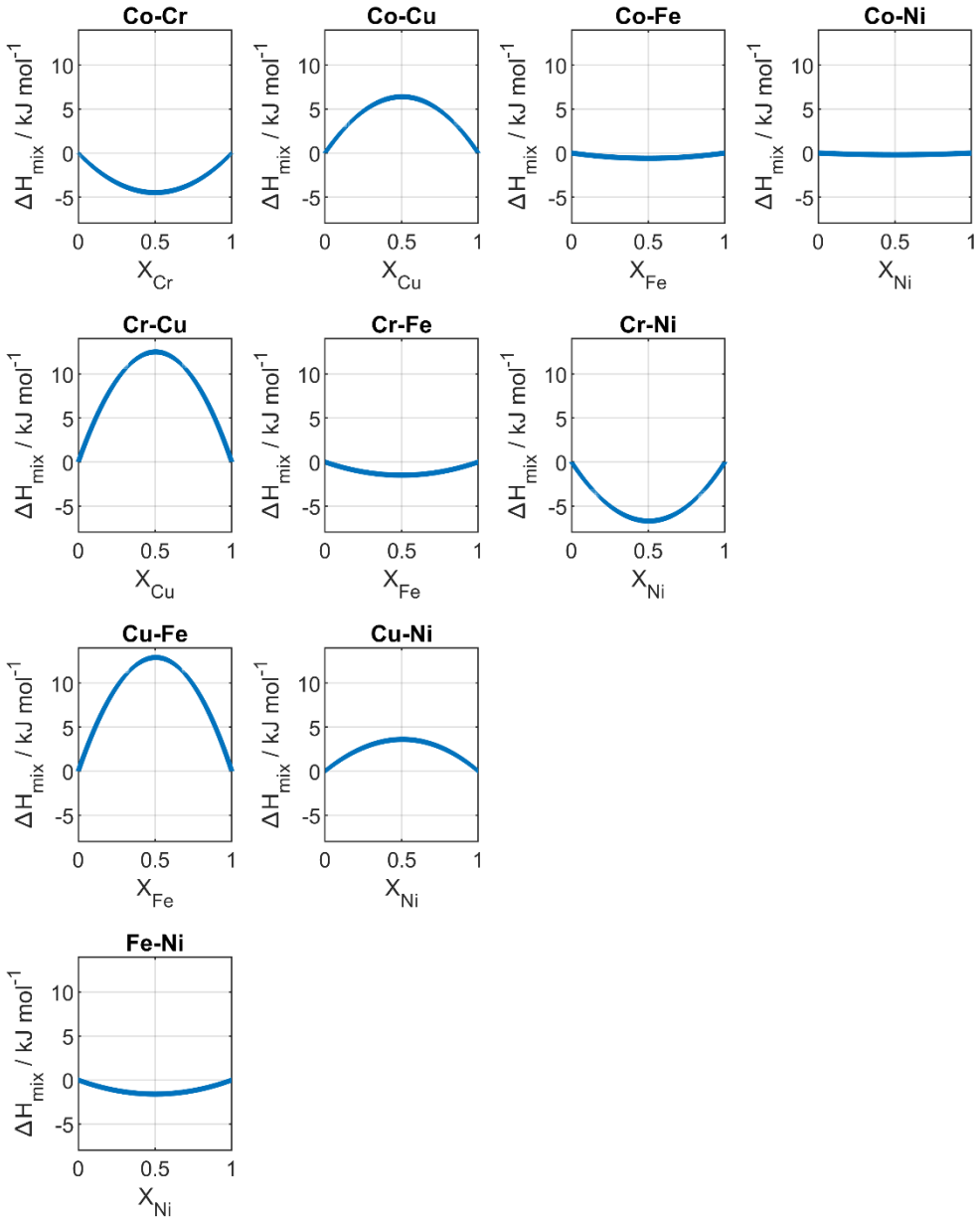

Figure 5.1 Enthalpies of mixing variation with composition for all binary pairs in $CoCrCuFeNi_{0.8}$ alloy calculated using sub-regular solution model.

These calculated enthalpies of mixing give potential insight into the behaviour of $CoCrCuFeNi_{0.8}$ during solidification or other phase transformations in terms of miscibility of the species. Most notably, Cu has a positive mixing enthalpy with all of the other alloying elements. In contrast, all possible pairs formed between Co, Cr, Fe and Ni, possess a negative mixing enthalpy. Such a configuration would suggest that in the event of a phase transformation such as LPS (echoing the work of Derimow et al. [134]), solidification, or precipitation, Cu would be the most likely to de-mix with the other elements and occupy a significant atomic fraction of the newly forming phase.

5.3 Arc-melted $CoCrCuFeNi_{0.8}$

5.3.1 Microstructure analysis

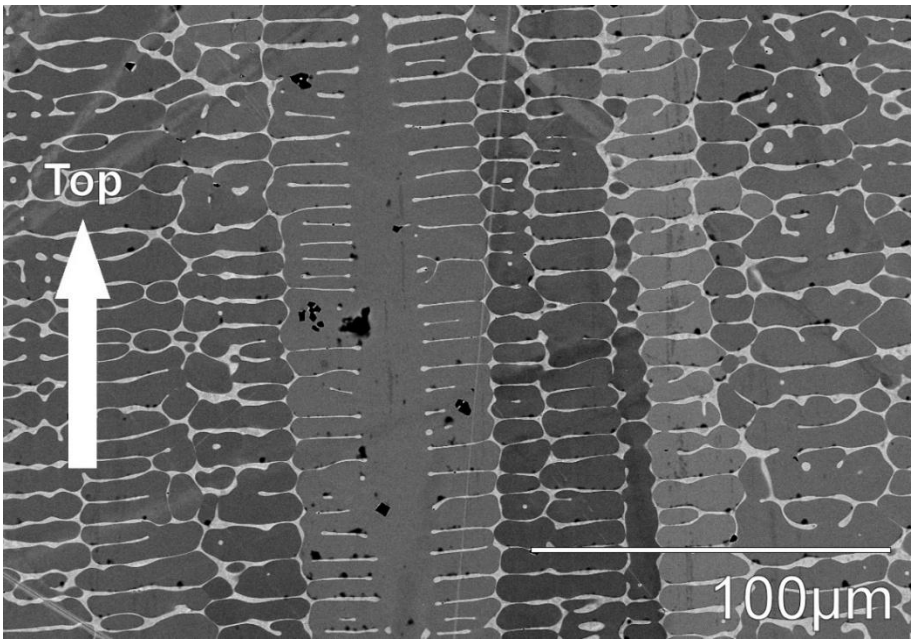

Figure 5.2 SEM BSE micrograph of common dendritic structure found in arc-melted ingot of $CoCrCuFeNi_{0.8}$. White arrow shows direction towards top of ingot exposed to Ar atmosphere.

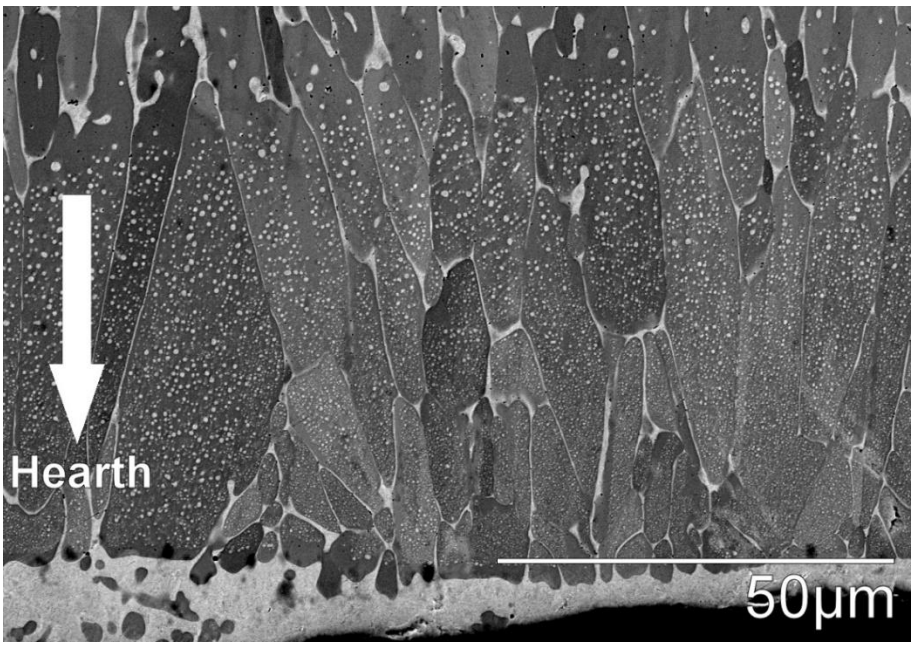

Figure 5.3 SEM BSE micrograph of dispersed, web-like, and macrosegregated phase structures observed near hearth region of arc-melted ingot of $CoCrCuFeNi_{0.8}$ White arrow shows direction towards water-cooled Cu hearth of arc-melter.

Figure 5.2 and Figure 5.3 show the prevailing microstructures in the arc-melted and sectioned $CoCrCuFeNi_{0.8}$ ingot. SEM backscatter analysis of the ingot morphology shows that the large majority of the ingot microstructure seems to consist of two principle phases on the microscale. These are a dark-grey dendritic phase (DP) and a light-grey interdendritic phase (IDP). Columnar dendrites radiate out from near the bottom of the ingot (closer to the hearth) towards the top of the arc-melted button, suggesting that the a significant proportion of the initial nucleation event(s) in the melt originated near the water-cooled hearth of the arc-melter. This is what would be expected given that the copper hearth provides heterogenous nucleation sites.

In some regions near the hearth, however, there is also a substantial change in microstructure from a dendritic morphology to a cellular morphology. The interdendritic light-grey phase creates an interconnected web-like structure which surrounds discrete cells of the dark-grey phase. This structure predominates in a region between 200 μm to 50 μm above the hearth. In the cellular regions nearest to the hearth, the dark-grey cells are filled with fine spherical dispersions of a lighter phase of similar colour to the light-grey interdendritic phase. These dispersoids populate the cells until they abruptly cease to appear a few microns from the lower edge of the dark-grey cells above the ingot contact point with the water-cooled hearth. Finally, in certain regions of the ingot sample adjacent to the water-cooled hearth, a thin layer of lighter phase is observed at the meeting point between the ingot and the hearth.

5.3.2 Composition analysis

Table 5.2 SEM-EDX composition analysis of phases in $CoCrCuFeNi_{0.8}$ arc-melted ingot

Location (Phase)	Co /at%	Cr /at%	Cu /at%	Fe /at%	Ni /at%
Predicted (Alloy)	20.8	20.8	20.8	20.8	16.7
Overall (Ingot)	20.72 ± 0.08	22.12 ± 0.03	20.70 ± 0.18	20.43 ± 0.06	16.03 ± 0.06
Hearth (DP)	24.19 ± 0.32	25.05 ± 0.17	9.97 ± 0.25	23.93 ± 0.21	16.85 ± 0.38
Hearth (IDP)	4.11 ± 0.97	4.31 ± 1.66	81.29 ± 4.92	4.17 ± 1.31	6.12 ± 1.32
Centre (DP)	25.54 ± 0.21	25.40 ± 0.16	9.79 ± 0.22	23.95 ± 0.30	16.32 ± 0.35
Centre (IDP)	3.26 ± 0.12	2.71 ± 0.17	83.83 ± 0.73	3.27 ± 0.20	6.93 ± 0.35
Top (DP)	24.40 ± 0.64	25.15 ± 0.19	9.79 ± 0.11	24.06 ± 0.23	16.61 ± 0.94
Top (IDP)	3.30 ± 0.34	2.92 ± 0.49	83.20 ± 2.25	3.39 ± 0.52	7.19 ± 1.36

Table 5.2 shows approximate composition values taken from different areas with the arc-melted ingot. Standard deviation error is used in all measurements. For consistency, these compositions were all taken from regions in each area (Hearth, Centre and Top) that exhibited dendritic or near-dendritic structures (as opposed to the web-like structure near the hearth in Figure 5.3). This allowed potential changes in composition with cooling rate to be analysed in the arc-melted ingot while keeping the microstructural morphology from which the data was gathered consistent. Data on the overall composition of the alloy ingot was also collected to compare to the desired theoretical alloy composition to determine the impact of the alloy manufacturing process on the final element ratio.

The overall ingot composition values generally correlate well with the desired at% values required for the $CoCrCuFeNi_{0.8}$ alloy. The largest deviation from the desired value is in Cr, which is slightly more prevalent than was desired. Cr content in the alloy is slightly above 22.1 at%, about 1.3 at% higher than desired. Ni is the next most deviant, with a composition of 0.7 at% lower than the goal value. Co, Cu and Fe are present in quantities within 0.2 at% of the desired value. The high Cr content is likely be a consequence of the alloy melting sequence. As discussed in section 4.1.1, the alloy was sanded after each melting step to remove the oxide layer accumulated on the ingot surface and limit the impact of oxide impurities on solidification microstructure during arc-melting and eventual drop-tube processing. Because Cr was added last,

comparatively less of this component was removed via this sanding process compared to the other components. The result is a slightly higher Cr content.

As only the bottom of the ingot was in contact with the water-cooled copper hearth of the arc-melter, the assumption is that the highest cooling rates are experienced in this region. Intermediate cooling rates are found in the centre of the ingot, and the lowest cooling rates are achieved near the top part of the ingot (although at the interface between the liquid metal and the Ar-rich gas atmosphere, the cooling rate may perhaps rise again compared to that within the bulk). Importantly however, the highest cooling rates achieved anywhere in the melt are likely only on the order of 2000 K s^{-1} [141]. This means that only the fastest cooling region of the ingot may be defined as having been subjected to a rapid solidification environment (according to [16]). Additionally, the hearth provides a large number of heterogenous nucleation sites, and the arc-melted sample of $CoCrCuFeNi_{0.8}$ is therefore predicted to have solidified with minimal undercooling. The arc-melted sample can therefore be used as an analogue for near-equilibrium (or as-cast) solidification. Conversely, given that the drop-tube is capable of inducing theoretical cooling rates orders of magnitude larger than those prevailing in the arc-melter, and that solidification in free-fall reduces the likelihood of heterogenous nucleation, the microstructures that result are likely to be affected drastically. Microstructures created in drop-tube can therefore be compared to the structures obtained in the arc-melted ingot to determine the effects of rapid solidification and high undercooling on the resultant microstructure.

Table 5.2 shows that in all locations on the ingot, the interdendritic light-grey phase is found to be Cu-rich with between 81 at% and 84 at% Cu. Such a value is comparable to that found in equiatomic CoCrCuFeNi solidified at near-equilibrium conditions by Derimow et al. [134] and Park et al. [227] among others. Other elements in the Cu-rich phase are present at levels below 5 at% with the exception of Ni, which is present in quantities from 6-7 at%. The dark-grey dendritic phase is thus CoCrFeNi-rich. Independent from the location in the ingot, this phase is near equiatomic in terms of Co, Cr and Fe at about 24 at% each. The large majority of the Ni in the original alloy is still present in this CoCrFeNi-rich phase. However, due to its slight enrichment in the Cu-rich phase compared to Co, Cr and Fe, and the reduction in atomic ratio in the alloy compared to the equiatomic, it is present in a smaller quantity at about 16-17 at%. Cu is also still present in this phase, but at the much reduced composition of around 10 at%. The layer of lighter phase at the contact point between the bottom surface of the ingot and the water-cooled hearth (in the bottom region of Figure 5.3) is also highly enriched in Cu. The composition does not deviate

significantly from the Cu-rich ID phase in the rest of the alloy. The significant presence of this Cu-rich phase in a stratified layer at the bottom of the sample points to potential macrosegregation followed by a movement of the lower melting point and denser Cu-rich phase through the dendritic or web-like network of CoCrFeNi-rich phase to the bottom of the sample via Stokes motion. The dispersions and the inter-cell web structure between the HEA-rich cells are also Cu-rich and of similar composition to the Cu-rich IDP. This area of dispersoids was analysed in a more detailed manner using SEM-EDX.

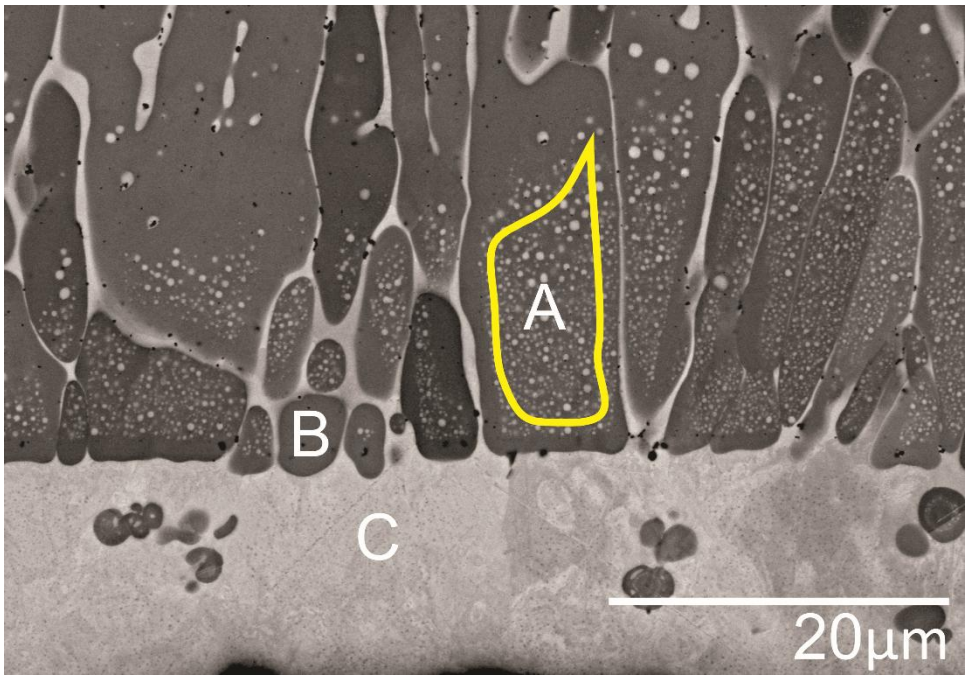

Figure 5.4 SEM BSE electron micrograph of arc-melted ingot of $CoCrCuFeNi_{0.8}$ showing dispersions, web-like structures and separated Cu-rich phase. Locations of EDX composition analysis of dispersed region (A), CoCrFeNi-rich phase (B) and Cu-rich phase (C) are indicated.

Figure 5.4 shows a magnified region of the unusual structures near the contact area between the water-cooled copper hearth of the arc-melter and the bottom surface of the ingot. Of particular note are the regions showing groups of small circular light-grey phases dispersed in cells of the dark-grey CoCrFeNi-rich phase. These dispersoids, and the spaces between them, appear to be smaller than 1 µm in size. In addition to the phase compositions of the CoCrFeNi-rich dark phase without dispersions (B) and the Cu-rich lighter phase (C), EDX was used to gather the sum-spectrum of the region (A) outlined in yellow. This spectrum was used to calculate the composition of this region, in effect, a weighted average of the circular dispersoids present and the CoCrFeNi-rich phase which surrounds them. These compositions are shown in Table 5.3. Standard deviation error is used in all measurements.

Table 5.3 SEM-EDX derived composition data for phases and/or regions in arc-melted $CoCrCuFeNi_{0.8}$ near ingot-hearth contact point

	Alloy	A	B	C
Cr /at%	22.12 ± 0.03	22.11 ± 0.14	24.96 ± 0.80	1.81 ± 0.15
Fe /at%	20.43 ± 0.06	20.59 ± 0.09	23.38 ± 0.02	2.34 ± 0.11
Co /at%	20.72 ± 0.08	20.52 ± 0.08	23.12 ± 0.37	2.20 ± 0.13
Ni /at%	16.03 ± 0.06	16.04 ± 0.02	17.86 ± 0.01	5.73 ± 0.49
Cu /at%	20.70 ± 0.18	20.73 ± 0.18	10.70 ± 1.16	87.94 ± 0.87

Based on the overall composition value in (A) and the colours of the phases in the SEM micrograph, it is predicted that the dark-grey phase between the dispersoids, like (B), is CoCrFeNi-rich while the fine dispersoids are Cu-rich (these phases are too fine for their composition to be measured directly via SEM-EDX due to the large interaction volume). The compositions of the Cu-rich and CoCrFeNi-rich phases are similar to those calculated elsewhere in the alloy, and are likely caused by more immiscible Cu partitioning from the growing CoCrFeNi-rich phase and enriching the interdendritic phase. However, the table also shows that the average composition of the region (A), framed in yellow (i.e. dispersoids and the matrix in which they are present) is very close to the nominal composition of the $CoCrCuFeNi_{0.8}$ arc-melted ingot. The startling similarity in composition necessitates further detailed study of this microstructure and how it was formed during solidification. Furthermore, the occurrence of such dispersions in only one part of the ingot microstructure suggests a dependence on cooling rate and/or undercooling that is not satisfied throughout the solidification process. Such a dependence was studied further using analysis performed on prevailing microstructures in the droplets obtained from the drop-tube.

5.3.3 DSC analysis

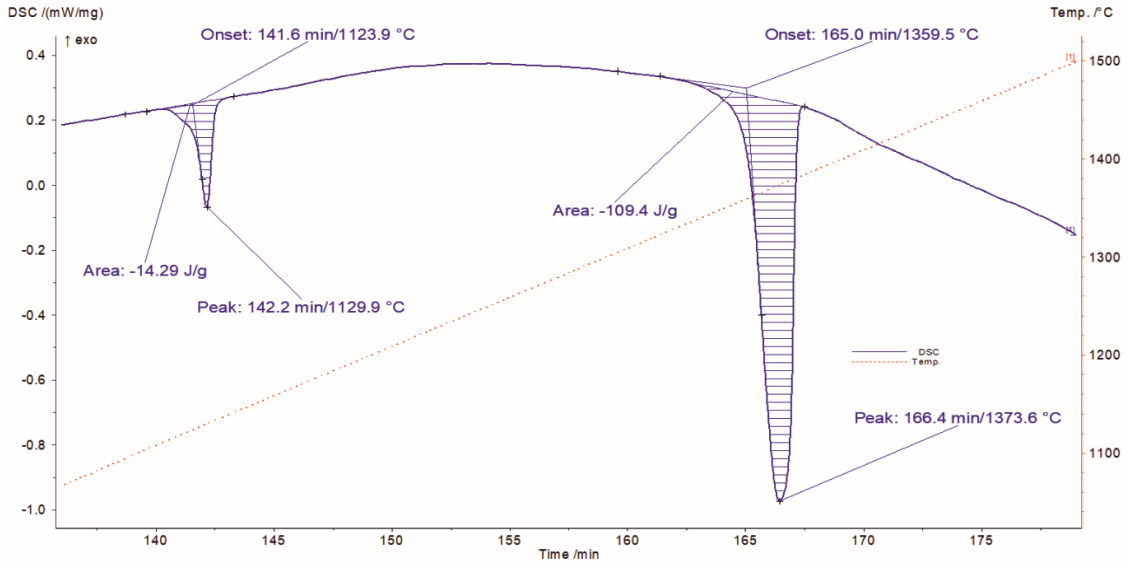

Figure 5.5 DSC analysis curve including endothermic phase changes during heating of $CoCrCuFeNi_{0.8}$ arc-melted ingot. Two such changes are observed, likely indicating melting of the two principal phases in the $CoCrCuFeNi_{0.8}$ alloy.

The results of the DSC analysis shown in Figure 5.5 indicate two significant endothermic phase changes occurring in $CoCrCuFeNi_{0.8}$ during heating. These begin at about 1124 °C and 1359 °C (1397 K and 1632 K respectively) and end at about 1150 °C and 1383 °C (1423 K and 1656 K respectively). In the absence of other phase changes, these endothermic reactions are likely to represent the melting of the Cu-rich and CoCrFeNi-rich phases at the lower and higher temperatures respectively. This analysis substantiates the prediction that the $CoCrCuFeNi_{0.8}$ alloy consists of a dual-phase structure. From this analysis, the solidus temperature of the alloy was determined to be located at the onset of melting of the Cu-rich phase (1397 K). the liquidus temperature was estimated at the end of the endothermic peak of the melting of the CoCrFeNi-rich phase at 1656 K. Furthermore, the latent heat of fusion $L_{f(alloy)}$ of the alloy were determined by summing the area of the peaks. In this case, the two areas outlined by the phase transitions sum to $(-14.29 + (-109.4) =)$ -123.69 J g^{-1} or -123690 J kg^{-1}.

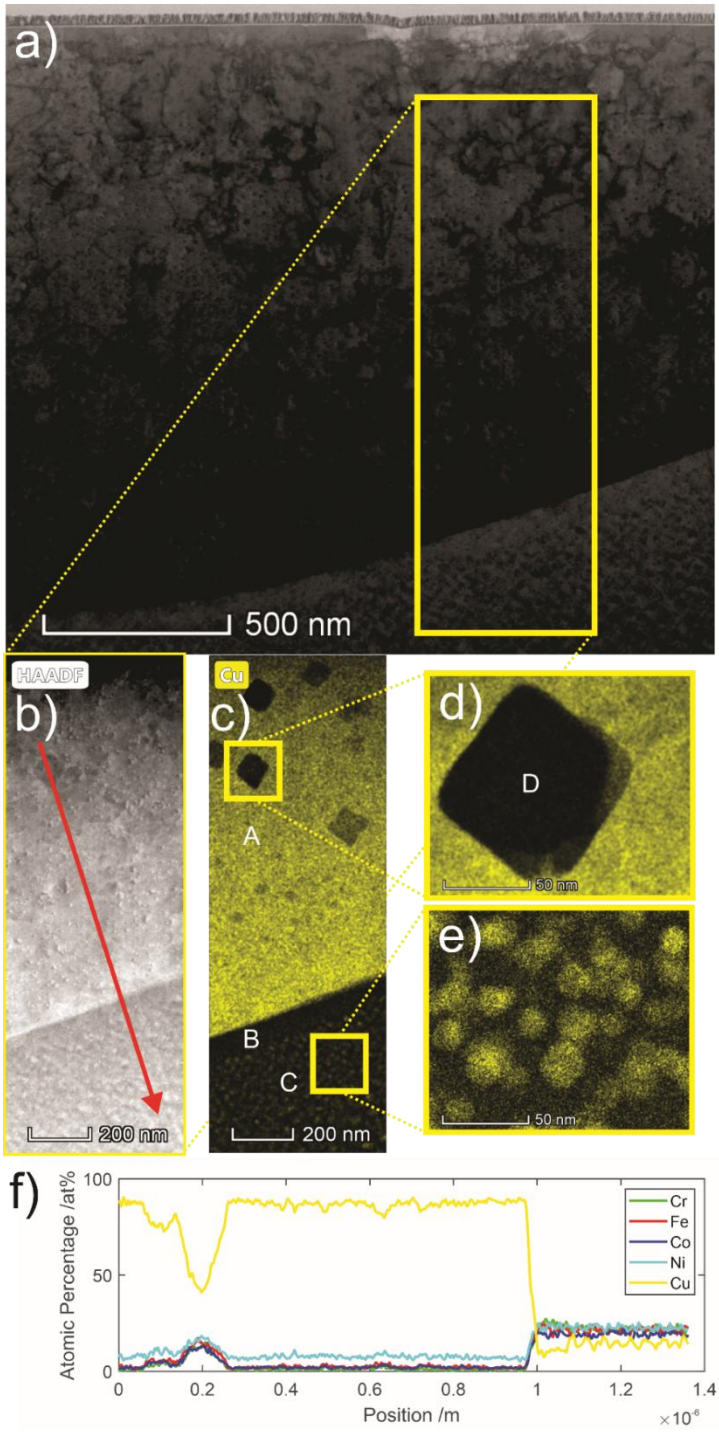

Figure 5.6 TEM composition analysis of phases in arc-melted $CoCrCuFeNi_{0.8}$ ingot. (a) Original bright-field TEM electron micrograph of phase boundary between CoCrFeNi-rich and Cu-rich phases. (b) HAADF view of phase boundary region from yellow inset in (a) and location of compositional line scan (red arrow). (c) EDX composition map of phase boundary region showing relative atomic percentage of Cu (yellow). (d) Magnified EDX composition map of angular dispersoid in Cu-rich interdendritic phase. (e) Magnified EDX composition map of Cu-rich nanophases in CoCrFeNi-rich dendritic phase. (f) Graphical result of EDX composition line scan in (b) showing variation in atomic percentage of constituent elements across dendritic-interdendritic phase boundary. Locations of EDX composition analysis on regions A-D are indicated.

Figure 5.6 displays the results of TEM-EDX compositional analysis of the arc-melted $CoCrCuFeNi_{0.8}$ ingot sample. Figure 5.6a shows a bright-field TEM (BFTEM) image of the dendritic structure within the ingot with the light Cu-rich and dark CoCrFeNi-rich primary phases. The inset in this figure is selected for composition analysis and is shown in Figure 5.6b. From this, Figure 5.6c shows the results of composition analysis of the inset, displaying the microstructure in terms of Cu atomic percentage. The insets in Figure 5.6c are shown in higher magnification and in terms of Cu atomic percentage in Figure 5.6d and Figure 5.6e. Finally, Figure 5.6f shows the results of a composition line scan conducted on the region shown in Figure 5.6b (delineated in location and direction by the red arrow).

Table 5.4 TEM-EDX derived composition data for phases in arc-melted $CoCrCuFeNi_{0.8}$ ingot

	A	B	C	D
Cr /at%	0.67 ± 0.14	24.35 ± 0.36	22.55 ± 1.13	18.83 ± 4.18
Fe /at%	1.22 ± 0.12	22.86 ± 1.16	21.54 ± 1.43	21.34 ± 3.71
Co /at%	1.05 ± 0.09	19.05 ± 0.37	18.55 ± 0.66	17.10 ± 3.81
Ni /at%	5.84 ± 0.21	23.82 ± 0.81	23.45 ± 0.39	21.72 ± 3.71
Cu /at%	91.22 ± 0.32	9.91 ± 0.34	13.92 ± 0.58	21.01 ± 15.05

Table 5.4 provides numerical composition data for specific lettered regions defined in Figure 5.6c and Figure 5.6d. Region (A) defines the bulk Cu-rich phase. Region (B) indicates a highly Cu-lean band in the CoCrFeNi-rich dendritic phase directly adjacent to the phase boundary. Further from this boundary, region (C) provides an average composition of the CoCrFeNi-rich phase, factoring in the relatively Cu-rich nanophase structures and the spaces between (as seen in Figure 5.6e). Finally, region (D) shows an average composition of the nano-sized angular phase regions present in the Cu-rich interdendritic phase. Standard deviation error is used in all measurements.

Similar to SEM-EDX analysis, TEM-EDX confirms that CoCrFeNi-rich dendritic and Cu-rich interdendritic phases dominate the ingot microstructure. However, the higher resolution of the TEM reveals further regions of interest. First, the region in the CoCrFeNi-rich phase immediately adjacent to the phase boundary is lean in Cu even in comparison to the bulk dendritic phase. Furthermore Cu concentration in the dendrite bulk (i.e. further away from this boundary) seems to fluctuate significantly, with Cu-rich regions of diameter <50 nm observable throughout. Reciprocally, polygonal nanosized particles of a comparatively

CoCrFeNi-rich phase are observable in the Cu-rich interdendritic phase. These particles, qualitatively, increase in size as distance from the dendritic-interdendritic phase boundary increases.

Such nanophases are indicative of secondary decomposition or phase separation reactions occurring in both the dendritic and interdendritic phases following solidification. Similar morphologies in as-cast samples have been found in arc-melted AlCoCrCuFeNi. Singh et al. [167] and Zhang et al. [256] show that immediately after dendritic solidification of this alloy, dendrites decompose into FCC and BCC phases. The occurrence of nanoscale phase separation and spinodal decomposition is attributed to the relation of each element to the others in terms of mixing enthalpy. This explains the formation of Cu-rich phases (positive enthalpy of mixing with other constituents) as well as the formation of Al-Ni rich phases (highly negative enthalpy of mixing between Al and Ni). Furthermore, the observation of spinodal decomposition and nanophase separation in even rapidly cooled samples of these alloys means that it is likely impossible to fully inhibit these reactions by increasing the cooling rate. Even more pertinently, in melt-spun $Al_{0.5}$CoCrCuFeNi, Xu et al. [257] also observed nano-scale Cu-rich and correspondingly CoCrFeNi-rich domains in much the same configuration as that in Figure 5.6e. This alloy was previously thought to consist of a single FCC phase. Ultra-high resolution scanning transmission electron microscopy (STEM) images gathered by Xu et al. show that the nano-scale separation of Cu results in a reduction in lattice distortion within the Cu-rich and CoCrFeNi-rich phases, concentrating such distortion at the interface between these two phases in the form of misfit strain. The authors suggest that the formation of these Cu-rich domains serves as a method to alleviate significant lattice distortion caused by the addition of relatively large Al atoms to the CoCrCuFeNi alloy. It is interesting, therefore, that these domains are also observed in a $CoCrCuFeNi_{0.8}$ alloy devoid of these Al atoms and thus, with a low predicted atomic size difference.

5.4 Drop-tube processed $CoCrCuFeNi_{0.8}$

5.4.1 Calculation of drop-tube cooling rates

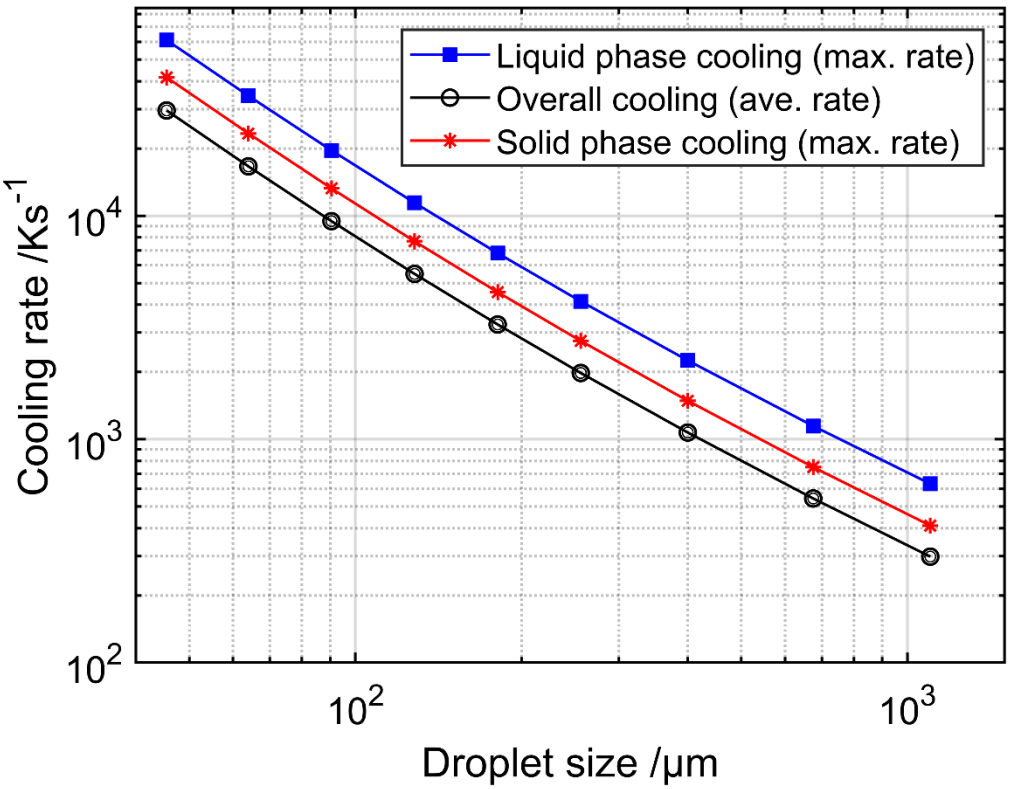

Figure 5.7 Correlation between droplet size and calculated cooling rate for drop-tube processed $CoCrCuFeNi_{0.8}$ alloy. The overall cooling rate is shown in black with spherical data points. Maximum liquid phase and solid phase cooling rates are shown in blue (square data points) and red (star data points) respectively.

Figure 5.7 shows the results of the calculation of droplet cooling rates at different sizes (diameters). As can be seen, the maximum liquid phase cooling rate $dT_{d(l)}/dt$ (blue, square markers) is the highest at each size fraction. This ranges from 600 K s^{-1} at the largest droplet size fraction to 60000 K s^{-1} in the smallest. The maximum solid phase cooling rate $dT_{d(s)}/dt$ (red, asterisk markers) is lower for every droplet size, calculated to be between 400 K s^{-1} and 40000 K s^{-1}. This reflects that the temperature difference between the alloy droplets and the gas is lower now that the droplets have cooled and solidified. The average overall cooling rate dT_d/dt (black, circle markers) is calculated to be the lowest of the three cooling rates estimated for each droplet size fraction. This is explainable given that the overall cooling rate factors in the phase change from liquid to solid during cooling and the corresponding release of significant latent heat. Average cooling rates throughout the whole solidification

process therefore range from 300 K s^{-1} in the largest droplets to 30000 K s^{-1} in the smallest.

The cooling rates estimated above for each droplet size use a value for droplet diameter that is the average of the maximum and minimum diameters encountered in each sieved size fraction. For example, the cooling rates calculated for the 500 – 300 μm size fraction were calculated by assuming a diameter of 400 μm. If the lowest possible droplet diameter (38 μm) is used, the highest liquid phase cooling rate may rise to higher than 80000 K s^{-1}, while the lowest overall cooling rate would be somewhere near 250 K s^{-1} for the largest droplet diameters of over 1 mm. An extremely large range of cooling rates is, therefore, likely observed in this alloy, encompassing more than two orders of magnitude. Regardless of which characteristic cooling rate is considered, cooling rate may be related to droplet size through a power relationship. The equations governing this relationship are stated in Equation 5.1, Equation 5.2 and Equation 5.3 for the overall cooling rate, the maximum liquid phase cooling rate and the maximum solid phase cooling rate respectively. Thermophysical data used for the calculation of cooling rate based on droplet size in each scenario is presented in Table 5.5.

$$\frac{dT_d}{dt} = 6.45 \times 10^6 d^{-1.44} \quad 5.1$$

$$\frac{dT_{d(l)}}{dt} = 1.29 \times 10^7 d^{-1.44} \quad 5.2$$

$$\frac{dT_{d(s)}}{dt} = 9.33 \times 10^6 d^{-1.45} \quad 5.3$$

The data and the resultant fitted power law relationships show that a comparatively small reduction in diameter can cause a drastic increase in prevailing cooling rate within a given droplet. Calculated maximum liquid phase and solid phase cooling rates can be used to study the impact of cooling rate on phase transformations in these particular states. However, unless otherwise stated, plots which include cooling rate as one of the axes will refer to the overall cooling rate $\frac{dT_d}{dt}$.

Table 5.5 Thermophysical properties for estimation of droplet cooling rate in drop-tube processed $CoCrCuFeNi_{0.8}$ alloy

Species	Property	State	Quantity	Source/Comments
Cobalt/Co	$c_{p(Co)}$ /J kg^{-1} K^{-1}	Liquid (1656 K)	590	Estimated through data or correlations found in [231] for pure metal in the required state and specified temperature
		Solid (1397 K)	816	
	$\rho_{Co(l)}$ /kg m^{-3}	Liquid (1656 K)	7631	
		Solid (1397 K)	8860	
	ε_{Co}	Liquid	0.335	[258]
Chromium/Cr	$c_{p(Cr)}$ /J kg^{-1} K^{-1}	Liquid (1656 K)	780	Estimated through data or correlations found in [231] for pure metal in the required state and specified temperature
		Solid (1397 K)	732	
	$\rho_{Cr(l)}$ /kg m^{-3}	Liquid (1656 K)	5920	
		Solid (1397 K)	7150	
	ε_{Cr}	Liquid	0.262	[258]
Copper/Cu	$c_{p(Cu)}$ /J kg^{-1} K^{-1}	Liquid (1656 K)	495	Estimated through data or correlations found in [231] for pure metal in the required state and specified temperature
		Solid (1397 K)	485	
	$\rho_{Cu(l)}$ /kg m^{-3}	Liquid (Cu m.p.)	8000	
		Solid (1397 K)	8960	
	ε_{Cu}	Liquid	0.147	[258]
Iron/Fe	$c_{p(Fe)}$ /J kg^{-1} K^{-1}	Liquid (1656 K)	795	Estimated through data or correlations found in [231] for pure metal in the required state and specified temperature
		Solid (1397 K)	705	
	$\rho_{Fe(l)}$ /kg m^{-3}	Liquid (1656 K)	6873	
		Solid (1397 K)	7870	
	ε_{Fe}	Liquid	0.357	[258]
Nickel/Ni	$c_{p(Ni)}$ /J kg^{-1} K^{-1}	Liquid (1656 K)	620	Estimated through data or correlations found in [231] for pure metal in the required state and specified temperature
		Solid (1397 K)	607	
	$\rho_{Ni(l)}$ /kg m^{-3}	Liquid (1656 K)	7811	
		Solid (1397 K)	8900	
	ε_{Ni}	Liquid	0.346	
Alloy	X_{Co}		0.208	Atomic ratios of each alloying element
	X_{Cr}		0.208	
	X_{Cu}		0.208	
	X_{Fe}		0.208	
	X_{Ni}		0.167	
	$c_{p(l)}$ /J kg^{-1} K^{-1}	Liquid (1656 K)	657.5	Estimated through the mixture rule
	$c_{p(s)}$ /J kg^{-1} K^{-1}	Solid (1397 K)	671.8	
	$c_{p(eff)}$ /J kg^{-1} K^{-1}	Overall	1135.5	$= \frac{c_{p(l)} + c_{p(s)}}{2} + \frac{L_{f(alloy)}}{T_l - T_s}$
	$\rho_{alloy(l)}$ /kg m^{-3}	Liquid (1656 K)	7224	Estimated through the mixture rule
	$\rho_{alloy(s)}$ /kg m^{-3}	Solid (1397 K)	8325	
	$\rho_{alloy(eff)}$ /kg m^{-3}	Overall	7743	Ave. of $\rho_{alloy(l)}$ and $\rho_{alloy(s)}$
	ε_{alloy}	Liquid	0.287	Estimated through the mixture rule
	T_l /K		1656	Onset of solidification from DSC analysis
	T_s /K		1397	End of solidification from DSC analysis
	$L_{f(alloy)}$/J kg^{-1} K^{-1}		123690	Determined from DSC analysis
Nitrogen/N_2	$c_{p(g)}$ /J kg^{-1} K^{-1}	Gas (295K)	1039.0	[247]
	ρ_g /kg m^{-3}		1.165	
	μ_g /m^2 s^{-1}		1.76*10^{-5}	
	κ_g /W m^{-1} K^{-1}		0.024	

5.4.2 General composition analysis

Table 5.6 Comparison between composition of drop-tube processed $CoCrCuFeNi_{0.8}$ with arc-melted ingot and predicted composition

	Co /at%	Cr /at%	Cu /at%	Fe /at%	Ni /at%
Predicted	20.8	20.8	20.8	20.8	16.7
Ingot	20.72 ± 0.08	22.12 ± 0.03	20.70 ± 0.18	20.43 ± 0.06	16.03 ± 0.06
Droplets (d = 75 – 53 μm)	20.56 ± 0.02	21.74 ± 0.07	20.55 ± 0.04	20.87 ± 0.06	16.29 ± 0.03

Table 5.6 shows a comparison between arc-melted and drop-tube processed $CoCrCuFeNi_{0.8}$ alloy in terms of global composition gathered from SEM-EDX measurements. Droplets from the 75 – 53 μm size fraction were chosen as a point of comparison to the arc-melted sample. Standard deviation error is used in all measurements. Generally, the compositions are very similar, droplets subjected to some of the highest cooling rates may be lower in Cr and Co while being slightly higher in Fe and Ni. Cu content variation is within the uncertainty values (determined from standard deviation measurement based on multiple trials of composition measurement). However, in all elements, the difference in atomic percent is below 0.50 at%.

5.4.3 Dispersions in dendritic and grain-refined droplets

5.4.3.1 Prevalence with droplet size/cooling rate

Following Equation 4.9, the occurrence rate of dispersions in dendritic and grain-refined droplets is plotted against the average droplet diameter for each size fraction as well as the calculated overall droplet cooling rates. The resultant plot is shown in Figure 5.8.

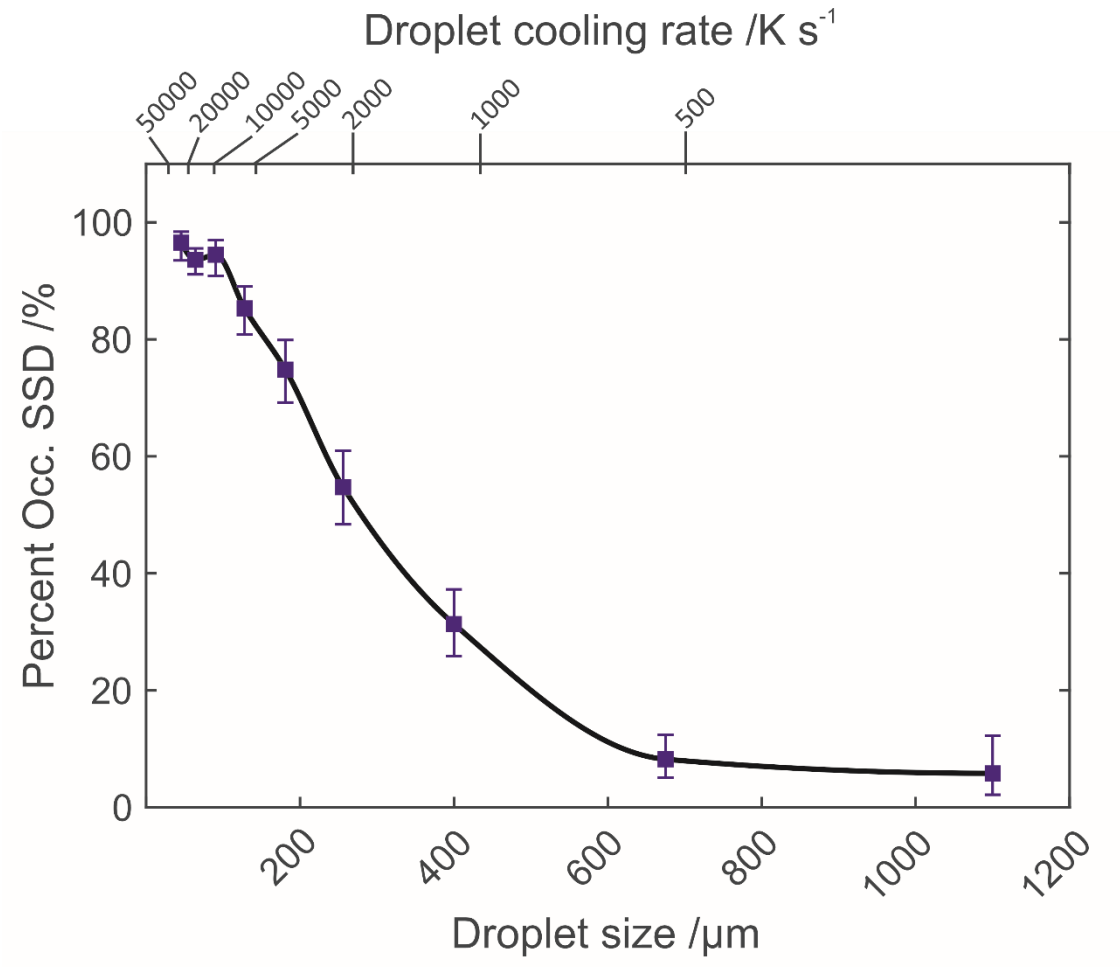

Figure 5.8 Correlation between droplet size/cooling rate and occurrence of dispersions in dendrite arms and refined grains in drop-tube processed $CoCrCuFeNi_{0.8}$.

Figure 5.8 indicates that the occurrence of Cu-rich dispersions in drop-tube processed $CoCrCuFeNi_{0.8}$ increases nearly monotonically with prevailing cooling rate (with the exception of a small drop between the occurrence rate in the 106 – 75 μm and 53 – 75 μm size fractions). By the time cooling rate rises above 10000 K s^{-1}, over 90% of analysed droplets contain these Cu-rich dispersoids as part of the microstructure. In contrast, the largest droplet size fractions (subject to cooling rates below about 700 K s^{-1}) feature these dispersoids only 10 % of the time. The largest increase in occurrence of dispersoids thus occurs between 700 K s^{-1} and 10000 K s^{-1}.

Importantly however, a small number of droplets in the smallest size fractions do not contain dispersoids. In addition, a measurable portion of even the slowest cooling droplets (largest diameter) have been observed to contain these dispersoid structures. This indicates that the appearance (or not) of these Cu-rich dispersoids is likely a phenomenon that is undercooling dependent. As a result, their formation is likely only indirectly dependent on cooling rate. Because of the relative ease with which dispersion structures can be identified

within dendritic or grain-refined structures in these droplets, as well as the regularity with which they occur in comparison to other structures (particularly at high cooling rates) uncertainty for occurrence rate is quite low. For ease of study, the remainder of this section will focus exclusively on Cu-rich dispersoids present in dendrite arms. Dispersoids in grain-refined grains will be covered later in section 5.4.5.

5.4.3.2 Microstructural analysis – SEM

The presence of Cu-rich dispersoids is a trend that is observable across droplets sizes. Additionally, these dispersoids are present in drastically different configurations depending on the droplet in which they are observed.

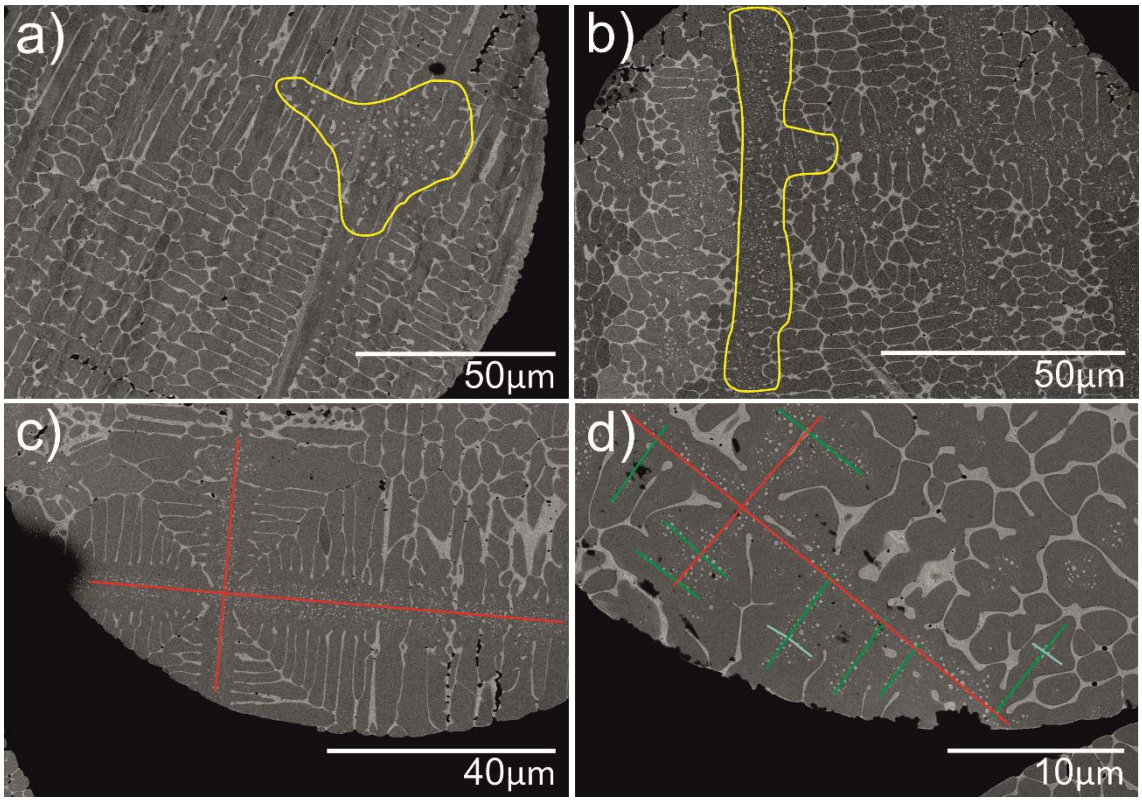

Figure 5.9 SEM BSE micrographs of Cu-rich dispersoids in dendrite arms of drop-tube processed $CoCrCuFeNi_{0.8}$. (a) 212 – 150 µm droplet with small Cu-rich dispersion region shown in yellow enclosed area. (b) 150 – 106 µm droplet with more extensive Cu-rich dispersion regions throughout the microstructure (example shown in yellow enclosed area). (c) 150 – 106 µm droplet with Cu-rich dispersions confined exclusively to primary dendrite arm cores (mapped by red lines). (d) 53 – 38 µm droplet with Cu-rich dispersions present in primary (mapped by red lines), secondary (mapped by green lines), and tertiary (mapped by cyan lines) dendrite cores.

Figure 5.9 shows different configurations of intradendritic dispersoids present in droplets of $CoCrCuFeNi_{0.8}$ alloys at various sizes and thus, solidified at various cooling rates. Figure 5.9a shows a 212 – 150 µm droplet where dispersoids have only formed in a small region of the droplet cross-section area and are

localised preferentially in only the base of the primary dendrite trunks (outlined in yellow). Conversely, Figure 5.9b shows a smaller 150 – 106 µm droplet where dispersoids are much more prevalent in dendrites throughout the microstructure (some dendrites outlined in yellow). Figure 5.9c shows a droplet from the 150 – 106 µm size fraction where Cu-rich dispersoids are observed exclusively in the primary dendrite arms (marked in red). Finally, Figure 5.9d shows a droplet in the 53 – 38 µm size fraction where Cu-rich dispersoids are present in primary (red) secondary (green) and even tertiary (cyan) dendrite arms.

Although it is clear that Cu-rich dispersoids may occur in primary, secondary or tertiary dendrite arms, they are overwhelmingly located in the primary dendrite arms and, even more specifically, in the cores of these arms. Such a trend is readily observable in the primary arms in Figure 5.9c, where the dispersoids do not populate the entire width of the primary dendrite arms, but stop before the edge of the primary arm from which the secondary arms branch. The dispersoids therefore tend to trace a more primitive dendrite network within the CoCrFeNi-rich dendrites. In other words, they appear to map out the dendritic network of a particular droplet at an earlier point during the dendritic growth and coarsening process in said droplet. In this regard, it is important to note that in droplets where dispersoids are found in secondary and tertiary dendrite arms, they must also be present in the primary arms of the same dendrite. Of the droplets analysed, there was not a single example found where Cu-rich dispersoids were observed solely in secondary and/or tertiary dendrite arms.

Regardless of in which dendrites they are found in any one droplet, the occurrence of Cu-rich dispersoids solely in the dendrite cores rather than throughout the dendrite cross-section suggests that they formed after dendritic solidification had been initiated. This points to the formation mechanism being a decomposition reaction in the solid state.

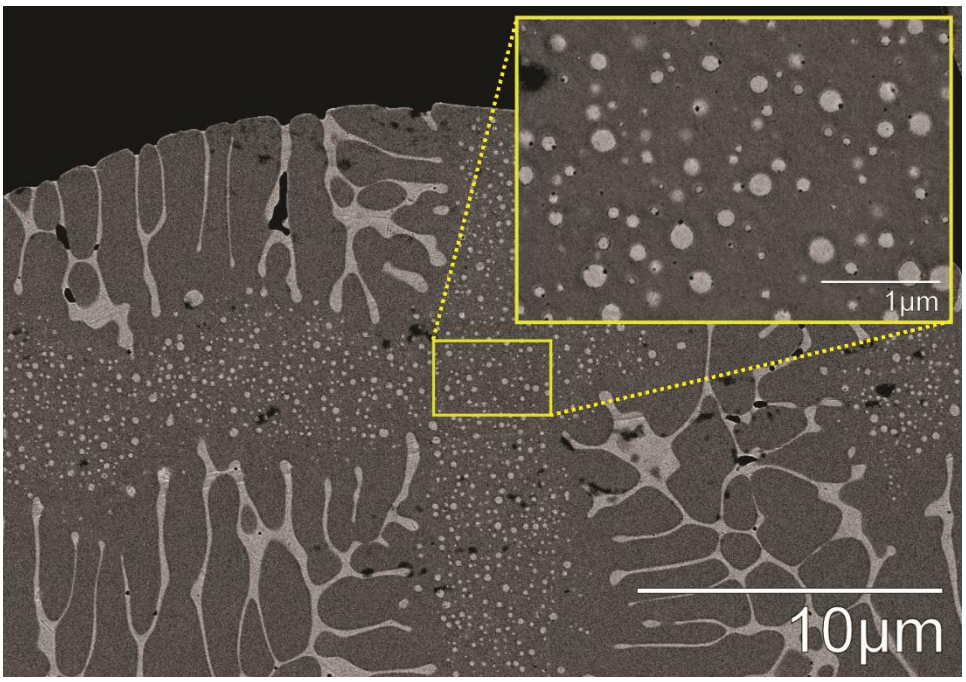

Figure 5.10 SEM BSE micrograph of droplet in 53 – 38 µm size fraction showing Cu-rich dispersoids in the cores of dendrite arms. A magnified image of the Cu-rich dispersoids in the dendrite core is shown in the included inset (delineated in yellow).

The inset in Figure 5.10 shows, in more detail, the shape of dispersoids present in dendrite arms of a substantial amount of $CoCrCuFeNi_{0.8}$ droplets after drop-tube processing. The dispersoids are non-faceted, and are circular or ovular in two dimensions, which points to spherical or spheroidal morphology in three dimensions. Diffuse dispersoids are observable in the inset as well, and are thought to be hidden below the surface of the sample, but revealed in the SEM image due to the interaction volume inherent in BSE analysis. Accelerated electrons are able to penetrate deep into the sample due to the accelerating voltage and reveal dispersoids buried under the surface. Qualitatively, diameter of these dispersoids decreases with droplet diameter and thus, with increasing cooling rate. Within a single droplet, the size of the dispersoids do not seem to change depending on where in the dispersions they are located. Large dispersoids can be located on the centreline of the dendrite arm or at the very edge of the dispersion regions. This is also true for smaller dispersoids.

The dispersions in the dendrites of droplet samples were subjected to a similar SEM-EDX mapping analysis to that applied to the dispersions in the arc-melted ingot (see section 5.3.2). In order to perform this analysis, dendrites were divided into groups based on their order of formation and the presence of dispersions. Three of these configurations were analysed and named. The first are primary dendrite arms containing Cu-rich dispersoids (PDD). The second are primary arms which contain no Cu-rich dispersoids (PDND). The final group consists of secondary dendrite arms which contain no dispersoids (SDND). In

each case, the core of the dendrite was mapped via EDX to find a sum spectrum and calculate an average composition factoring in the Cu-rich dispersoids and the CoCrFeNi-rich phase in between. Example droplets, along with the mapped regions (outlined in yellow) are shown in Figure 5.11. Figure 5.11a shows a PDD dendrite, Figure 5.11b, a PDND dendrite, and Figure 5.11c, a SDND dendrite. This analysis was performed for 4 out of the 9 gathered droplet size fractions to provide the ability to analyse any composition trends across the entire droplet diameter/cooling rate range.

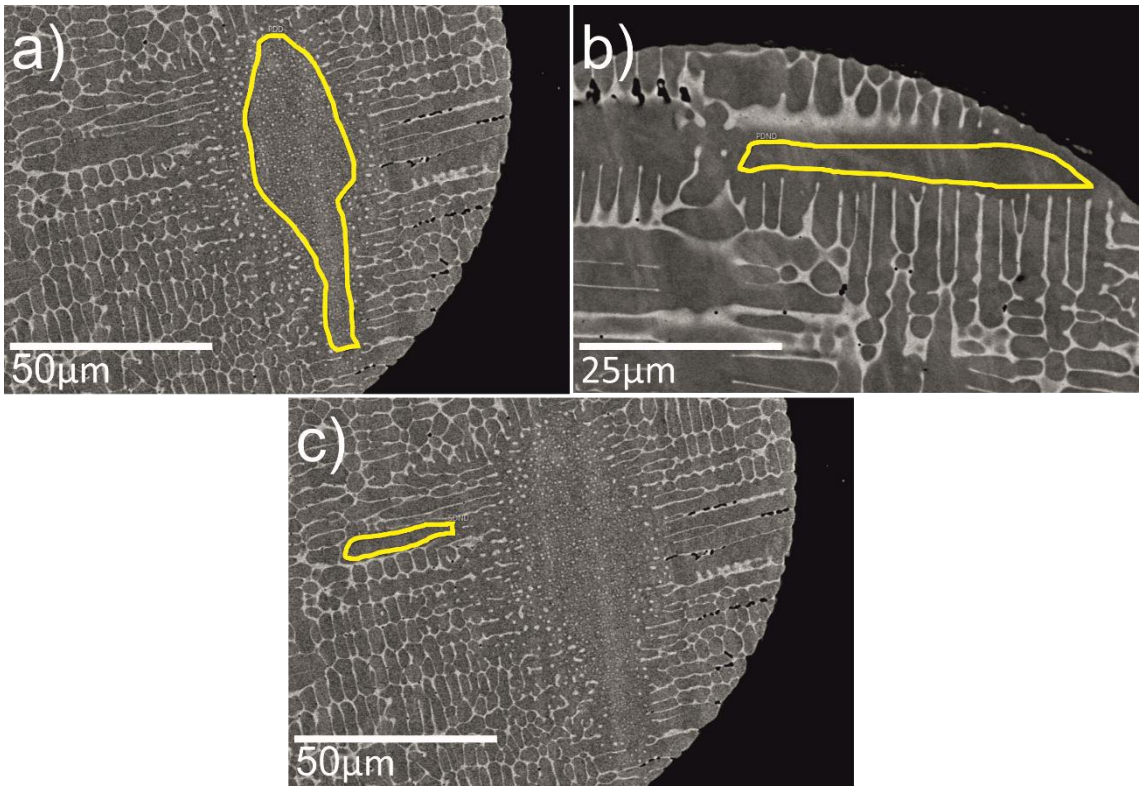

Figure 5.11 SEM BSE micrographs showing example SEM-EDX mapped regions of primary and secondary dendrites (with or without Cu-rich dispersions) in drop-tube processed $CoCrCuFeNi_{0.8}$ alloy. All regions from which data was taken are outlined in yellow (a) Example of dendrite core region in primary dendrite with dispersoids (PDD). (b) Example of dendrite core region in primary dendrite with no dispersoids (PDND). (c) Example of dendrite core region in secondary dendrite with no dispersoids (SDND).

Table 5.7, Table 5.8, and Table 5.9 represent the calculated compositions for dendrite core regions in PDD, PDND, and SDND dendrites respectively. For each dendrite type, compositions are taken for droplets from the 500 – 300 µm, 300 –212 µm, 212 – 150 µm and 53 – 75 µm size fractions. Standard deviation error is used in all measurements.

Table 5.7 Change in average composition of core regions of PDD dendrites with decreasing droplet diameter in drop-tube processed $CoCrCuFeNi_{0.8}$

	Droplet size fraction /μm			
	500-300	**300-212**	**212-150**	**53-75**
Cr /at %	21.65 ± 0.06	21.80 ± 0.22	21.64 ± 0.19	21.77 ± 0.09
Fe /at %	20.78 ± 0.14	20.91 ± 0.22	20.81 ± 0.09	21.08 ± 0.16
Co /at %	20.78 ± 0.06	20.86 ± 0.23	21.07 ± 0.16	20.98 ± 0.11
Ni /at %	16.44 ± 0.15	16.32 ± 0.09	16.56 ± 0.18	16.44 ± 0.04
Cu /at %	20.35 ± 0.34	20.12 ± 0.51	19.92 ± 0.29	19.72 ± 0.34

Table 5.8 Change in average composition of core regions of PDND dendrites with decreasing droplet diameter in drop-tube processed $CoCrCuFeNi_{0.8}$

	Droplet size fraction /μm			
	500-300	**300-212**	**212-150**	**53-75**
Cr /at %	23.84 ± 1.15	23.13 ± 1.14	24.39 ± 0.02	No data
Fe /at %	23.96 ± 0.10	23.80 ± 0.13	24.02 ± 0.02	No data
Co /at %	24.42 ± 0.48	24.75 ± 0.50	24.60 ± 0.24	No data
Ni /at %	17.00 ± 0.20	16.98 ± 0.21	16.68 ± 0.14	No data
Cu /at %	10.78 ± 0.61	11.34 ± 0.63	10.32 ± 0.04	No data

Table 5.9 Change in average composition of core regions of SDND dendrites with decreasing droplet diameter in drop-tube processed $CoCrCuFeNi_{0.8}$

	Droplet size fraction /μm			
	500-300	**300-212**	**212-150**	**53-75**
Cr /at %	24.53 ± 0.18	24.36 ± 0.25	24.26 ± 0.73	23.77 ± 0.43
Fe /at %	23.93 ± 0.34	24.22 ± 0.29	23.77 ± 0.38	23.38 ± 0.55
Co /at %	24.42 ± 0.26	24.56 ± 0.36	24.62 ± 0.78	23.62 ± 0.46
Ni /at %	16.71 ± 0.24	16.65 ± 0.16	16.88 ± 0.91	16.61 ± 0.17
Cu /at %	10.40 ± 0.29	10.21 ± 0.36	10.46 ± 0.83	12.63 ± 1.40

Table 5.8 and Table 5.9 show that in dendrites with no dispersions present (PDND and SDND respectively), all of the dendrites are CoCrFeNi-rich and correspondingly Cu-lean. The average composition of PDD dendrites differs substantially from the compositions of the other dendrite types studied here. The PDD dendrites are much richer in Cu (~20 at % in PDD compared to 10-13 at% in PDND and SDND). They are also concurrently leaner in Co, Cr, and Fe with a drop in each of about 1-3 at%. Ni content is consistently very slightly higher (about 0.1-0.2 at%) in PDND and SDND dendrites compared to PDD dendrites, although this small difference is lower than the standard deviation and could be the result of instrument-derived error.

Two unusual findings from this data are apparent. First, in all tables, there is no statistically significant change in composition with droplet size (and therefore, cooling rate). Any fluctuations in the at% of each element across different droplet sizes is accounted for by standard deviation error in the measurements. The only substantial difference in composition in one particular type of dendrite is the sudden rise in Cu from 10.46 at % to 12.36 at% in PDND dendrites as the droplet size reduces from an average of 181 um to 64 um. This change is likely accounted for by the decrease in the size of features such as dendrite arm thickness and the thickness of the interdendritic phase. If the size, in any physical dimension, of these features approaches the interaction volume of the electrons fired at the sample by the SEM, composition data may be gathered from the desired dendritic region as well as the interdendritic phase that surrounds it. Because the interdendritic phase is known to be very Cu-rich, any interaction with this phase by the SEM-EDX electrons may return a higher Cu concentration than is actually present. Such a phenomenon is much more likely to occur when gathering data on smaller features in the lowest diameter droplets.

The second interesting finding is from the data in Table 5.7. Here, similar to the measurements in the dispersion regions in the arc-melted ingot (see Table 5.3), the average composition of the PDD dendrite dispersion regions is very close to that of the overall composition of the droplets and the arc-melted ingot provided in Table 5.6. Because these compositions also do not change substantially with droplet size, they do not appear to be dependent on droplet cooing rate.

Two further facts must therefore be combined with the results of this analysis. The first is that average composition of dendrite core regions with Cu-rich dispersoids present is the same as that of the starting alloy liquid. The second is that, if Cu-rich dispersoids are believed to be the result of a solid-state decomposition reaction, the precursor of this decomposition reaction likely solidified in a chemically partitionless manner. It is therefore appropriate to see

if the prevalence of these dispersoid regions is impacted by rapid solidification (i.e. changes in cooling rate and average undercooling before solidification). This is more easily done for drop-tube processed droplets than for the arc-melted ingot. The results of such an analysis (based on the methodology in section 4.3.4.1) are presented below in section 5.4.3.3.

5.4.3.3 Dispersoid prevalence with cooling rate

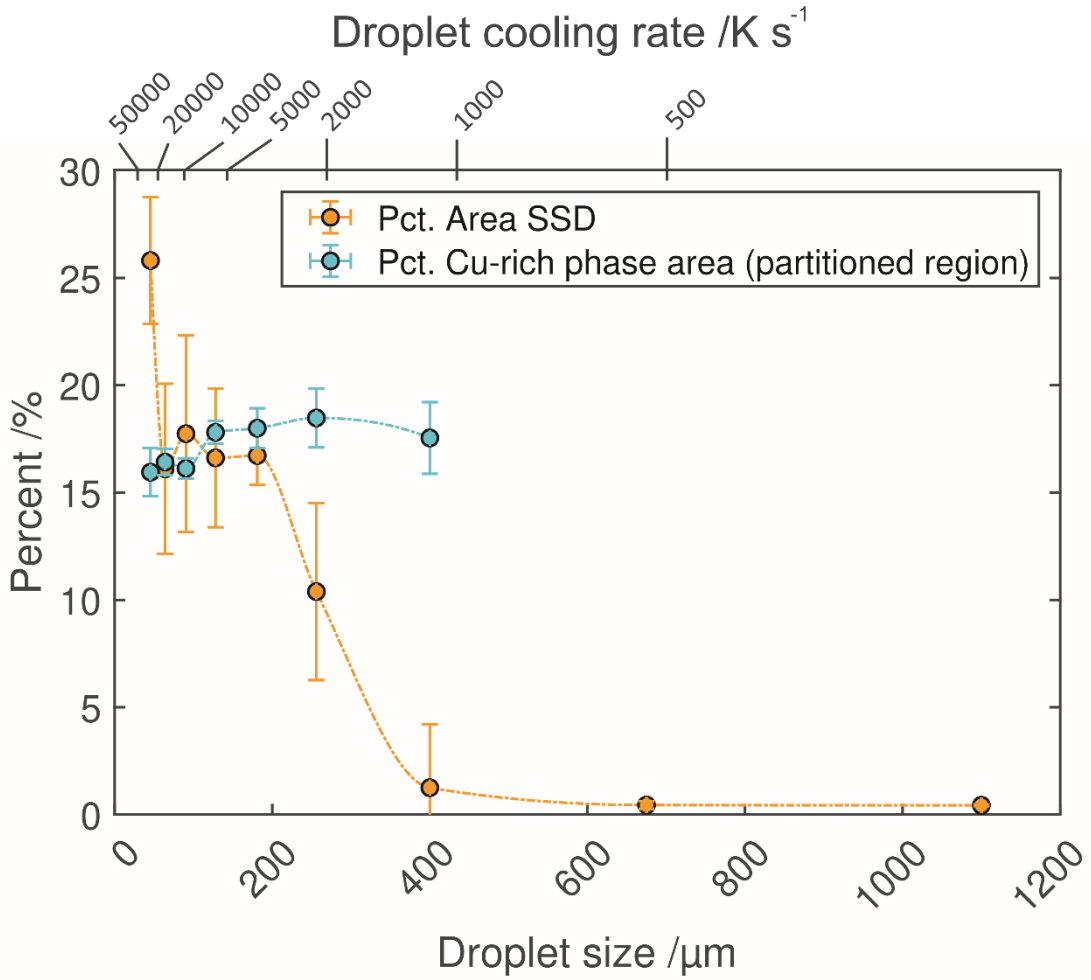

Figure 5.12 Area fraction of solid-state dispersion occupied zones (orange) and Cu-rich phase fraction of partitioned droplet regions (cyan) plotted against droplet size and cooling rate.

Based on the image analysis described in section 4.3.4.1, Figure 5.12 shows the variance of two key measured values with droplet diameter and overall cooling rate. As previously stated, this analysis is confined exclusively to purely dendritic droplets with dispersions featured in the dendrite cores (SCDD and MCDD structures).

The first curve (shown in orange), shows the trend in area percentage occupied by Cu-rich dispersoids $A\%_{disp}$ as droplet size decreases (cooling rate increases). This is the area percentage calculated using Equation 4.23. An example of the area measured is shown by the blue regions in Figure 4.12b.

The analysis shows that the area occupied by Cu-rich dispersions increases with increasing cooling rate. In the largest droplets, the occupied area percentage is negligible. The initial increase begins to occur at liquid-phase cooling rates above 1000 K s^{-1}. From here the occupied area percentage increases to around 17% at 4000 K s^{-1} and plateaus until the maximum cooling rate of 30000 K s^{-1} is reached at the smallest droplet sizes. At this very high cooling rate, the area percentage of dendritic droplets occupied by Cu-rich dispersions again increases, peaking at about 25%. Using the area percentage as a proxy measurement for the volume percentage, it is clear that more significant proportions of dendritic droplets are occupied by dispersed regions if they are cooled more rapidly. These regions are assumed to be preceded by a chemically partitionless solidified region (as mentioned in section 5.4.3.2).

The second curve, (shown in cyan), shows the trend in area percentage of the non-dispersed regions occupied by the light grey (Cu-rich) interdendritic phase. This is the area percentage $A\%_{IDP}$ calculated using Equation 4.25. An example of the area measured is shown in Figure 4.12d. Note that, because of the numerous grains present in the largest droplets and the resultant difficulty in enhancing colour contrast for image thresholding, the percentage of the Cu-rich interdendritic phase is not calculated for the two largest droplet size fractions. The curve shows that the area percentage occupied by the Cu-rich interdendritic phase in the remaining droplet area (i.e. the area without Cu-rich dispersoids present) does not change appreciably with droplet size or cooling rate. This is in direct contrast to the area percentage of Cu-rich dispersions, which increases as droplet size decreases. Instead, the interdendritic Cu-rich phase continues to occupy 15% – 20% of the droplet face (once the dispersed regions are removed from the measured area). Uncertainty in both area percentage measurements is given by the standard deviation.

5.4.3.4 Microstructural analysis – TEM

In the TEM, two regions from a droplet of drop-tube processed $CoCrCuFeNi_{0.8}$ which featured dispersoids in the dendrite arms, were selected for further investigation. The first such region comprised the dendritic and interdendritic phases from the dendrite arms away from the central trunk of the dendrite where dispersoids were present. The next region contained the dispersoids and the phase between these dispersoids in the core of the dendrite arm. In line with section 4.1.6.3, FIB sections were taken from a droplet from the 212 – 150 μm size fraction which featured a dendritic structure with dispersoids in the primary arms.

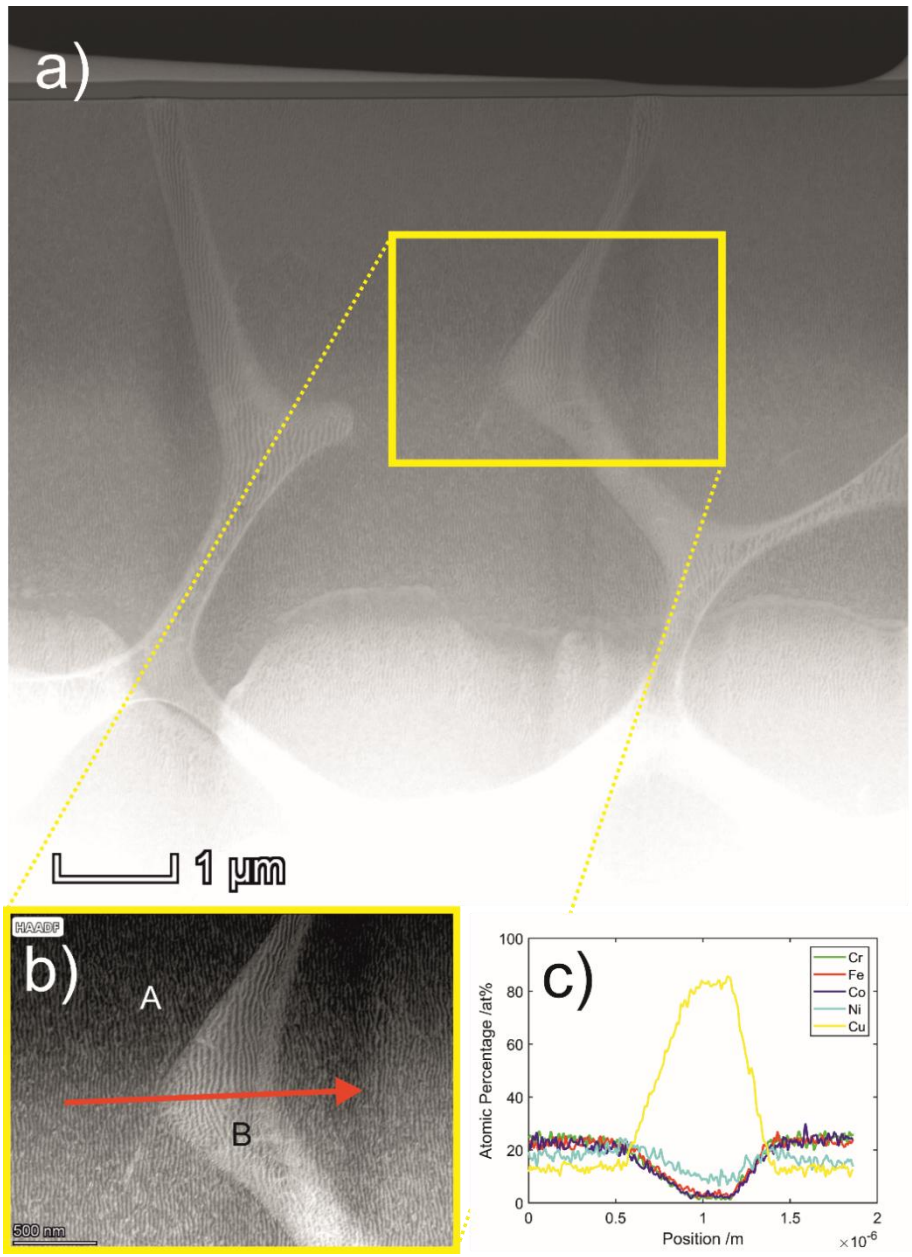

Figure 5.13 TEM micrograph and TEM-EDX composition line scan of dendritic and interdendritic phases in droplet of drop-tube processed $CoCrCuFeNi_{0.8}$ (212 – 150 µm). (a) Original bright-field TEM electron micrograph of phase boundary between CoCrFeNi-rich and Cu-rich phases. (b) HAADF view of phase boundary region from yellow inset in (a) showing location of compositional line scan (red arrow). (c) Graphical result of EDX composition line scan in (b) showing variation in atomic percentage of constituent elements across dendritic-interdendritic phase boundary. Locations of EDX composition analysis on regions A and B are indicated.

Figure 5.13a shows a large scale image of the first region studied, showing a CoCrFeNi-rich dendritic phase encircled by a web of the Cu-rich interdendritic phase. The inset (delineated by the yellow square) is magnified in Figure 5.13b. The red arrow shows the approximate area where a TEM-EDX line scan was conducted (red arrow in direction from left to right). The resultant graph in

Figure 5.13c shows the change in composition with position, encompassing the dendritic and interdendritic phases, and the phase boundaries between them. The scan shows a transition in composition over a distance of about 500 nm between the CoCrFeNi-rich phase and the Cu-rich phase. Approximate compositions of the CoCrFeNi-rich phase (A) and the Cu-rich interdendritic (B) are given in Table 5.10 below. Striations visible across both phases in the TEM micrographs in Figure 5.13 are the result of curtaining during the FIB milling process. This is supported by the lack of compositional change across these striations in the line scan (Figure 5.13b). Similar curtaining is observed in all subsequent TEM micrographs in this section.

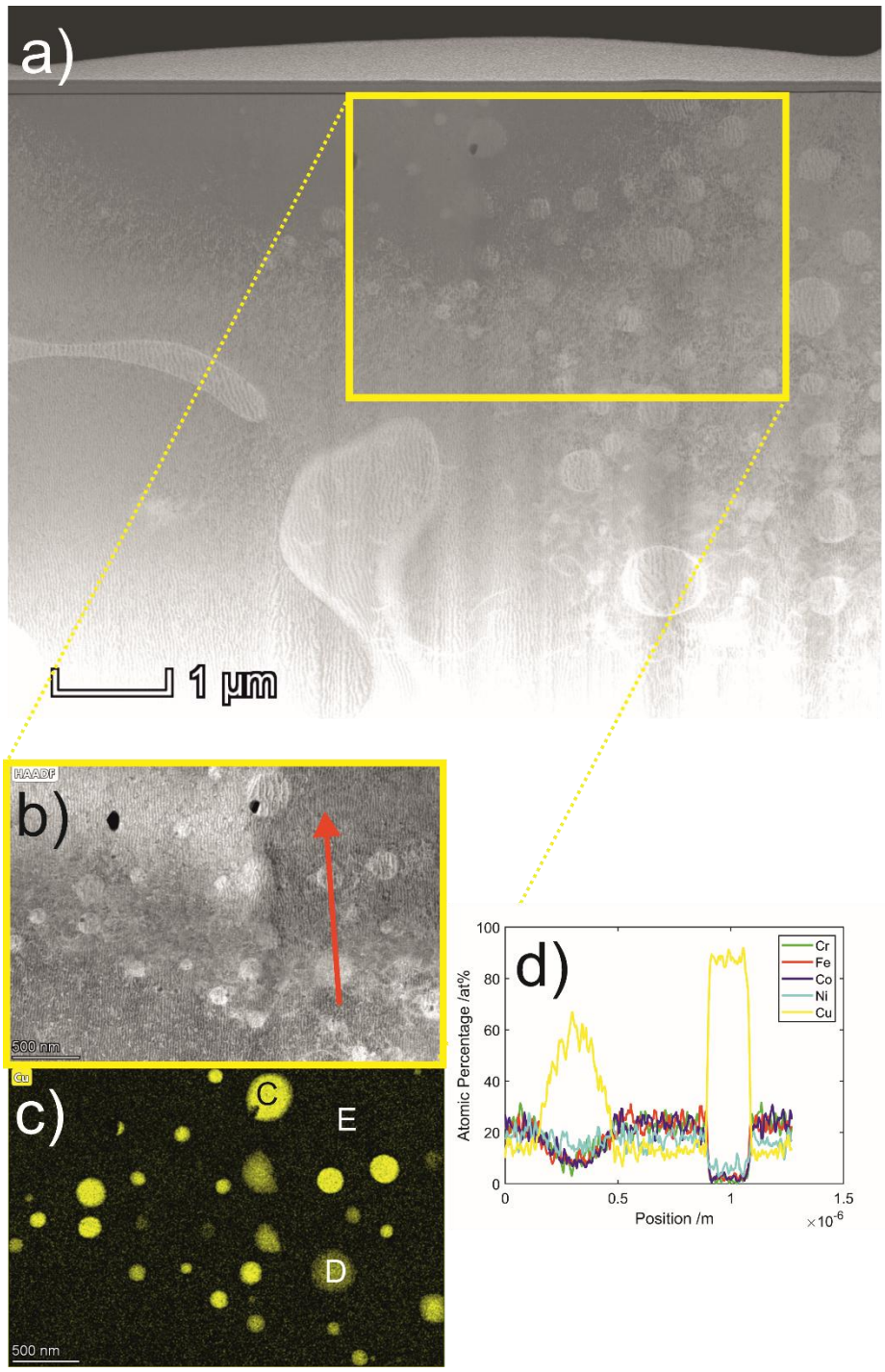

Figure 5.14 TEM micrograph and TEM-EDX composition line scan of dendritic dispersoids in droplet of drop-tube processed $CoCrCuFeNi_{0.8}$ (212 – 150 µm). (a) Original bright-field TEM electron micrograph of phase CoCrFeNi-rich phase and Cu-rich dispersoids. (b) HAADF view of region from yellow inset in (a) showing location of compositional line scan (red arrow). (c) EDX composition map of phase boundary region showing relative atomic percentage of Cu (yellow). (d) Graphical result of EDX composition line scan in (b) showing variation in atomic percentage of constituent elements across well-defined and diffuse dispersoid phase boundaries. Locations of EDX composition analysis on regions C-E are indicated.

A second FIB section was taken from the core of the dendrite in which the dispersoids were located. A magnified image of the resultant FIB section is shown in Figure 5.14a. The smaller region on which TEM-EDX mapping analysis was performed (inset defined by yellow square) is shown in Figure 5.14b. Figure 5.14c shows the relative Cu content of different regions in the microstructure. The Cu-rich dispersoids are largely circular, although some hemispherical shapes are also observed. It can be noticed that, while all dispersoids are Cu-rich compared to the surrounding matrix, some, such as that marked (C), appear much more defined (the difference in composition is much more pronounced). Conversely, other individual dispersoids, such as that that marked in (D), are more diffuse. The composition difference is not as significant between the droplet and the matrix, and the phase boundary is not as well defined. This difference is quantified in Figure 5.14d which shows the results of the TEM-EDX line scan across a diffuse and well-defined dispersoid respectively (scan taken along red arrow shown in Figure 5.14b from south to north). Across the diffuse dispersoid, there is a much more gradual increase in Cu at% as the phase boundary is crossed compared to that of the well-defined dispersoid, where a near step-wise increase in Cu at% is observed at the phase boundary. In addition, the Cu content in the diffuse dispersoids peaks between 50 at% and 70 at%, while the Cu contained in the well-defined dispersoids is above 80 at%. The gradual and step-wise increases in Cu content in the are matched by gradual and step-wise decreases in Co, Cr, Fe and Ni across the phase boundary of the diffuse and well-defined dispersoids respectively. The approximate composition of the phase between these Cu-rich dispersoids, marked in (E), is tabulated along with the preceding compositions discussed, in Table 5.10. Standard deviation error is used in all measurements.

Table 5.10 Composition data from TEM-EDX analysis of intradendritic Cu-rich dispersoids and dendrite arms in drop-tube processed $CoCrCuFeNi_{0.8}$

	Alloy	PDD	A	B	C	D	E
Cr /at%	21.6	21.6	24.05 ± 0.34	1.83 ± 0.24	1.77 ± 1.16	8.91 ± 0.81	23.41 ± 0.55
Fe /at%	20.7	20.8	23.07 ± 0.50	3.37 ± 0.11	2.71 ± 1.48	9.92 ± 0.43	22.62 ± 0.33
Co /at%	20.6	21.1	24.25 ± 0.93	2.67 ± 0.39	2.60 ± 1.27	8.91 ± 1.28	23.04 ± 0.27
Ni /at%	16.5	16.6	15.96 ± 0.83	10.40 ± 1.38	5.34 ± 1.58	13.22 ± 1.74	17.10 ± 0.40
Cu /at%	20.6	19.9	12.67 ± 0.14	81.73 ± 2.12	87.58 ± 5.46	59.04 ± 2.79	13.83 ± 0.34

Table 5.10 compares the compositions of the regions defined in Figure 5.13 and

Figure 5.14 to the average composition of drop-tube processed droplets of $CoCrCuFeNi_{0.8}$ and the average composition of the PDD dendrites in the 212 – 150 µm size fraction. Compositions (A) and (B) represent the CoCrFeNi-rich dendritic phase and the Cu-rich interdendritic respectively. These compositions compare readily to the composition of dendritic and interdendritic phases in the arc-melted ingot sample (see Table 5.2). (C) and (D) show the average compositions of the well-defined and diffuse Cu-rich dispersoids in the dendrite cores. The data in the EDX line-scan (see Figure 5.14d) is largely reflected by these precise composition values. The well-defined dispersoids have a much higher Cu composition (87.58 at%) than that of the diffuse dispersoids (59.05 at%). The well-defined dispersoids are therefore also much more lean in the other alloy constituents than the diffuse dispersoids. Finally, the composition of the phase between dispersoids (E) is CoCrFeNi-rich and largely similar to the composition of the dendritic phase (A). The Cu content is higher by roughly 1 at% while the composition of the other elements is simultaneously depleted by 1 at%.

The reason for occurrence of well-defined and diffuse boundaries between the Cu-rich dispersoids and the CoCrFeNi-rich dendritic phase between them merits discussion. One explanation for this occurrence could be sectioning effects due to the nature of the TEM sample preparation process. The scale bars in Figure 5.14 show that Cu-rich spherical dispersoids may possess a diameter up to, or perhaps even in excess of, 500 nm. This thickness is much larger than the thickness of the FIB section created for analysis (80-90 nm). In some cases, certain dispersoids may be sectioned above or below the equator, such that only part of it will be analysed by the TEM. Because of this sectioning, the edges of the dispersoid will be thinner than the centre, making it more likely that a higher Cu-reading will result in the centre. Alternatively, the presence of both diffuse and well-defined dispersoids in similar areas of the sample could be explained through the conjecture that diffuse boundaries indicate a dispersoid in the intermediate stages of the formation process. The driving force for the reaction responsible for dispersoid formation was likely reduced to zero before it could proceed to completion. Regardless which of these explanations is true, it is reasonable to hypothesise that the well-defined dispersoids represent the result of a reaction which has proceeded nearly to completion.

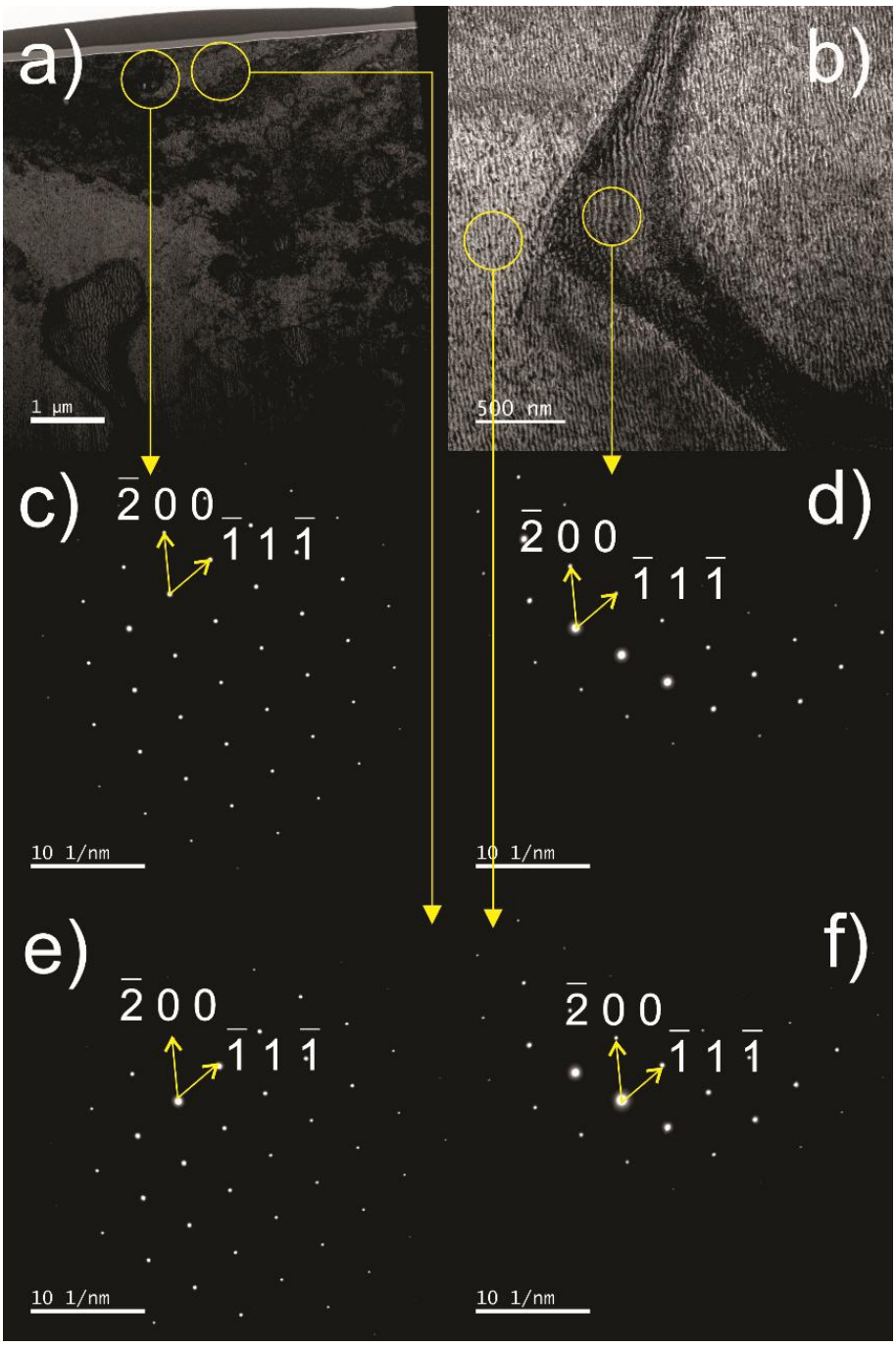

Figure 5.15 TEM-derived electron micrographs and SAED patterns for phases in droplets of drop-tube processed $CoCrCuFeNi_{0.8}$ alloy. (a) TEM electron micrograph of dispersed region in dendrite core of drop-tube processed $CoCrCuFeNi_{0.8}$ (212 – 150 µm size fraction). Cu-rich dispersoid and CoCrFeNi-rich phase are defined in yellow circles. (b) TEM electron micrograph of dendritic, dispersoid-free region of drop-tube processed $CoCrCuFeNi_{0.8}$ (212 – 150 µm size fraction). Cu-rich interdendritic phase and CoCrFeNi-rich phase are defined in yellow circles. (c) TEM derived SAED pattern of Cu-rich dispersoid phase. (d) TEM derived SAED pattern of Cu-rich interdendritic phase. (e) TEM derived SAED pattern of CoCrFeNi-rich phase between dispersoids. (f) TEM derived SAED pattern of CoCrFeNi-rich dendritic phase.

TEM derived SAED patterns were used to identify the crystal structures of the key phases in the alloy. Similar to the composition analysis in Table 5.10, four separate phases are identified. These are the CoCrFeNi-rich dendritic phase, the Cu-rich interdendritic phase, the Cu-rich dispersoids, and the CoCrFeNi-rich phase in between dispersoids. In this case, the Cu-rich dispersoids, diffuse or well-defined, are assumed to consist of one phase. Figure 5.15 shows the resultant SAED patterns and the approximate locations from where they were obtained (delineated by yellow circles). Figure 5.15a shows the core of the dendrite where dispersoids are located, Figure 5.15c and Figure 5.15e show the SAED patterns from the Cu-rich dispersoids and the CoCrFeNi-rich region between them respectively. Figure 5.15b shows the dendritic region of the microstructure further away from the dispersoids. Figure 5.15d and Figure 5.15f show SAED patterns for the Cu-rich interdendritic phase and the CoCrFeNi-rich dendritic phase respectively. In all images, the zone axis is in the [0 1 1] direction. The methodology described in section 4.1.6.4 was used to determine the crystal structure of each phase. The two characteristic lengths A and B, and the angle θ between them, were compared to commonly encountered structures in [244]. It was determined that each phase consisted of an FCC crystal structure. Furthermore, the lattice parameter for each phase was estimated through Equation 4.1 for an FCC crystal structure. Table 5.11 shows the results of such an analysis. In line with the work of Zhang et al. [245] a minimum uncertainty of 0.5% must be considered for lattice parameters estimated in this way. Based on this, and the error inherent in the TEM instrument used for such measurements (see section 4.1.6.4), a 4% error is assumed for calculation of lattice parameter from TEM-derived SAED patterns.

Table 5.11 Determined crystal structure and estimated lattice parameter for primary phases in dendrites and dendritic dispersions of drop-tube processed $CoCrCuFeNi_{0.8}$

Fig.	Phase	Phase structure	Lattice parameter /Å
5.15c	Cu-rich spherical dispersoids	FCC	3.70 ± 4%
5.15d	Cu-rich interdendritic	FCC	3.69 ± 4%
5.15e	CoCrFeNi-rich between dispersoids	FCC	3.69 ± 4%
5.15f	CoCrFeNi-rich dendritic far from dispersoids	FCC	3.67 ± 4%

Table 5.11 shows that there is high degree of similarity between lattice parameters for all four phases treated here. Most notably, the difference

between the lattice parameter of the Cu-rich spherical dispersoid phase (Figure 5.15c) and that of the CoCrFeNi-rich phase that surrounds them (Figure 5.15e) is only 0.5%. The largest difference between the measured lattice parameters of any of the four phases is found in the difference between the lattice parameter of the Cu-rich spherical dispersoids (Figure 5.15c) and that of the CoCrFeNi-rich dendritic phase far from any dispersoids (Figure 5.15f). This error is still only just above 1%. When the uncertainty in the measurements is factored in, the significant overlap between the ranges of all of these lattice parameters makes it difficult to distinguish one from the other definitively in terms of magnitude. However, the main conclusions that can be drawn from this analysis is that there is likely a small difference in the lattice parameter for each of the phases, and that each phase has the same FCC phase structure. In line with section 2.2.3.1, such conditions are likely to result in a semi-coherent phase boundary with a very small lattice misfit energy (see Equation 2.9) which is consistent with the non-faceted interface observed between the Cu-rich solid-state dispersoids and the CoCrFeNi-rich dendritic phase in which they are located.

5.4.4 Large dispersion regions

5.4.4.1 Prevalence with droplet size/cooling rate

Large dispersions were initially regarded to be structurally distinct from dendritic dispersions or dispersions in grain-refined grains in that they do not appear to be easily linked or confined to any particular structural features. Instead, they appear usually on the periphery of the droplet diameter and occupy a significant proportion of the visible internal droplet microstructure. The occurrence of large dispersions is calculated via an amalgamation of the the sub-groups consisting of LDOP and CDOP structures (see Equation 4.10). The occurrence rate of such structure at various droplet sizes/cooling rates is shown in Figure 5.16.

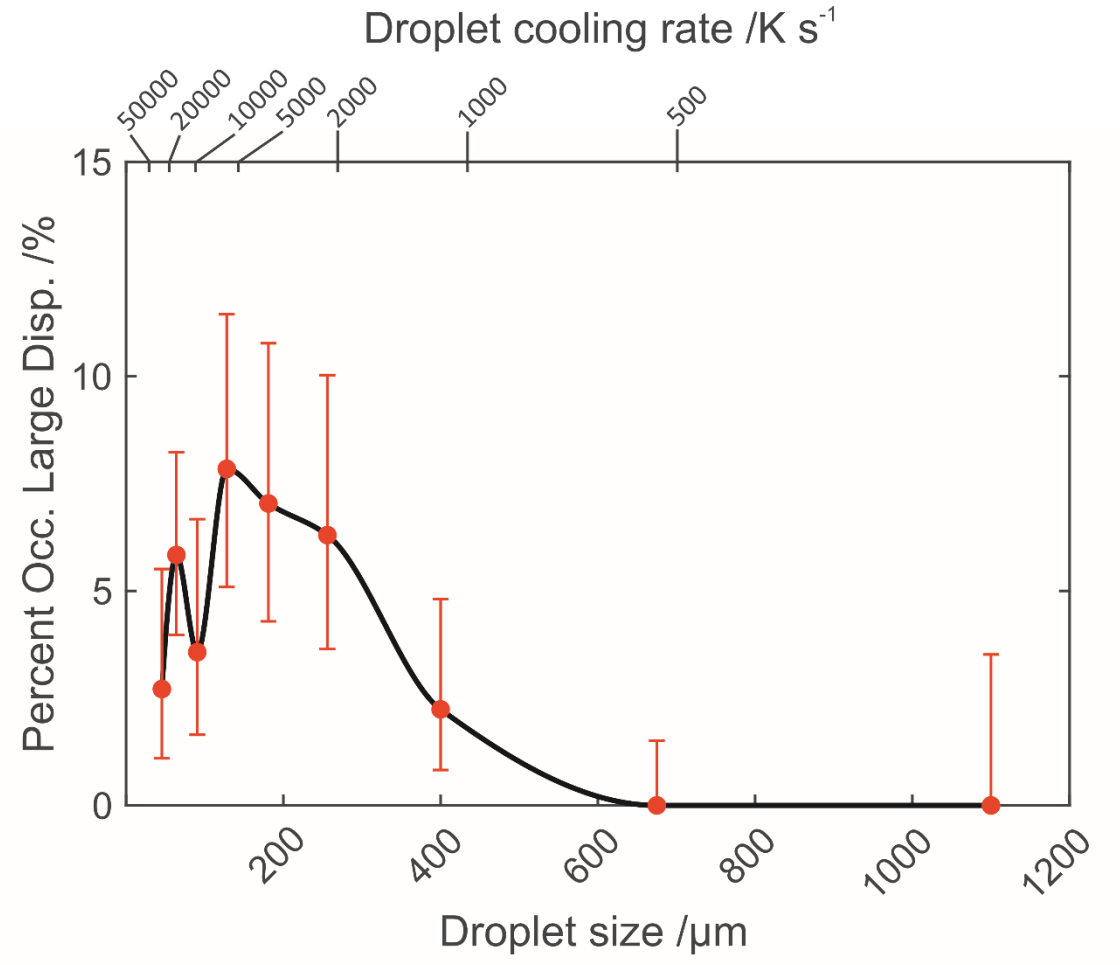

Figure 5.16 Occurrence rate of large dispersions correlated with droplet size and cooling rate for drop-tube processed $CoCrCuFeNi_{0.8}$ alloy.

Based on Equation 4.15, uncertainty in occurrence rate is higher than in Figure 5.16 than in the previous correlation in Figure 5.8 due to the lower overall number of catalogued droplets in each size fraction which exhibit the large dispersion structure compared to dendrite or refined-grain dispersion structures. Large dispersions are not observed to occur when droplet diameter is larger than about 600 μm and cooling rate is below about 600 K s^{-1}. Occurrence rate peaks at 7-8 % in intermediate droplet sizes (corresponding to cooling rates of 2000 K s^{-1} to 8000 K s^{-1}. In the smallest droplet size fractions with prevailing cooling rates above 10000 K s^{-1}, occurrence appears to decrease once more. Critically however, the significant calculated error inherent in these measurements means that this trend is much more uncertain. It is likely that more data must be collected from a larger data set before more concrete conclusions can be made regarding the trend in large dispersion occurrence with cooling rate.

5.4.4.2 Microstructural analysis – SEM

As with dispersion regions in the ingot and in dendrite cores, SEM analysis was used to determine the average composition of these dispersed regions, factoring in the Cu-rich dispersoids and the CoCrFeNi-rich phase between. An example of the LDOP and CDOP droplets in the 300 – 212 μm size fraction from which the average composition data was gathered in is shown in Figure 5.17. Figure 5.17a shows a lower magnification SEM micrograph of a LDOP droplet. Figure 5.17b shows a magnified image of the region of Figure 5.17a delineated by the yellow square. SEM-EDX composition maps and the resultant summed composition spectra were gathered from uniform dispersed regions such as that outlined in the yellow shape in Figure 5.17b.

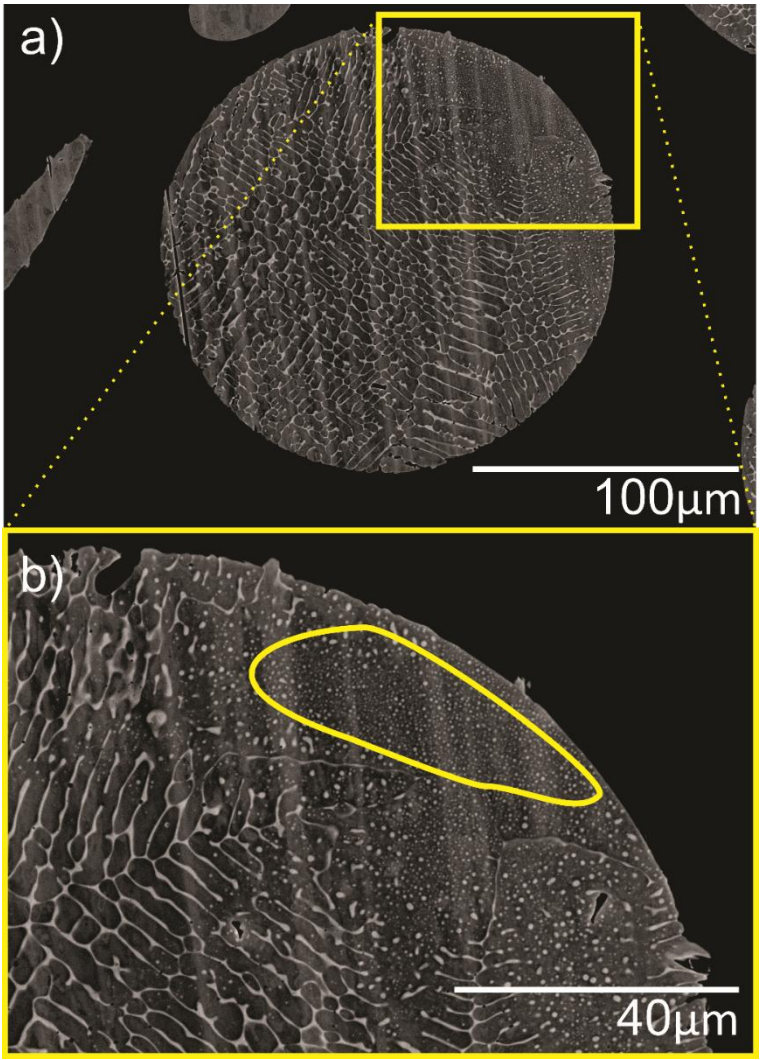

Figure 5.17 SEM BSE micrographs of large dispersions on periphery (LDOP) in droplet in the 300 – 212 μm size fraction. (a) Low magnification image of full droplet. (b) Magnified large dispersoid region from yellow rectangular inset in (a) with EDX composition analysis region outlined in yellow.

The resultant average composition data for large dispersion regions in the 300 – 212 μm size fraction is compared to the average composition of similar regions in PDD dendrites in droplets of the same size and dispersion regions in the arc-melted ingot in Table 5.12. Standard deviation error is used in all measurements.

Table 5.12 Comparison of average composition in dispersion regions in arc-melted ingot, and PDD dendrites and large dispersion regions of drop-tube processed $CoCrCuFeNi_{0.8}$

	Region/Area of Composition			
	Overall (Droplets)	**Ingot Disp.**	**PDD (256 μm)**	**Large Disp. (256 μm)**
Cr /at %	21.6	22.11 ± 0.14	21.80 ± 0.22	21.89 ± 0.08
Fe /at %	20.7	20.59 ± 0.09	20.91 ± 0.22	20.92 ± 0.05
Co /at %	20.6	20.52 ± 0.08	20.86 ± 0.23	20.71 ± 0.09
Ni /at %	16.5	16.04 ± 0.02	16.32 ± 0.09	16.30 ± 0.07
Cu /at %	20.6	20.73 ± 0.18	20.12 ± 0.51	20.18 ± 0.16

Table 5.12 shows stark similarities between the compositions of all of the dispersed regions which prevail at various different cooling rates and are even consistent in composition following different solidification techniques. Just as important is the fact that these compositions are all similar to the overall composition of the drop-tube processed alloy droplets and that of the arc-melted ingot.

5.4.4.3 Microstructural analysis – TEM

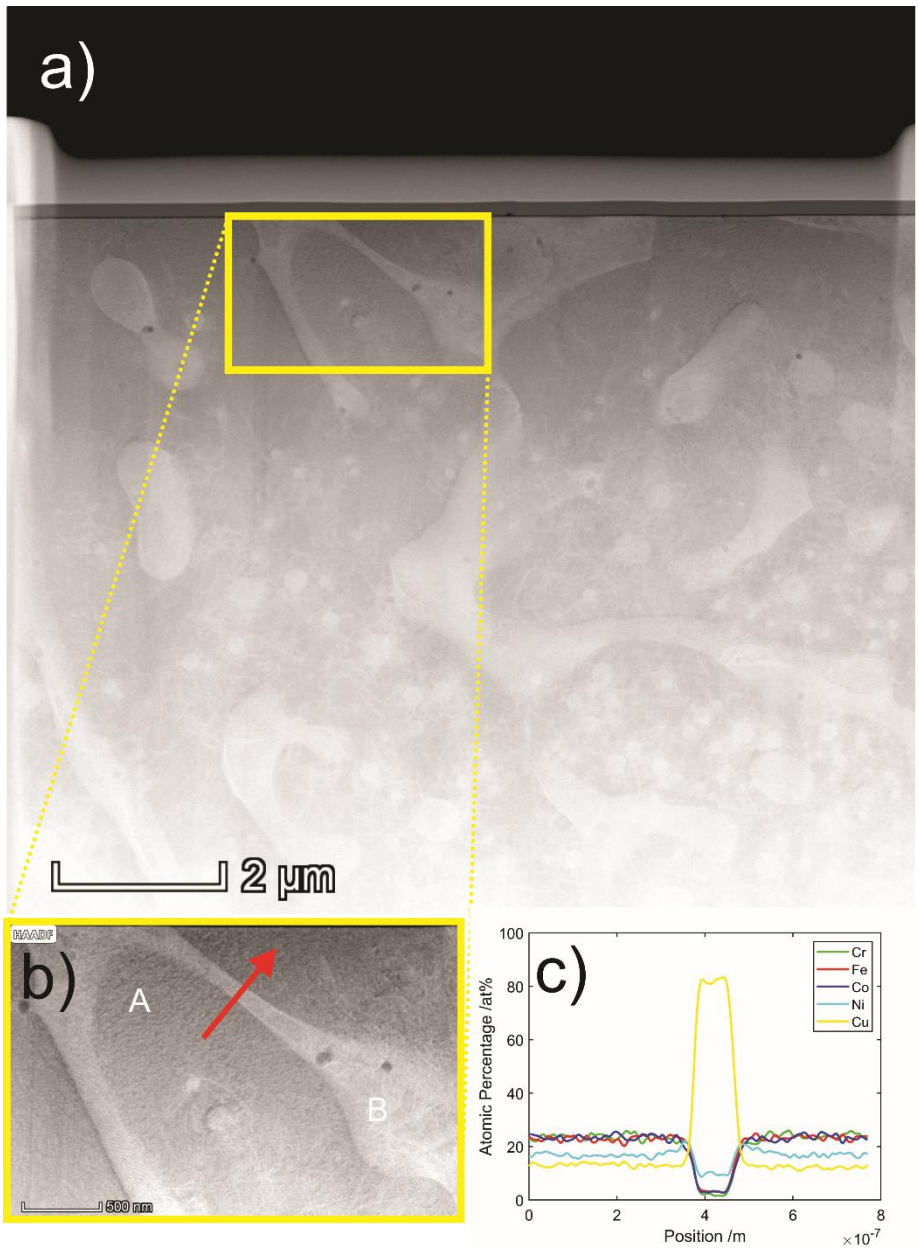

Figure 5.18 TEM micrograph and TEM-EDX composition line scan of dendritic and interdendritic phases in LDOP droplet of drop-tube processed $CoCrCuFeNi_{0.8}$ (212 – 150 µm). (a) Original bright-field TEM electron micrograph of phase boundary between CoCrFeNi-rich and Cu-rich phases. (b) HAADF view of phase boundary region from yellow inset in (a) showing location of compositional line scan (red arrow). (c) Graphical result of EDX composition line scan in (b) showing variation in atomic percentage of constituent elements across dendritic-interdendritic phase boundary. Locations of EDX composition analysis on regions A and B are indicated.

Figure 5.18 shows the results of TEM analysis of the dendritic region of a LDOP droplet. Figure 5.18a displays a bright field image of the original FIB section from which a key region was selected for further analysis. The selected region, marked in yellow, is magnified in Figure 5.18b. Figure 5.18c shows the results

of a composition line-scan taken along the direction of the red arrow in Figure 5.18b. As with other droplets with dendritic structures, the dark-grey dendritic phase (A) is CoCrFeNi-rich while the interdendritic phase (B) is Cu-rich with a minor addition of Ni. In the region of the line scan, the phase boundary is well defined with a transition region of about 30 nm.

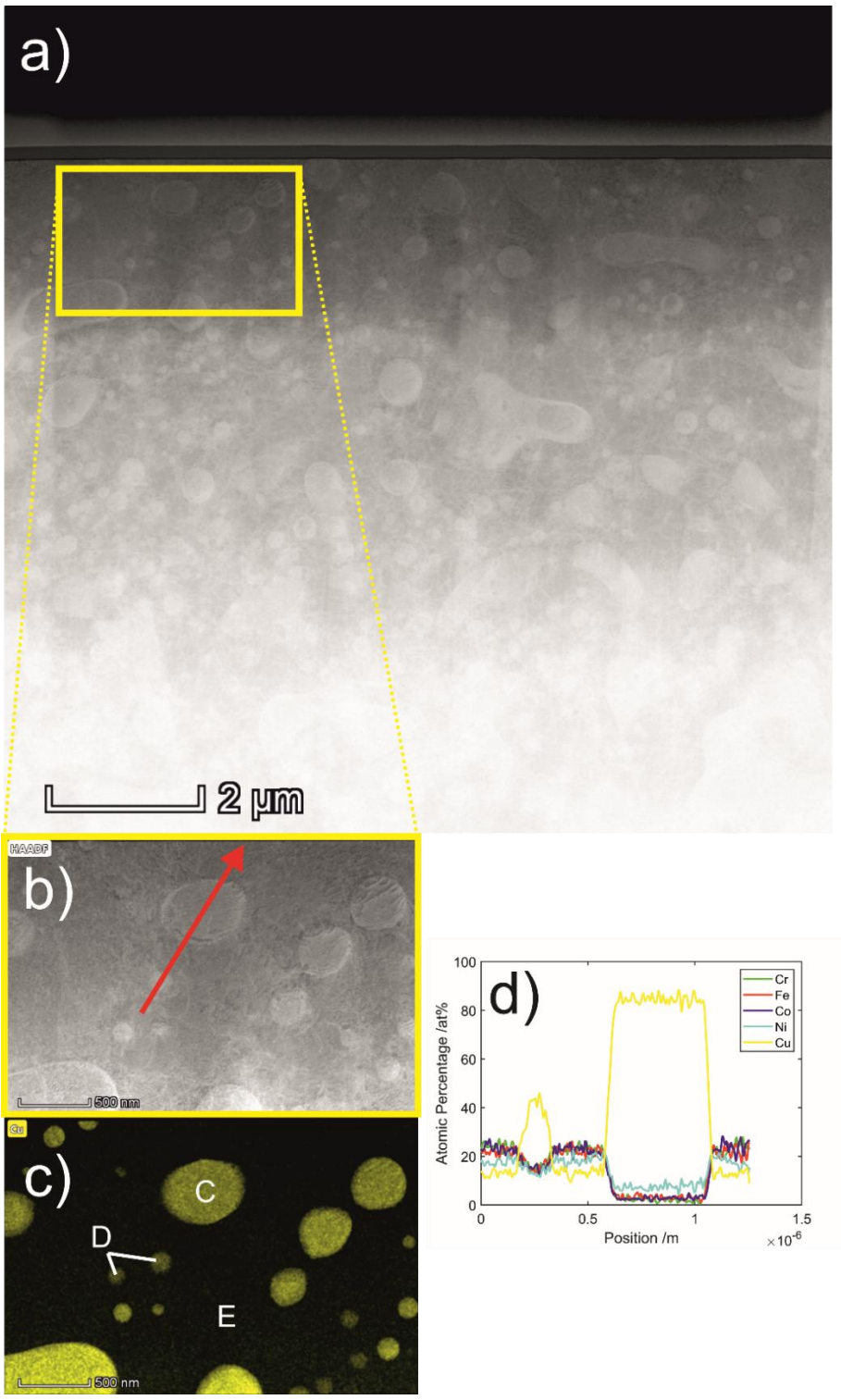

Figure 5.19 TEM micrograph and TEM-EDX composition line scan of dispersed region in LDOP droplet of drop-tube processed $CoCrCuFeNi_{0.8}$ (212 – 150 µm). (a) Original bright-field TEM electron micrograph of phase CoCrFeNi-rich phase and Cu-rich dispersoids. (b) HAADF view of region from yellow inset in (a) showing location of compositional line scan (red arrow). (c) EDX composition map of phase boundary region showing relative atomic percentage of Cu (yellow) (d) Graphical result of EDX composition line scan in (b) showing variation in atomic percentage of constituent elements across well-defined and diffuse dispersoid phase boundaries. Locations of EDX composition analysis on regions C-E are indicated.

Figure 5.19 shows the results of TEM analysis of other region of interest in the LDOP droplet, the large dispersion region. Figure 5.19a shows the BF image of the region of the FIB section which features such dispersions, and a smaller area was selected for compositional analysis. This region is shown in the yellow rectangle inset and is shown in Figure 5.19b. Figure 5.19c shows a compositional analysis of the selected region in terms of Cu at%. Cu-rich regions are shown in yellow, while correspondingly Cu-lean (and, therefore, CoCrFeNi-rich) regions are shown in black. Similar to the analysis of the dispersoids in dendrite cores in Figure 5.14, dispersoids in the LDOP droplet are Cu-rich while the surrounding dendritic phase is Cu-lean. Additionally, some dispersoids are well-defined while some are more compositionally diffuse. The results of a compositional line scan taken across two such dispersoids is shown in Figure 5.19d. The area and direction of the scan is shown by the red arrow in Figure 5.19b.

The line scan reveals a compositional difference between well-defined dispersoids (C) and diffuse dispersoids (D). Well-defined dispersoids, similar to the interdendritic phase, are extremely Cu-rich with a Cu content of over 80 at%. The boundary between phases is also comparatively well-delineated, with a 30 nm transition zone between phases. Diffuse dispersoids are also Cu-rich but to a much lesser extent. The boundary between phases is much less defined, represented by a more gradual rise in Cu content from the phase boundary to the maximum value in the centre (which, in this example, is just above 40 at% Cu). Between these dispersoids, the region of very similar composition to the dendritic CoCrFeNi-rich phase in other droplets predominates. This has been labelled phase (E).

In addition to the above analysis, Table 5.13 shows average composition values (gathered from TEM-EDX derived composition spectra) for each of the principle phases (see Figure 5.18b and Figure 5.19b) in LDOP droplets. Uncertainty is given by the standard deviation.

Table 5.13 Composition data from TEM-EDX analysis of intradendritic Cu-rich dispersoids within large dispersions in drop-tube processed $CoCrCuFeNi_{0.8}$

	Alloy	A	B	C	D	E
Cr /at%	21.6	24.08 ± 0.29	1.57 ± 0.07	1.32 ± 0.31	17.65 ± 2.63	24.38 ± 0.68
Fe /at%	20.7	23.09 ± 0.34	2.06 ± 0.63	1.90 ± 0.31	17.07 ± 2.39	22.02 ± 0.48
Co /at%	20.6	23.00 ± 0.43	1.69 ± 0.69	1.35 ± 0.07	17.67 ± 2.30	24.00 ± 1.09
Ni /at%	16.5	16.53 ± 0.19	6.49 ± 1.99	5.06 ± 1.09	13.68 ± 1.11	16.86 ± 1.25
Cu /at%	20.6	13.30 ± 0.49	88.19 ± 3.26	90.36 ± 1.47	33.93 ± 8.22	12.74 ± 0.35

The data from Table 5.13 reveals similar phase configurations and compositions to the dispersoids in the dendrite arms in Table 5.10. Compositions (A) and (B) represent the CoCrFeNi-rich dendritic and Cu-rich interdendritic phases that are common in most droplets solidifying in the form of dendrites. Compositions (C) and (D) represent compositions between well-defined dispersoids and diffuse dispersoids respectively. These values, and the line scan in Figure 5.19d show that well-defined dispersoids appear to feature a much higher Cu composition (about 90 at%) compared to diffuse dispersoids which, although still rich in Cu, only consist of about 34 at% of it on average. The composition of the diffuse dispersoids is much also much more variable depending on which one is measured, as is shown by the higher standard deviation uncertainty in values compared to that for well-defined dispersoids. Finally, composition (E), the composition of the CoCrFeNi-rich dendritic phase between Cu-rich dispersoids, is largely indistinguishable from that of CoCrFeNi-rich dendrites, composition (A).

The potential reasons for the large difference in composition between well-defined and diffuse dispersoids may be similar to those discussed regarding dendritic dispersoids in section 5.4.3.4 above.

5.4.5 Grain refinement

5.4.5.1 Microstructural analysis – SEM

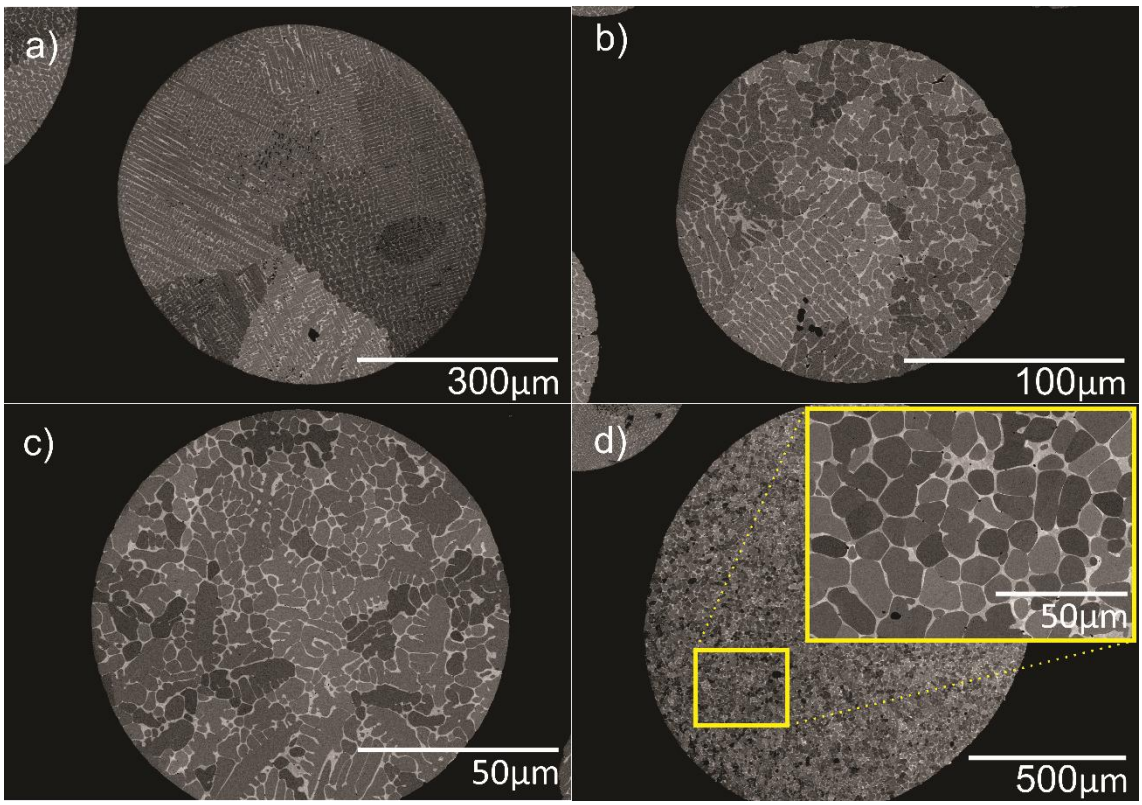

Figure 5.20 SEM BSE micrographs describing shift in grain morphology from large crystalline to partially refined/fully refined grain structures in drop-tube processed $CoCrCuFeNi_{0.8}$. (a) Multicrystalline dendritic droplet from 850 – 500 µm size fraction featuring columnar dendrites and minimal grain refinement. (b) Partially grain refined droplet from 212 – 150 µm size fraction showing predominance of refined grains on right hand side and columnar dendritic character on the left. (c) Partially grain refined droplet from 150 – 106 µm size fraction showing partially refined grains throughout the microstructure, with maintenance of some columnar dendritic characteristics. (d) Fully grain refined droplet from 850+ µm size fraction showing equiaxed microstructure and complete loss of dendritic character. Magnified image of fully refined grains shown in yellow inset.

Figure 5.20 displays droplets which have undergone various degrees of grain refinement. Figure 5.20a shows a multicrystalline dendritic (MC) droplet from the 850 – 500 µm size fraction where columnar dendrites predominate and minimal grain refinement has occurred. Figure 5.20b shows a partially grain refined (PGR) droplet from the 212 – 150 µm size fraction. Here, columnar dendrites predominate in the left hand side of the droplet, but a substantial reduction in grain size and a loss of consistent growth direction is observable on the right hand side of the droplet. Figure 5.20c shows another example of a partially grain refined (PGR) microstructure from the 150 – 106 µm. In this case, grains throughout the entire droplet maintain some of their dendritic character,

but have nearly all been subject to significant refinement so that the consistent columnar configuration has been lost and the dendrite orientation is noticeably more inconsistent. Finally Figure 5.20d shows a fully grain refined (FGR) droplet in the 850+ µm size fraction. Little to no evidence of a directional columnar dendritic structure remains and the microstructure takes the form of near-equiaxed grains (see inset). There has also been a large drop in grain size compared to that in droplets of a similar diameter (see the large columnar grains in Figure 5.20a as an example for comparison).

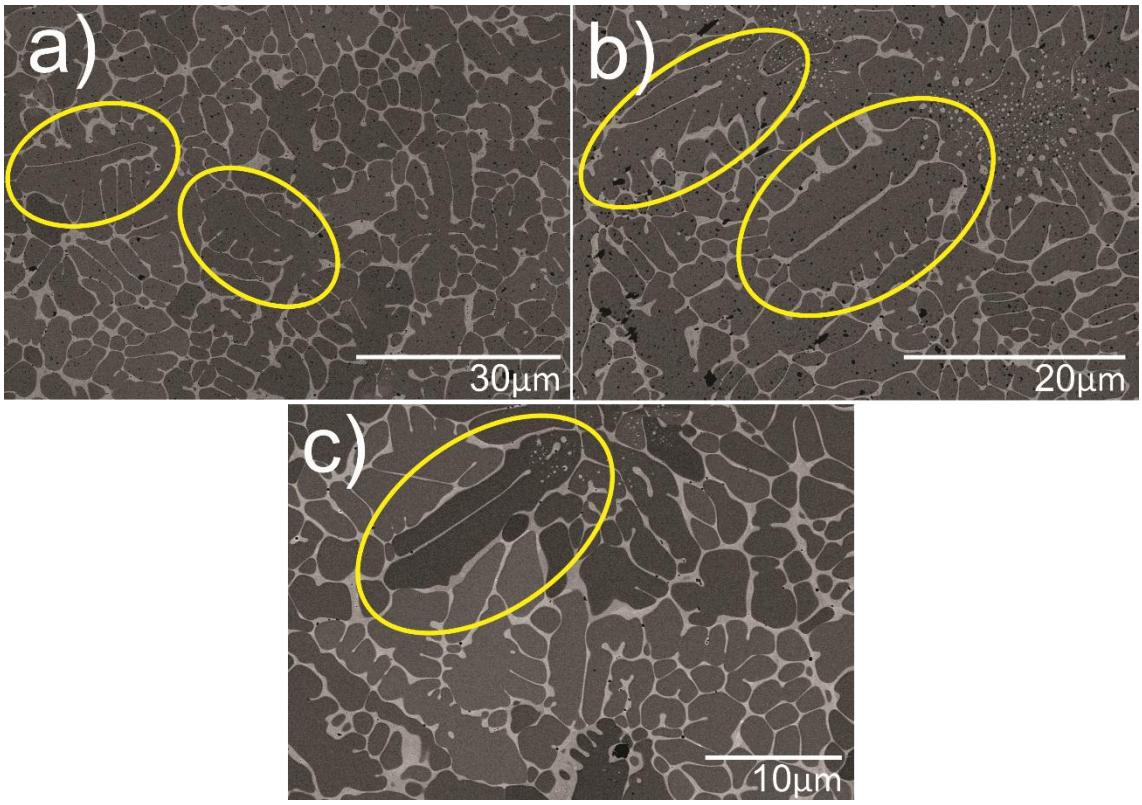

Figure 5.21 SEM BSE micrographs indicating examples of dendrite tip-splitting in partially grain refined droplets of drop-tube processed $CoCrCuFeNi_{0.8}$. Three separate droplets are shown from the (a-b) 150 – 106 µm, and (c) 106 – 75 µm size fractions featuring similar instances of splitting.

Figure 5.21a and Figure 5.21b show examples of dendrite tip splitting in the 150 – 106 µm droplet size fraction while Figure 5.21c shows an example in the 106 – 75 µm size fraction. In all cases, suggested instances of dendrite tip-splitting are indicated with yellow ovals. Such tip-splitting morphology is similar to that previously modelled by Mullis [36, 213] in alloy melts, and could result from undercooling induced growth instabilities in the alloy melt as the dendrites grow into the residual liquid. The re-melting of this “dendritic seaweed” may be what causes grain-refinement in $CoCrCuFeNi_{0.8}$ as has been predicted in pure Cu [215] and in some Cu-Ni alloys [216, 217].

5.4.5.2 Prevalence with droplet size/cooling rate

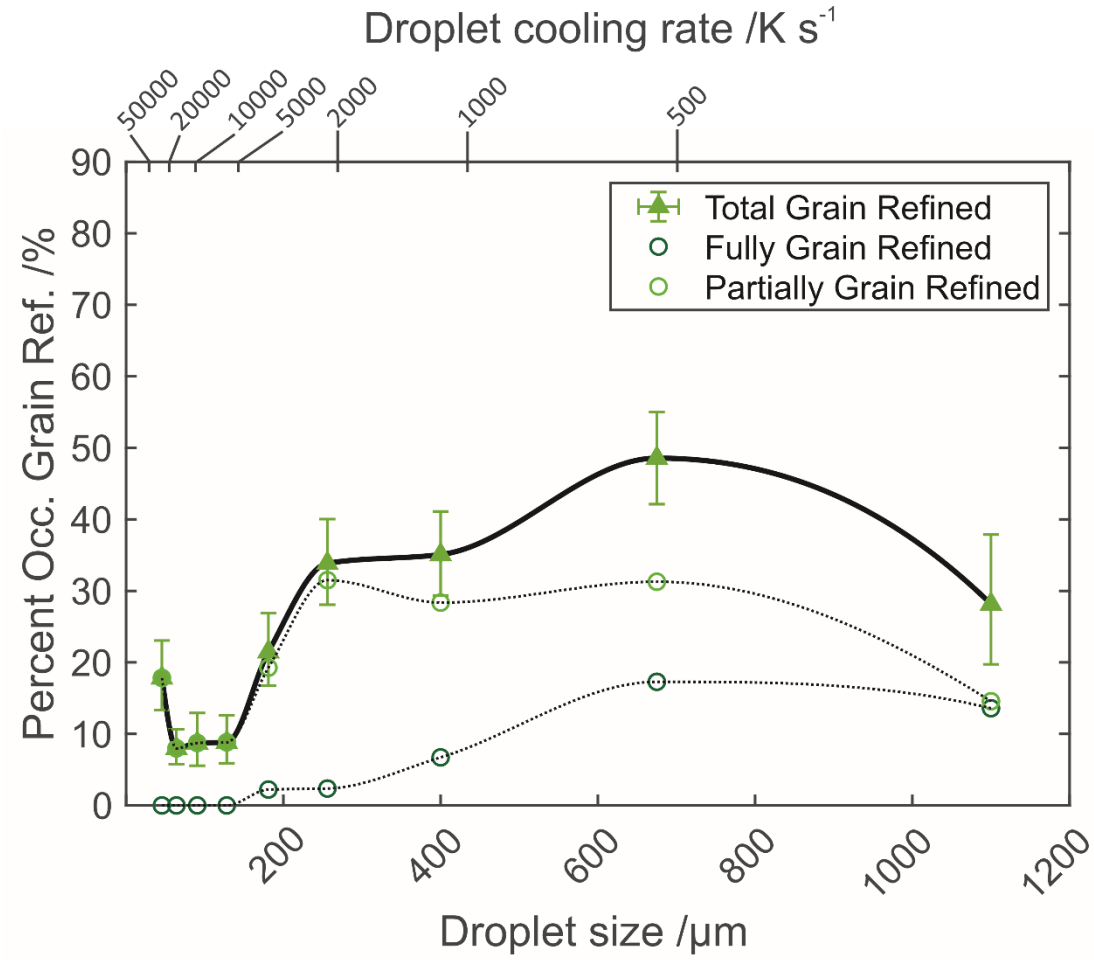

Figure 5.22 Occurrence rate of spontaneous grain-refinement correlated with droplet size and cooling rate for drop-tube processed $CoCrCuFeNi_{0.8}$ alloy. Subsets of the grain refined population are also shown, split into fully and partially grain refined droplets respectively.

Figure 5.22 shows the change in prevalence of partially grain refined (PGR) and fully grain refined (FGR) droplet microstructures as droplet size decreases and cooling rate increases. In total, the occurrence rate of such structures is highest at low to intermediate cooling rates, peaking at nearly 50% occurrence at cooling rates of around 600 K s^{-1}. From this value, the most precipitous drop occurs between 2000 K s^{-1} and 5000 K s^{-1} to an occurrence rate of below 10%. A small rise is observed at the highest cooling rates (above 20000 K s^{-1}) to just under 20%. Because of the inherent uncertainty in these measurements (calculated using Equation 4.15) it is not certain that this increase at the highest cooling rates is the representation of a true physical phenomenon or an artefact. The conclusion of a peak in occurrence at low cooling rates is comparatively more certain. In nearly all size fractions (with the exception of the two largest), the large majority of grain refined droplets are only partially refined. Examples of such PGR structures are given in Figure 4.8c and in Figure 5.20b and Figure 5.20c. Only in the largest droplets (850+ μm diameter) does the amount of fully

grain refined (FGR) droplets nearly equal the amount of PGR structures. FGR structures are only present in statistically detectable quantities below cooling rates of 5000 K s^{-1}. Above this, only PGR structures remain.

5.4.5.3 Grain refinement and solid-state dispersions

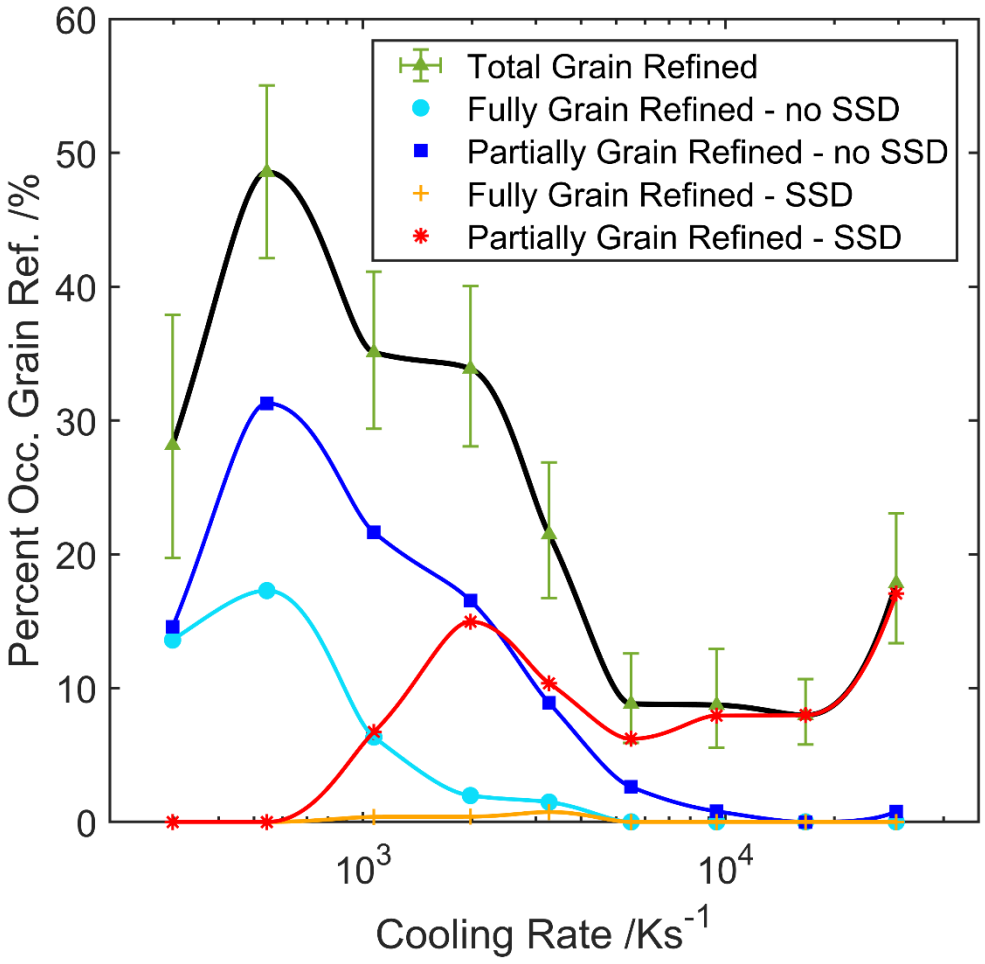

Figure 5.23 Prevalence of different structural combinations of grain refinement and solid state dispersions with cooling rate in droplets of drop-tube processed $CoCrCuFeNi_{0.8}$.

Figure 5.23 further subdivides the fully and partially grain refined structures in Figure 5.22 to factor in the possibility of the simultaneous occurrence of grain refined structures and solid-state dispersions in the droplet microstructures. Within these two structural categories, four distinct droplet structures are possible. These include partially and fully grain-refined droplets with and without dispersions present. This separation provides more detail regarding the types of grain-refined structures that predominate at various cooling rates. At lower cooling rates, where the bulk of grain refined structures are observed, very few of these refined grains contain Cu-rich dispersions. Dispersions begin to appear with some regularity in grain-refined droplets at cooling rates below 1000 K s^{-1}.

By the time cooling rates are above 3000 K s^{-1}, refined droplets featuring dispersions become more common than those that do not. Above cooling rates of 10000 K s^{-1}, grain-refined droplets that are observed almost all contain dispersions. Notably, grain-refined droplets that also feature dispersions are almost always partial, rather than fully, grain-refined droplets. The occurrence rate of fully grain-refined structures that also contain dispersions is vanishingly small across the entire range of cooling rates, and is only statistically significant at cooling rates between 1000 K s^{-1} – 3000 K s^{-1}.

5.4.5.4 Grain refined grain structural analysis

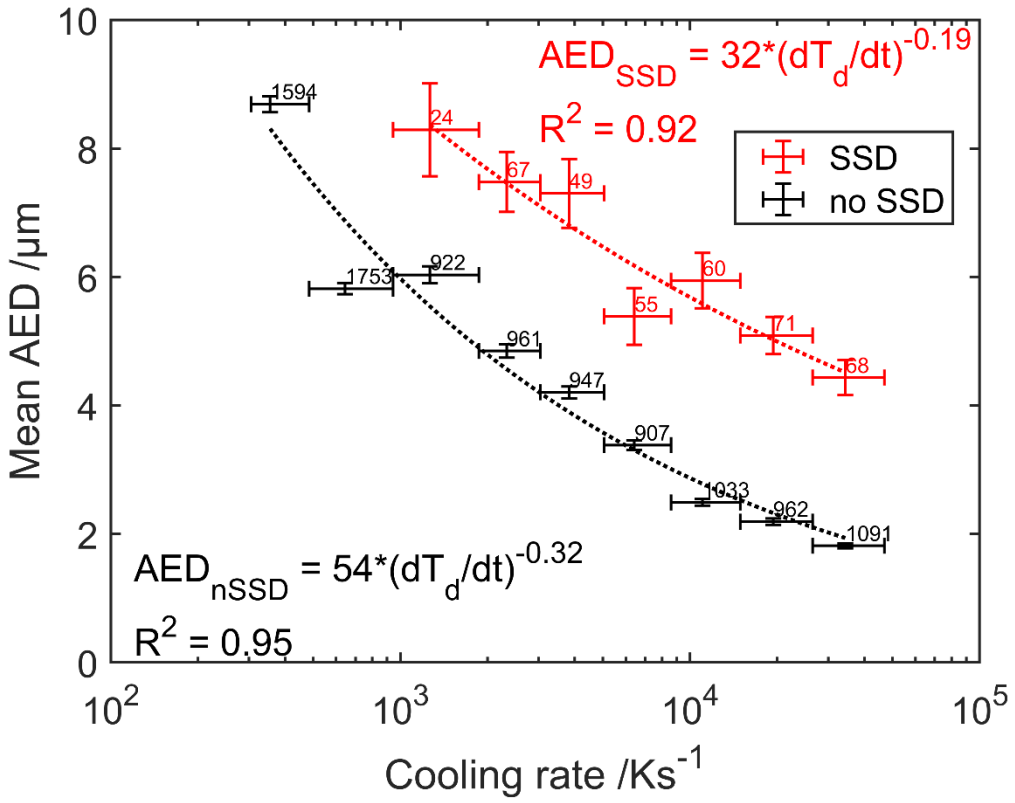

Figure 5.24 Correlation of mean area equivalent diameter of grain-refined grains with cooling rate in drop-tube processed $CoCrCuFeNi_{0.8}$. Grain refined grains which feature solid-state dispersoids form dataset plotted in red, while those which do not feature solid-state dispersoids form the dataset plotted in black. The number adjacent to each data point shows the number of refined grains from which the mean area equivalent diameter was calculated.

Figure 5.24 shows the change in average grain area equivalent diameter (AED) in grain-refined droplets with increasing droplet cooling rate. Within the droplets measured, the grains have been divided into two groups for which mean AED is calculated. These groups are the refined grains devoid of Cu-rich dispersoids (shown in black, AED_{nSSD}) and the refined grains which also feature Cu-rich dispersoids within (shown in red, AED_{SSD}). The values adjacent to each data

point represent the number of refined grains over which the mean value for AED is calculated. For example, in the 53 – 38 μm size fraction, 1091 of the grain-refined grains analysed were devoid of Cu-rich dispersoids, while 68 refined grains contained such dispersoids.

Here, it is clear that a rise in cooling rate results in a drop in the mean AED of grain refined grains in the droplets. This drop occurs regardless of whether or not the refined grains feature Cu-rich dispersoids. However, in each size fraction, the mean AED of refined grains with dispersoids in them is larger than the mean AED of the refined grains which do not feature dispersoids. The AED can be related to cooling rate through a power law function as shown. When they do not feature Cu-rich dispersoids, grain-refined grains in droplets experiencing the highest overall cooling rates are less than 25% the size of grain refined grains in the largest droplets which cool the slowest. Vertical error bars show the standard error (see Equation 4.28). Horizontal error bars represent the range of possible overall cooling rates achievable in each size fraction based on the lowest and highest droplet diameters from each size fraction.

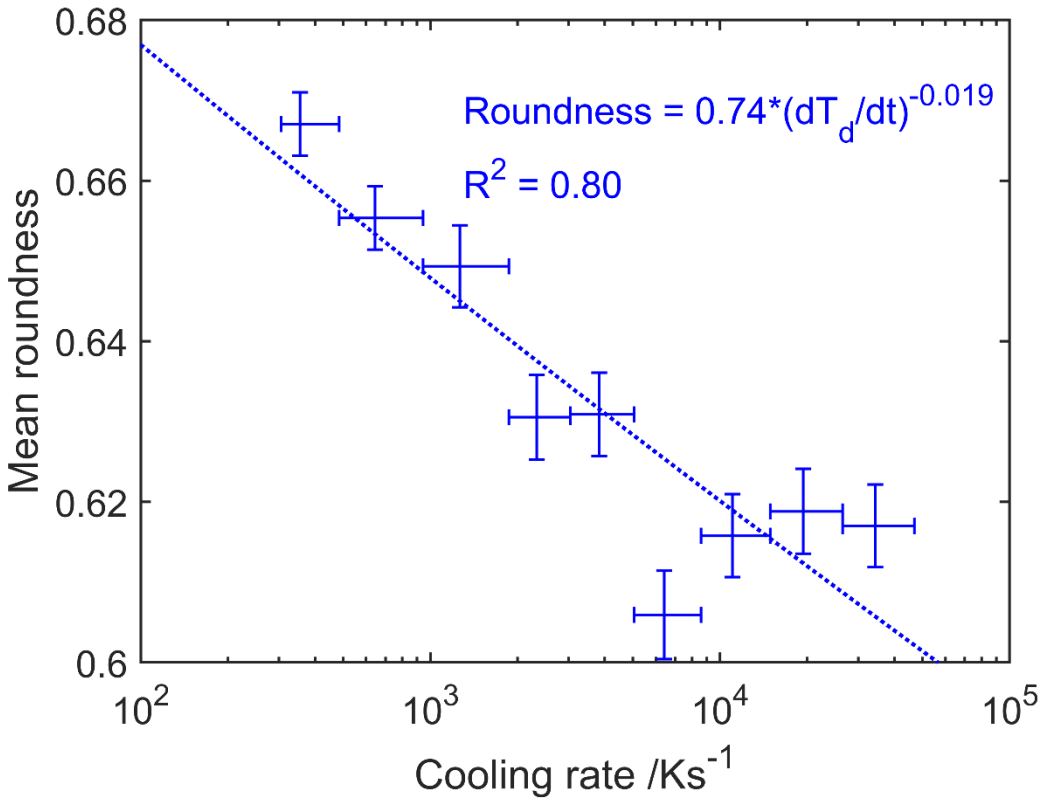

Figure 5.25 Correlation of mean roundness of grain-refined grains with cooling rate in drop-tube processed $CoCrCuFeNi_{0.8}$

Figure 5.25 shows a noticeable reduction in roundness in grain refined grains with increasing cooling rate. The roundness values can also be related to cooling rate via a power law relationship. Although the drop in mean roundness values is not high in real terms (a small decrease from 0.67 – 0.62 can be observed, representing a reduction less than 10%), a clear trend emerges in that grain refined grains from smaller droplets are less round than those of larger droplets. Vertical error bars show the standard error (see Equation 4.28). Horizontal error bars represent the range of possible overall cooling rates achievable in each size fraction based on the lowest and highest droplet diameters from each size fraction.

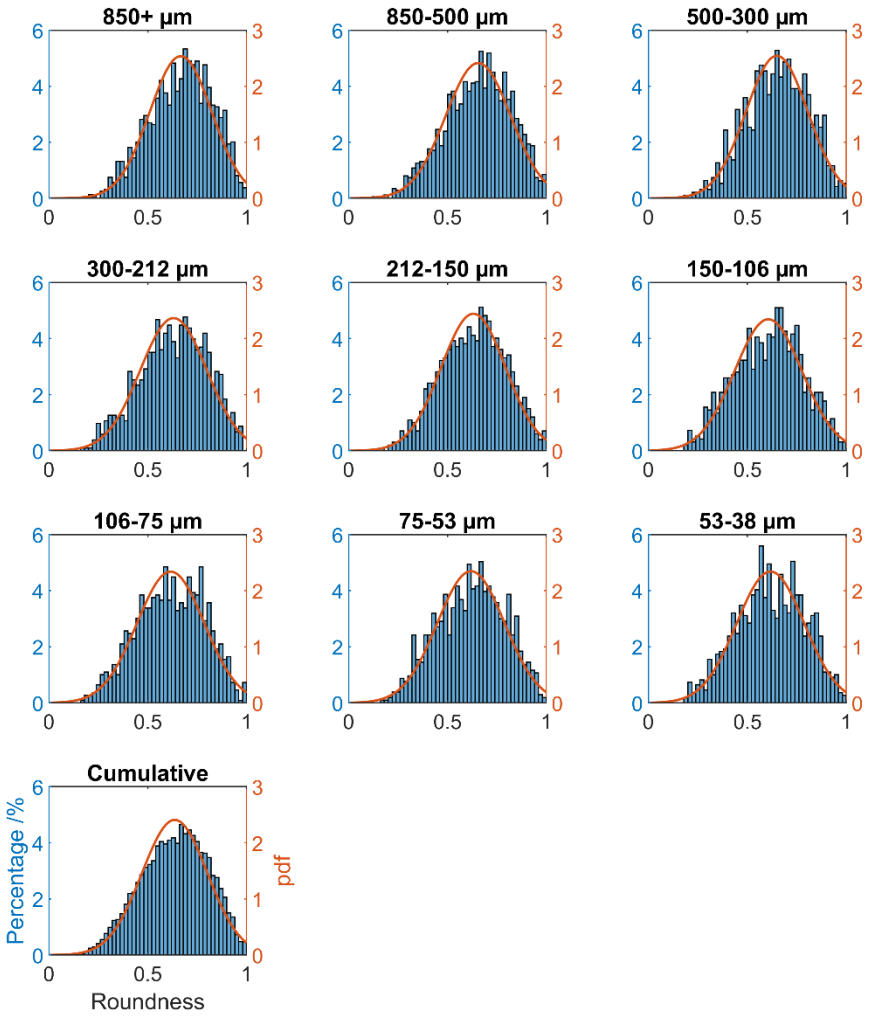

Figure 5.26 Histograms showing the spread in roundness values for each size fraction and superimposed theoretical normal distribution for each droplet size fraction dataset.

Figure 5.26 shows the histogram distributions for roundness values in each droplet size fraction and cumulatively for all droplets. For each data set, the theoretical normal distribution is superimposed over the histogram columns.

Visually, particularly in the largest size fractions, there are noticeably more droplets counted in the higher roundness values compared to the relevant normal distribution. Histogram columns in these high roundness values exceed the percentage value delineated by the normal distribution much more often than for lower roundness values. Furthermore, the distribution appears to undergo significant flattening compared to the normal distribution as droplet size decreases. For this reason, analysis of the skew and kurtosis values for each droplet size fraction may provide further understanding of the mechanisms of formation of grain-refined grains, or the interaction between such formation mechanisms and increasing droplet cooling rate.

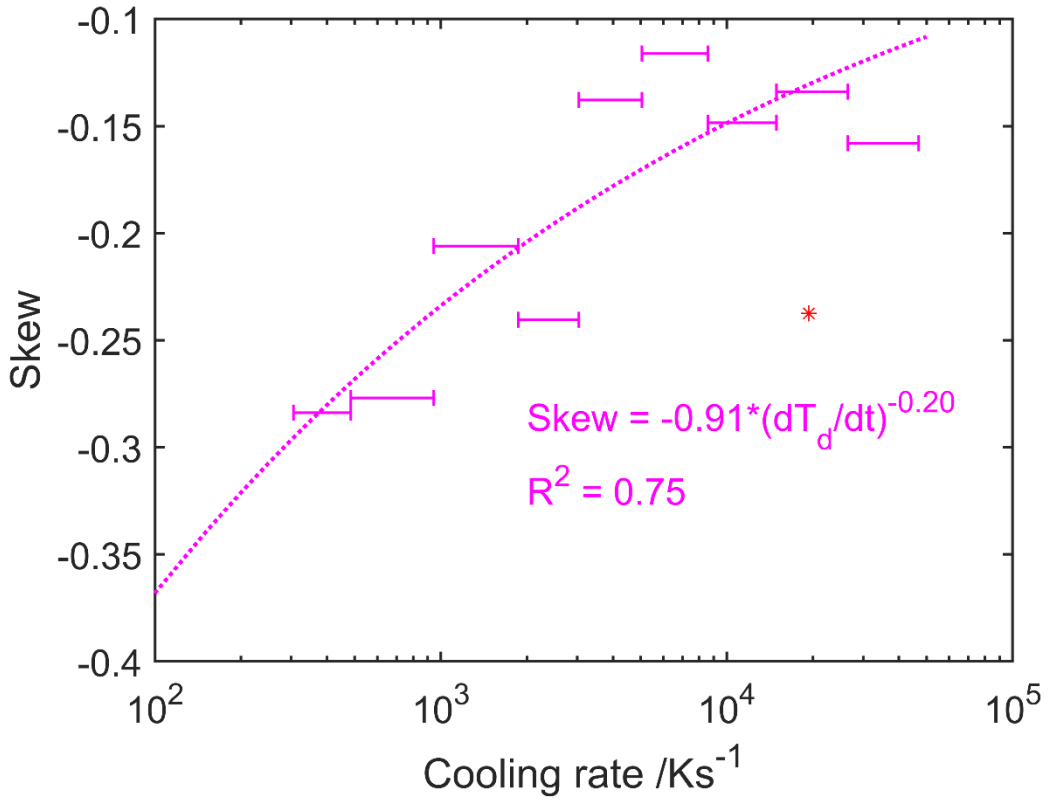

Figure 5.27 Correlation of skew in roundness values of grain-refined grains with cooling rate in drop-tube processed $CoCrCuFeNi_{0.8}$.

Figure 5.27 demonstrates that all size fraction data sets yield a negative skew value. This means that for all size fractions (and therefore, cooling rates), a more significant tail is present on the left hand side (i.e. at lower roundness values) than on the right hand side. In each size fraction therefore, more of the grain-refined grains are higher in roundness than the mean value compared to what would be expected if the data followed a normal distribution. The skew becomes less negative as cooling rate increases. In the largest droplet size fractions, with the highest (most negative) skew, a large proportion of the data is situated on the right hand side of the graph. Such a phenomenon is observable visually when comparing the histogram data to that of the superimposed normal

distributions in Figure 5.26, particularly for large droplet size fractions (lower cooling rates). In physical terms, this means that more droplets have a higher roundness value than would be expected if the data followed a normal distribution. Horizontal error bars represent the range of possible overall cooling rates achievable in each size fraction.

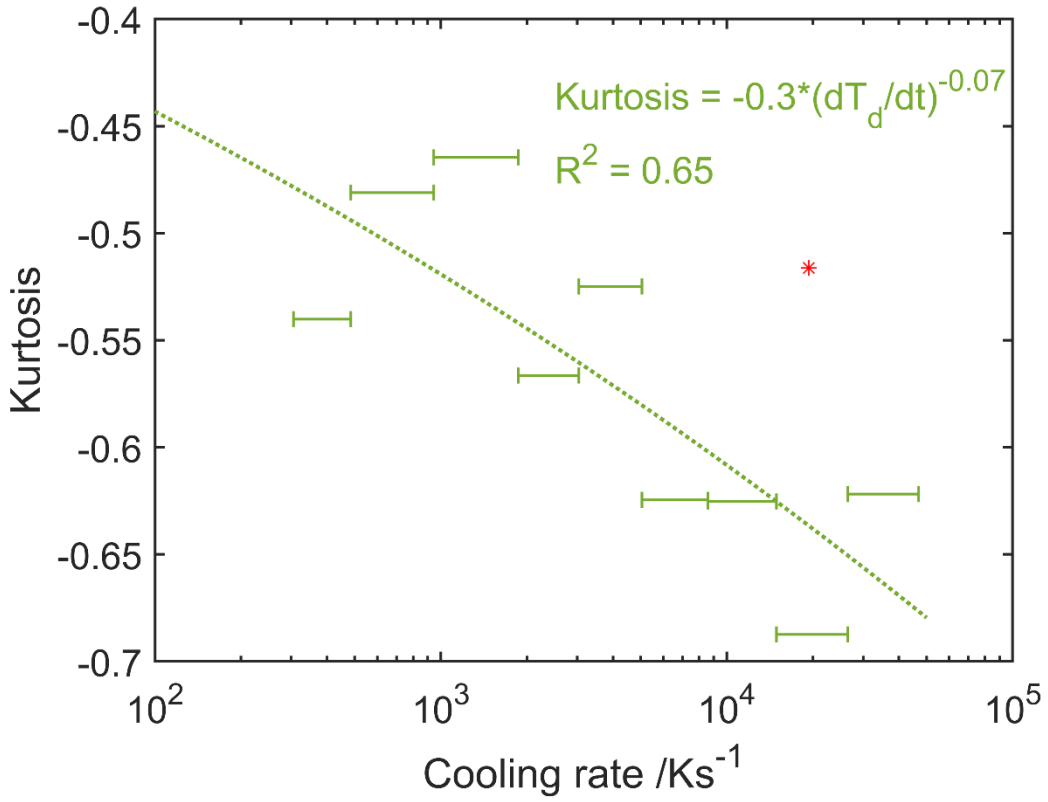

Figure 5.28 Correlation of kurtosis in roundness values of grain-refined grains with cooling rate in drop-tube processed $CoCrCuFeNi_{0.8}$.

Figure 5.28 indicates that kurtosis becomes more severely negative as cooling rate increases. Broadly, the kurtosis value for all size fractions is negative, meaning that all distributions are flatter when compared to the theoretical normal distribution for the dataset. A R^2 value of 0.65 means the power law correlation proposed is less representative of the data than it is for the skew, mean roundness, and mean AED. However, the general trend seems to be that spread of roundness values increases and the distribution flattens out more severely (compared to the relevant normal distribution) at high cooling rates than at lower cooling rates. Horizontal error bars represent the range of possible overall cooling rates achievable in each size fraction.

In the graphs of the trend of skew and kurtosis with cooling rate (Figure 5.27 and Figure 5.28 respectively). The red star data point shows the result of the skew/kurtosis calculation based on an initial data set that was gathered for the 75 – 53 μm droplet size fraction. The large difference in the skew/kurtosis value

from the values from other similar size fractions prompted a recalculation of this value based on an entirely different data set (i.e. a different set of droplets from which the grain refined grains were analysed). The latter data set was used in the formal analysis, the former was deemed an outlier.

5.4.5.5 Hardness testing

To aid with determination of a mechanism responsible for the extensive grain refinement in $CoCrCuFeNi_{0.8}$, the average Vickers microhardness was measured for dendritic droplets and grain-refined droplets across the largest four size fractions of drop-tube processed droplets (i.e. the size fractions in which, statistically, the most grain-refined droplets can be found). Droplets were selected which featured only a dendritic or a grain-refined structure respectively, without the competing effects of dispersions, phase-separation, or other microstructural features. The result of such an analysis is presented in Table 5.14.

Table 5.14 Average Vickers microhardness data for dendritic and grain-refined droplets of drop-tube processed $CoCrCuFeNi_{0.8}$

	Droplet size fraction /μm			
	850+	**850-500**	**500-300**	**300-212**
$HV_{0.01}$ (Dendritic)	223 ± 13	223 ± 13	212 ± 8	214 ± 15
$HV_{0.01}$ (GR)	214 ± 17	219 ± 8	203 ± 12	213 ± 15

The microhardness data in Table 5.14 shows that there is a negligible difference in average microhardness of droplets whether or not they consist of grain-refined or simple dendritic microstructures. For each particular droplet size fraction, the differences in microhardness values are accounted for by the standard deviation error. Additionally, there is also an insignificant difference in hardness values as droplet size decreases and cooling rate increases. However, it is important to note that across these droplet sizes, cooling rate increases by less than one order of magnitude (from about 300 K s^{-1} to 2000 K s^{-1}).

5.4.6 Liquid phase separated structures

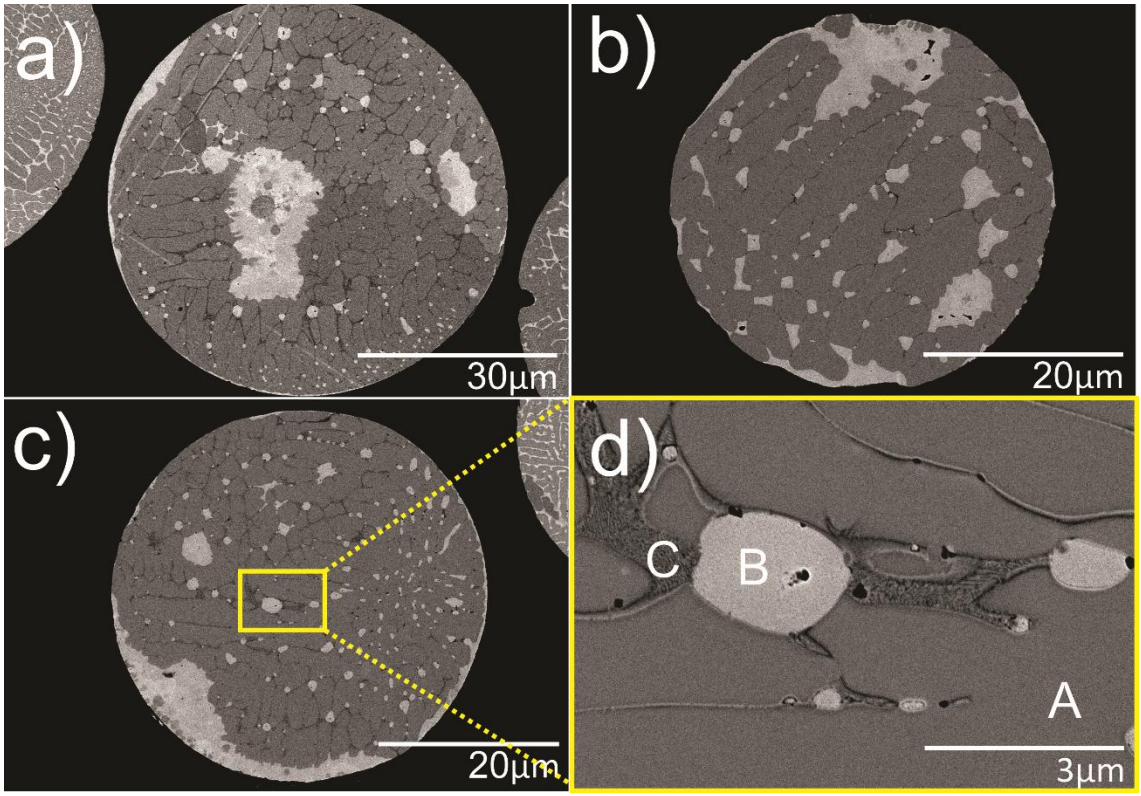

Figure 5.29 SEM BSE micrographs of example liquid phase separated structures in 53 – 38 µm size fraction of drop-tube processed $CoCrCuFeNi_{0.8}$. (a-c) examples of different configurations of the separated Cu-rich liquid in pockets throughout the microstructure or accumulating around the periphery of the droplet. (d) magnified rectangular inset in (c) showing detailed three-phase configuration of liquid phase separated droplets. Locations of EDX composition analysis on regions A-C are indicated.

Figure 5.29a-c shows examples of LPS structures that were obtained in the smallest droplet size fraction (53 – 38 µm) of the drop-tube processed alloy. Although the number of these LPS structures was deemed statistically insignificant based on the structural analysis presented in section 4.3, their occurrence at only the highest cooling rates merits discussion. Figure 5.29d shows a further magnified image of the droplet microstructure in Figure 5.29c. This image indicates that, contrary to previous microstructures that have been discussed, three main phases are present within the microstructure. SEM-EDX derived composition data for the phases marked (A), (B) and (C) are shown below in Table 5.15.

Table 5.15 SEM-EDX derived composition data for phases in liquid phase separated microstructures within droplets of drop-tube processed $CoCrCuFeNi_{0.8}$

	A	B	C
Cr /at%	23.25 ± 0.58	2.89 ± 0.35	47.22 ± 0.14
Fe /at%	23.95 ± 0.21	2.95 ± 0.77	19.43 ± 0.04
Co /at%	24.21 ± 0.36	2.81 ± 0.61	18.37 ± 0.13
Ni /at%	17.42 ± 0.34	6.39 ± 2.47	11.02 ± 0.23
Cu /at%	11.18 ± 0.41	84.96 ± 3.86	3.98 ± 0.02

As Table 5.15 shows, the three labelled phases in Figure 5.29d are compositionally distinct. Phases (A) and (B) are, respectively, CoCrFeNi-rich and Cu-rich, in much the same way as the two primary phases in the ingot sample and drop-tube processed droplets. However, phase (C) is different from any of the other phases analysed, being highly Cr-rich with minority additions of Fe and Co. Cr constitutes almost half of the phase in terms of at%. The microstructure therefore consists of three primary phases. These are CoCrFeNi-rich, Cu-rich and CrFe-rich respectively.

Similar structures were observed in equiatomic CoCrCuFeNi alloys studied by Liu et al. [143] and Guo et al. [146] who observed a Cr-Fe rich phase occurring in lightly undercooled CoCrCuFeNi equiatomic alloy in addition to the above dendritic and interdendritic phases. Liu et al. [143] observe rod-like Cr-rich phases at grain boundaries and within the Cu-rich interdendritic phase at lower undercoolings of about 80 K. As undercooling increases above 160 K, the Cu-rich phase between dendrites gains more spherical character, suggesting that LPS has now occurred. In $CoCrCuFeNi_{0.8}$, the spherical nature of the Cu-rich phase, as well as its accumulation either in the centre or the periphery of the droplets in question, points to a similar LPS phenomenon. The microstructures presented in Figure 5.29 closely resemble the structures obtained in the work of Liu et al. in $CoCrCuFe_xNi$ at intermediate undercoolings, with spherical globules of Cu-rich phase occurring in between CoCrFeNi-rich dendrites and a Cr-rich phase.

The three-phase microstructure is also observed by Guo et al. [146] in equiatomic CoCrCuFeNi undercooled by up to 100 K. Non-uniform pockets of the Cu-rich phase are present in the inter-dendritic regions. However, the authors suggest that these are likely the result of non-equilibrium solidification

rather than LPS. Only at an undercooling of 100 K does the Cu-rich interdendritic phase coalesce into spheres indicative of LPS. An even larger undercooling of 260 K causes any remaining residual Cu-rich phase between CoCrFeNi-rich dendrites to disappear. This is because it has been able to coalesce into Cu-rich spheres and/or the “egg-type” microstructure suggestive of complete LPS when held at this undercooling for sufficient time.

The clear coalescence of the Cu-rich phase in the centre and/or on the periphery of droplets of $CoCrCuFeNi_{0.8}$ suggest that the droplets may have been undergoing initial stages of LPS before solidification. Furthermore, a more even distribution of Cu-rich phase in LPS microstructures of drop-tube processed $CoCrCuFeNi_{0.8}$ (as opposed to a stratified “egg-type” microstructure) is likely due to the lessening of Stokes sedimentation during solidification in free-fall.

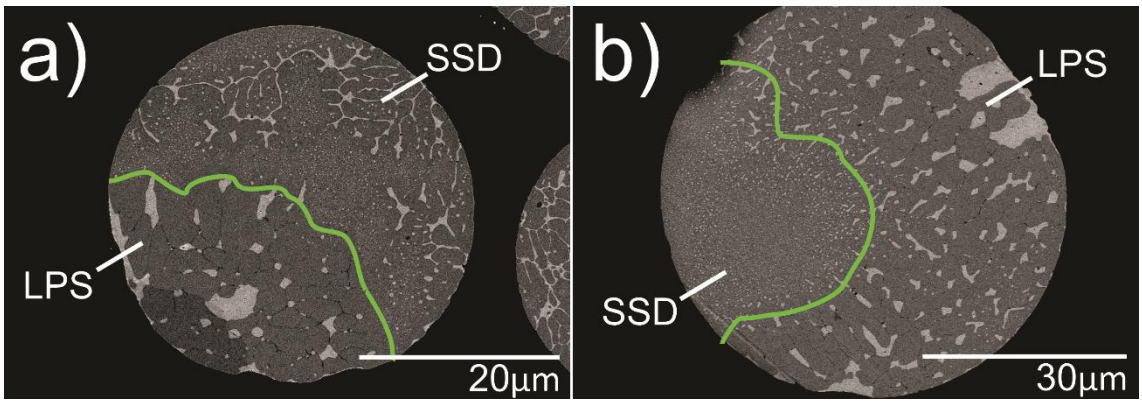

Figure 5.30 SEM BSE micrographs showing example hybrid liquid phase separation and fine dispersoid structures in 53 – 38 µm size fraction of drop-tube processed $CoCrCuFeNi_{0.8}$. (a) Liquid phase separation occupying minority volume fraction of droplet. (b) Liquid phase separation occupying majority volume fraction of droplet. Location of transition region between liquid phase separation and solid-sate dispersoid microstructures shown with a green line.

Figure 5.30a shows an example of a hybrid structure comprising an LPS structure as in Figure 5.29 and a dendritic solid-state dispersoid structure like those shown in Figure 5.10. Figure 5.30b shows a similar hybrid structure formed from an LPS structure and an LDOP structure as described in Figure 5.17. In both cases, the green curve delineates the approximate transition area between the two microstructures. The concurrence of these microstructures suggests that their occurrence is dependent on similar underlying phenomena. Furthermore, the fact that one structure does not occur in the same part of the microstructure as the other shows that the formation of one may inhibit the formation of the other, or that certain conditions which favour LPS may not be the same as those which favour dendritic solidification and formation of dispersoids within dendrite arms.

Chapter 6 – Discussion

6.1 Hume-Rothery parameters and alloy selection

Insofar as H-R parameters can be used to determine the likelihood of formation of a HEA featuring stabilised solid solutions, $CoCrCuFeNi_{0.8}$ seemed like a near perfect candidate in this regard. The values of all thermodynamic parameters, particularly the most important quantities δ, ΔH_{mix}^{Alloy} and ΔS_{mix}^{Alloy} fall within the ideal ranges presented based on numerous sources [112, 114-116]. Furthermore, the calculated value of VEC predicts that the solid solution will be FCC based on the work of Guo et al. [255]. The occurrence of solid solutions in lieu of intermetallic compounds, and the FCC structure of those solid solutions, have both been confirmed by crystallographic analysis on the drop-tube processed alloy in the TEM (see Figure 5.15 and Table 5.11). The absence of super-lattice spots in any of the SAED patterns indicated that no chemical ordering was present in the rapidly solidified samples, implying the presence of disordered FCC solid-solutions rather than ordered phases such as L_{12} or intermetallic compounds. The more positive enthalpy of mixing compared to the equiatomic alloy also suggested that LPS, provided it remained metastable, would be theoretically easier to achieve (i.e. a lower undercooling would be required to initiate LPS during cooling. Without the ability to directly measure the enthalpy of mixing of the alloy, and due to a lack of experimentally determined phase diagrams for complete thermodynamic modelling, the only prediction that can be made with a degree of substantiation is that the reduction in Ni content has caused a corresponding reduction in critical undercooling for LPS ΔT_{LPS}^{*} [135]. Because the equiatomic alloy has been observed to undergo LPS at an average of ΔT_{LPS}^{*} = 180 K, and $CoCrCuFeNi_{0.5}$ was experimentally observed to undergo stable LPS, the most viable prediction would be that metastable LPS occurs in this $CoCrCuFeNi_{0.8}$ at a critical undercooling ΔT_{LPS}^{*} < 180 K. The metastable nature of LPS in the system can be argued due to the a lack of observation of extensive macrosegregation and stratification throughout the arc-melted material. This is discussed further in section 6.2.1 below.

6.2 Arc-melted $CoCrCuFeNi_{0.8}$

On its face, it seems that the reduction in Ni in the alloy compared to equiatomic CoCrCuFeNi has not had a profound effect on the overall microstructure of the arc-melted ingot. A dendritic structure is prevalent throughout, featuring CoCrFeNi-rich dendrites in a Cu-rich interdendritic phase. Compositions of the dendritic and interdendritic phases, shown in Table 5.2, do not change

appreciably with a change in location in the ingot at which the measurement was taken. As with other similar alloys, the composition of both phases is explainable by referring to the enthalpy of mixing between each binary pair of constituent elements [134, 227]. This also confirms the theoretical analysis based on the binary enthalpies of mixing presented in Figure 5.1. In this two phase FCC structure, growing dendrites reject solute into the interdendritic liquid, which correspondingly becomes enriched in said solute. Cu, with its positive enthalpy of mixing with all of the other elements, is the prime candidate element to be rejected from growing dendrites into the interdendritic phase, particularly given that the other element pairs (e.g. Co-Fe, Cr-Ni etc…) have a negative enthalpy of mixing and are less likely to be rejected in large quantities into the interdendritic liquid during solidification. They are instead more likely to be retained in the dendritic phase. Having determined that Cu forms the massive bulk of the interdendritic phase, we can continue this logic to predict the composition of minor elements in the interdendritic phase. While all of the other constituent elements have a positive mixing enthalpy with Cu, Ni has the lowest positive value, and is predictably present in the largest quantities in the Cu-rich phase. At the other end of the spectrum, Cr, which has the largest positive mixing enthalpy with Cu, is present in vanishingly small quantities in the interdendritic phase. The opposite scenario prevails in the dendrites themselves. Cr is present in the highest quantities, while Cu forms the least significant portion in terms of atomic fraction.

Such a dendritic phase reflects what is predicted to form in this alloy at near-equilibrium solidification based on past literature. Generally the only significant difference compared to the equiatomic alloy is the small reduction in Ni content due to the change in composition for this study. However, it is clear that there are two significant differences between the arc-melted sample of this alloy and those of similar alloys in previous literature. One concerns the presence of a small but significant layer of Cu-rich phase at the bottom of the arc-melted sample. Such a morphology is an indication of macrosegregation in the alloy. The other is the presence of Cu-rich dispersoids appearing near the contact point between the arc-melted ingot and the water-cooled hearth of the arc-melter. These must therefore be discussed thoroughly.

6.2.1 Cu-rich phase layer

As can be seen in Figure 5.3, there is a noticeable accumulation of Cu-rich phase in certain parts of the bottom portion of the arc-melted ingot sample, which is evidence of macrosegregation occurring in the alloy. The immediate and most obvious explanation for this structural type is the occurrence of LPS.

However, there are certain morphological features that complicate this possibility. For example, this Cu-rich layer does not seem to be continuous across the bottom of the entire ingot cross-section as it is in arc-melted samples like that of Munitz et al. [133] in Figure 3.6. Instead, it is present in only select regions. Such inconsistent placement brings into question the suggestion that LPS was the phenomenon that caused this to occur. Perhaps there are other explanations for this. One possibility is improper mixing of the alloy during arc-melting, leaving an un-mixed Cu-rich region. This is unlikely given that the Cu-rich phase has the same composition as that of the Cu-rich interdendritic phase, with minority additions of Co, Cr, Fe and Ni (shown in Table 5.3). Another explanation is the heat from the alloy or the arc-melting process itself causing a small scale melting of the Cu in the water-cooled hearth and subsequent adherence to the bottom of the arc-melted ingot sample. This also seems rather unlikely due to the composition, and the interconnected nature of this large Cu-rich deposit and the web-like network of interdendritic Cu-rich phase propagating near the bottom of the sample. The most likely scenario is that the layer is caused by an accumulation of Cu-rich liquid during solidification. Due to the rather large difference in melting point between the CoCrFeNi-rich dendrites and the Cu-rich interdendritic phase (about 250 K based on DSC analysis in Figure 5.5), it is possible that the latter phase remained in the liquid state for long enough during solidification that it was able to trickle down through the solidifying dendritic structure after partitioning and pool near the bottom of the arc-melted ingot. Because the Cu-rich phase is more dense than the CoCrFeNi-rich phase, such a phenomenon is even more likely.

6.2.2 Cu-rich dispersoids

Perhaps the most noticeable difference between the morphology of the arc-melted sample of $CoCrCuFeNi_{0.8}$ and those achieved in similar alloys is the presence of CoCrFeNi-rich dendritic regions near the contact point between the ingot sample and arc-melter hearth which feature Cu-rich spherical dispersoids in their centre (see Figure 5.3and Figure 5.4). Such an occurrence does not seem to have been reported in previous literature on similar $CoCrCu_xFe_yNi_z$ alloys solidified using similar methods. As discussed in the previous section, these dispersoids only occur at specific points in the sample. The CoCrFeNi-rich dendritic phase seems to radiate outwards from the contact area and grow upwards from the bottom to the top of the sample, suggesting that this is one of the points from which the solidification phase transformation initiated in this sample. This area is very close to the contact point between sample and water-cooled hearth. As such, this region is likely to have experienced the highest cooling rates achieved in the arc-melter during preparation of the sample. The

liquid in the area is also therefore likely to have been more undercooled than adjacent regions prior to solidification. It is important, therefore to determine whether these dispersoids are the result of cooling rate or undercooling mediated phenomenon. The cooling rates achieved are likely to be relatively consistent across the full contact area between the ingot and the water-cooled hearth. The fact that a dispersed region occurs only in one specific area (shown in Figure 5.4) and not the full contact area between sample and hearth suggests that this phenomenon is undercooling mediated rather than purely cooling rate dependent. It is unlikely that this particular region would experience cooling rates much higher than the regions adjacent. However, because undercooling is stochastic rather than deterministic (as will be discussed at length later), undercooling may be drastically different in regions which are solidifying under very similar cooling rates.

If this is the case, the conditions under which this part of the material solidifies are very different from other regions of the arc-melted ingot. The difference in morphology makes this seem obvious, but cannot definitively point to what caused such a structural change. Because of the extensive contact between the alloy melt and the water-cooled copper hearth during the arc-melting process, it is odd that a high enough undercooling is reached to initiate the growth of metastable phases in any part of the sample. It is potentially the case that the copper hearth is a poor nucleant for the CoCrFeNi-rich dendritic phase. This has perhaps allowed certain regions of the ingot to achieve substantial undercooling before the solid nucleates. Such undercooling would therefore facilitate phase transformations that are not accessible during solidification at equilibrium.

As discussed in section 5.4.3.2, visual examination of the morphology suggests that these spherical Cu-rich dispersoids are precipitates caused by a decomposition reaction in the solid state. Given that they are located preferentially in the centres of CoCrFeNi-rich regions of the ingot microstructure, it is difficult to conceptualise a scenario in which these dispersoids formed as a result of a different phenomenon such as LPS. Were this to be the case, Cu-rich globules would be dispersed throughout the CoCrFeNi-rich regions with no preferential placement.

Most strikingly, EDX-derived composition analysis in manually defined regions such as region (A) in Figure 5.4 indicates that the average composition of the decomposed region in the arc-melted ingot is the same composition as the starting alloy (within the standard deviation error of the measurements). This similarity is shown in Table 5.3. Such a finding suggests that these regions consisted of a phase which had solidified without the partitioning of solute

(partitionless solidification) and had subsequently decomposed upon further cooling. It is therefore of prime importance to determine whether any partitionless solidification is the result of extreme kinetic solute trapping due to a massive increase in dendrite growth velocity, or if it is due to the thermodynamic argument presented by Baker and Cahn [64] which involves undercooling below the alloy T_0 temperature of the alloy at the specific composition used.

Perhaps drop-tube processing the alloy may provide some answers. Because these dispersoids are located in the area of the sample which is subjected to the highest cooling rates (and thus, likely the highest undercoolings), it is important to see if such Cu-rich dispersoids are present in the structure of drop-tube processed $CoCrCuFeNi_{0.8}$ droplets. The gradual reduction in size of the droplets is likely to result in an increase in cooling rate and a corresponding increase in average undercooling. In particular, the smaller droplets are likely to have experienced cooling rates orders of magnitude higher than the arc-melted ingot. Corresponding undercooling attained in some of these droplets is likely not achievable during arc-melting, and may enable access to a wider range of phase transformations during solidification.

6.3 Drop-tube processed $CoCrCuFeNi_{0.8}$

6.3.1 Intradendritic and large dispersoids

As discussed in sections 5.4.3 and 5.4.4, Cu-rich dispersoids have been found to occupy the solidified microstructure of a significant amount of droplets. Like in the arc-melted ingot, these dispersoids are found surrounded by CoCrFeNi-rich dendritic regions. In the case of dendritic droplets such as those of SCDD and MCDD structures, it is clear that these dispersions are preferentially located in the cores of dendrite arms. In LDOP and CDOP droplets (i.e. those with large dispersed regions) the dispersoids are found throughout these large regions and often extend into the cores of dendrites which originate from this large region (such a phenomenon is shown in Figure 4.8k as well as in Figure 5.17). EDX-derived average composition analysis of PDD dendrites in dendritic droplets (Table 5.7) and large dispersed regions (Table 5.12) shows that the average composition of these regions is the same as that of the original droplet. More detailed TEM composition analysis has shown that the dispersoids are highly Cu-rich (composition C in Table 5.10 and Table 5.13 for dendritic dispersoids and large dispersoids respectively) and share a similar composition with the Cu-rich interdendritic FCC phase that makes up one of the primary phases of this alloy. Correspondingly, the dendritic region between these

dispersoids (composition E in Table 5.10 and Table 5.13) is highly CoCrFeNi-rich.

Given that the average composition of the dispersed regions is the same as that of the original alloy, the presence of Cu-rich and Cu-lean regions in the final microstructure suggest a decomposition reaction has occurred in the dendrite cores and in larger dispersed regions of LDOP and CDOP droplets. The composition of the reaction products also suggests solute partitioning during this decomposition is similar to that occurring between the dendrites and interdendritic phases in arc-melted $CoCrCuFeNi_{0.8}$ and other similar alloys during solidification, with Cu-being preferentially rejected from the precursor phase [21, 134, 135, 145]. It is clear that the decomposition reaction is therefore occurring in the solid state to eliminate the Cu supersaturation. As the alloy cools, a precursor solidified phase become either metastable or unstable and decomposition is initiated to form the final dispersed microstructure. This precursor phase is of prime importance as it consists of a phase with a composition nearly identical to that of the original alloy. Clearly therefore, conditions are prevailing during the initial stages of alloy solidification where partitioning between the two primary phases observed in the arc-melted material is being severely hindered, and potentially, even completely inhibited. Partitioning of solute, discussed at length in Chapter 2, is therefore of primary importance to this analysis. However, because of the nature of HEAs, with many constituent elements in near-equal concentrations, it is often difficult to discuss phase transformations using the terms solute and solvent. To simplify analysis of solute partitioning in $CoCrCuFeNi_{0.8}$, the alloy is discussed as a pseudobinary Cu-HEA system. Because one of the primary phases in this alloy consists overwhelmingly of Cu, any discussion regarding solute during this discussion refers primarily to Cu.

6.3.1.1 Solid-state dispersions in dendrite cores

It is helpful to first narrow the focus on decomposed regions in dendritically solidified droplets. The locations where solid-state decomposition occurs in dendrites of drop-tube $CoCrCuFeNi_{0.8}$ appears to follow a very specific logic. Three initial assertions are listed below:

1. In a subset of dendritic droplets, certain conditions during solidification cause a solid-state decomposition reaction in some of the dendrite arms of that droplet. These conditions can be met in droplets of any size, but are met more consistently in smaller droplets.
2. In droplets where such solid-state decomposition occurs, the reaction occurs overwhelmingly in the primary dendrite arms.

3. Within dendrite arms where solid-state decomposition occurs, the reaction occurs overwhelmingly in the cores of the dendrite arms, away from the external edges adjacent to other phases.

The likelihood of solid-state decomposition is therefore maximised in the cores of primary dendrites in small droplets. To determine the reason for this, attention must be given to the nature of solidification in the drop-tube. In such an environment, the two primary variables to consider are cooling rate and the liquid undercooling prior to solidification. These are related, but notably different concepts. The primary difference is that cooling rate is a deterministic value whereas maximum undercooling achieved before solidification is a stochastic phenomenon. Equation 4.2 tells us that a droplet with a lower diameter will invariably cool faster than a larger droplet of the same material if environmental conditions are kept constant. However, this does not necessarily mean that the smaller droplet will always reach a higher undercooling prior to solidification. Rather than being deterministic, undercooling achieved in the liquid before solidification is a stochastic quantity. Droplets of similar diameters may therefore achieve drastically different undercooling. In general however, a higher cooling rate will, on average, facilitate a higher undercooling in a given droplet [18, 19, 259, 260]. This is due, in part, to the effect of melt subdivision. In order to achieve a high undercooling before solidification, heterogenous nucleation must be inhibited. However, nucleation of the solid phase is often initiated in the melt by entrained oxides, impurity elements and other contaminants, which limit the achievable undercooling. When a liquid metal is dispersed into droplets during drop-tube processing, the likelihood of an individual droplet containing said impurities decreases, which enhances the undercooling achievable before the first solid nucleates. This effect becomes more severe as the melt is subdivided into larger numbers of smaller droplets. Because of the stochastic nature of the undercooling however, it also remains possible, although unlikely, for much larger droplets to achieve the high undercoolings expected in smaller droplets. This can occur despite the fact that a larger droplet will cool much slower than a small one.

The statistical analysis of solid-state dispersion occurrence in Figure 5.8 shows that, although it is much less likely in the largest droplets, there are still some which feature regions in which solid-state dispersoids form. This suggests that the presence of these dispersoids is dependent on the droplet attained undercooling rather than the cooling rate. If the latter was true, it would be expected that no solid-state dispersoids would occur below a certain droplet cooling rate. This is not the case, at least for the range of cooling rates calculated in this experiment. Solid-state dispersions are present, to some

extent, in every droplet size. Furthermore, the noticeable step-change in occurrence of these dispersions between liquid phase cooling rates of 2000 K s^{-1} and 10000 K s^{-1} also indicates a dependence on undercooling. For a dependence on cooling rate, a more consistent, gentle increase in occurrence rate would be expected as the cooling rate increases. The conclusion to be drawn here is that the occurrence rate of solid-state dispersions appears to be undercooling dependent and that a critical undercooling is required to bring about their formation.

Further analysis of PDD, PDND and SDND dendrites (Table 5.7, Table 5.8, and Table 5.9 respectively) reveals that the average compositions of decomposed and undecomposed dendrites are essentially binary. In PDD dendrites, the average composition of the decomposed dendrite core is that of the original alloy liquid. Conversely, PDND and SDND dendrites are highly CoCrFeNi-rich and depleted in Cu, similar to dendrites viewable in the arc-melted ingot. However, an even more interesting finding lies in the trend in composition of each category of dendrite with cooling rate. The aforementioned tables indicate that in each case, there is no significant change in composition of these dendrites with droplet size. PDD dendrites remain at an average composition that is the same as that of the original liquid, and PDND and SDND dendrites maintain the same elemental ratio within the standard deviation. The only significant deviation from this trend is the increase in Cu content from about 10 at% to above 12 at% between SDND dendrites in the 212 – 150 μm size fraction and the 75 – 53 μm size fraction. This discrepancy can be accounted for by the interaction volume inherent in SEM-EDX composition measurements. Because the secondary dendrites are often shorter and thinner than the primary arms from which they branch, there comes a point where they can reduce in size to a width comparable to the interaction volume of the incident electrons used during EDX analysis. Because of this, the EDX detector may pick up signals from the dendrite, but also the interdendritic phase that surrounds it. Because the interdendritic phase is Cu-rich, an artificially high average Cu composition may result. The fact that a similar increase in Cu content does not occur in PDND dendrites of the 75 – 53 μm size fraction seems to confirm that this is the result of measurement error.

It is helpful to think of these compositions in terms of the solute partition coefficient k introduced in section 2.1.3 and 3.3.2. PDD dendrites, with compositions at the original alloy composition, appear to have a partition coefficient of $k = 1$. On the other hand, PDND and SDND dendrites, with composition similar to that of dendrites in the arc-melted sample, seemingly possess a partition coefficient near that at equilibrium ($k \cong k_e$). In all cases

however, the partition coefficient does not appear to change significantly with cooling rate. Solidification is either partitionless, or the same as during equilibrium solidification.

This binary selection of possibilities for dendrite composition is not easily explainable using the models of kinetic solute trapping described in sections 3.3.2 and 3.3.3. A partition coefficient of $k = 1$ removes the applicability of the CGM and its variants. The models of Sobolev [171] and Galenko [175], although allowing for the possibility of partitionless solidification, also predict a consistent increase in partition coefficient as dendrite growth velocity increases. This does not accurately reflect the apparent abrupt increase in partition coefficient that occurs in this alloy. The experimental evidence suggests that the change in average composition in decomposed areas of a dendrite and those which have undergone equilibrium partitioning is best approximated by a step change function (down to the 1 μm interaction volume of the EDX apparatus used to gather composition data). This points to an essentially binary set of compositions. Based on this, Figure 6.1 shows a comparison between the predicted behaviour of the solute (Cu) partition coefficient with increasing dimensionless dendrite growth velocity (V/V_{Db}) according to kinetic models and the apparent behaviour observed based on the experimental data. Here, the equilibrium partition coefficient k_e is assumed to be 0.155 (based on the ratio between the Cu content in regions C and E in Table 5.10). The initial concentration solute in the alloy X_0, is given by the atomic fraction of Cu in the alloy (0.208). The ratio of solute diffusion velocity in the bulk to that at the interface (V_{Db}/V_{Di}) is given the value of 1.25 based on the work of Galenko [175].

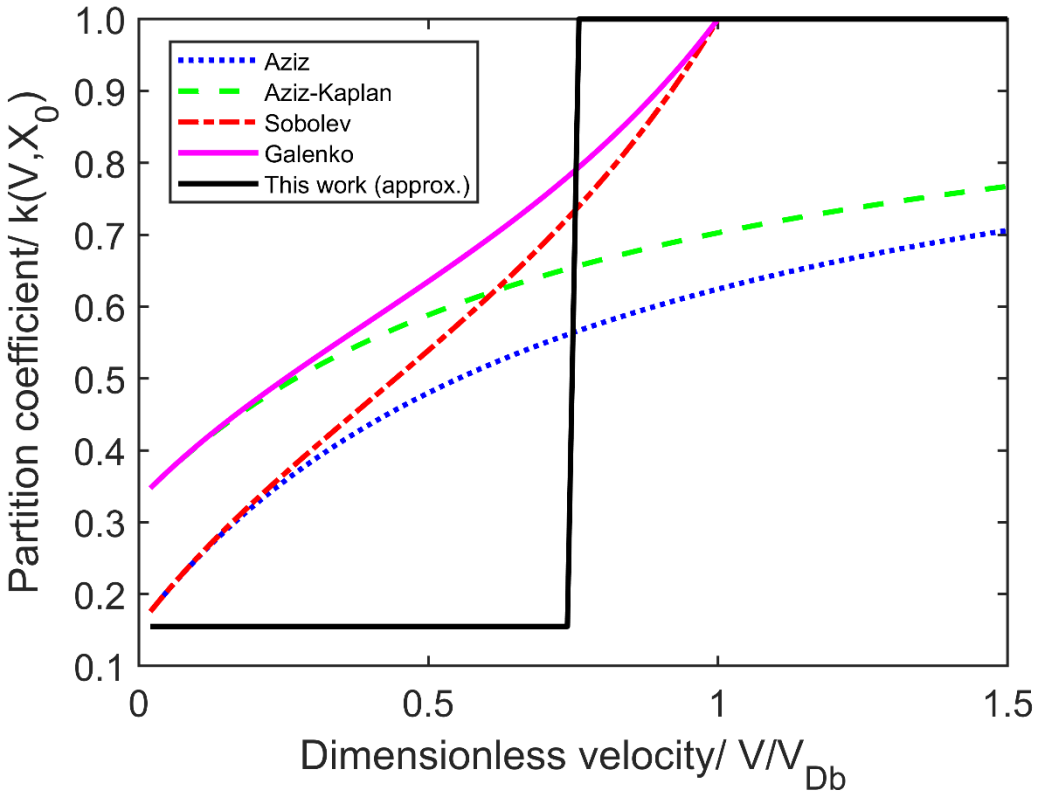

Figure 6.1 Comparison between kinetic models and experimental observation of step-change in partition coefficient of solute in drop-tube processed $CoCrCuFeNi_{0.8}$.

Figure 6.1 shows that it is difficult to account for an apparent step change in the partition coefficient through the use of kinetic models of solute trapping. It is therefore important to note that the location of the step change at a dimensionless velocity of 0.75 is assigned purely arbitrarily for the purposes of visual comparison. Because this step change is not dependent on reaction kinetics, the change in partition coefficient can likely occur regardless of prevailing dendrite growth velocity provided certain thermodynamic conditions are met. These are discussed further below. The nature of dendritic solidification in similar alloys also does little to support the argument for kinetic solute trapping. Past literature on solidification kinetics of the Co-Cr-Cu-Fe-Ni alloy family seems to reveal sluggish dendritic growth compared to the binary and ternary alloys that make up a subset of the 5-element HEA. A comparison of experimentally measured dendrite growth velocities in Co-Cr-Cu-Fe-Ni based alloys is shown in Table 6.1.

Table 6.1 Dendrite growth velocities in equiatomic Co-Cr-Cu-Fe-Ni family alloys with increasing undercooling

Alloy	$V_{(\Delta T=50\ K)}$	$V_{(\Delta T=100\ K)}$	$V_{(\Delta T=200\ K)}$	Source
CoFe	~1	~5	~20	[261]
CoNi	~4	~15	~50	[262, 263]
CoFeNi	~4	~15	~35	[263]
CuFeNi	2.9	8.1	22.6	[264]
CoCrFeNi	0.0001	0.006	0.36	[147]
CoCrCuFeNi	0.02	0.12	0.81	[147]
	0.02	0.15	1	[145]
	0.02	0.27	3.51	[24]

As shown in Table 6.1, measured dendrite growth velocity in binary and ternary alloys is often larger than corresponding velocities in quinary CoCrCuFeNi by between one and two orders of magnitude at comparable undercooling.

Given that the drop-tube technique used in this experiment precludes the direct measurement of dendrite growth velocity, it is difficult to confirm whether the growth characteristics are the same as the equiatomic alloy. Experimentally determined dendritic growth velocities can also be highly variable. One example is the work of Andreoli et al. [25] who found dendritic growth velocities in CoCrFeNi that were more comparable in magnitude to that of binary and ternary alloys rather than the extremely low values calculated for CoCrCuFeNi [24, 145, 147]. Furthermore, it has been argued that it is the presence of specific elements such as Cr [263], and not the large amount of elements in the alloy, that is responsible for comparatively sluggish dendritic growth in Co-Cr-Cu-Fe-Ni based alloys. However, the exact cause of this sluggish growth is secondary to the overall argument presented here. Because the $CoCrCuFeNi_{0.8}$ alloy studied is both a quinary alloy, and contains a substantial amount of Cr, it is a reasonable conclusion that dendritic growth velocities in the material will be comparable to those in the equiatomic alloy at similar undercooling. These are likely sluggish compared to similar binary and ternary alloys. Given that significant kinetic solute trapping requires dendrite growth velocities to approach the velocity of solute diffusion across the interface and/or through the bulk

material, the sluggish dendrite growth kinetics in CoCrCuFeNi make it unlikely that this is the true cause of solute partitioning behaviour in this case.

The kinetic solute trapping phenomenon largely fails to explain the severity or consistency of solute trapping behaviour observed in rapidly solidified $CoCrCuFeNi_{0.8}$. An alternative argument must therefore be explored.

The thermodynamic argument regarding the T_0 temperature presented in section 2.1.3 is considered the most likely explanation of the behaviour in this alloy. In this case, undercooling an alloy above a critical value ΔT_{PS} causes the temperature of the alloy to decrease below the equilibrium T_0 temperature defined by the phase diagram. Because of this, the phase change from liquid to a solid of identical composition results in a reduction in Gibbs free energy. Below the T_0 temperature therefore, partitionless solidification is thermodynamically possible [64]. The partition coefficient k is equal to unity ($k = 1$) and the dendrite growth is controlled by the diffusion of latent heat rather than the diffusion of solute. This argument has been used extensively to explain the occurrence of chemically partitionless solidification in binary alloys [162, 176-181] as well as HEAs [182-185].

The key benefit of the thermodynamic argument is that it removes the requirement of attaining a specific (and usually rather high) dendritic growth velocity as a prerequisite for partitionless solidification. In reference to a drop-tube study, partitionless solidification could conceivably occur in any droplet as long as the droplet undercooling reaches the critical value ΔT_0 and the liquid temperature is therefore at or below T_0 when solidification is initiated. Given the stochastic nature of undercooling, it is possible for large droplets to achieve this level of undercooling in rare cases. This is likely why small partitionless solidification regions are observable even in some large droplets. Following this argument, decomposed regions in dendrite cores of the droplets analysed were likely preceded by a region devoid of solute partitioning which solidified when the alloy was cooled below T_0. Importantly however, the solidification process is accompanied by a necessary release of latent heat as the liquid transforms into solid. This causes the temperature of the remaining liquid to increase (recalescence). If enough heat is released at a high enough rate to cause the residual liquid temperature to rise back above T_0, the thermodynamic conditions for partitionless solidification are no longer satisfied. In this case, solute partitioning would resume and subsequent dendrite growth with fall under a solute-diffusion control regime. This is indeed what we see in the $CoCrCuFeNi_{0.8}$ droplets. No droplet solidifies fully in a partitionless manner, and all droplets that feature solid-state dispersoids are invariably a combination of

regions which have solidified with no solute partitioning and surrounding regions which have partitioned in terms of solute as would occur at equilibrium.

Now that the conditions governing partitionless solidification in drop-tube processed $CoCrCuFeNi_{0.8}$ have been discussed, we can use these arguments to explain observed trends regarding partitionless solidification and the occurrence of decomposition reactions that result from this phenomenon. A higher percentage of the smaller droplets feature these dispersions (see Figure 5.8) because, on average, a higher percentage of smaller droplets will achieve undercoolings below T_0 before the onset of solidification. This is due to the high cooling rates and the effect of phenomena such as the aforementioned melt subdivision.

The area of the exposed droplet face occupied by these dispersions also increases with increasing cooling rate (see Figure 5.12). Such a trend indicates that the volume fraction of solid that solidifies in a partitionless manner is increasing with increasing cooling rate. A trend such as this emerges because smaller droplets, which cool much faster, are more likely to experience undercooling further below T_0 than larger droplets. Because of this, a comparatively larger volume of the droplet can undergo partitionless solidification before the release of latent heat raises the temperature of the remaining liquid above T_0 and initiate solute partitioning. The further the droplet is undercooled below T_0, the higher the volume percentage of liquid in the droplet that can solidify in a partitionless manner.

Mathematically, the volume of a dendritic droplet featuring solid-state dispersoids in some dendrite cores is made up of two principle volume fractions: the fraction of material which solidified in a partitionless manner f_0, and that which solidified via solute prtitioning f_p. Together, these volume fractions make up the entirety of the droplet. Equation 6.1 describes this balance.

$$f_0 + f_p = 1 \tag{6.1}$$

In partitionless solidification mediated by the T_0 temperature, the fraction of the solid which solidifies partitionlessly, f_0, is given by the ratio of the magnitude of undercooling below the T_0 temperature (defined as ΔT_0) and the hypercooling limit ΔT_{HYP}. This is shown in Equation 6.2. The hypercooling limit is the undercooling at which there is no longer a solidification plateau time following recalescence during solidification [265]. It is defined mathematically by the ratio between the latent heat of fusion of the alloy and the specific heat capacity of

the alloy [266] (here we can assume a constant value for specific heat capacity $c_{p(eff)}$). The mathematical definition for the hypercooling limit is shown in Equation 6.3.

$$f_0 = \frac{\Delta T_0}{\Delta T_{HYP}} = \frac{T_0 - T}{\Delta T_{HYP}} \quad 6.2$$

$$\Delta T_{HYP} = \frac{L_{f(alloy)}}{c_{p(eff)}} \quad 6.3$$

Equation 6.2 essentially shows that once the alloy is undercooled below the T_0 temperature, the volume fraction of the undercooled liquid which will solidify in a partitionless manner depends on how far further below T_0 the temperature is reduced. The further the minimum temperature T is below T_0 (i.e. the higher the value of ΔT_0) the more latent heat release is necessary to heat the residual liquid back above T_0 once solidification begins. If more latent heat must be released, the volume of the droplet which must solidify to release this heat increases as well. Given that solidification will be initiated below T_0, any solidification that occurs (at least initially) will be partitionless. Hence, as we undercool further below T_0, a higher volume fraction of the alloy can solidify partitionlessly. f_0 will therefore increase. In dendritic droplets of $CoCrCuFeNi_{0.8}$, the remaining fraction f_p of the droplet solidifies via solute partitioning once the temperature is raised back above T_0. This fraction f_p can therefore be determined via a rearrangement of Equation 6.1. As the fraction of the alloy solidified partitionlessly increases, the remaining volume, which solidifies via solute partitioning, will decrease. The manifestation of this phenomenon causes the trend we observe in Figure 5.12, where the volume fraction of droplets solidified partitionlessly, f_0, is increasing with increasing undercooling. The undercooling is, on average, being increased by increasing cooling rate in the drop-tube.

As has previously been discussed, solid-state decomposition is more likely in very specific regions, usually the core regions of primary dendrites. What is so important about these regions? Why are these areas more likely to be sites for partitionless solidification? The likely answer is simply that these are the regions of the droplet which solidify first. They are therefore much more likely to solidify from a liquid that is undercooled below the critical undercooling required for

partitionless solidification. The primary dendrite will always form before the secondary and tertiary branches of the same dendrite. It is therefore more likely that the primary dendrite solidifies into a liquid undercooled below T_0. By the time secondary and tertiary branching begins, the liquid temperature may have risen to a point where partitionless solidification no longer occurs. The logic is the same when discussing the presence of dispersions in the dendrite cores and not on the periphery adjacent to the interdendritic Cu-rich phase. Dendrite growth during solidification is accompanied by coarsening of the already formed dendrites. A clear “buffer zone” is visible where solute partitioning has resumed in the area of the dendrite trunk adjacent to the Cu-rich interdendritic phase, which structurally represents the moment when solute partitioning resumed during dendrite coarsening.

Although partitionless solidification is likely the result of thermodynamic conditions, the solidification kinetics become more relevant in explaining the lack of change in composition of PDND and SDND dendrites (which have undergone solute partitioning during solidification) with cooling rate. As discussed above, dendritic growth in $CoCrCuFeNi_{0.8}$ is predicted to be sluggish compared to similar binary and ternary alloys. Because dendritic growth velocity is likely slow compared to the velocity of solute diffusion, even at high undercoolings, it is unlikely that appreciable kinetic solute trapping will occur. Therefore, a minimal composition difference will be found between undecomposed dendrites of the larges and smallest droplets. The partition coefficient will therefore remain close to that measured at equilibrium ($k \cong k_e$) until undercooling increases above ΔT_{PS} in which case $k \to 1$.

Although the behaviour of this alloy seems to be explainable, it is puzzling that such Cu-rich dispersoids have not been observed in other heavily undercooled alloys of similar composition. This is particularly true given the high occurrence rate of these solid-state dispersoids in the droplets produced in this study. Previous glass-fluxing and EML studies involving the undercooling of $CoCrCu_xFe_yNi_z$ do not report extensive observation of partitionless solidification or of dispersed structures in the alloy microstructure [143-148]. The most obvious reason for this discrepancy is the ability of the alloys processed in previous studies to undergo a phase separation in the liquid state prior to solidification. In each case, the LPS causes the formation of Cu-rich and CoCrFeNi-rich phases in lieu of a single phase. The CoCrFeNi-rich phase, after LPS, is already very depleted in Cu prior to solidification. When both of these phases then solidify upon further cooling, they likely do not provide the conditions necessary for phase decomposition to occur. Further cooling is unlikely to provide the driving force necessary to cause the remaining Cu in this

phase to precipitate out of solution. This would likely be the case even if the phase separated liquids both solidified in a partitionless manner after LPS. A lack of remaining Co, Cr, Fe and Ni in the Cu-rich phase also potentially reduces the likelihood of decomposition in this phase as well.

Based on this discussion, we can begin to suggest some conditions which may favour partitionless solidification in HEAs. The most important consideration is the use of a solidification technique that routinely allows the alloy liquid to be undercooled below T_0 for the chosen composition. This is the fundamental thermodynamic condition for partitionless solidification. Additionally, this may be favoured by sluggish dendritic growth in the alloy, even at high undercoolings, which limits the extent of kinetic solute trapping. A low atomic size difference and an enthalpy of mixing which is not highly negative are important characteristics for the stabilisation of solid solutions in HEAs [3]. They are also conditions which correspondingly inhibit the formation of metallic glasses. Ordinarily, one would expect that addition of increasing numbers of elements to an alloy might make glass formation more favourable, particularly if rapid solidification techniques are used [96]. However, Inoue [267] notes that a large atomic size difference and a highly negative enthalpy of mixing are also important conditions for achieving glass formation. Such conditions are not satisfied by $CoCrCuFeNi_{0.8}$, which has a predicted enthalpy of mixing of -3.70 kJ mol^{-1} and an atomic size difference of only 1.05 % (see Table 5.1). The very conditions which favour the formation of solid-solution based HEAs are likely those which simultaneously lower glass formation potential. Finally, the use of rapid cooling techniques such as drop-tube processing may also be beneficial for the study of partitionless solidification given the ability of such techniques to inhibit competing phase transformations such as LPS. This is discussed further in section 6.3.3.2 below.

6.3.1.2 Large dispersions independent from dendrite cores

The initial structural classification process made the distinction between droplets with dispersions confined to dendrite cores and refined grains, and droplets with large dispersions on the periphery or in the centre which could not be directly attributed to specific dendrites. It was initially thought that these LDOP and CDOP droplets were caused by LPS and the initial formation of Cu-rich minority phase droplets before the onset of solidification.

In particular, these dispersoids were hypothesized to be the result of LPS occurring at high cooling rates and causing the formation of fine dispersions. It was thought that, because the Cu-rich phase occupied only a small minority volume fraction of the final droplet microstructure, (below 15%), there would not

be enough time for nucleated minority phase droplets to migrate and coalesce via Marangoni convection before complete solidification of the droplet in question. This would explain the finely dispersed structure, which have been extensively observed in drop-tube processed alloys undergoing stable [125] and metastable [126, 128] LPS. However, the overall lack of evidence of LPS occurring extensively in this alloy after drop-tube processing threw this conclusion into doubt. Even if the large dispersions were considered LPS structures, they occupy a maximum of only 8 % of droplets in any given size fraction (see Figure 5.16). SEM analysis (see Figure 5.17 and Table 5.12) shows that the dispersed regions in LDOP and CDOP droplets also have an average composition that is the same as the original alloy, indicating potential partitionless solidification. Confoundingly, a finely dispersed LPS structure that had subsequently solidified would conceivably also have an average composition equivalent to the starting alloy, meaning more evidence is needed to differentiate between the two possibilities and determine the root cause of the microstructure. This evidence lies in the TEM-EDX derived composition data. This was undertaken for a droplet exhibiting a LDOP structure (see Figure 5.19and Table 5.13) for comparison to the results of equivalent analysis done for a droplet with a SCDD dendritic structure. The compositions of the Cu-rich dispersoids and CoCrFeNi-rich phase between them (compositions C and E respectively) are similar regardless of the droplet analysed. If these droplets had formed through a different mechanism (i.e. one via LPS and one via solid-state decomposition), it seems rather unlikely that they would consist of similar dispersed morphologies and that the corresponding separated phases would be largely of the same composition. For these reasons, it is argued that the intradendritic dispersions and the large dispersions are morphologically different manifestations of the same solid-state decomposition phenomenon. This equivalence is made in similar studies from the literature. For example, McKeown et al. [177, 178] who solidified droplets of U-6wt%Nb alloy via a centrifugal atomisation technique observe intradendritic decomposed structures and large decomposed structures occupying a significant portion of the exposed droplet face (see Figure 3.11). In both cases, the average composition of these regions is the same as that of the original alloy, indicating partitionless solidification occurred extensively in this alloy. The large dispersion areas occupy a larger percentage of the overall droplet area as undercooling increases. This is comparable to the increase in the area occupied by intradendritic dispersoids observed in $CoCrCuFeNi_{0.8}$ with increasing cooling rate (see Figure 5.12). However, the relationship between the occurrence rate of these large decomposed areas with cooling rate is not discussed.

A discrepancy therefore lies in the trend in structural occurrence of intradendritic dispersoids and large dispersions, even though they seem to be separate representations of the same reaction pathway. Figure 5.8 shows that the percentage occurrence of dispersoids in dendrites and refined grains seems to increase nearly monotonically with increasing cooling rate. Conversely, Figure 5.16 seems to conclude that the occurrence rate of larger dispersions peaks at intermediate cooling rates, decreasing as droplets reach their smallest size. The most likely explanation is uncertainty in the process of structural determination. This is perhaps due to the comparative difficulty in determining the critical size of a large dispersion required to define a droplet structurally as LDOP/CDOP. Nucleation points for dendritic growth on the droplet periphery are sometimes large enough to be classified as large dispersions rather than simple intradendritic dispersoids. The reduction in size of the droplets analysed also makes it more difficult to make this distinction with full certainty. Furthermore, the low number of droplets classified as featuring large dispersions in general increases the inherent uncertainty in measurement of their occurrence with cooling rate (this is represented graphically in Figure 5.16 by the much larger error bars bracketing each data point).

6.3.1.3 Dispersion formation mechanisms

The mechanism of formation of these dispersoids must now be discussed. At a fundamental level, the occurrence of a decomposition reaction in the solid necessitates the presence of a miscibility gap in $CoCrCuFeNi_{0.8}$ in the solid state (i.e. below the alloy liquidus temperature). TEM analysis has shown that $CoCrCuFeNi_{0.8}$ is a solid solution alloy with a dual-phase FCC crystal structure. Due to the current lack of comprehensive experimentally derived data on phase behaviour of the alloy studied, the CALPHAD method can therefore be utilised to model the pseudobinary $CoCrFeNi_{0.8}$-Cu (i.e. HEA-Cu) phase diagram assuming an FCC crystal structure. The behaviour of this five component alloy was estimated through the weighted average of binary interaction parameters between each of the component element pairs in a FCC crystalline phase. These binary interaction parameters were gathered from SGSOL solutions database version 4.42 which were compiled by Scientific Group Thermodata Europe (SGTE). The methodology used for determination of Gibbs free energy curves, binode and spinode are described in more detail in 4.3.3.2. The final calculated miscibility gap is shown in Figure 6.2. The composition of the partitionlessly solidified precursor phase (i.e. the composition of the original alloy) is labelled on the diagram in yellow (a Cu atomic ratio of 0.208).

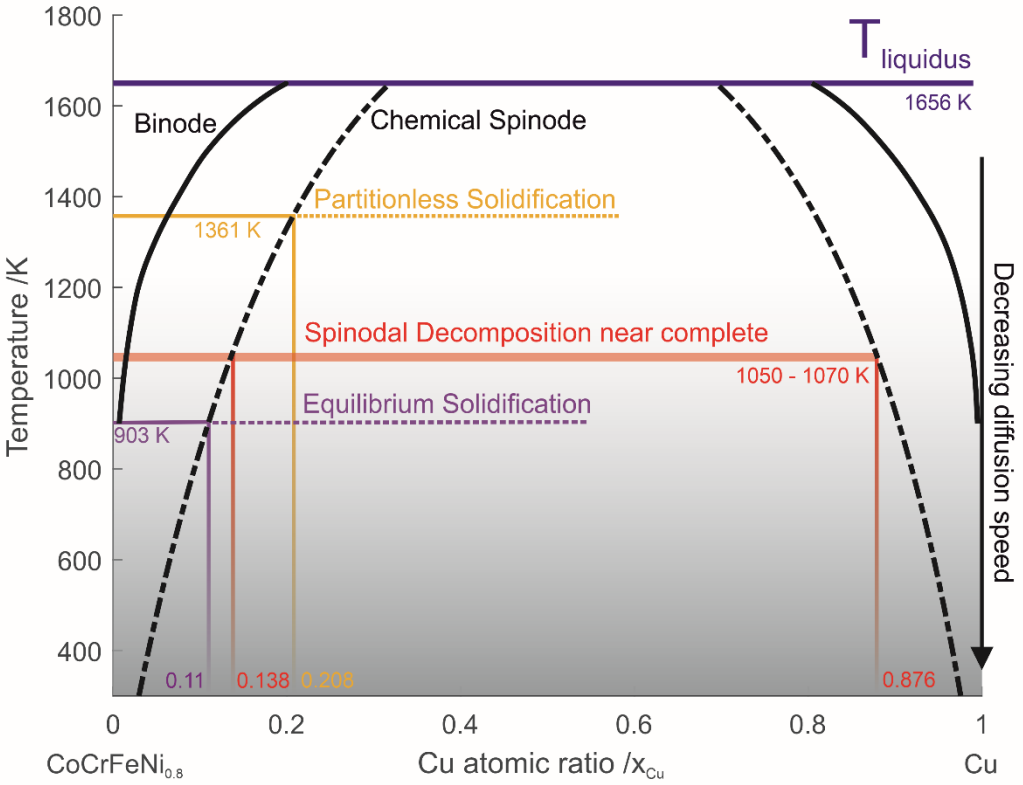

Figure 6.2 Solid-state miscibility gap in FCC solid solution phase $CoCrCuFeNi_{0.8}$ alloy following a $CoCrFeNi_{0.8}$-Cu pseudobinary configuration.

The graphical results from Figure 6.2 predict that there is indeed a solid-state miscibility gap present in FCC $CoCrCuFeNi_{0.8}$. Once the partitionlessly solidified FCC phase is cooled, it is therefore likely to separate into a Cu-rich and CoCrFeNi-rich phase. This corroborates the observation of the decomposed structures in the dendrite cores and the composition of the respective phases. However, because the miscibility gap naturally encompasses a region where the single phase will be thermodynamically metastable (between the binode and spinode) and thermodynamically unstable (below the spinode), the question remains as to whether the decomposition reaction proceeded via a nucleation and growth mechanism or a solid-state spinodal decomposition.

When the partitionless solidified alloy is cooled into the metastable region between the binode and spinode, phase separation may occur via a nucleation and growth mechanism, Cu-rich precipitates will nucleate and grow via a diffusion controlled process. Because the initial precursor phase requires the formation of a cluster of solute atoms in close proximity, the reaction is not spontaneous and requires a nucleus of critical size to stabilise the precipitated phase particle [268]. Therefore, nucleation may be initiated at any temperature between the binode and spinode curves for the specific alloy composition. In

this case, the interval for the reaction is between the liquidus temperature (1656 K) and 1361 K. If this does not occur, the solidified alloy will cool to a predicted 1361 K, upon which precipitation will occur via a spinodal decomposition. There is no energy barrier to the formation of the new phase, so such a reaction will occur spontaneously at the specified temperature. If T_0 for this alloy is found to be below 1361 K, the modelled miscibility gap predicts that only a spinodal mechanism can be responsible for the decomposition reaction.

Because there are morphological and compositional characteristics of the dispersed microstructure which support both a nucleation and growth and a spinodal decomposition mechanism, both are discussed here before a decision is made on the more likely possibility.

The first morphological evidence for a nucleation and growth mechanism is the wide size distribution in the population of Cu-rich dispersoids in a given droplet size (and even in a single dendrite core). Figure 5.14c shows a range of sizes of Cu-rich dispersoids in the dendrite core of a 212 – 150 μm diameter droplet with diameters ranging from 30 nm to 300 nm. Similarly, Figure 5.19c shows the dispersoids in a large dispersion region of a droplet in the same size fraction. Here, diameters of the Cu-rich dispersoids range from 50 nm to more than 500 nm. In each case, the diameters of these dispersoids are distributed across a range of at least an order of magnitude. In both of these droplets, the well-defined dispersoids (i.e. those which have not been impacted by sectioning effects) feature a well-defined boundary between the phases. In the case of spinodal decomposition, particularly in the earlier stages of the reaction, the boundary would likely be rather diffuse. Finally, the spherical/spheroidal morphology of the Cu-rich dispersoids is a morphology that is heavily associated with classic nucleation models [269]. The sheer density of dispersoids in the dendrite cores, implies extremely copious nucleation. This seems rather unusual. However, it is possible, especially in the rapid-cooling environment inherent in drop-tube processing. Because the cooling rate is so high, defects such as vacancies and dislocations created during the solidification process can be more readily retained in the crystal lattice down to lower temperatures below the liquidus. These defects, along with entrained oxides, may provide more favourable sites for heterogenous nucleation of Cu-rich precipitates within the areas of the dendrite cores that have solidified in a partitionless manner [26].

The most important indication of spinodal decomposition is the apparent inability to suppress the occurrence of the decomposition reaction, even at the maximum encountered solid-phase cooling rate of 40000 K s^{-1}. Such a phenomenon suggests a decomposition that occurs spontaneously during

cooling, and is not unique to the HEA studied. In as-cast AlCoCrCuFeNi, Singh et al. [167] observe decomposition of the solidifying dendritic phase, which they attribute to a spinodal mechanism. An interconnected network of B2 phase precipitates out of solution, aligned preferentially in the <1 1 0> directions (likely due to elastic anisotropies in the crystal lattice). Of prime importance is the fact that splat-quenching the same alloy (and achieving cooling rates of 10^6 – 10^7 K s^{-1}) did not seem to be enough to suppress a decomposition from occurring. Nanoscale ordered BCC domains were observed within the grains of the splat-quenched sample. Zhang et al. [256] cooled the same alloy by melt-spinning and spray casting, achieving similar cooling rates to the aforementioned splat-quenching. This work seems to have removed any doubt regarding the reaction mechanism. The same B2 aligned network is clearly observed in decomposed dendrites in all cases, reaffirming the choice of spinodal decomposition as the phase formation mechanism.

As discussed in section 2.2.1, it is sometimes possible to visually distinguish between decomposition reaction mechanisms through examination of the newly formed phase morphology. A series of discrete precipitates is likely the result of a nucleation and growth mechanism, while an interconnected network is generally attributed to the occurrence of spinodal decomposition [65, 70]. It is therefore very easy to look at the discrete spherical Cu-rich dispersoids formed in CoCrCuFeNi and immediately attribute this to a nucleation and growth mechanism. However, deeper examination of spinodal decomposition morphologies makes this conclusion less certain. Indeed, the previous studies mentioned [167, 256] adhere to this trend. In both cases, a percolated interconnected network is formed rather than discrete nuclei, pointing heavily to spinodal decomposition. Determining reaction mechanism solely based on final phase morphology is not always infallible, however. Numerous scenarios are possible during which the new phase formed by a spinodal decomposition can take the form of discrete dispersoids. The key variable governing this possibility is the volume fraction of the minority phase. In two-phase systems where the volume ratio heavily favours one, it is possible for the final spinodal structure to manifest in the form of discrete dispersoids as opposed to a percolated network [270]. While the minimum volume fraction of the minority phase required to form a percolated network likely varies with solidification conditions and the alloy studied, Cahn et al. [271] suggest a percolated network will form as long as the volume fraction of the minority phase is above 15%. For comparison, part of the dendritic arc-melted ingot and a sample of 5 droplets (consisting exclusively of SC/MC microstructures) were subjected to the ImageJ thresholding methodology shown in section 4.3.4.2 for grain refined droplets. This allowed an

estimate of the volume fraction ratio of the Cu-rich (white) phase and the HEA (black) phase respectively. Though this, the volume fraction ratio of Cu-rich phase to HEA phase in $CoCrCuFeNi_{0.8}$ was estimated to be an average of 12:88 in the ingot sample and an average of 14:86 in the drop-tube processed droplets. This value is likely below the percolation threshold for the alloy. If not enough Cu-rich phase is available to allow percolation, a discrete island structure can be formed in lieu of the classic network structure expected [272-274].

Another possibility is that a combination of both nucleation and growth and spinodal decomposition has occurred at two different characteristic temperatures during the cooling of the alloy.

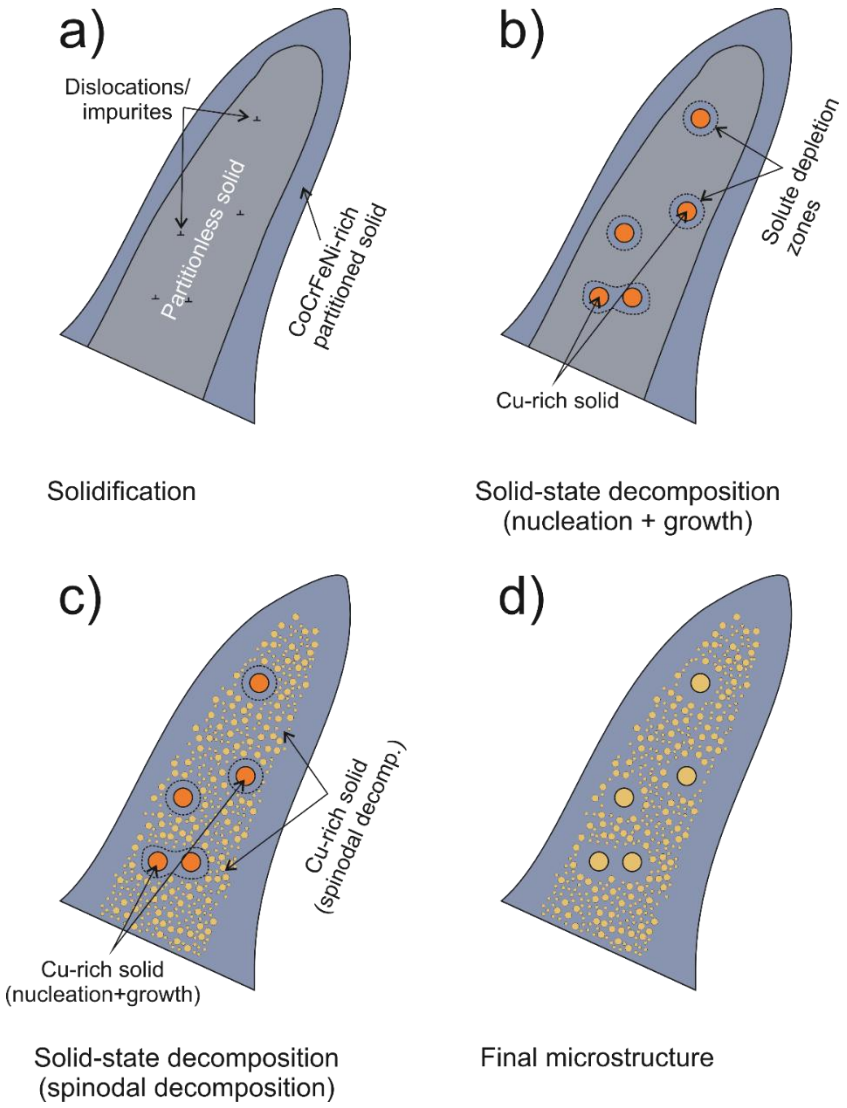

Figure 6.3 Diagram of possible solid-state decomposition microstructure via a combination of binodal nucleation and growth and spinodal decomposition mechanisms in dendritic $CoCrCuFeNi_{0.8}$. (a) Initial partitionless solidification of dendrite with retained impurities and dislocations serving as potential nucleation sites. (b) Nucleation of Cu-rich dispersoids followed by growth via a diffusion based process, creating solute (Cu) depleted zones in the area surrounding each dispersoid. (c) Spinodal decomposition in all areas of partitionlessly solidified dendrite core apart from areas near nucleated solid which are already depleted in Cu solute. (d) Example final microstructure showing the morphological configuration of Cu-rich dispersoids as the result of combined nucleation and growth and spinodal decomposition in the solid state.

According to the calculated miscibility gap in the FCC solid (see Figure 6.2) reduction in temperature of the alloy to any temperature between 1656 K (the alloy liquidus) and 1361 K may result in nucleation of the Cu-rich phase within the CoCrFeNi-rich dendrite cores. Once below 1361 K the decomposition mechanism is predicted to be solely spinodal. This sequence does not preclude the possibility that nucleation and growth may occur and then be followed by a

spinodal decomposition in the same dendrite. A possible mechanism for this occurrence, and the microstructure that may result, is shown graphically in Figure 6.3.

In the temperature interval between the binode and spinode, nucleation might be initiated on impurities or dislocations present in the partitionless solid crystal lattice (Figure 6.3a). As the nuclei grow via solute diffusion, a solute depleted region is formed around each nucleus (Figure 6.3b) [26]. Once the temperature drops below 1361 K, spinodal decomposition can occur as long as the chosen region is not within these solute depleted regions (Figure 6.3c).

Such a coincidence of both mechanisms may also be a cause of the large size distribution of the Cu-rich dispersoids. Nucleated Cu-rich dispersoids will likely be present in lower numbers than for a spinodal reaction. Additionally, because the nucleation occurs before (and at a higher temperature than) the spinodal reaction, stable nuclei would have more time to coarsen and reach a larger size. Conversely, subsequent spinodal decomposition would form fine dispersoids which have less time to coarsen before diffusion processes are suppressed by the falling temperature. Furthermore, the spontaneous nature of the spinodal reaction means that once dispersoids form, the matrix phase would also rapidly become depleted in Cu solute, reducing the driving force for further coarsening processes. A representation of the resultant dispersoid size distribution is shown in Figure 6.3d.

In order to confirm the possibility that both decomposition mechanisms occur, a more detailed compositional analysis of multiple Cu-rich solid-state dispersoids would need to be conducted. If nucleation and growth occurs, nucleated dispersoids will likely have compositions that are both distinct from the composition predicted by the spinodal curve, and which will vary within the range of compositions defined by the binode within the temperature interval 1656 K – 1361 K. A combination of nucleation and growth and spinodal decomposition would result in Cu-rich dispersoids with a large size distribution, but also, with a notably wide range of compositions. This is unlikely when decomposition occurs solely via a spinodal mechanism, where the entire microstructure would undergo decomposition at the same temperature (1361 K). Another indicator of nucleation and growth which could be observed compositionally would be the presence of solute-depleted zones (i.e. areas lean in Cu) surrounding the Cu-rich dispersoids. Such zones would not be present in the event of a spinodal decomposition.

Definitive confirmation of the mechanism responsible is challenging, and likely requires the use of experimental techniques [81] well beyond the scope of this

work. Analysis at extremely high spatial resolution is required to gather information about the progression of the decomposition reaction at the nanoscale. One method used to achieve this is to age a rapidly quenched (and therefore, supersaturated) alloy at intermediate temperatures and measure the changing amplitude of composition fluctuations with time. These composition fluctuations are often on the order of 1 nm at the initial stages of solidification [269]. One example of such an investigation is that of Zhu et al. [275] who aged Fe-29at% Cr-14at% Co-21at% Al-0.15at%Zr. The group were able to log the changing amplitude of composition fluctuations with time using a combination of experimental techniques. Thus, they determined that a spinodal mechanism was responsible for the decomposition reaction in this alloy.

Based on the arguments made from the gathered data, it is more likely that the dispersoids formed as the result of a solid-state spinodal decomposition than through a nucleation and growth mechanism. The key argument behind this is the inability to suppress the decomposition reaction at high undercoolings.

Finally, some attention should be paid to the shape of the dispersoids themselves. In contrast to the work of Singh et al. [167] and Zhang et al. [256] there does not seem to be an obvious preferred growth orientation in the Cu-rich phase precipitated in $CoCrFeNi_{0.8}$-rich dendrites of the alloy studied. They are instead present as spheres, indicating a non-faceted interface. The final precipitate shape in solid-state reactions is the result of a complex interplay between multiple variables. In a simplified explanation, the newly forming phase often possesses a different crystal structure and/or interplanar spacing to that of the surrounding phase. The growth of the precipitated phase therefore often introduces a certain degree of misfit strains in the crystal lattice. The globular, web-like, percolated network often characteristic of spinodal decomposition (see Figure 2.9 and Figure 2.10b) usually prevails when the two phases formed during spinodal decomposition have a similar volume fraction, and when their formation induces only limited lattice misfit strain. This is often due to elastic isotropy in the system [271]. If the phase structures differ to the point where the lattice misfit increases above 0.5%, the shape of the precipitated phase is likely to become faceted. Rather than spheres, they will now grow as plates or cubes along preferred crystallographic directions because of elastic anisotropies in the majority phase [84, 270, 276]. Examples of the impact of asymmetric elastic strains on morphologies of spinodal decomposed structures, both discrete and interconnected, have been modelled by Nishimori et al. [274]. A highly angular network is also visible in the previously discussed dendrites of AlCoCrCuFeNi [167, 256], where spinodal decomposition is suggested to have occurred. A preferred growth direction (in this case, along the <1 1 0> direction) is

explainable due to the different phase structure between an Al-Ni rich (B2) phase and a Fe-Cr rich (BCC) phase.

In contrast, the decomposition products in $CoCrCuFeNi_{0.8}$ (the CoCrFeNi-rich and Cu-rich phases) have been found to have the same FCC crystal structure and a lattice misfit of 0.5%. This, combined with the low volume fraction of Cu-rich phase, is consistent with a discrete dispersoid morphology and a non-faceted interface between phases. Instead, the a spherical interface likely forms to minimise the overall interface energy [26].

The miscibility gap in Figure 6.2 predicts that spinodal decomposition is initiated at 1361 K. However, the final phase compositions in the decomposed structures are likely the result of significant coarsening following the initial decomposition. Such coarsening is a diffusive process and is likely to proceed from the initial decomposition to a point in the cooling regime where diffusion of solute through the solid matrix becomes kinetically suppressed at low temperatures. The composition of the well-defined Cu-rich dispersoids and the CoCrFeNi-rich phase between them (compositions C and E in Table 5.10) can be plotted to predict the temperature at which the spinodal decomposition and associated coarsening is nearly complete. This temperature is predicted to be in the range of 1050 – 1070 K. If the equivalent compositions are used for the droplet with large dispersions (compositions C and E in Table 5.13), the composition at which the decomposition reaction is near complete is comparable, but slightly lower in the range of 900 K – 1000 K.

If Cu is considered as the solute in this pseudobinary system, diffusion is likely to be substitutional. Such diffusion is likely to be significant in the solid state as long as the temperature is above $0.5T_l$ – $0.7T_l$ where T_l is the alloy liquidus temperature [85, 86]. Assuming an average value of $0.6T_l$ determines that diffusion controlled coarsening will be significant in this alloy down to a temperature of about 990 K (based on a liquidus temperature of 1656 K). This provides an explanation as to why it is essential for the precursor phase of the solid-state decomposition structure to be a solid that has solidified in a partitionless manner. As stated in the previous paragraph, the compositions of Cu-rich dispersoids and the surrounding CoCrFeNi-rich phase suggest a spinodal decomposition and coarsening which proceeds down to a minimum of 900 K. In general, it is likely that the kinetic conditions will allow sufficient coarsening for the decomposition reaction to proceed to a significant extent. However, if the chosen precursor phase is a CoCrFeNi-rich dendrite which has undergone partitioning as it would at equilibrium (e.g. PDD and SDND dendrites in drop-tube processed droplets, or the dendrites in the arc-melted ingot). The temperature is unlikely to be sufficient to allow the reaction to proceed to a

significant extent. Assuming a Cu atomic fraction in the dendrites (at equilibrium) of about 0.11 at% Cu, the temperature at which spinodal decomposition would be initiated is 903 K, well below the temperature at which substitutional diffusion is considered significant. Therefore, it is predictable that partitioned dendrites would not undergo spinodal decomposition to any meaningful extent after solidification is complete.

6.3.1.4 Impacts as a method for visualizing the T_0 transition

As part of drop-tube processing, a large amount of droplets of varying diameters are nearly simultaneously ejected at speed through a small orifice. During freefall, the higher cooling rates prevailing in smaller droplets naturally means that they become fully solid much more quickly than larger droplets. Because of this, there is a statistically significant number of instances where a smaller already-solidified droplet will impact a larger droplet that is still liquid, but also significantly undercooled below the liquidus. In many cases, the impacting smaller droplet becomes partially embedded in the larger droplet. These droplets remain fused during sample preparation and are mounted, ground and polished together. In this way, it becomes possible to analyse the changes in microstructure of the larger droplet which occur due to the impact. The influence of the impact on solidification characteristics of these droplets is often profound. A strong impact may result in a change in solidification pathway, which creates a different microstructure than would otherwise be predicted. Essentially, the location of the impact often becomes the nucleation point for the solid phase in the still-liquid larger droplet. Because of this, it is easier to determine where solidification began in the droplet, and form an understanding of the prevailing structures at each stage of solidification. If differing microstructures are present depending on distance from the impact point, it is likely that solidification is occurring under different conditions (i.e. different cooling rates and/or undercoolings). While this analysis does not tell us the exact cooling rate at which each structure prevails, it may be used to develop an order of occurrence of these structures in terms of cooling rate and/or undercooling.

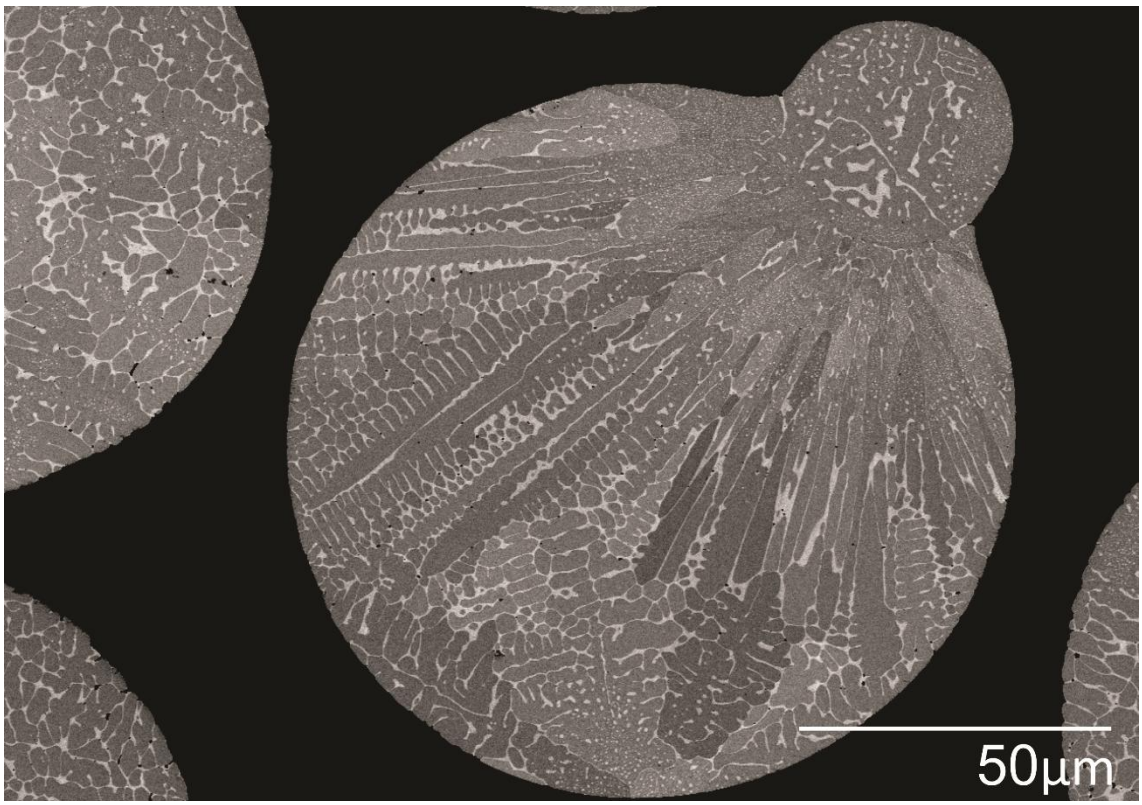

Figure 6.4 SEM BSE micrograph of impact of small droplet into larger droplet in drop-tube processed $CoCrCuFeNi_{0.8}$. Large droplet microstructure near the impact site shows a structure composed mainly of Cu-rich dispersion regions. This transitions to a dendritic microstructure largely devoid of dispersions as distance from the impact site increases.

The example impact microstructure in Figure 6.4 shows a stark similarity between impacted drop-tube processed droplets and the selected region of the arc-melter in Figure 5.3. In the arc-melted sample, nucleation of the CoCrFeNi-rich solid phase seems to occur at the point just above the Cu-rich phase that has macrosegregated at the bottom of the sample. The growing dendrites radiate upwards from this point away from the water-cooled Cu-hearth. In many of the inter-droplet impact microstructures, similar behaviour can be observed.

The microstructure of the larger droplet in Figure 6.4 similarly shows dendrites radiating outwards from the apparent nucleation point. In both cases, there is initially very little branching of secondary arms. The columnar dendrites instead feature Cu-rich dispersoids within the primary arm, which echoes those seen in primary arms of other solidified droplets. As we move away from the nucleation point, the assumed solid-state dispersoids cease to appear in the dendrite cores. In nearly the same region, secondary arm branching begins to occur and more Cu-rich interdendritic phase is visible in between the dendrites. The impact has allowed us to directly observe the transition from partitionless growth to solute partitioning with increasing distance from a known nucleation point.

Such a transition is what we would expect to see as the latent heat that is released at the solidification front increases the temperature of the remaining undercooled liquid. The point at which the solid-state dispersoids disappear allows us to visualise the time when continuous latent heat release caused the remaining liquid temperature to reach above T_0. Solute partitioning is then resumed.

The most obvious difference between this transition in drop-tube processed droplets and arc-melted samples is that the Cu-rich interdendritic phase which has accumulated at the nucleation point in the arc-melted sample is not present in the drop-tube processed droplet at the impact site. This is potentially because the droplets are solidified in freefall, which eliminates the possibility of accumulation of Cu-rich liquid at a specific region in the sample (in the absence of LPS).

6.3.2 Grain refinement

As has been discussed briefly before, a substantial amount of spontaneous grain refinement has been observed in drop-tube processed $CoCrCuFeNi_{0.8}$. The partially and fully refined structures defined (shown in Figure 5.20c and Figure 5.20d respectively) consist of discrete spherical and near-spherical CoCrFeNi-rich particles separated by a network of the Cu-rich interdendritic phase.

The occurrence of spontaneous grain-refinement in this alloy presents the rare opportunity to discuss the phenomenon in dual-phase solid-solution alloys. The bulk of experimental studies regarding grain refinement have been based on single-phase mutually soluble alloys such as Cu-Ni and Fe-Ni. It is therefore interesting to discuss how the introduction of an additional phase affects the grain refinement process and the final microstructure. Conveniently, the substantial composition difference between the two phases allows the morphology of grain-refined structures to be readily observed in detail. There is no additional requirement for destructive acid etching during sample preparation to reveal grain boundaries. Because of this, the mechanism behind the spontaneous grain refinement can potentially be determined with more certainty by visual inspection than would be the case for a single-phase microstructure.

6.3.2.1 Grain refinement occurrence rate in $CoCrCuFeNi_{0.8}$

The easiest comparison in grain refinement occurrence to past literature can be made to the extensive drop-tube studies performed by Norman et al. [221] on Ni-Cu alloys. As discussed in section 3.4.5, the authors note an interesting trend in the occurrence rate of grain-refined microstructures with cooling rate. In

high-purity alloy samples drop-tube processed under a high vacuum, occurrence rate of grain refinement tends to increase with decreasing droplet size and peaks at sizes of 100 – 200 μm. However, in samples of commercial purity and/or after drop-tube processing at a lower vacuum, the opposite trend is found. Larger droplets of diameter 1000 μm feature the highest occurrence of grain refinement. This occurrence rate decreases monotonically as droplet size decreases. Figure 5.22 indicates that drop-tube processed $CoCrCuFeNi_{0.8}$ more closely follows the latter trend. This is particularly apparent when considering the occurrence rate of fully grain refined microstructures in $CoCrCuFeNi_{0.8}$. These can be compared directly to the droplets described as “grain-refined” in the work of Norman et al. [221]. In $CoCrCuFeNi_{0.8}$, fully grain-refined droplets occur most readily at the highest droplet sizes above 500 μm in diameter. This then decreases monotonically until a droplet size of about 150 μm where fully grain refined droplets are no longer observed.

6.3.2.2 Grain refinement morphology in $CoCrCuFeNi_{0.8}$

The morphology of the grain-refined microstructures indicates that the $CoCrCuFeNi_{0.8}$ alloy underwent grain refinement via dendrite re-melting and fragmentation. In nearly all cases, the observed grain-refined microstructure consists of what appear to be fragments of the CoCrFeNi-rich dendritic phase at various stages of remelting and coarsening. Importantly, the vast majority of all of these CoCrFeNi-rich fragments are completely (or nearly completely) surrounded by the Cu-rich phase. Because this Cu-rich phase is the lower melting point phase in the system, it is assumed that this phase either re-melted or remained liquid during the recalescence phase and the subsequent fragmentation of the CoCrFeNi-rich dendrites as the re-melting process occurred. Flow of the residual liquid has then caused the partially remelted grains to be rotated or moved slightly from the original location of the dendrite from which they formed. However, due to the lack of induced liquid flow in drop-tube processing (in contrast to EML experiments, for example), bulk flow of the residual liquid is expected to be negligible. Change in the placement of dendrite fragments is therefore likely to be confined mostly to rotation in place, or slight movements within the Cu-rich liquid by which a particular fragment is directly surrounded. Had grain-refinement via recrystallisation occurred, the CuCrFeNi-rich regions of the microstructure would likely themselves consist of multiple grains, with low-angle grain-boundaries present between them. The Cu-rich interdendritic phase would be absent in between these grain boundaries given that the recrystallized grains would have originated from a single dendrite crystal precursor. A re-melting mechanism is therefore the most likely cause of grain-refinement in this alloy.

As discussed previously, alloys are suggested to feature two episodes of grain refinement at two characteristic undercoolings. These are $\Delta T_{GR}^{(1)}$ and $\Delta T_{GR}^{(2)}$ where $\Delta T_{GR}^{(2)} > \Delta T_{GR}^{(1)}$. The mechanisms that have been discussed are numerous (see section 3.4), and interestingly, the two refinement episodes in the same alloy have often been attributed to different mechanisms. However, given that microstructural analysis of drop-tube processed $CoCrCuFeNi_{0.8}$ indicates grain refinement via remelting, it is beneficial to discuss the grain refinement occurring in the $CoCrCuFeNi_{0.8}$ alloy through the lens of the most commonly discussed remelting and fragmentation models. These are the models of Schwarz et al. and Karma [40, 41], Li et al. [42] and Mullis and Cochrane [36, 211, 212].

6.3.2.3 Fragmentation and remelting – Schwarz and Karma

As part of their grain refinement model, Schwarz et al. and Karma [40, 41] begin with the assertion that the behaviour in tip-radius of a dendrite growing into an undercooled melt can be modelled [277, 278] based on the well-known 'marginal stability theory' [279] of dendrite growth.

Initially, increasing undercooling causes a decrease in the dendrite tip radius to a local minimum. The increase in tip-radius to a local maximum then occurs due to the change in the conditions upon which dendrite growth is contingent. Initially (at low undercoolings), dendrite growth is mediated by diffusion of solute across the solid-liquid interface. As undercooling increases further, this diffusion becomes inhibited due to the occurrence of significant solute trapping at high dendrite growth velocities. This causes a gradual recovery in dendrite-tip radius. Once a critical undercooling ΔT^* is reached (according to the work of Eckler [62] and modelled by the work of Sobolev [171] and Galenko [175]), growth of dendrites at a critical velocity inhibits the diffusion of solute altogether, and dendritic growth in the alloy now becomes controlled by the diffusion of heat across the interface, as it would in a pure metal. As undercooling increases further, dendrite-tip radius then begins to decrease again [277, 278, 280].

Marginal stability theory has since become the subject of some controversy regarding its applicability to all dendrite growth systems. Primarily of concern was the fact that the surface energy between the growing dendrite and the liquid was considered to be constant, even as the dendrite shape is unstable in nature [281]. The theory has, therefore, been superseded by comparatively more recent analyses such as microscopic solvability theory [282, 283] which consider anisotropies in stability across the dendrite-liquid interface. These tend to accurately predict experimental data in a more complete, mathematically rigorous fashion, without the need for initial assumptions [284].

In spite of this, marginal stability theory remains a valid method for qualitative analysis of dendrite tip-radius with undercooling given that the underlying governing equations which determine dendrite length scales are the same as those for the more recent microscopic solvability theory [284]. Additionally, regardless of the theoretical description for dendrite growth that is chosen, the evidence for two separate grain refinement transitions occurring at distinct undercoolings in alloys is largely supported by experimental data. Other models [36, 280, 285] with a stronger theoretical basis, have been suggested which, under certain input conditions, indeed predict a local minimum and local maximum in dendrite tip radius as undercooling increases, although this has yet to be fully observed and directly measured experimentally [36]. The dendrite break-up model will thus be discussed bearing in mind such caveats.

As mentioned in section 3.4.1, Schwarz et al. and Karma [40, 41] next propose a dendrite break-up time (Δt_{bu}), which is a function of the dendrite tip radius r_{tip}. Marginal stability theory predicts that there are two undercoolings at which dendrite tip-radius will decrease below a certain critical value r_{tip}^{*}. In each case, a reduction in tip-radius below this value reduces the characteristic dendrite break-up time to fall below the post-recalescence plateau time (Δt_{pl}) such that $\Delta t_{bu} < \Delta t_{pl}$. There is now enough time for sufficient dendrite remelting and fragmentation to occur and produce the characteristic equiaxed refined microstructures commonly associated with spontaneously grain-refined alloys. In alloys, the two characteristic undercoolings at which Δt_{bu} first falls below Δt_{pl} are then referred to as the characteristic refinement undercoolings $\Delta T_{GR}^{(1)}$ and $\Delta T_{GR}^{(2)}$ respectively.

During drop-tube processing of liquid alloys, a smaller droplet (and thus, a higher cooling rate) will generally facilitate a higher undercooling. Given this relationship, it might be assumed that there would be an observed peak in occurrence of grain-refinement at low and high cooling rates respectively when analysing the drop-tube processed material. This is not shown conclusively in Figure 5.22. While there seems to be a peak in occurrence of grain-refined structures at low cooling rates, the behaviour at higher cooling rates is much less definitive. Unfortunately, the interplay between cooling rate and undercooling in drop-tube processed droplets renders this analysis more complex.

The dendrite break-up time Δt_{bu} depends on the dendrite-tip radius (which is, in turn, dependent on the undercooling) [187]. As stated previously, a droplet solidifying at a higher cooling rate will generally achieve a higher undercooling prior to solidification. Simultaneously, the other key time interval Δt_{pl}, is heavily impacted by the rate at which heat is extracted from the alloy melt during

solidification (i.e. the cooling rate) [187]. In the drop-tube for example, larger droplets subject to lower cooling rates will allow a longer plateau time Δt_{pl}. As droplet size decreases and predicted cooling rate increases, this plateau time will begin to decrease, allowing less time for the dendrite break up process to occur. For a given breakup time Δt_{bu}, a higher cooling rate will reduce the time for the grain refinement transition. The act of increasing cooling rate in drop-tube processing therefore introduces competing effects with regards to grain refinement. A higher cooling rate will (on average) reduce break-up time, but will also simultaneously reduce plateau time.

Given this complexity, perhaps another method can be used to link the two characteristic grain refinement transitions to the data gathered on $CoCrCuFeNi_{0.8.}$ This can indeed be done by dividing grain-refined grains into two groups. The first of these groups contains refined grains which come from dendrite fragments that have solidified via solute-controlled growth, where at low undercoolings, the first minimum in dendrite tip radius occurs. The second of these groups contains grains which originate from dendrite fragments that have solidified via thermal-diffusion controlled growth at high undercoolings, where there is a second reduction in dendrite tip radius below the critical value r_{tip}^{*}.

Based on the extensive statistical analysis of structural prevalence conducted, it is clear that solid-state dispersions present in dendrites can also be present in those that are partially fragmented, or fully equiaxed. In other words, a droplet which undergoes partitionless solidification in some of the microstructure can also be subject to grain refinement. Examples of such morphologies can be found in Figure 4.8h and Figure 4.8i. Evidently, the occurrence of partitionless solidification does not preclude the occurrence of grain refinement. In terms of undercooling, the difference between grain-refined grains which feature solid-state decomposition and those that do not is likely the same as the difference between dendrites which feature solid-state decomposition an those that do not. Different dendrites in a given droplet may have attained drastically different undercoolings upon solidification. This does not change if these dendrites partially re-melt during a grain-refinement process, given that such refinement occurs much later, well into the solidification process. A grain-refined grain with solid-state dispersoids therefore originated from a liquid that was undercooled much more than the equivalent grain with no dispersoids present, and therefore solidified partitionlessly.

Conveniently therefore, grain-refined grains can be rudimentarily categorised as the fragments of dendrites that grew via solute-controlled or thermal-controlled growth based on the presence or absence of Cu-rich dispersoids within the

grains. If the grain is devoid of Cu-rich dispersoids, it is likely the product of a dendrite that solidified primarily under solute controlled growth. Conversely, if a grain features Cu-rich dispersoids, it is likely the fragment of a dendrite which grew partitionlessly under thermal-controlled growth.

For this reason, it is helpful to delineate between grain-refined grains that show SSD and those that do not when discussing important dimensions such as the area equivalent diameter AED. This distinction is made in Figure 5.24 which plots the mean AED of droplets (with and without SSD) with cooling rate. It is clear that a decrease in grain-refined grain AED occurs with increasing cooling rate regardless of whether or not the refined grains show a decomposed microstructure. However, there is also a notable difference in AED for grains which feature solid-state dispersoids and those that do not in the same size fraction. In all size fractions in which solid-state decomposition has been observed to some extent in the dataset, the AED for such refined grains featuring the resultant Cu-rich dispersoids is noticeably larger than the AED for those without. It should be noted that the mean AED determined for refined grains featuring solid-state dispersoids is less certain that that determined for refined grains without solid-state dispersoids. This is due to a smaller available dataset from which to calculate the mean (i.e. only a small subset of refined grains in each size-fraction featured solid-state dispersoids). This uncertainty is highest in larger size fractions which feature very few refined grains with Cu-rich solid-state dispersoids in them. However, the general trend is evident. Refined grains formed from dendrites that solidified in a partitionless manner are generally larger than those formed from their partitioned counterparts, even at similar cooling rates. As cooling rate increases, the decrease in AED in those grains featuring solid-state dispersoids is also less severe than the decrease in size of those which do not feature solid-state dispersoids.

As has been discussed in section 6.3.1.1, the solute trapping that occurs in $CoCrCuFeNi_{0.8}$ is likely not the result of undercooling mediated kinetic solute trapping. Rather, it is caused by the undercooling of the alloy liquid below the characteristic T_0 line at the given composition. This causes fully partitionless growth, which is controlled by the diffusion of thermal energy. Once undercooling is reduced so that the temperature rises above T_0, solute partitioning resumes, with a partition coefficient similar to that predicted under equilibrium solidification conditions. Therefore, the increase of dendrite tip radius with undercooling that occurs between $\Delta T_{GR}^{(1)}$ and $\Delta T_{GR}^{(2)}$ should not be represented by a gradual slope towards a local maximum (as it is in Figure 2.1 [36, 39] for binary alloy such as Cu-Ni and Fe-Ni). Instead, it is better represented by a step-change that occurs when liquid undercooling is such that

$T = T_0$. This critical undercooling can therefore be represented as the previously mentioned ΔT_{PS} where $\Delta T_{PS} = T_l - T_0$. Based on this, we can alter the predicted variation of the dendrite-tip radius with alloy undercooling as given in Figure 2.1 to factor in the step-change in solute partition coefficient that seems to occur in $CoCrCuFeNi_{0.8}$. This is shown in Figure 6.5.

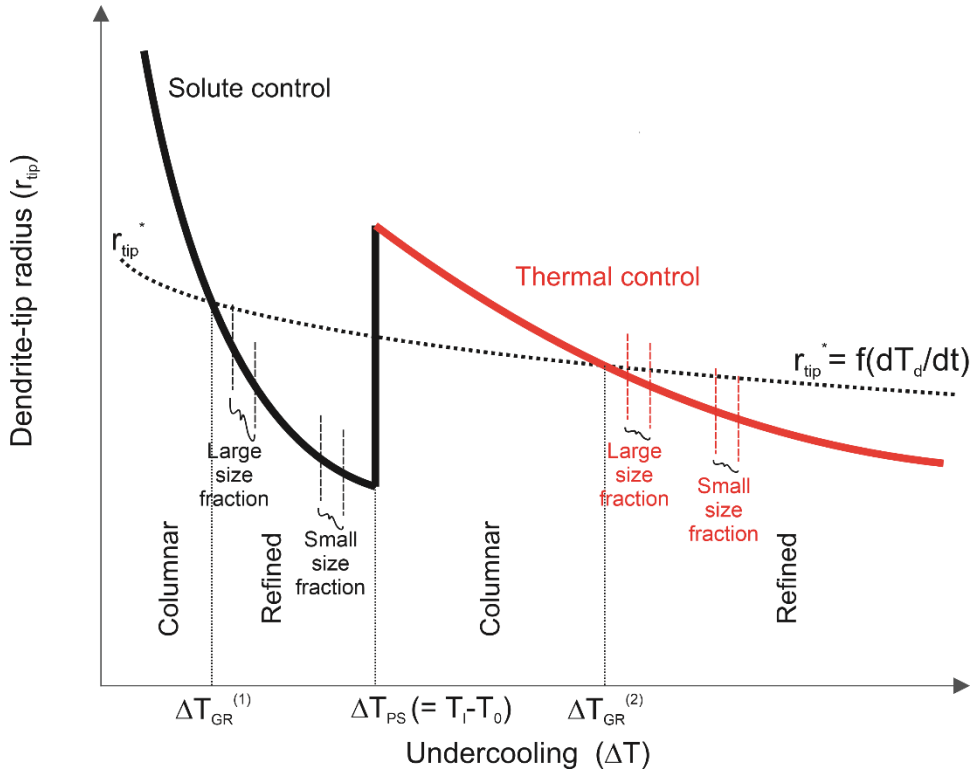

Figure 6.5 Qualitative variation in grain morphology and dendrite tip – radius in $CoCrCuFeNi_{0.8}$ with undercooling adapted from [36, 39]. The step change increase in dendrite tip radius at ΔT_{PS} is due to the nature of transition from equilibrium partitioning to complete solute trapping in $CoCrCuFeNi_{0.8}$, a behaviour not observed in alloys where solute trapping is gradual and kinetically driven.

Also reflected in Figure 6.5 is the reduction in slope of the curve after the step-change transition to complete solute trapping at ΔT_{PS}. The rate of this decrease as undercooling increases is now different due to the change from solute diffusion to thermal diffusion as the mechanism for dendrite growth. This is largely due to the rate of heat diffusion through the remaining liquid being faster than solute diffusion by orders of magnitude.

Depending on whether dendrite growth is under solute or thermal control, the stability of growing dendrites is impacted by the relevant system Peclet number. This dimensionless value quantifies the relative effects transport of solute or heat via conduction or diffusion (i.e. the diffusive transport of heat or of solute through the liquid). In simple terms, undercooling can be seen as a function of

this Peclet number [286, 287]. The solute and thermal Peclet numbers P_t are shown in Equation 6.4.

$$P_t = \begin{cases} \frac{Vr_{tip}}{2D}, & solute\ control \\ \frac{Vr_{tip}}{2\alpha_t}, & thermal\ control \end{cases} \quad 6.4$$

where D is the diffusion coefficient of solute thought the remaining melt and α_t is the thermal diffusivity of the remaining melt. If dendrite growth is under solute diffusion control, the rate of reduction in the size of features such as the tip-radius will depend on the diffusion speed of solute through the residual liquid as solute is rejected from the growing dendrites. Conversely, once dendrite growth is under thermal control, the rate of decrease of dendrite-tip radius will depend on the thermal diffusivity of the residual liquid. Partitionless solidification, as is believed to occur in $CoCrCuFeNi_{0.8}$ is therefore controlled solely by the diffusion of heat through the liquid. During solidification, the thermal diffusivity of the material determines the rate at which latent heat evolved from the solidifying dendrites can be transported through the residual liquid. The rate of such heat transfer is determined by the thermal diffusivity of the material in the liquid state.

Generally, thermal diffusivity values are orders of magnitude larger than equivalent solute diffusivity in a particular material in the liquid state. For example, thermal diffusivities of conventional alloy steels have been measured between 5×10^{-6} – 9×10^{-6} $m^2\ s^{-1}$ in the liquid state depending on temperature [288]. For selected nickel-based superalloys this is slightly lower, in a range 4×10^{-6} – 6×10^{-6} $m^2\ s^{-1}$ [289]. Data on thermal diffusivity properties in liquid HEAs is much less extensively available. However, Uporov et al. [290] calculate a value of 5×10^{-6} $m^2\ s^{-1}$ in liquid AlCoCrFeNi. In contrast, solute diffusivities in more simple alloys such as binary Al-based alloys are calculated to be between 10^{-9} and 10^{-8} $m^2\ s^{-1}$ in the liquid state [291]. Barring the unlikely possibility that solute diffusion is orders of magnitude quicker in liquid HEAs than conventional alloys, any solute diffusion likely occurs much more slowly than diffusion of heat through the same material.

The apparent reduction in dependence of dendrite-tip radius on undercooling in the thermal controlled growth regime compared to the solute controlled growth regime seems to corroborate with the trend in grain-refined grain AED with cooling rate as shown in Figure 5.24. Because of the complicated partitioning behaviour in this alloy, two dendrites in the same droplet (i.e. solidified at the

same cooling rate) may solidify via very different mechanisms and still both subsequently undergo grain-refinement. It may be the case that two characteristic refinement undercoolings ($\Delta T_{GR}^{(1)}$ and $\Delta T_{GR}^{(2)}$) observed in alloys are represented by grain-refinement of solute partitioned and partitionless dendrites respectively in drop-tube processed $CoCrCuFeNi_{0.8}$.

The droplets in a particular size fraction have solidified at similar cooling rates. However, the stochastic nature of undercooling means that they have likely achieved different undercoolings before solidification, even at the same cooling rate. In particular, this means that some of these dendrites solidify in a partitionless manner, and others in the same size fraction (or even the same droplet!) solidify via solute partitioning. The fact that these dendrites then undergo grain-refinement tells us the range of undercoolings that are possible if the behaviour of the dendrite tip radius follows the trend described in Figure 6.5. Grain-refined grains with no Cu-rich dispersoids formed from dendrites which achieved undercoolings in the interval $\Delta T_{GR}^{(1)} < \Delta T < \Delta T_{PS}$. Grain-refined grains in the same droplet which feature Cu-rich dispersoids formed from dendrites solidified via thermal diffusion controlled growth in the range of undercoolings where $\Delta T_{GR}^{(2)} < \Delta T$. Because the slope of the trend in dendrite-tip radius with undercooling is more shallow in the region of thermal controlled growth than it is in that of solute controlled growth, the average dendrite-tip radius of the partitionlessly solidified dendrites will likely be larger (on average) than those that solidified through the partition of solute over the defined range of undercoolings. This is shown using the two example size fractions marked on Figure 6.5. A larger droplet size fraction will be subject to lower cooling rates and will thus, on average, achieve lower undercoolings than a smaller size fraction. Even if part of the droplet solidifies under solute-control while another part solidifies under thermal-control, this comparison still holds. If we compare the ‘large size fraction’ undercooling interval in the regions of solute and thermal controlled growth, it is clear that the average value of tip radius will be larger in the region of thermal controlled growth than that of solute controlled growth for the same size fraction. The same holds true if we compare the equivalent ranges in the ‘small size fraction’. This means that dendrites growing under thermal control (i.e. partitionlessly) will have a larger tip-radius than those that grow under solute control for a given undercooling. The resultant AED of the grain-refined grains tends to scale with the dendrite tip radius [40, 187]. As a result, both types of dendrites will fragment when undercooling is high enough, but the refined grains with Cu-rich dispersoids (i.e. those that have undergone partitionless solidification and spinodal decomposition) will be larger in terms of AED than those without said dispersoids. This is what we observe in Figure

5.24 for each droplet size fraction that features both partitioned and partitionlessly solidified grain-refined grains.

In terms of future work, it would be interesting to find more proof for this hypothesis by examining partially grain-refined droplets more closely, particularly those which also appear to have undergone partitionless solidification. If the above explanation is correct, there would likely be instances where secondary dendrite arms, which solidified via solute partitioning, have fragmented at the lower undercooling $\Delta T_{GR}^{(1)}$ whereas the primary arms, which have undergone partitionless solidification, have remained intact ($\Delta T_{GR}^{(2)}$ was not reached). If this is the case, the resultant microstructure should consist of partially grain-refined structures where the secondary arms have partially re-melted and fragmented, resulting in refined grains. However, the primary arms, which solidified in a partitionless manner, would be predicted to remain intact and undergo subsequent spinodal decomposition.

The extensive qualitative agreement between the discussed dendrite breakup model and the occurrence and characteristics of grain refinement in drop-tube processed $CoCrCuFeNi_{0.8}$ is surprising when we consider the drastic difference between drop-tube processing and other experiments such as EML, on which the fragmentation model of Schwarz et al. and Karma [40, 41] is based. Indeed, the very occurrence of grain refinement to any extent is unusual, especially at the highest prevailing cooling rates in the drop-tube (well above 10^4 K s^{-1}). When describing the dendrite break-up model and the interplay between breakup time and plateau time with increasing undercooling and cooling rate respectively, Herlach et al. [187] only provide examples of calculated plateau times based on cooling rates of up to 1000 K s^{-1} which shows undercooling ranges at which the condition $\Delta t_{bu} < \Delta t_{pl}$ can still be satisfied. Grain refinement has been observed in the equiatomic HEA CoCrCuFeNi by Yan et al. [24], but such refinement was achieved, as with many binary alloys, by EML processing. Plateau times in this experiment were likely longer than would be expected had the equivalent alloy been drop-tube processed.

The extremely high predicted cooling rates in the drop-tube mean that the plateau time is predicted to be prohibitively short. In their study, Norman et al. [221] estimate plateau times experienced by Ni-Cu alloys during drop-tube processing and gas atomization. They conclude that these plateau times are much too short for the model proposed by Schwarz et al. and Karma [40, 41] to accurately predict undercoolings at which grain refinement is possible. There is simply no calculated breakup time, at any undercooling, which is lower than the calculated plateau times

This presents a quandary. The model fails to predict any grain refinement in drop-tube processed samples, but grain-refinement is nevertheless observed extensively throughout the samples, as it is in drop-tube processed $CoCrCuFeNi_{0.8}$. The data presented in the current work seems to correspond to fragmentation models, but such a comparison has so far been made only qualitatively. Calculating the dendrite break-up time and plateau time for $CoCrCuFeNi_{0.8}$ is difficult due to the lack of adequate thermophysical data for the alloy.

To explain this, Norman et al. [221] suggest a possible deviation between the dimensions of dendrite tip-radius and the corresponding dendrite trunk at high cooling rates which would impact the resultant calculation of dendrite breakup time. They also suggest that a reduction in scale of the droplet means that the droplet size may be reduced to the equivalent scale of solute and thermal diffusion fields in the droplet, which may influence the solidification and grain refinement behaviour. Proving or disproving these hypotheses is out of the scope of the current work, but should be considered given that grain refinement observed in drop-tube processed binary alloys has also been observed in HEAs processed via the same method.

6.3.2.4 Superheating model

In contrast to the dendrite remelting model of Schwarz et al. and Karma [40, 41], the superheating model proposed by Li et al. [42] suggests that dendrites re-melt and fragment during, rather than after, the recalescence phase of solidification. The fraction of solidified dendrites that remelt (Equation 3.6) is dependent on a calculated dimensionless superheating (Equation 3.5), and peaks at a specific range of undercooling. The key discrepancy between this model and the experimental results lies in the fact that the dimensionless superheating peaks only at one undercooling. This suggests that only one grain refinement transition (i.e. $\Delta T_{GR}^{(1)}$) can be attributed to dendrite re-melting.

At high undercoolings, it is seen as impossible to attain the level of superheating required to re-melt enough of the solidified dendrites during recalescence and allow grain refinement to occur. Grain refinement at higher undercoolings, say Li et al., must therefore be attributed to another mechanism. Various other studies reach a similar conclusion, suggesting that the second grain refinement episode proceeds via recrystallisation.

Recrystallization behaviour has not been observed to a statistically significant extent in drop-tube processed $CoCrCuFeNi_{0.8}$. In contrast to Ni-Cu solidified at high undercoolings [42], there seems to be minimal presence of annealing twins in the grain-refined grains of $CoCrCuFeNi_{0.8}$ regardless of droplet size.

Additionally, visual observation of the contrast in relevant SEM micrographs suggests that the grain-refined particles which are separated by the Cu-rich interdendritic phase are overwhelmingly made up of single crystals. Importantly, this visual inspection of contrast in the SEM backscatter images is not an accurate method for determining the presence of a single-grain or multi-grain structure. EBSD would likely be required to confirm or refute this claim. However, other morphological clues are present which tend to refute recrystallisation. One such clue is revealed in the visible grain boundaries between the two primary phases. In the vast majority of cases, the boundary between the CoCrFeNi-rich grain-refined grains and the Cu-rich interdendritic phase is rounded, rather than angular or straight, which suggests recrystallisation is not the primary method of transformation [198]. Finally, at least in the larger droplet size fractions, there was no discernible change in microhardness between dendritic and grain-refined droplets (see Table 5.14). This is in direct conflict with other studies, where dendritic microstructures which underwent grain-refinement via recrystallisation seem to experience a substantial drop in microhardness compared to the dendritic precursor [196, 197].

The most obvious conclusion based on these discrepancies would be that the superheating model does not serve as a valid description of the grain refinement which occurs in drop-tube processed $CoCrCuFeNi_{0.8}$. The apparent lack of recrystallisation in favour of two separate episodes of dendrite remelting mean that the dimensionless superheating would be required to peak at two separate undercoolings, something that is not borne out in work on more simple binary alloys such as Cu-Ni [42, 189, 190] and Fe-Ni [202].

Alternatively, because of the partitionless solidification that occurs in some dendrite cores in $CoCrCuFeNi_{0.8}$, perhaps these regions behave as pure metals during solidification and subsequent grain refinement. It could therefore be the case that the two grain refinement episodes that appear observable in $CoCrCuFeNi_{0.8}$ are instead the $\Delta T_{GR}^{(1)}$ transition for the partitioned dendrites and the singular ΔT_{GR}^{*} transition for the partitionless dendrites respectively. We are effectively dealing with two very different compositions, and the peak in dimensionless superheating would vary as such.

6.3.2.5 Re-melting of dendritic seaweed

On an additional note, tip-splitting and dendritic seaweed structures are indeed observed in certain partially grain-refined droplets of $CoCrCuFeNi_{0.8}$. Examples of these are shown in Figure 5.21. The work of Mullis and Cochrane [36, 211, 212] suggests that these are the result of instabilities occurring during rapid

dendrite growth at high, (and possibly also at low) undercooling. Furthermore, these dendritic seaweed structures have been observed in partially grain-refined samples of dilute Cu-Ni alloys created by Castle et al. [216]. Unfortunately occurrence of seaweed structures could not be measured statistically across droplet cooling rates. It is still unknown whether the precursor structure for grain refinement is dendrites grown with a specific tip radius as is predicted by Schwarz et al. and Karma [40, 41], or if the final refined microstructure is the result of remelting of seaweed structures created via unstable dendrite growth. Experimentation where solidification microstructures can be viewed in-situ may allow this to be discussed with more certainty.

6.3.2.6 General grain refinement morphology and cooling rate

As discussed above, drop-tube processing may be considered an experiment that achieves high undercooling, which is important in order to initiate the grain refinement process. However, the drop-tube achieves said undercooling via imposition of a large temperature gradient and therefore, a high cooling rate, in addition to melt subdivision. The rapid extraction of heat and its impact on microstructural formation must also be given due diligence here. For example, the rate of the heat extraction is incredibly important to the length of the characteristic plateau time defined by Schwarz et al. and Karma [40, 41]. A higher cooling rate means, by definition, a higher rate of heat transfer from the cooling alloy to the environment.

Because of the massively high cooling rates experienced by smaller droplets, it may also be the case that the rapid heat extraction reduces or even prevents the re-melting and fragmentation process to occur to the fullest extent possible. In this event, dendrite fragmentation and re-melting would likely be severely inhibited. This suggests that grain refinement would occur to a lesser extent at higher cooling rates compared to lower cooling rates. This appears to be borne out by the experimental data in Figure 5.23 where there a reduction in the occurrence of grain refinement begins to occur once cooling rates exceed 2000 K s^{-1}. It is even more evident when we consider the complete lack of fully grain-refined structures at cooling rates above some 5000 K s^{-1} and the reduction in average roundness of the grain refined grains with increasing cooling rate shown in Figure 5.25 (discussed further in section 6.3.2.8 below).

Figure 5.22 shows that droplets with microstructures that are at least partially grain-refined form a statistically significant portion of the total droplets analysed in each size fraction. In essence, the grain-refinement process can occur at least partially in any droplet regardless of cooling rate. This likely confirms the

well-developed hypothesis that the occurrence of grain refinement is depending on undercooling. Conversely, the occurrence of fully grain-refined microstructures is nowhere near as consistent. The occurrence rate of fully grain-refined microstructures becomes statistically insignificant once droplet diameter is reduced below 200 μm and when the corresponding cooling rate is raised above some 5000 K s^{-1}. At the most basic level, this indicates that there is a time requirement for the grain refinement transformation to proceed, which affects the final extent of refinement once the droplet has fully solidified.

6.3.2.7 Trend in AED with cooling rate

Having analysed the bifurcation in AED of grain-refined grains with and without solid-state dispersoids in section 6.3.2.3, we can now conclude our analysis of the trend in AED with cooling rate shown in Figure 5.24. It is clear that in both cases, whether growth is controlled by diffusion of solute or diffusion of heat, the average AED tends to decrease with cooling rate. The defined size fraction undercooling ranges in Figure 6.5 show this trend graphically. A rise in cooling rate results in a corresponding rise in undercooling (on average). This results in a reduction of the dendrite-tip radius. A droplet in a smaller size fraction will cool faster, and thus generally achieve higher undercooling than a larger one. The dendrite-tip radius will therefore be lower compared to a larger droplet. If the droplet undergoes grain refinement, the resultant AED of the refined grains will be lower than the AED of refined grains in a larger droplet. Importantly, this reduction in tip radius with increasing undercooling occurs regardless of the growth mechanism. Partitioned or thermal dendrites will both decrease in tip radius as the cooling rate (and therefore, the undercooling) increases. The only difference is the range of undercooling over which this decrease occurs. Because only grain-refined grains are taken into account in the analysis in Figure 5.24, the regions of the graph that are represented by the data include only the regions which yield a grain-refined morphology. In other words, the trends in reduction in AED represent the regions where the dendrite tip radius is below the critical radius for grain-refinement ($r_{tip} = r^*_{tip}$). In both data sets therefore, the decrease in mean AED with cooling rates reflects the decrease dendrite tip radius with average undercooling.

6.3.2.8 Trend in roundness with cooling rate

In addition to data on occurrence rate of fully and partially grain-refined structures with cooling rate, further statistical analysis has allowed an understanding of the impact of increasing cooling rate on final grain refinement morphology. Figure 5.25 shows, in grain-refined droplets, that the mean roundness of the grains tends to decrease with cooling rate. Because a re-

melting mechanism is the most likely cause for grain refinement in this alloy, models such as that of Schwarz et al. and Karma [40, 41] are the most effective tools with which to describe the effect of cooling rate on the full solidification and coarsening process after re-melting. The model defines a finite time interval (the plateau time Δt_{pl}) over which re-melting and fragmentation processes are able to occur during the grain refinement process. The refinement mechanisms inherent in models such as that of Schwarz et al. and Karma [40, 41] rely on Rayleigh instabilities and the effect of surface tension, which causes spheroidization of the partially remelted dendrite fragments. This is shown very prominently in the experimental work of Mullis and Haque [188] (see Figure 3.15). During the plateau time Δt_{pl}, re-melted dendrite fragments will coarsen and attempt to form a spherical interface with the enveloping phase to reduce interface energy. Naturally, higher cooling rates mean that this available time is likely to be reduced in smaller droplets compared to large ones. The rate of heat extraction increases exponentially as droplet diameter decreases. Much less time is therefore available for re-melting and spheroidization of grain refined grains. This results in a higher probability that more dendrite fragments will be in the intermediate stages of spheroidization when temperature decreases to a point where microstructural change is no longer possible. Fewer dendrite fragments will have time to fully spherodize and will be less round as a result.

6.3.2.9 Skew and kurtosis in roundness of grain-refined grains

The trend in skew of the roundness data with cooling rate is shown in Figure 5.27. The negative value of the skew for all size fraction data sets shows that at all cooling rates, more grain-refined grains have a roundness value higher than that which would be estimated if roundness in each size fraction followed a normal distribution. The trend also shows that this negative skew is most severe in larger size fractions. In the largest droplets, more grains are of a higher roundness value compared to the normal distribution than in the smallest droplets.

One possibility is that this skew is the result of the same phenomena which determines the roundness in general as described in section 6.3.2.8 above. After the initial dendrite remelting, the spheroidization of the resultant fragments is a process which requires time. In larger droplets, where the cooling rate is lower and the plateau time Δt_{pl} is longer, it is likely that the spheroidization process is able to continue for a more substantial amount of time. Consequently, re-melted fragments have more time to undergo spheroidization that they would have if a high cooling rate had reduced the plateau time. More refined grains would reach higher values of roundness and would skew the data

distribution more significantly to higher roundness values in the larger droplet size fractions.

Another possible explanation of this occurrence is that it is an artefact of the a bias inherent in image analysis method used. Because the automatic grain size analysis performed by the ImageJ program is reliant on the entire grain being within the processed SEM micrograph, grains which are only partially visible on the periphery of the image are not catalogued and are therefore not included in subsequent analysis. This exclusion occurs even if only a small portion of a particular grain is not visible in the SEM micrograph. The likelihood that grains will be excluded is increased if grains are large. Because, in an individual droplet, the smallest grains are usually more round than the larger grains, it is more likely that the larger grains that are preferentially excluded are also less round. This preferential exclusion of less round droplets may cause the skew to develop. This is more likely to occur in larger droplets, where the exclusion of larger grains is more likely compared to the exclusion of smaller grains.

Figure 5.28 shows that the opposite trend occurs in the kurtosis values across the droplet size fractions, there is a negative kurtosis across all values, meaning that in all cases, the data is flatter than would be expected for a normal distribution. There is a slight accumulation of data points at the extremes of the spectrum of roundness values. Compared to a normal distribution, there are a higher number of very round or very irregular grain-refined grains in the droplets. In contrast to the trend in skew, the kurtosis becomes more negative with increasing cooling rate, meaning that as cooling rate increases, data accumulates at the edges of the roundness range with increasing severity. This perhaps reflects the discrepancy in the degree of refinement possible in primary and secondary dendrites. Thinner secondary dendrites will be more likely to have time to re-melt, fragment and coarsen during solidification, particularly at the highest cooling rates. In contrast, the larger, often partitionlessly solidified dendrites will not be able to undergo such coarsening and will remain elongated or irregular in structure. The difference between these two scenarios will likely become accentuated as cooling rate increases and the refinement process becomes more and more extensively kinetically inhibited.

6.3.2.10 Cellular structures

Figure 4.8e shows an example of a cellular structure formed in some droplets of drop-tube processed $CoCrCuFeNi_{0.8}$. Initially, it was thought that these regions were structurally distinct from all other possible microstructures in the alloy. However extensive analysis of the grain-refined droplets present in drop-tube processed alloy (particularly those that are nearly fully refined) shows that

substantial spheroidization of the dendrite grain fragments is possible before solidification. These cellular structures are never catalogued on their own, and only occur as part of a partially or fully grain-refined droplet. This trend suggests that the cellular structures are the result of a grain-refinement transformation that has been allowed sufficient time to progress, such that a nearly complete spherodization of refined grains is made possible.

6.3.2.11 Highly globular dendritic structures

In contrast to the cellular structures, highly globular dendritic structures with dispersions (HGDD) are thought to be the result of a partial grain-refinement where dendrites have retained their dendritic characteristics enough so as to not directly considered partially or fully grain-refined. However, the structure (an example of which is shown in Figure 4.8n). Seems to show the beginnings of Rayleigh instabilities occurring in the dendrite arms. Such a process has potentially been arrested by the falling temperature before it can proceed to completion.

6.3.3 Liquid phase separation

The discovery that large dispersed regions in the droplets are the result of decomposition of partitionlessly solidified regions, rather than LPS, brings up another fundamental question. One of the initial aims of this investigation was to study metastable LPS in HEAs via the tailoring of alloy composition to achieve it as readily as possible. This naturally informed the choice of alloy studied. Based on analysis of past literature and consideration of thermodynamic parameters (see section 3.5.1), $CoCrCuFeNi_{0.8}$ was believed to be a prime candidate alloy in which metastable LPS could be achieved at low levels of undercooling. However, this was revealed not to be the case. Instead of a predicted high percentage of core-shell and finely dispersed LPS microstructures, other phenomena such as spontaneous grain-refinement and partitionless solidification are much more commonly observed. The occurrence of LPS is statistically insignificant in this experiment. If most other similar alloys have been extensively observed to undergo metastable, or even stable, LPS, why has such behaviour only been minimally observed in drop-tube processed $CoCrCuFeNi_{0.8}$? Because drop-tube processing has demonstrably achieved undercooling in the hundreds of Kelvin [259], the key issue may lie in the alloy composition, or be based on other aspects of the solidification process.

6.3.3.1 Lack of liquid phase separation - composition

The first potential explanation could be the slight discrepancy in composition of the actual alloy studied compared to that which was calculated based on the

precise atomic ratios. The arc-melting and sanding process for alloy preparation naturally caused slight deviations in the final alloy composition. The most obvious difference is the Cr composition, which is higher than the desired composition by 1-2 at%. Ni concentration is lower by 0.5-0.7 at% than that desired. The impact of small changes in alloy composition on overall alloy behaviour should not be discounted, particularly as they pertain to changes in critical undercooling required for metastable LPS. Liu et al. [143] showed that increasing relative Fe content from $CoCrCuFe_{1.5}Ni$ to $CoCrCuFe_2Ni$ caused an increase critical undercooling for LPS of 100 K. If Fe or Ni content are reduced by half from the equiatomic CoCrCuFeNi composition, LPS becomes entirely stable [144], representing a decrease in critical undercooling required of 180 K. It is therefore not inconceivable that a small change in the compositions of one or two alloy constituents could alter critical undercooling by a significant amount. However, it must be said that the difference between desired and measured compositions in $CoCrCuFeNi_{0.8}$ alloy produced in this study is much lower than the deliberate changes that have been made in previous literature. Massive changes in critical undercooling because of this small composition difference should therefore be deemed unlikely.

Furthermore, it is difficult to reconcile the lack of LPS with an increase in Cr content and/or a decrease in Ni content specifically. As shown in the assortment of previous LPS studies on $CoCrCu_xFe_yNi_z$ alloys in Table 3.1, a decrease in Ni content was found to decrease the critical undercooling required for metastable LPS. Furthermore, an extensive survey of the impact of various elements on LPS in HEAs was undertaken by Munitz et al. [135] which came to a similar conclusion about Ni additions to transition metal HEAs. Furthermore, they note that an increase in Cr content can have the same effect of reducing the critical undercooling for metastable LPS. Because this alloy features a planned reduction in Ni compared to the equiatomic alloy, it is predicted that critical undercooling would have been easier to achieve than in equiatomic CoCrCuFeNi. Furthermore, the further slight reduction in Ni and increase in Cr content, if they had any impact at all, would be predicted to further reduce required undercooling. This reasoning, of course, ignores the impact of unforeseen effects of chosen compositions on thermophysical properties of the alloy (represented by the cocktail effect in HEAs) [3, 6]. But it seems unlikely that this specific composition interval between CoCrCuFeNi and $CoCrCuFeNi_{0.5}$ would be the compositional area within which a massive increase in undercooling would be required to initiate LPS.

6.3.3.2 Lack of liquid phase separation – inhibiting nucleation and growth

A further potentially surprising possibility is the inhibition of LPS due to the extremely high cooling rates achievable during drop-tube processing, particularly compared to more commonly used experimental techniques such as EML or glass-fluxing. These latter techniques rely solely on the inhibition of heterogeneous nucleation in the sample. Because of this, the cooling rate to which the liquid alloy is subjected is often much lower than in drop-tube processing. Furthermore, these techniques allow the liquid to be held in an undercooled state at timescales that are orders of magnitude longer than would be possible in a drop-tube environment, where undercooling is often only achieved for a fraction of a second before the onset of solidification [18, 292]. It is therefore possible that the extreme reduction in experimental time-scale has rendered it impossible to initiate LPS via a nucleation and growth mechanism. A similar scenario was previously observed in a study on drop-tube processed $Fe_{62.5}Cu_{27.5}Sn_{10}$ ternary alloy by Xia et al. [293]. Initially, they observe a structural progression similar to that of Jegede et al. [128], where fully coalesced core-shell microstructures give way to finely dispersed LPS structures at higher cooling rates. However, a key difference lies in in the smallest droplets (i.e. at the highest cooling rates). Here, LPS structures give way to a dual-phase equiaxed dendritic structure, with dendrites of a Fe-rich solid solution growing in to an interdendritic intermetallic phase of composition Cu_2FeSn [293]. Such work demonstrates that it is possible for LPS to be inhibited if high enough cooling rates are achieved in the solidification process.

Another potential cause of inhibition of nucleation and growth in lies in the fundamentals of nucleation theory. During binodal LPS, the nucleation of the minority phase liquid L_2 in the form of minority phase droplets would require the formation of a cluster precursor of sufficient radius to become stable. This cluster formation occurs stochastically [268]. In the case of $CoCrCuFeNi_{0.8}$, with a highly Cu-rich minority phase, an embryonic cluster of a sufficient number of Cu atoms would need to form in the liquid alloy. It is postulated that the addition of more elements to an alloy in roughly equiatomic proportions would reduce the probability that a cluster of Cu atoms of sufficient size would form to allow the nucleation process to begin.

6.3.3.3 Liquid phase separation in $CoCrCuFeNi_{0.8}$ – possible mechanisms

While LPS has not occurred extensively enough to be deemed statistically significant based on the statistical analysis in section 4.3, the LPS that does occur is microstructurally consistent enough that it merits discussion in its own right. Figure 5.29 shows examples of such LPS microstructures which are found

exclusively in the smallest droplets attained in this study (75 – 53 μm and 53 – 38 μm size fractions). Here, the Cu-rich phase, present either in discrete pools in the centre of the droplet or an incomplete shell on the periphery, is reminiscent of partially realised LPS structures discussed in previous studies. Additionally, these droplets feature the notable presence of a third primary phase. This is a rod-like phase located between CoCrFeNi-rich dendrites. While it is also very lean in Cu, it is compositionally distinct from the CoCrFeNi-rich dendrites formed in the bulk of the drop-tube processed droplets, with a much higher Cr content and minor additions of Co and Fe.

As discussed in section 5.4.6, similar three-phase structures are achieved at relatively low undercooling (50 K) in the glass-fluxing experiment by Guo et al. [146]. The team argue that this is a non-equilibrium precursor phase to LPS. When the same alloy is undercooled by 100 K, a more realised LPS structure forms, with the Cu-rich phase that has accumulated between the CoCrFeNi-rich dendrites coalescing into spherical minority phase droplets. These then coalesce at the bottom of the sample due to Stokes motion. Liu et al. [143] observe similar behaviour in their work on $CoCrCuFe_xNi$ alloys, with a similar three-phase structure visible at undercoolings of some 80 K. The group quote a higher range of critical undercooling required for significant LPS (160 K – 300 K depending on Fe content). It appears that in some cases, a CrCoFe-rich phase is another phase which forms during the LPS transformation in $CoCrCu_xFe_yNi_z$ alloys. In the drop-tube processed $CoCrCuFeNi_{0.8}$ droplets shown in Figure 5.29 the presence of this phase seems to confirm that these droplets are in the initial stages of LPS.

Given the occurrence of LPS exclusively at the highest cooling rates, a spinodal decomposition is likely responsible for LPS rather than a traditional nucleation and growth mechanism. Co-Cu [294], Cr-Cu [295] and Cu-Fe [296] phase diagrams all feature metastable miscibility gaps with the critical point at or near 50 at% of the minority component. Moreover, the calculated isopleth for the pseudobinary phase diagram of the $CoCrFeNi_{0.8}$-Cu system (with the caveat that it erroneously predicts LPS in the stable regime) features a miscibility gap with a critical point near 40 at% Cu. This isopleth is shown in Figure 6.6 below (calculated using the MTDATA software in [297]). The alloy composition $CoCrCuFeNi_{0.8}$ is marked by the vertical blue line. It is clear that this composition is a substantial distance away from the predicted critical point.

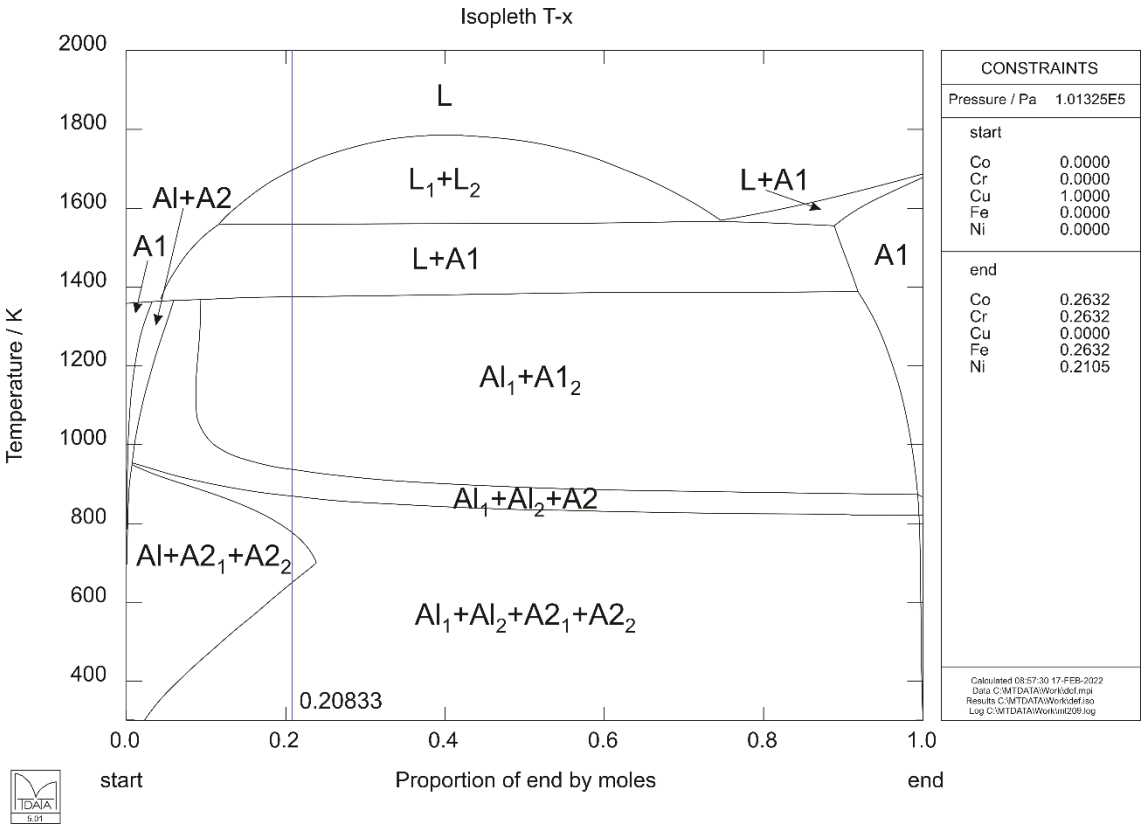

Figure 6.6 Calculated isopleth of pseudobinary Cu-CoCrFeNi$_{0.8}$ system. Location of alloy CoCrCuFeNi$_{0.8}$ is indicated by the vertical blue line, far from the critical point in the centre of the miscibility gap.

Following qualitative analysis of the relevant phase diagrams, and because such high cooling rates are required to initiate LPS, it is suggested that the alloy composition being studied is located away from the critical point of the miscibility gap for the CoCrFeNi$_{0.8}$-Cu pseudobinary system. If this is the case, a higher undercooling is required to initiate metastable LPS. More importantly, for a given composition, the difference in undercooling required for nucleation and growth and spinodal decomposition (i.e. the temperature interval between the binode and spinode at the chosen composition) will be much larger than it would be for compositions near the critical point.

The explanation for the drastically different behaviour of drop-tube processed CoCrCuFeNi$_{0.8}$ likely relies on a combination of the increase in droplet undercooling and a drastic reduction in cooling time. Both of these occur as the result of an increasing prevailing cooling rate in the drop-tube. A droplet with a lower diameter will cool much faster, and will also (on average) reach a higher undercooling prior to solidification. It is proposed that high cooling rates accessed during drop-tube processing suppress the occurrence of metastable LPS via a nucleation and growth mechanism. Concurrently, these rapidly cooling droplets achieve a high enough undercooling to undergo spinodal decomposition in the metastable regime by crossing the spinode curve of the

liquid-phase miscibility gap. The combination of these two phenomena are demonstrated in Figure 6.7 and Figure 6.8.

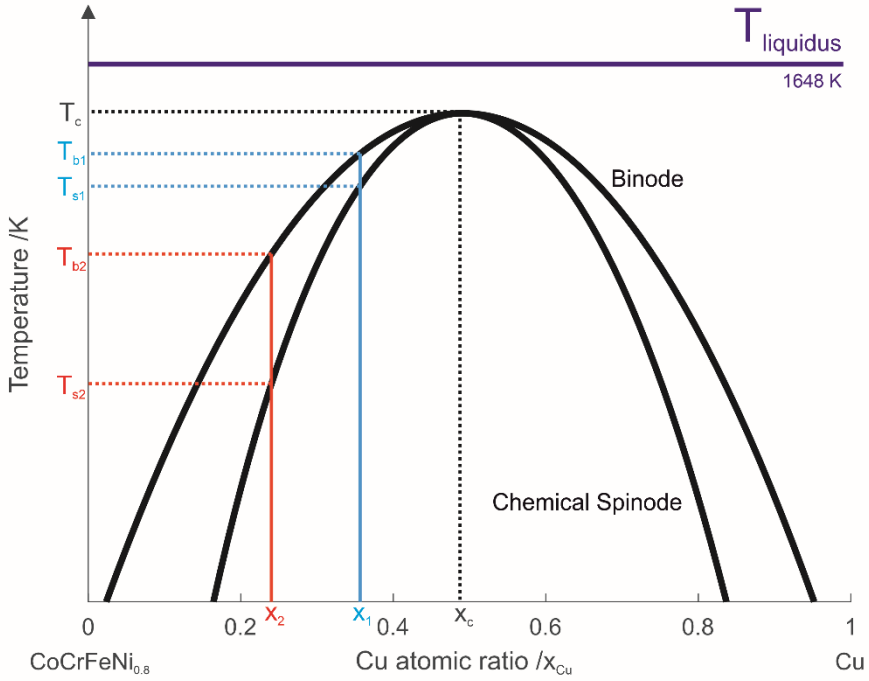

Figure 6.7 Example schematic of predicted metastable miscibility gap in $CoCrCuFeNi_{0.8}$ in the liquid state with two example solidification compositions and corresponding binode and spinode temperatures. As composition deviates from the critical composition X_c, undercoolings required to access the binode and spinode both increase. In addition, the interval between the binode and spinode also increases as deviation from the critical composition increases.

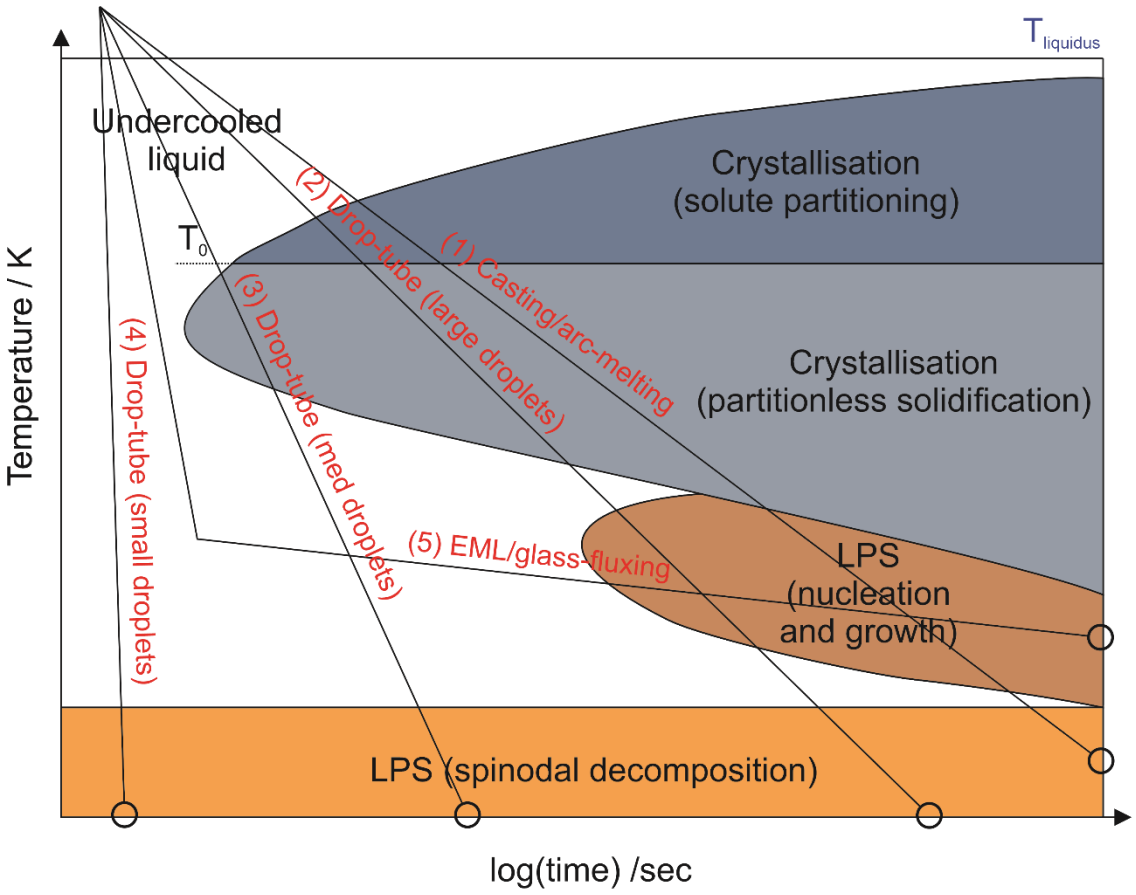

Figure 6.8 Schematic of qualitative Time-Temperature-Transformation curve for Co-Cr-Cu-Fe-Ni alloys solidified at varying cooling rates. Solidification pathways for typical non-equilibrium solidification techniques are superimposed on the diagram.

Figure 6.7 shows a qualitative example relationship between the binodal and spinodal curves in the metastable liquid-phase miscibility gap of a pseudobinary $CoCrFeNi_{0.8}$-Cu system. The critical temperature T_c and composition X_c are marked, showing the composition where LPS via nucleation and growth, and that occurring via spinodal decomposition, are predicted to occur at the same temperature. As we move further from the critical point, the critical undercoolings required to reach the binode and spinode both increase. More importantly, the difference between these undercoolings also increases. Composition X_2 for example, is farther from the critical composition than X_1. The phase separation temperatures T_{b2} and T_{s2} are both lower than the equivalent temperatures at composition X_1 (T_{b1} and T_{s1}). Additionally, at composition X_2, the temperature interval between the binode and spinode ($T_{b2} - T_{s2}$) is also larger than the equivalent interval ($T_{b1} - T_{s1}$) at composition X_1. If a droplet is cooled at a high enough cooling rate where LPS via nucleation and growth is inhibited, the undercooling must be high enough to access the spinode at the same composition for LPS is to occur and be observed in the final microstructure. Away from the critical point, the additional undercooling required

to reach the spinode becomes much larger. In the drop-tube, such undercoolings would likely only be routinely accessible in small droplets that have solidified extremely rapidly.

Figure 6.8 shows an example Time-Temperature-Transformation (TTT) curve that compares the behaviour of the $CoCrCuFeNi_{0.8}$ alloy (and other Co-Cr-Cu-Fe-Ni based alloys) cooled at various cooling rates and reaching various undercoolings before nucleation of a phase transformation. Conventionally cast and arc-melted samples do not experience extremely high cooling rates, nor can they be used to extensively undercool a sample below the liquidus before solidification. This is usually due to the enhancement of nucleation by impurities in the melt or via contact with the container walls. Therefore, it is unlikely that extensive phase separation occurs using these techniques. This is observed in the arc-melted sample (Figure 5.2) where a dendritic structure predominates throughout the vast majority of the ingot. Glass-fluxing experiments such as those in [143-148] and the EML experiment discussed by Yan et al. [24], allow liquid alloy droplets to be held at high undercoolings for exponentially longer than would be possible in drop-tube processing due to the inhibition of heterogenous nucleation. For a droplet undercooled into the metastable miscibility gap, such solidification techniques allow sufficient time for nucleation of minority phase droplets and even subsequent growth and coalescence into core-shell structures. The metastable binode is therefore accessible using these techniques. Accessing the binode is apparently not possible in drop-tube experiments on similar alloys, likely because of the comparatively high cooling rates. Even the larger droplets of $CoCrCuFeNi_{0.8}$ are predicted to have been at rates of nearly 1000 K s^{-1}. The average droplet cools even faster, upwards of 5000 K s^{-1} in the liquid state. However, the lack of LPS observed in these droplets shows that these cooling rates are still likely not enough to achieve the undercooling required to initiate spinodal decomposition.

In the smallest droplets, which experience liquid-phase cooling rates of nearly 60000 K s^{-1}. It seems that it has been occasionally possible to cool the droplets so rapidly that the spinode in the metastable liquid phase miscibility gap can be accessed. Once this is the case, LPS will occur spontaneously. Therefore, LPS structures are observed, but only in some of the highest cooling rate droplets.

This conjecture, while unconfirmed, explains both the general lack of occurrence of LPS in drop-tube processed Co-Cr-Cu-Fe-Ni based alloys compared to those processed by EML or glass-fluxing, and the occurrence of LPS in only the smallest droplets of $CoCrCuFeNi_{0.8}$ created in the drop-tube.

Similar logic can also be used to explain the lack of fully-realised LPS structures. The formation of macro-segregated LPS structures such as egg-type and core-shell structures depends on the available time for coalescence of minority phase droplets by Stokes motion or Marangoni convection respectively. In the absence of the time required, the Cu-rich minority phase droplets would not have enough time to move through liquid and coalesce before solidification, preserving a finely dispersed microstructure. The droplets in Figure 5.29, with pockets of Cu-rich phase dispersed between the CoCrFeNi-rich dendrites, is particularly comparable to LPS structures where coalescence has been arrested in the initial stages. The high cooling rates which allow LPS to occur via a spinodal mechanism may also hinder the subsequent structural formation. The dispersed morphology is also consistent with droplets in which the minority phase occupies a low volume fraction [125]. Because of this, extensive coalescence of minority phase droplets into a fully formed core-shell structure is rendered more unlikely, particularly given the reduced amount of time available in the rapid-cooling environment of the drop-tube.

6.4 Unified pathways of solidification in $CoCrCuFeNi_{0.8}$

As a final discussion point, it is helpful to attempt to summarize the occurrence of the most statistically prevalent and/or most notable solidification morphologies to begin to form a full description of the solidification paths in $CoCrCuFeNi_{0.8}$. A complicated and varied series of structures formed demands a similarly complicated explanation of the interplay between the specific thermodynamic and kinetic conditions inherent in there formation. This will be briefly attempted here.

At the lowest undercoolings below the first grain refinement transition $\Delta T < \Delta T_{GR}^{(1)}$ the alloy will most often solidify in a classically dendritic fashion. With CoCrFeNi-rich dendrites nucleating and rejecting solute (mostly Cu) into the residual liquid. This results in the formation of a Cu-rich interdendritic phase.

As undercooling increases in the range where $\Delta T_{GR}^{(1)} < \Delta T < \Delta T_{PS}$, grain refinement is now possible via dendrite remelting and fragmentation. From here, the extent of grain refinement is determined by the droplet cooling rate. Droplets which cool slower will consist of more refined, spherodized grains, while those which cannot fully refine in the available time will form a partially refined structure consisting of smaller spherodised grains located between larger fragments which have preserved some of their dendritic characteristics. A clear growth direction of these dendrites can be deduced and side branches may still be visible.

Between $\Delta T_{GR}^{(1)}$ and $\Delta T_{GR}^{(2)}$ lies the undercooling ΔT_{PS} at which partitionless solidificaiton becomes thermodynamically possible. When undercooling falls in the range $\Delta T_{PS} < \Delta T < \Delta T_{GR}^{(2)}$ the temperature of the undercooled droplet falls below T_0 and the solid which nucleates in the melt is of the same composition as the liquid from which it nucleates. Growth of such dendrites is now thermally-controlled. The dendrites grow and release energy in the form of latent heat into the remaining liquid which begins to decrease undercooling. At a certain point, the temperature of the remaining liquid rises back above T_0 and solute partitioning resumes. Parts of the droplet which solidify later in the transformation (e.g. secondary and tertiary dendrite arms, as well as the outer edges of primary dendrites) solidify under solute controlled growth. As the droplet cools further, the primary dendrite cores which have solidified without solute partitioning become unstable at a specific temperature. Solid-state decomposition is initiated and spherical, Cu-rich precipitates form in these regions. It is debatable, but more likely, that these form via a spinodal mechanism.

At yet higher undercoolings when $\Delta T_{GR}^{(2)} < \Delta T < \Delta T_{LPS}$, a second episode of grain-refinement will occur. Because the droplet is also undercooled below the T_0 temperature, some dendrites will solidify in a partitionless manner before grain refinement occurs. As the dendrites partially re-melt and fragment, the resultant grain refined grains that are formed of the partitionless dendrites will subsequently undergo a decomposition reaction in the solid-state. Cu-rich dispersoids will form in these refined grains just as they formed in their parent dendrites. However, as with the grain-refinement encountered at lower undercoolings (ΔT_1^{GR}) the cooling rate controls the extent to which grain refinement can occur in the rapidly solidified droplets. In this case, because cooling rates are likely much higher than before, there are some cases where the time required for grain refinement is drastically reduced. Instances of grain refinement will therefore mostly only be to a partial extent. Furthermore, such high cooling rates may inhibit the grain-refinement process altogether.

Finally, once undercooling has reached the characteristic undercooling required for LPS via a spinodal mechanism $\Delta T_{LPS} < \Delta T$, minority phase droplet of Cu-rich liquid are formed throughout the droplet volume. These then coalesce and coarsen via a diffusion process, although this process is significantly inhibited by the very high cooling rate at which LPS occurs in this alloy. Minority phase droplets may migrate to the centre or accumulate at the edges of the droplet before solidification begins. Once solidification begins, CoCrFeNi-rich dendrites grow into the melt. Instead of rejecting Cu into the residual liquid, an interdendritic phase that is Cr-Fe rich forms instead. A three-phase structure is

thus the result of LPS in this alloy. These transformations are represented graphically in Figure 6.9.

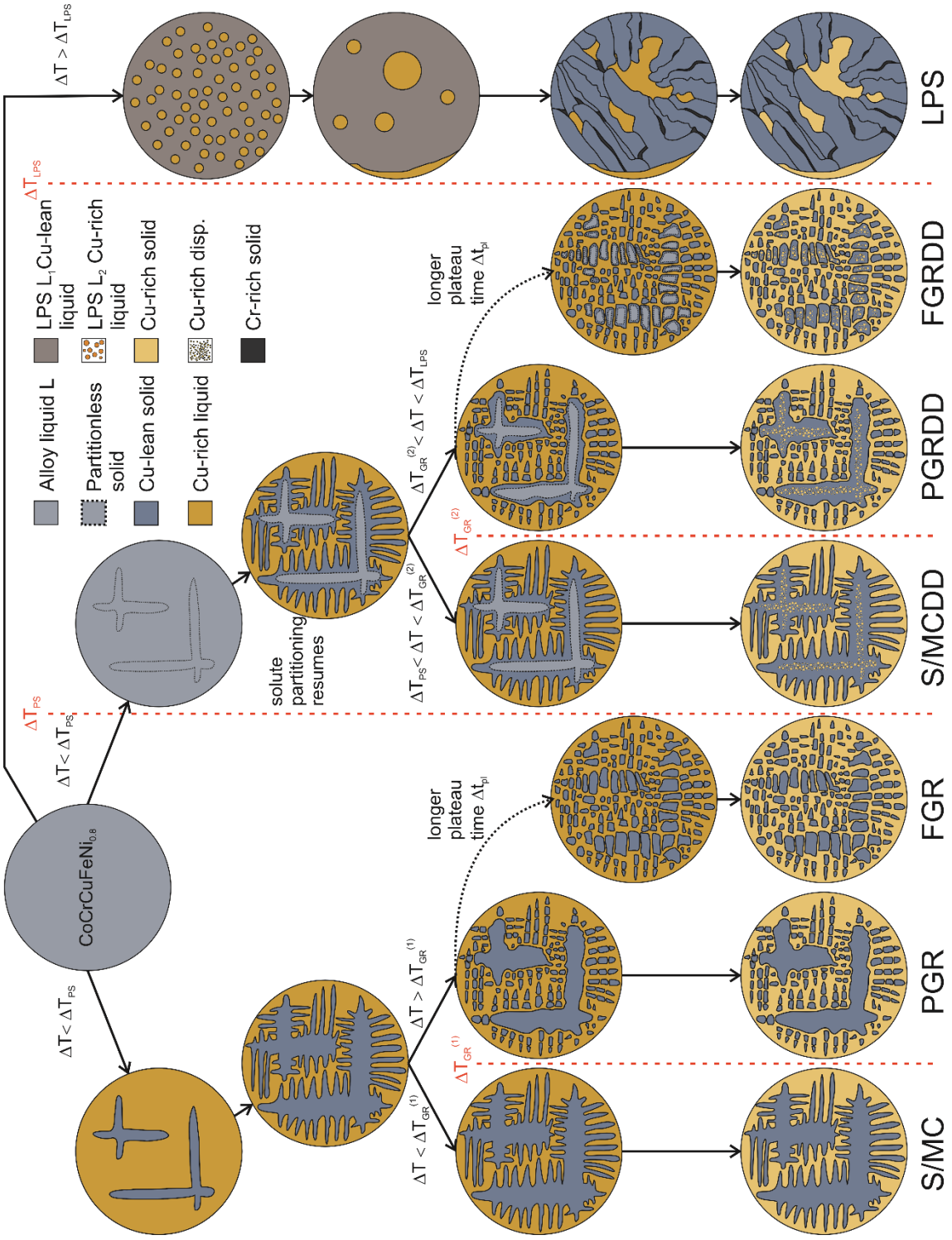

Figure 6.9 Structural formation diagram of principal formed microstructures in drop-tube processed $CoCrCuFeNi_{0.8}$

Chapter 7 – Conclusions

Based on extensive theoretical and experimental work conducted throughout this investigation, the initially stated experimental objectives can now be addressed, and conclusions, made, about the nature of solidification in $CoCrCuFeNi_{0.8}$ at high cooling rates.

1. A $CoCrCuFeNi_{0.8}$ dual-phase FCC HEA has been successfully processed via arc-melting and drop-tube processing solidification techniques. Arc-melting has allowed alloy phase transformations to be studied as they occur at lower cooling rates in a near-equilibrium solidification environment. Drop-tube processing has allowed solidification of the alloy in a containerless, low-gravity environment and the achievement of maximum calculated cooling rates of between 600 K s^{-1} and 60000 K s^{-1} in the largest and smallest droplets respectively.
2. Droplets were obtained with diameters ranging from above 1000 μm to 38 μm divided into 9 distinct sieve size fractions (e.g. > 850 μm, 850 – 500 μm, …53 – 38 μm). A survey was taken of the possible obtainable microstructures in each size fraction of the drop-tube processed alloy and droplets in each size fraction were then classified based on prevailing microstructure. Quantification of the difference in structural occurrence between randomly selected samples of droplets in each size fraction allowed a minimum sample size of 250 to be justified as a statistically representative sample for each size fraction. As a result, about 2500 individual droplets across the full diameter range were analysed and classified according to the type of prevailing microstructure in the droplet. Statistical analysis was then successfully conducted to determine changes in occurrence rate in each structure with droplet size and cooling rate. This analysis also made estimation of uncertainty in occurrence rate possible.
3. Contrary to the initial hypothesis made during tailoring of the alloy composition, LPS in the metastable regime was not observed to a statistically significant extent in drop-tube processed $CoCrCuFeNi_{0.8}$. The occurrence rate of liquid phase separation microstructures such as core-shell structures is vanishingly small. This result was compared to previous studies in which similar alloys were solidified via various solidification techniques. The lack of LPS was attributed to the alloy composition, which was likely located far from the critical composition, and the high cooling rates in the drop-tube which potentially suppressed nucleation and growth mechanisms responsible for binodal liquid phase

separation. This highlights the importance of the alloy selection and solidification technique used when discussing obtainable structures during non-equilibrium solidification of HEAs.

4. In lieu of the predicted structures, numerous other microstructures were found to occur to a statistically significant extent and were catalogued. Of these, the two most common were the occurrence of Cu-rich dispersoids located in primary dendrite cores, and of spontaneous grain-refinement.
5. Cu-rich dispersoids in dendrite cores were found to be the result of decomposition in the solid state. This decomposition was caused by supersaturation of cores of dendrites that had undergone chemically partitionless solidification. Rather than being the result of severe kinetic solute trapping due to rapid dendritic growth, partitionless solidification was concluded to be the result of undercooling below the alloy T_0 temperature. The resultant decomposition and formation of Cu-rich dispersoids is thought, on balance, to be the result of a spinodal mechanism. Partitionless solidification is therefore only dependent on alloy cooling rate because cooling rate increases the average obtainable undercooling before solidification begins. Dendrite growth velocity seems to play a minimal role in changing the nature of solute partitioning in $CoCrCuFeNi_{0.8}$.
6. Spontaneous grain refinement in $CoCrCuFeNi_{0.8}$ was deemed to have been caused by a dendrite remelting and fragmentation mechanism defined by the models of Schwarz et al. and Karma [40, 41]. In contrast, the superheating model of Li et al. [42] appears to have been disproven for this alloy and minimal evidence has been found for the occurrence of grain-refinement via recrystallisation. the high cooling rates obtained in the drop-tube were found to have a substantial effect on refinement morphology and, therefore, the extent of grain refinement possible in the alloy.
7. LPS was found to have occurred in droplets solidified at the highest cooling rates (and hence, at very high predicted undercooling). It was therefore deemed to have initiated via a spinodal mechanism. Interestingly, the occurrence of LPS appears to preclude the possibility of partitionless solidification. This is likely due to the reduction in driving force caused by the reduction of Cu supersaturation of the CoCrFeNi-rich phase after LPS.

Chapter 8 – Future Work

While the investigations contained within this study have allowed for significant elucidation of phase transformations in rapidly solidified $CoCrCuFeNi_{0.8}$, further work is encouraged to resolve some of the questions which have resulted from the preceding theoretical and experimental analyses. A non-exhaustive list of avenues for further exploration is provided below:

1. The reasons for the lack of predicted metastable LPS in $CoCrCuFeNi_{0.8}$ should be studied further. Solidification of $CoCrCuFeNi_{0.8}$ in an EML or glass-fluxing environment may shed light on whether or not metastable LPS is possible in this alloy if sufficient time is provided for such a transformation to take place in the undercooled alloy before solidification. In addition or alternatively, drop-tube studies should be undertaken for equiatomic CoCrCuFeNi (an alloy that has been shown to undergo metastable LPS) to determine if the high cooling-rate environment of the drop-tube is prohibitive to the occurrence of LPS in general. Use of EML or glass-fluxing techniques may also allow for measurement of the undercooling required for some, or all, of the phase transformations observed in $CoCrCuFeNi_{0.8}$
2. To more conclusively determine the mechanism of the solid-state decomposition reactions in partitionlessly solidified dendrite cores, more extensive and detailed composition analysis of the nanoscale Cu-rich dispersoids is required. Variation in composition of these dispersoids may indicate a nucleation and growth mechanism in lieu of spinodal decomposition, or even the occurrence of both nucleation and growth and spinodal decomposition in the same dendrite core. Determining the presence, or not, of Cu-lean zones surrounding some, or all, of the dispersoids could also allow identification of the primary mechanism(s) involved in the decomposition reaction. This analysis can be done using compositional point spectra or line scans in a TEM.
3. More work should be undertaken to fully substantiate the chosen mechanism for grain-refinement in $CoCrCuFeNi_{0.8}$. EBSD analysis may provide a more validated analysis of grain orientation, and the presence, or not, of grain boundaries within the CoCrFeNi-rich grain-refined grains. This could allow for elimination of more suggested refinement mechanisms (such as recrystallisation) or the acquisition of more data in favour of one.
4. As with many HEA systems, more work should be undertaken to determine the phase diagram either via more complete thermodynamic

modelling, or direct experimental evaluation. This will allow for more precise phase selection and tailoring of alloy composition.

Sources Cited

1. Tsai, M.-H. and Yeh, J.-W. High-entropy alloys: a critical review. *Materials Research Letters*. 2014, **2**(3), pp.107-123.
2. George, E.P., Raabe, D. and Ritchie, R.O. High-entropy alloys. *Nature Reviews Materials*. 2019, **4**(8), pp.515-534.
3. Murty, B.S., Yeh, J.-W., Ranganathan, S. and Bhattacharjee, P. *High-entropy alloys.* Elsevier, 2019.
4. Cantor, B., Chang, I., Knight, P. and Vincent, A. Microstructural development in equiatomic multicomponent alloys. *Materials Science and Engineering: A*. 2004, **375**, pp.213-218.
5. Yeh, J.W., Chen, S.K., Lin, S.J., Gan, J.Y., Chin, T.S., Shun, T.T., Tsau, C.H. and Chang, S.Y. Nanostructured high-entropy alloys with multiple principal elements: novel alloy design concepts and outcomes. *Advanced Engineering Materials*. 2004, **6**(5), pp.299-303.
6. Ranganathan, S. Alloyed pleasures: multimetallic cocktails. *Current science*. 2003, **85**(10), pp.1404-1406.
7. Li, Z., Pradeep, K.G., Deng, Y., Raabe, D. and Tasan, C.C. Metastable high-entropy dual-phase alloys overcome the strength–ductility trade-off. *Nature*. 2016, **534**(7606), pp.227-230.
8. Pan, Q., Zhang, L., Feng, R., Lu, Q., An, K., Chuang, A.C., Poplawsky, J.D., Liaw, P.K. and Lu, L. Gradient cell–structured high-entropy alloy with exceptional strength and ductility. *Science*. 2021, **374**(6570), pp.984-989.
9. Kumar, N.K., Li, C., Leonard, K., Bei, H. and Zinkle, S. Microstructural stability and mechanical behavior of FeNiMnCr high entropy alloy under ion irradiation. *Acta materialia*. 2016, **113**, pp.230-244.
10. El-Atwani, O., Li, N., Li, M., Devaraj, A., Baldwin, J., Schneider, M.M., Sobieraj, D., Wróbel, J.S., Nguyen-Manh, D. and Maloy, S.A. Outstanding radiation resistance of tungsten-based high-entropy alloys. *Science advances*. 2019, **5**(3), p.eaav2002.
11. Senkov, O.N., Wilks, G.B., Scott, J.M. and Miracle, D.B. Mechanical properties of Nb25Mo25Ta25W25 and V20Nb20Mo20Ta20W20 refractory high entropy alloys. *Intermetallics*. 2011, **19**(5), pp.698-706.
12. Senkov, O., Scott, J., Senkova, S., Meisenkothen, F., Miracle, D. and Woodward, C. Microstructure and elevated temperature properties of a refractory TaNbHfZrTi alloy. *Journal of materials science*. 2012, **47**, pp.4062-4074.
13. Xie, P., Yao, Y., Huang, Z., Liu, Z., Zhang, J., Li, T., Wang, G., Shahbazian-Yassar, R., Hu, L. and Wang, C. Highly efficient decomposition of ammonia using high-entropy alloy catalysts. *Nature communications*. 2019, **10**(1), p.4011.
14. Li, H., Han, Y., Zhao, H., Qi, W., Zhang, D., Yu, Y., Cai, W., Li, S., Lai, J. and Huang, B. Fast site-to-site electron transfer of high-entropy alloy nanocatalyst driving redox electrocatalysis. *Nature communications*. 2020, **11**(1), p.5437.

15. Jones, H. The status of rapid solidification of alloys in research and application. *Journal of materials science*. 1984, **19**, pp.1043-1076.
16. Lavernia, E.J. and Srivatsan, T.S. The rapid solidification processing of materials: science, principles, technology, advances, and applications. *Journal of materials science*. 2010, **45**, pp.287-325.
17. Jacobson, L.A. and McKittrick, J. Rapid solidification processing. *Materials Science and Engineering: R: Reports*. 1994, **11**(8), pp.355-408.
18. Herlach, D., Cochrane, R., Egry, I., Fecht, H. and Greer, A. Containerless processing in the study of metallic melts and their solidification. *International Materials Reviews*. 1993, **38**(6), pp.273-347.
19. Oloyede, O., Bigg, T.D., Cochrane, R.F. and Mullis, A.M. Microstructure evolution and mechanical properties of drop-tube processed, rapidly solidified grey cast iron. *Materials Science and Engineering: A*. 2016, **654**, pp.143-150.
20. Abul, M.R., Cochrane, R.F. and Mullis, A.M. Microstructural development and mechanical properties of drop tube atomized Al-2.85 wt% Fe. *Journal of Materials Science & Technology*. 2022, **104**, pp.41-51.
21. Derimow, N. and Abbaschian, R. Liquid phase separation in high-entropy alloys—a review. *Entropy*. 2018, **20**(11), p.890.
22. Zhang, H., Pan, Y. and He, Y.-Z. Synthesis and characterization of FeCoNiCrCu high-entropy alloy coating by laser cladding. *Materials & Design*. 2011, **32**(4), pp.1910-1915.
23. Zhang, H., He, Y.-Z., Pan, Y. and Guo, S. Thermally stable laser cladded CoCrCuFeNi high-entropy alloy coating with low stacking fault energy. *Journal of alloys and compounds*. 2014, **600**, pp.210-214.
24. Yan, P., Chang, J., Wang, W., Zhu, X., Lin, M. and Wei, B. Metastable phase separation and crystalline orientation feature of electromagnetic levitation processed CoCrCuFeNi high entropy alloy. *Acta materialia*. 2024, p.119778.
25. Andreoli, A.F., Shuleshova, O., Witusiewicz, V.T., Wu, Y., Yang, Y., Ivashko, O., Dippel, A.-C., Zimmermann, M.v., Nielsch, K. and Kaban, I. In situ study of non-equilibrium solidification of CoCrFeNi high-entropy alloy and CrFeNi and CoCrNi ternary suballoys. *Acta materialia*. 2021, **212**, p.116880.
26. Porter, D.A. and Easterling, K.E. *Phase transformations in metals and alloys (revised reprint).* CRC press, 2009.
27. Kurz, W. and Fisher, D. *Fundamentals of Solidification.* Trans Tech Publications Limited, 1998.
28. Callister Jr, W.D. and Rethwisch, D.G. *Materials science and engineering: an introduction.* John wiley & sons, 2020.
29. Greer, A. Grain refinement in rapidly solidified alloys. *Materials Science and Engineering: A*. 1991, **133**, pp.16-21.
30. Ma, M., Wang, Z. and Zeng, X. A comparison on metallurgical behaviors of 316L stainless steel by selective laser melting and laser cladding deposition. *Materials Science and Engineering: A*. 2017, **685**, pp.265-273.
31. Chen, Z., Lei, Y. and Zhang, H. Structure and properties of nanostructured A357 alloy produced by melt spinning compared with direct chill ingot. *Journal of alloys and compounds*. 2011, **509**(27), pp.7473-7477.

32. Zhang, Y., Huang, B. and Li, J. Microstructural evolution with a wide range of solidification cooling rates in a Ni-based superalloy. *Metallurgical and materials transactions A*. 2013, **44**, pp.1641-1644.
33. Seetharaman, V. and Trivedi, R. Eutectic growth: Selection of interlamellar spacings. *Metallurgical transactions A*. 1988, **19**, pp.2955-2964.
34. Çadirli, E. and Gündüz, M. The dependence of lamellar spacing on growth rate and temperature gradient in the lead–tin eutectic alloy. *Journal of Materials Processing Technology*. 2000, **97**(1-3), pp.74-81.
35. Wang, Q. Microstructural effects on the tensile and fracture behavior of aluminum casting alloys A356/357. *Metallurgical and materials transactions A*. 2003, **34**, pp.2887-2899.
36. Mullis, A.M. The origins of spontaneous grain refinement in deeply undercooled metallic melts. *Metals*. 2014, **4**(2), pp.155-167.
37. Pierre, G.R.S. *Physical Chemistry of Process Metallurgy.* Interscience, 1961.
38. Wang, H., Liu, F. and Tan, Y. Modeling grain refinement for undercooled single-phase solid-solution alloys. *Acta materialia*. 2011, **59**(12), pp.4787-4797.
39. Trivedi, R., Lipton, J. and Kurz, W. Effect of growth rate dependent partition coefficient on the dendritic growth in undercooled melts. *Acta metallurgica*. 1987, **35**(4), pp.965-970.
40. Schwarz, M., Karma, A., Eckler, K. and Herlach, D. Physical mechanism of grain refinement in solidification of undercooled melts. *Physical review letters*. 1994, **73**(10), p.1380.
41. Karma, A. Model of grain refinement in solidification of undercooled melts. *International Journal of Non-Equilibrium Processing(UK)*. 1998, **11**(2), pp.201-233.
42. Li, J., Liu, Y., Lu, Y., Yang, G. and Zhou, Y. Structural evolution of undercooled Ni–Cu alloys. *Journal of crystal growth*. 1998, **192**(3-4), pp.462-470.
43. Vitek, J., Dasgupta, A. and David, S. Microstructural modification of austenitic stainless steels by rapid solidification. *Metallurgical transactions A*. 1983, **14**, pp.1833-1841.
44. Pryds, N. and Pedersen, A.S. Rapid solidification of martensitic stainless steel atomized droplets. *Metallurgical and materials transactions A*. 2002, **33**, pp.3755-3761.
45. Jones, H. Formation of metastable crystalline phases in light-metal systems by rapid solidification. *Philosophical Magazine B*. 1990, **61**(4), pp.487-509.
46. Hehmann, F., Sommer, F. and Predel, B. Extension of solid solubility in magnesium by rapid solidification. *Materials Science and Engineering: A*. 1990, **125**(2), pp.249-265.
47. Xinming, Z., Yuantao, N. and Qubo, L. Extension of solid solubility of rare earth metals in copper by rapid solidification. *Journal of alloys and compounds*. 1992, **183**, pp.168-173.
48. Yuantao, N. and Xinming, Z. Metastable extension of solid solubility of alloying elements in silver. *Journal of alloys and compounds*. 1992, **182**(1), pp.131-144.
49. Fecht, H. and Perepezko, J. Metastable phase equilibria in the lead-tin alloy system: Part I. Experimental. *Metallurgical transactions A*. 1989, **20**, pp.785-794.

50. Boettinger, W., Coriell, S. and Sekerka, R. Mechanisms of microsegregation-free solidification. *Materials Science and Engineering*. 1984, **65**(1), pp.27-36.
51. Colligan, G. and Bayles, B. Dendrite growth velocity in undercooled nickel melts. *Acta metallurgica*. 1962, **10**(9), pp.895-897.
52. Battersby, S., Cochrane, R. and Mullis, A. Growth velocity-undercooling relationships and microstructural evolution in undercooled Ge and dilute Ge-Fe alloys. *Journal of materials science*. 1999, **34**, pp.2049-2056.
53. Luo, S., Wang, W., Chang, J., Xia, Z. and Wei, B. A comparative study of dendritic growth within undercooled liquid pure Fe and Fe50Cu50 alloy. *Acta materialia*. 2014, **69**, pp.355-364.
54. Funke, O., Phanikumar, G., Galenko, P., Chernova, L., Reutzel, S., Kolbe, M. and Herlach, D. Dendrite growth velocity in levitated undercooled nickel melts. *Journal of crystal growth*. 2006, **297**(1), pp.211-222.
55. Herlach, D.M. Solidification from undercooled melts. *Materials Science and Engineering: A*. 1997, **226**, pp.348-356.
56. Herlach, D.M. Dendrite growth kinetics in undercooled melts of intermetallic compounds. *Crystals*. 2015, **5**(3), pp.355-375.
57. Biloni, H. and Chalmers, B. Predendritic solidification. *Transactions of the Metallurgical Society of AIME*. 1965, **233**, p.373.
58. Baker, J. and Gahn, J. Solute trapping by rapid solidification. *Acta metallurgica*. 1969, **17**(5), pp.575-578.
59. Aziz, M.J. and Kaplan, T. Continuous growth model for interface motion during alloy solidification. *Acta metallurgica*. 1988, **36**(8), pp.2335-2347.
60. Aziz, M.J. Model for solute redistribution during rapid solidification. *Journal of Applied Physics*. 1982, **53**(2), pp.1158-1168.
61. Willnecker, R., Herlach, D. and Feuerbacher, B. Evidence of nonequilibrium processes in rapid solidification of undercooled metals. *Physical review letters*. 1989, **62**(23), p.2707.
62. Eckler, K., Cochrane, R., Herlach, D., Feuerbacher, B. and Jurisch, M. Evidence for a transition from diffusion-controlled to thermally controlled solidification in metallic alloys. *Physical Review B*. 1992, **45**(9), p.5019.
63. Galenko, P. and Danilov, D. Local nonequilibrium effect on rapid dendritic growth in a binary alloy melt. *Physics Letters A*. 1997, **235**(3), pp.271-280.
64. Baker, J.C. and Cahn, J.W. *Thermodynamics of solidification*. American Society for Metals Metals Park, Ohio. 1971, p.23.
65. Kostorz, G. *Phase transformations in materials.* Wiley Online Library, 2001.
66. Zhao, J.-Z., Ahmed, T., Jiang, H.-X., He, J. and Sun, Q. Solidification of immiscible alloys: a review. *Acta Metallurgica Sinica (English Letters)*. 2017, **30**(1), pp.1-28.
67. Ratke, L. and Diefenbach, S. Liquid immiscible alloys. *Materials Science and Engineering: R: Reports*. 1995, **15**(7-8), pp.263-347.
68. Singh, R. and Sommer, F. Segregation and immiscibility in liquid binary alloys. *Reports on Progress in physics*. 1997, **60**(1), p.57.
69. Kim, D., Kim, W., Park, E., Mattern, N. and Eckert, J. Phase separation in metallic glasses. *Progress in Materials Science*. 2013, **58**(8), pp.1103-1172.
70. Kaban, I., Köhler, M., Ratke, L., Nowak, R., Sobczak, N., Mattern, N., Eckert, J., Greer, A., Sohn, S. and Kim, D. Phase separation in

monotectic alloys as a route for liquid state fabrication of composite materials. *Journal of materials science*. 2012, **47**(24), pp.8360-8366.
71. Cochrane, R., Evans, P. and Greer, A. Containerless solidification of alloys in a drop-tube. *Materials Science and Engineering*. 1988, **98**, pp.99-103.
72. Nakagawa, Y. Liquid immiscibility in copper-iron and copper-cobalt systems in the supercooled state. *Acta metallurgica*. 1958, **6**(11), pp.704-711.
73. James, P. Liquid-phase separation in glass-forming systems. *Journal of materials science*. 1975, **10**(10), pp.1802-1825.
74. Ratke, L. and Thieringer, W. The influence of particle motion on Ostwald ripening in liquids. *Acta metallurgica*. 1985, **33**(10), pp.1793-1802.
75. JIA, J. and LI, Q. Modeling and simulation of the microstructure evolution during a cooling of immiscible alloys in the miscibility gap. *J. Mater. Sci. Technol*. 2002, **18**(3).
76. Landau, L.D. and Lifshitz, E.M. Hydrodynamik. *Lehrbuch der theoretischen Physik*. 1966.
77. Probstein, R.F. *Physicochemical hydrodynamics: an introduction.* John Wiley & Sons, 2005.
78. Legros, J., Sanfeld, A. and Velarde, M. *Fluid Sciences and Materials Science in Space*. Springer-Verlag, Berlin, Germany. 1987.
79. Mebed, A. and Miyazaki, T. Computer simulation and experimental investigation of the spinodal decomposition in the β Ti-Cr binary alloy system. *Metallurgical and materials transactions A*. 1998, **29**, pp.739-749.
80. Murray, J.L. Phase diagram of titanium alloys. *ASM*. 1987, **182**.
81. Findik, F. Improvements in spinodal alloys from past to present. *Materials & Design*. 2012, **42**, pp.131-146.
82. Tang, M. and Karma, A. Surface modes of coherent spinodal decomposition. *Physical review letters*. 2012, **108**(26), p.265701.
83. Smallman, R.E. *Modern physical metallurgy.* Elsevier, 2016.
84. Khachaturyan, A.G. *Theory of structural transformations in solids.* Courier Corporation, 2013.
85. Kazakov, N.F. *Diffusion bonding of materials.* Elsevier, 2013.
86. Laughlin, D.E. and Hono, K. *Physical metallurgy.* Newnes, 2014.
87. Liebermann, H. The dependence of the geometry of glassy alloy ribbons on the chill block melt-spinning process parameters. *Materials Science and Engineering*. 1980, **43**(3), pp.203-210.
88. Herlach, D.M. Containerless Undercooling and Solidification of Pure Metals. 1990.
89. Kui, H., Greer, A.L. and Turnbull, D. Formation of bulk metallic glass by fluxing. *Applied Physics Letters*. 1984, **45**(6), pp.615-616.
90. Willnecker, R., Herlach, D. and Feuerbacher, B. Containerless undercooling of bulk Fe-Ni melts. *Applied Physics Letters*. 1986, **49**(20), pp.1339-1341.
91. Dragnevski, K.I., Mullis, A.M. and Cochrane, R.F. The effect of experimental variables on the levels of melt undercooling. *Materials Science and Engineering: A*. 2004, **375**, pp.485-487.
92. Cao, C., Letzig, T., Görler, G. and Herlach, D. Liquid phase separation in undercooled Co–Cu alloys processed by electromagnetic levitation and differential thermal analysis. *Journal of alloys and compounds*. 2001, **325**(1-2), pp.113-117.

93. Matson, D., Battezzati, L., Galenko, P., Gandin, C.-A., Gangopadhyay, A., Henein, H., Kelton, K., Kolbe, M., Valloton, J. and Vogel, S. Electromagnetic levitation containerless processing of metallic materials in microgravity: rapid solidification. *npj Microgravity*. 2023, **9**(1), p.65.
94. Binder, S., Galenko, P. and Herlach, D. The effect of fluid flow on the solidification of Ni2B from the undercooled melt. *Journal of Applied Physics*. 2014, **115**(5).
95. Herlach, D.M. and Matson, D.M. *Solidification of containerless undercooled melts.* John Wiley & Sons, 2012.
96. Greer, A.L. Confusion by design. *Nature*. 1993, **366**(6453), pp.303-304.
97. Yeh, J.-W. Alloy design strategies and future trends in high-entropy alloys. *Jom*. 2013, **65**(12), pp.1759-1771.
98. Jien-Wei, Y. Recent progress in high entropy alloys. *Ann. Chim. Sci. Mat*. 2006, **31**(6), pp.633-648.
99. Miracle, D.B. and Senkov, O.N. A critical review of high entropy alloys and related concepts. *Acta materialia*. 2017, **122**, pp.448-511.
100. Yeh, J.-W., Chang, S.-Y., Hong, Y.-D., Chen, S.-K. and Lin, S.-J. Anomalous decrease in X-ray diffraction intensities of Cu–Ni–Al–Co–Cr–Fe–Si alloy systems with multi-principal elements. *Materials Chemistry and Physics*. 2007, **103**(1), pp.41-46.
101. He, Q. and Yang, Y. On lattice distortion in high entropy alloys. *Frontiers in Materials*. 2018, **5**, p.42.
102. Tsai, K.-Y., Tsai, M.-H. and Yeh, J.-W. Sluggish diffusion in Co–Cr–Fe–Mn–Ni high-entropy alloys. *Acta materialia*. 2013, **61**(13), pp.4887-4897.
103. Beke, D. and Erdélyi, G. On the diffusion in high-entropy alloys. *Materials Letters*. 2016, **164**, pp.111-113.
104. Vaidya, M., Pradeep, K., Murty, B., Wilde, G. and Divinski, S. Bulk tracer diffusion in CoCrFeNi and CoCrFeMnNi high entropy alloys. *Acta materialia*. 2018, **146**, pp.211-224.
105. Hume-Rothery, W. Phase stability in metals and alloys. *Series in Material Science and Engineering*. 1967, pp.3-23.
106. Massalski, T.B. and Mizutani, U. Electronic structure of Hume-Rothery phases. *Progress in Materials Science*. 1978, **22**(3-4), pp.151-262.
107. Hume-Rothery, W., Mabbott, G., W and Channel Evans, K. The freezing points, melting points, and solid solubility limits of the alloys of sliver and copper with the elements of the b sub-groups. *Philosophical Transactions of the Royal Society of London. Series A, Containing Papers of a Mathematical or Physical Character*. 1934, **233**(721-730), pp.1-97.
108. Poletti, M.G. and Battezzati, L. Electronic and thermodynamic criteria for the occurrence of high entropy alloys in metallic systems. *Acta materialia*. 2014, **75**, pp.297-306.
109. Smith, W.F., Hashemi, J. and Presuel-Moreno, F. *Foundations of materials science and engineering.* Mcgraw-Hill Publishing, 2006.
110. Zhang, Y., Zhou, Y.J., Lin, J.P., Chen, G.L. and Liaw, P.K. Solid-solution phase formation rules for multi-component alloys. *Advanced Engineering Materials*. 2008, **10**(6), pp.534-538.
111. Takeuchi, A. and Inoue, A. Mixing enthalpy of liquid phase calculated by Miedema's scheme and approximated with sub-regular solution model for assessing forming ability of amorphous and glassy alloys. *Intermetallics*. 2010, **18**(9), pp.1779-1789.

112. Sheng, G. and Liu, C.T. Phase stability in high entropy alloys: formation of solid-solution phase or amorphous phase. *Progress in Natural Science: Materials International*. 2011, **21**(6), pp.433-446.
113. Guo, S., Hu, Q., Ng, C. and Liu, C. More than entropy in high-entropy alloys: Forming solid solutions or amorphous phase. *Intermetallics*. 2013, **41**, pp.96-103.
114. Ren, M.-x., Li, B.-s. and Fu, H.-z. Formation condition of solid solution type high-entropy alloy. *Transactions of Nonferrous Metals Society of China*. 2013, **23**(4), pp.991-995.
115. Ye, Y., Wang, Q., Lu, J., Liu, C. and Yang, Y. High-entropy alloy: challenges and prospects. *Materials Today*. 2016, **19**(6), pp.349-362.
116. Takeuchi, A., Amiya, K., Wada, T., Yubuta, K., Zhang, W. and Makino, A. Entropies in alloy design for high-entropy and bulk glassy alloys. *Entropy*. 2013, **15**(9), pp.3810-3821.
117. Li, P., Wang, A. and Liu, C. A ductile high entropy alloy with attractive magnetic properties. *Journal of alloys and compounds*. 2017, **694**, pp.55-60.
118. Ahlborn, H. and Löhberg, K. Aluminium-indium-experiment SOLUOG-A sounding rocket experiment on immiscible alloys. In: *17th Aerospace Sciences Meeting*, 1979, p.172.
119. Potard, C. Directional solidification of Al-In alloys at microgravity-Results of basic preparatory investigations. In: *17th Aerospace Sciences Meeting*, 1979, p.173.
120. Wang, C., Liu, X., Ohnuma, I., Kainuma, R. and Ishida, K. Formation of immiscible alloy powders with egg-type microstructure. *Science*. 2002, **297**(5583), pp.990-993.
121. Wang, C.P., Liu, X.J., Shi, R.P., Shen, C., Wang, Y., Ohnuma, I., Kainuma, R. and Ishida, K. Design and formation mechanism of self-organized core/shell structure composite powder in immiscible liquid system. *Applied Physics Letters*. 2007, **91**(14), p.141904.
122. Dai, R., Zhang, S., Guo, X. and Li, J. Formation of core-type microstructure in Al–Bi monotectic alloys. *Materials Letters*. 2011, **65**(2), pp.322-325.
123. Dai, R., Zhang, S. and Li, J. One-step fabrication of Al/Sn-Bi core–shell spheres via phase separation. *Journal of electronic materials*. 2011, **40**(12), p.2458.
124. Dai, R., Zhang, J., Zhang, S. and Li, J. Liquid immiscibility and core-shell morphology formation in ternary Al–Bi–Sn alloys. *Materials Characterization*. 2013, **81**, pp.49-55.
125. Wang, N., Zhang, L., Peng, Y. and Yao, W. Composition-dependence of core-shell microstructure formation in monotectic alloys under reduced gravity conditions. *Journal of alloys and compounds*. 2016, **663**, pp.379-386.
126. Wang, W., Wu, Y., Li, L., Zhai, W., Zhang, X. and Wei, B. Liquid-liquid phase separation of freely falling undercooled ternary Fe-Cu-Sn alloy. *Scientific reports*. 2015, **5**, p.16335.
127. Yan, N., Hong, Z., Geng, D. and Wei, B. A comparison of acoustic levitation with microgravity processing for containerless solidification of ternary Al–Cu–Sn alloy. *Applied Physics A*. 2015, **120**(1), pp.207-213.
128. Jegede, O.E., Cochrane, R.F. and Mullis, A.M. Metastable monotectic phase separation in Co–Cu alloys. *Journal of materials science*. 2018, **53**(16), pp.11749-11764.

129. Wang, N. and Wei, B. Phase separation and structural evolution of undercooled Fe–Sn monotectic alloy. *Materials Science and Engineering: A*. 2003, **345**(1-2), pp.145-154.
130. Ratke, L., Korekt, G. and Drees, S. Solidification of immiscible alloys. In: *Space Station Utilisation*, 1996, p.247.
131. Hsu, U., Hung, U., Yeh, J., Chen, S., Huang, Y. and Yang, C. Alloying behavior of iron, gold and silver in AlCoCrCuNi-based equimolar high-entropy alloys. *Materials Science and Engineering: A*. 2007, **460**, pp.403-408.
132. Mishra, A.K., Samal, S. and Biswas, K. Solidification behaviour of Ti–Cu–Fe–Co–Ni high entropy alloys. *Transactions of the Indian Institute of Metals*. 2012, **65**, pp.725-730.
133. Munitz, A., Kaufman, M., Chandler, J., Kalaantari, H. and Abbaschian, R. Melt separation phenomena in CoNiCuAlCr high entropy alloy containing silver. *Materials Science and Engineering: A*. 2013, **560**, pp.633-642.
134. Derimow, N. and Abbaschian, R. Solidification microstructures and calculated mixing enthalpies in CoCrCu containing alloys. *Materials Today Communications*. 2018, **15**, pp.1-10.
135. Munitz, A., Kaufman, M. and Abbaschian, R. Liquid phase separation in transition element high entropy alloys. *Intermetallics*. 2017, **86**, pp.59-72.
136. Rahul, M., Samal, S. and Phanikumar, G. Effect of niobium addition in FeCoNiCuNb x high-entropy alloys. *Journal of Materials Research*. 2019, **34**(5), pp.700-708.
137. Churyumov, A.Y., Pozdniakov, A., Bazlov, A., Mao, H., Polkin, V. and Louzguine-Luzgin, D.V. Effect of Nb addition on microstructure and thermal and mechanical properties of Fe-Co-Ni-Cu-Cr multiprincipal-element (high-entropy) alloys in as-cast and heat-treated state. *Jom*. 2019, **71**, pp.3481-3489.
138. Wu, P., Liu, N., Yang, W., Zhu, Z., Lu, Y. and Wang, X. Microstructure and solidification behavior of multicomponent CoCrCuxFeMoNi high-entropy alloys. *Materials Science and Engineering: A*. 2015, **642**, pp.142-149.
139. Peng, Z., Liu, N., Zhang, S., Wu, P. and Wang, X. Liquid-phase separation of immiscible CrCu x FeMo y Ni high-entropy alloys. *Materials Science and Technology*. 2017, **33**(11), pp.1352-1359.
140. Rahul, M., Samal, S. and Phanikumar, G. Metastable microstructures in the solidification of undercooled high entropy alloys. *Journal of alloys and compounds*. 2020, **821**, p.153488.
141. Nagase, T., Todai, M. and Nakano, T. Liquid Phase Separation in Ag-Co-Cr-Fe-Mn-Ni, Co Cr-Cu-Fe-Mn-Ni and Co-Cr-Cu-Fe-Mn-Ni-B High Entropy Alloys for Biomedical Application. *Crystals*. 2020, **10**(6), p.527.
142. Nagase, T. Microstructure of Co-Cr-Fe-Mn-Ni-Cu and Co-Cr-Fe-Mn-Ni-Ag High Entropy Alloys with Liquid Phase Separation. In: *Materials Science Forum*: Trans Tech Publ, 2018, pp.1238-1241.
143. Liu, N., Wu, P., Zhou, P., Peng, Z., Wang, X. and Lu, Y. Rapid solidification and liquid-phase separation of undercooled CoCrCuFexNi high-entropy alloys. *Intermetallics*. 2016, **72**, pp.44-52.
144. Wu, P., Liu, N., Zhou, P., Peng, Z., Du, W., Wang, X. and Pan, Y. Microstructures and liquid phase separation in multicomponent CoCrCuFeNi high entropy alloys. *Materials Science and Technology*. 2016, **32**(6), pp.576-580.

145. Wang, W., Hu, L., Luo, S., Meng, L., Geng, D. and Wei, B. Liquid phase separation and rapid dendritic growth of high-entropy CoCrCuFeNi alloy. *Intermetallics*. 2016, **77**, pp.41-45.
146. Guo, T., Li, J., Wang, J., Wang, Y., Kou, H. and Niu, S. Liquid-phase separation in undercooled CoCrCuFeNi high entropy alloy. *Intermetallics*. 2017, **86**, pp.110-115.
147. Wang, W. and Kong, Z. Phase separation and microhardness of rapidly solidified high-entropy CoCrFeNiCux alloys. *Journal of alloys and compounds*. 2021, **853**, p.156451.
148. Lin, K., Wei, C., He, Y., Li, C., Zhang, P., Li, J. and Wang, J. Formation of core–shell structure in immiscible CoCrCuFe1. 5Ni0. 5 high-entropy alloy. *Materials Letters*. 2022, **321**, p.132452.
149. Wang, S., Chen, Z., Feng, L., Liu, Y., Zhang, P., He, Y., Meng, Q. and Zhang, J. Nano-phase formation accompanying phase separation in undercooled CoCrCuFeNi-3 at.% Sn high entropy alloy. *Materials Characterization*. 2018, **144**, pp.516-521.
150. Munitz, A., Samuha, S., Brosh, E., Salhov, S., Derimow, N. and Abbaschian, R. Liquid phase separation phenomena in Al2. 2CrCuFeNi2 HEA. *Intermetallics*. 2018, **97**, pp.77-84.
151. Munitz, A., Edry, I., Brosh, E., Derimow, N., MacDonald, B., Lavernia, E. and Abbaschian, R. Liquid phase separation in AlCrFeNiMo0. 3 high-entropy alloy. *Intermetallics*. 2019, **112**, p.106517.
152. Balakumar, T. and Medraj, M. Thermodynamic modeling of the Mg–Al–Sb system. *Calphad*. 2005, **29**(1), pp.24-36.
153. Schuh, B., Mendez-Martin, F., Völker, B., George, E.P., Clemens, H., Pippan, R. and Hohenwarter, A. Mechanical properties, microstructure and thermal stability of a nanocrystalline CoCrFeMnNi high-entropy alloy after severe plastic deformation. *Acta materialia*. 2015, **96**, pp.258-268.
154. Pickering, E., Muñoz-Moreno, R., Stone, H. and Jones, N. Precipitation in the equiatomic high-entropy alloy CrMnFeCoNi. *Scripta materialia*. 2016, **113**, pp.106-109.
155. Otto, F., Dlouhý, A., Pradeep, K.G., Kuběnová, M., Raabe, D., Eggeler, G. and George, E.P. Decomposition of the single-phase high-entropy alloy CrMnFeCoNi after prolonged anneals at intermediate temperatures. *Acta materialia*. 2016, **112**, pp.40-52.
156. Schuh, B., Völker, B., Todt, J., Schell, N., Perrière, L., Li, J., Couzinié, J. and Hohenwarter, A. Thermodynamic instability of a nanocrystalline, single-phase TiZrNbHfTa alloy and its impact on the mechanical properties. *Acta materialia*. 2018, **142**, pp.201-212.
157. Thiel, F., Geissler, D., Nielsch, K., Kauffmann, A., Seils, S., Heilmaier, M., Utt, D., Albe, K., Motylenko, M. and Rafaja, D. Origins of strength and plasticity in the precious metal based high-entropy alloy AuCuNiPdPt. *Acta materialia*. 2020, **185**, pp.400-411.
158. Yurchenko, N.Y., Stepanov, N.D., Tikhonovsky, M.A. and Salishchev, G.A. Phase evolution of the Al x NbTiVZr (x= 0; 0.5; 1; 1.5) high entropy alloys. *Metals*. 2016, **6**(12), p.298.
159. Yurchenko, N.Y., Stepanov, N., Gridneva, A., Mishunin, M., Salishchev, G. and Zherebtsov, S. Effect of Cr and Zr on phase stability of refractory Al-Cr-Nb-Ti-V-Zr high-entropy alloys. *Journal of alloys and compounds*. 2018, **757**, pp.403-414.

160. Shepelevich, V. and Gusakova, O. Decomposition of a supersaturated solid solution in thin foils of Sn-Bi alloys. *The Physics of Metals and Metallography*. 2009, **108**, pp.292-297.
161. Mykura, N., Zhu, Y. and Murphy, S. Solid-state reactions in Zn-Al based alloys. *Canadian Metallurgical Quarterly*. 1986, **25**(2), pp.151-159.
162. Gusakova, O.V., Galenko, P.K., Shepelevich, V.G., Alexandrov, D.V. and Rettenmayr, M. Diffusionless (chemically partitionless) crystallization and subsequent decomposition of supersaturated solid solutions in Sn–Bi eutectic alloy. *Philosophical Transactions of the Royal Society A*. 2019, **377**(2143), p.20180204.
163. Munitz, A., Meshi, L. and Kaufman, M. Heat treatments' effects on the microstructure and mechanical properties of an equiatomic Al-Cr-Fe-Mn-Ni high entropy alloy. *Materials Science and Engineering: A*. 2017, **689**, pp.384-394.
164. Wang, Y., Li, B., Ren, M., Yang, C. and Fu, H. Microstructure and compressive properties of AlCrFeCoNi high entropy alloy. *Materials Science and Engineering: A*. 2008, **491**(1-2), pp.154-158.
165. Manzoni, A., Daoud, H., Völkl, R., Glatzel, U. and Wanderka, N. Phase separation in equiatomic AlCoCrFeNi high-entropy alloy. *Ultramicroscopy*. 2013, **132**, pp.212-215.
166. Pickering, E., Stone, H. and Jones, N. Fine-scale precipitation in the high-entropy alloy Al0. 5CrFeCoNiCu. *Materials Science and Engineering: A*. 2015, **645**, pp.65-71.
167. Singh, S., Wanderka, N., Murty, B., Glatzel, U. and Banhart, J. Decomposition in multi-component AlCoCrCuFeNi high-entropy alloy. *Acta materialia*. 2011, **59**(1), pp.182-190.
168. Smith, P.M. and Aziz, M.J. Solute trapping in aluminum alloys. *Acta metallurgica et materialia*. 1994, **42**(10), pp.3515-3525.
169. Kittl, J., Sanders, P., Aziz, M., Brunco, D. and Thompson, M. Complete experimental test of kinetic models for rapid alloy solidification. *Acta materialia*. 2000, **48**(20), pp.4797-4811.
170. Kittl, J.A., Aziz, M., Brunco, D.P. and Thompson, M. Nonequilibrium partitioning during rapid solidification of Si□ As alloys. *Journal of crystal growth*. 1995, **148**(1-2), pp.172-182.
171. Sobolev, S. Local non-equilibrium diffusion model for solute trapping during rapid solidification. *Acta materialia*. 2012, **60**(6-7), pp.2711-2718.
172. Sobolev, S. Local-nonequilibrium model for rapid solidification of undercooled melts. *Physics Letters A*. 1995, **199**(5-6), pp.383-386.
173. Sobolev, S. Effects of local non-equilibrium solute diffusion on rapid solidification of alloys. *physica status solidi (a)*. 1996, **156**(2), pp.293-303.
174. Sobolev, S. On the transition from diffusion-limited to kinetic-limited regimes of alloy solidification. *Acta materialia*. 2013, **61**(20), pp.7881-7888.
175. Galenko, P. Solute trapping and diffusionless solidification in a binary system. *Physical Review E*. 2007, **76**(3), p.031606.
176. Cantor, B., Kim, W., Bewlay, B. and Gillen, A. Microstructure—cooling rate correlations in melt-spun alloys. *Journal of materials science*. 1991, **26**, pp.1266-1276.
177. McKeown, J.T., Hsiung, L.L., Ryu, H.J., Park, J.M., Turchi, P.E. and King, W.E. Rapidly solidified U–6 wt% Nb powders for dispersion-type nuclear fuels. *Journal of Nuclear Materials*. 2014, **448**(1-3), pp.72-79.

178. McKeown, J.T., Hsiung, L.L., Park, J.M., Ryu, H.J., Turchi, P.E. and King, W.E. Size-dependent microstructures in rapidly solidified uraniumniobium powder particles. *Journal of Nuclear Materials*. 2016, **479**, pp.1-10.
179. Abul, M.R., Cochrane, R.F. and Mullis, A.M. Partitionless solidification and anomalous triradiate crystal formation in drop-tube processed Al-3.9 wt% Fe alloys. *Materials Today Communications*. 2022, **31**, p.103274.
180. Abul, M.R., Cochrane, R.F., Mullis, A.M. and Nassar, A. Microstructural Evolution and Mechanical Properties of Drop Tube Processed Al-4.1 wt.% Fe-1.9 wt.% Si. *Journal of Materials Engineering and Performance*. 2023, pp.1-17.
181. Gusakova, O. Chemically partitionless crystallization in near-eutectic rapidly solidified Al–12, 6Si–0, 8Mg–0, 4Mn–0, 7Fe–0, 9Ni–1, 8Cu alloy. *The European Physical Journal Special Topics*. 2023, pp.1-11.
182. Vishwanadh, B., Sarkar, N., Gangil, S., Singh, S., Tewari, R., Dey, G. and Banerjee, S. Synthesis and microstructural characterization of a novel multicomponent equiatomic ZrNbAlTiV high entropy alloy. *Scripta materialia*. 2016, **124**, pp.146-150.
183. Ananiadis, E., Lentzaris, K., Georgatis, E., Mathiou, C., Poulia, A. and Karantzalis, A. AlNiCrFeMn equiatomic high entropy alloy: a further insight in its microstructural evolution, mechanical and surface degradation response. *Metals and Materials International*. 2020, **26**, pp.793-811.
184. Mathiou, C., Ganara, D., Georgatis, E., Poulia, A., Lentzaris, K. and Karantzalis, A. Adjustment of Hardness of (CrFeMn) x (Ni y Al) 1− x,(y= 1, 3 and x= 0.6, 0.72, 0.80) High Entropy Alloys by Deliberate Control of Intermetallic Phase Formation: Microstructural Evolution, Hardness and Dry-Sliding Wear Response. *Metals and Materials International*. 2021, **27**, pp.175-192.
185. Srimark, K., Dasari, S., Sharma, A., Wangyao, P., Gwalani, B., Rojhirunsakool, T., Gorsse, S. and Banerjee, R. Hierarchical phase evolution in a lamellar Al0. 7CoCrFeNi high entropy alloy involving competing metastable and stable phases. *Scripta materialia*. 2021, **204**, p.114137.
186. Bai, K., Ng, C.K., Lin, M., Cheng, B., Zeng, Y., Wuu, D., Lee, J.J., Teo, S.L., Ng, S.R. and Tan, D.C.C. Unexpected spinodal decomposition in as-cast eutectic high entropy alloy Al30Co10Cr30Fe15Ni15. *Materials & Design*. 2023, **236**, p.112508.
187. Herlach, D., Eckler, K., Karma, A. and Schwarz, M. Grain refinement through fragmentation of dendrites in undercooled melts. *Materials Science and Engineering: A*. 2001, **304**, pp.20-25.
188. Mullis, A.M. and Haque, N. Evidence for dendritic fragmentation in as-solidified samples of deeply undercooled melts. *Journal of crystal growth*. 2020, **529**, p.125276.
189. Li, J., Zhou, Y. and Yang, G. Effect of solidification time on the structural evolution of undercooled single phase alloys. *Journal of crystal growth*. 1999, **206**(1-2), pp.141-146.
190. Li, J., Zhou, Y. and Yang, G. Solidification behavior of undercooled Cu70Ni30 alloy melt. *Materials Science and Engineering: A*. 2000, **277**(1-2), pp.161-168.

191. Rios, P.R., Siciliano Jr, F., Sandim, H.R.Z., Plaut, R.L. and Padilha, A.F. Nucleation and growth during recrystallization. *Materials Research*. 2005, **8**, pp.225-238.
192. Powell, G. Comments on “Undercoolability of copper bulk samples”. *Journal of materials science letters*. 1991, **10**(13), pp.745-746.
193. Powell, G. The undercooling of Cu-20 wt pct Ag alloy. *TRANS METALL SOC AIME*. 1969, **245**(8), pp.1785-1788.
194. Jones, B. and Weston, G. *The structural features of undercooled nickel and nickel-oxygen alloys.* Defence Standards Laboratories, 1970.
195. Gupta, A., Khatirkar, R.K., Dandekar, T., Jha, J.S. and Mishra, S. Recrystallization behavior of a cold rolled Ti–15V–3Sn–3Cr–3Al alloy. *Journal of Materials Research*. 2019, **34**(18), pp.3082-3092.
196. Cochrane, R.F., Battersby, S.E. and Mullis, A.M. The mechanisms for spontaneous grain refinement in undercooled Cu–O and Cu–Sn melts. *Materials Science and Engineering: A*. 2001, **304**, pp.262-266.
197. Biswas, K., Phanikumar, G., Holland-Moritz, D., Herlach, D.M. and Chattopadhyay, K. Disorder trapping and grain refinement during solidification of undercooled Fe–18 at% Ge melts. *Philosophical Magazine*. 2007, **87**(25), pp.3817-3837.
198. Xu, X., Chen, Y. and Liu, F. Recrystallization mechanism of grain refinement in hypercooled single phase alloys. *Journal of crystal growth*. 2013, **377**, pp.153-159.
199. Haque, N., Cochrane, R.F. and Mullis, A.M. The role of recrystallization in spontaneous grain refinement of rapidly solidified Ni 3 Ge. *Metallurgical and materials transactions A*. 2017, **48**, pp.5424-5431.
200. Liu, F., Cai, Y., Guo, X. and Yang, G. Structure evolution in undercooled DD3 single crystal superalloy. *Materials Science and Engineering: A*. 2000, **291**(1-2), pp.9-16.
201. Liu, F. and Gencang, Y. Stress-induced recrystallization mechanism for grain refinement in highly undercooled superalloy. *Journal of crystal growth*. 2001, **231**(1-2), pp.295-305.
202. Chen, Y., Liu, F., Yang, G., Liu, N., Yang, C., Xie, H. and Zhou, Y. Grain refinement of Fe75Ni25 alloys at low undercooling. *Materials Characterization*. 2008, **59**(4), pp.412-416.
203. Kattamis, T. and Flemings, M. DENDRITE STRUCTURE AND GRAIN SIZE OF UNDER COOLED MELTS. *AIME MET SOC TRANS*. 1966, **236**(11), pp.1523-1532.
204. Wang, H., Liu, F. and Yang, G. Experimental study of grain refinement mechanism in undercooled Ni-15at.% Cu alloy. *Journal of Materials Research*. 2010, **25**, pp.1963-1974.
205. Yang, W., Liu, F., Xu, Z., Lu, B. and Yang, G. Use of recalescence behavior analysis for the prediction of grain refinement in undercooled Cu–Ni alloy. *Journal of materials science*. 2011, **46**, pp.3101-3107.
206. An, Y., Xu, X., Zhao, Y. and Hou, H. Nonequilibrium solidification velocity, recalescence degree and grain refinement of highly undercooled Ni-based single-phase alloys. *Journal of alloys and compounds*. 2021, **881**, p.160658.
207. An, Y., Xu, X., Liang, L., Zhao, Y. and Hou, H. Microstructure transformation and grain refinement during non-equilibrium solidification of a highly undercooled alloy system. *Journal of alloys and compounds*. 2021, **864**, p.158821.

208. Willnecker, R., Herlach, D. and Feuerbacher, B. Grain refinement induced by a critical crystal growth velocity in undercooled melts. *Applied Physics Letters*. 1990, **56**(4), pp.324-326.
209. Barth, M., Eckler, K., Herlach, D. and Alexander, H. Rapid crystal growth in undercooled Fe□ Ni melts. *Materials Science and Engineering: A*. 1991, **133**, pp.790-794.
210. Mullis, A.M. and Cochrane, R.F. On the Karma model for spontaneous grain refinement at high solid fractions. *International Journal of Non-Equilibrium Processing*. 2000, **11**(3), pp.283-297.
211. Mullis, A. and Cochrane, R. Grain refinement and the stability of dendrites growing into undercooled pure metals and alloys. *Journal of Applied Physics*. 1997, **82**(8), pp.3783-3790.
212. Mullis, A. and Cochrane, R. Grain refinement and growth instability in undercooled alloys at low undercooling. *Journal of Applied Physics*. 1998, **84**(9), pp.4905-4910.
213. Mullis, A. and Cochrane, R. A phase field model for spontaneous grain refinement in deeply undercooled metallic melts. *Acta materialia*. 2001, **49**(12), pp.2205-2214.
214. Brener, E., Müller-Krumbhaar, H. and Temkin, D. Kinetic phase diagram and scaling relations for stationary diffusional growth. *Europhysics Letters*. 1992, **17**(6), p.535.
215. Dragnevski, K., Cochrane, R. and Mullis, A. Experimental evidence for dendrite tip splitting in deeply undercooled, ultrahigh purity Cu. *Physical review letters*. 2002, **89**(21), p.215502.
216. Castle, E.G., Mullis, A.M. and Cochrane, R.F. Mechanism selection for spontaneous grain refinement in undercooled metallic melts. *Acta materialia*. 2014, **77**, pp.76-84.
217. Castle, E.G., Mullis, A.M. and Cochrane, R.F. Evidence for an extensive, undercooling-mediated transition in growth orientation, and novel dendritic seaweed microstructures in Cu–8.9 wt.% Ni. *Acta materialia*. 2014, **66**, pp.378-387.
218. Zhang, J., Wang, H., Zhang, F., Lü, X., Zhang, Y. and Zhou, Q. Growth kinetics and grain refinement mechanisms in an undercooled melt of a CoSi intermetallic compound. *Journal of alloys and compounds*. 2019, **781**, pp.13-25.
219. YASUDA, H., OHNAKA, I., ISHII, R., FUJITA, S. and TAMURA, Y. Investigation of the melt flow on solidified structure by a levitation technique using alternative and static magnetic fields. *ISIJ international*. 2005, **45**(7), pp.991-996.
220. Cochrane, R., Herlach, D. and Feuerbacher, B. Grain refinement in drop-tube-processed nickel-based alloys. *Materials Science and Engineering: A*. 1991, **133**, pp.706-710.
221. Norman, A., Eckler, K., Zambon, A., Gärtner, F., Moir, S., Ramous, E., Herlach, D. and Greer, A. Application of microstructure-selection maps to droplet solidification: a case study of the Ni–Cu system. *Acta materialia*. 1998, **46**(10), pp.3355-3370.
222. An, H., Saad, I., Hsien, W.L.Y., Siambun, N.J., Chuab, B.-L. and Wang, H. Microstructure Refinement in Solidification of a Deeply Undercooled Ternary Nickel Based Alloy. *Metals and Materials International*. 2024, pp.1-9.
223. Xu, X., Hao, Y., Wu, Q., Dong, R., Zhao, Y. and Hou, H. Microstructure refinement mechanisms in undercooled solidification of binary and

ternary nickel based alloys. *Journal of Materials Research and Technology*. 2023, **24**, pp.737-758.
224. Xu, X., Wu, Q., Hao, Y., Zhao, Y. and Hou, H. Rapid solidification structure refinement mechanism in highly undercooled Cu based ternary alloys. *Journal of Materials Research and Technology*. 2023, **24**, pp.5501-5513.
225. Andreoli, A.F., Han, X. and Kaban, I. In situ studies of non-equilibrium crystallization of AlxCoCrFeNi (x= 0.3, 1) high-entropy alloys. *Journal of alloys and compounds*. 2022, **922**, p.166209.
226. Zhang, J., Hua, D., Cui, D., Li, X., Hua, K., He, Y., Wang, H. and Zhao, Y. Subgrain-assisted spontaneous grain refinement in rapid solidification of undercooled melts. *Journal of Materials Science & Technology*. 2024, **174**, pp.234-248.
227. Park, N., Watanabe, I., Terada, D., Yokoyama, Y., Liaw, P.K. and Tsuji, N. Recrystallization behavior of CoCrCuFeNi high-entropy alloy. *Metallurgical and materials transactions A*. 2015, **46**, pp.1481-1487.
228. Verma, A., Chauhan, L., Kumar, T.S., Singh, P.K., Dommeti, S.G. and Thangaraju, S. Laser Cladding of CoCrCuFeNi and CoCrFeNi High-Entropy Alloys on DMR 249A Steel: Corrosion, Wear and Antibacterial Behaviour. *Jom*. 2023, **75**(7), pp.2701-2713.
229. Tong, C.-J., Chen, M.-R., Yeh, J.-W., Lin, S.-J., Chen, S.-K., Shun, T.-T. and Chang, S.-Y. Mechanical performance of the Al x CoCrCuFeNi high-entropy alloy system with multiprincipal elements. *Metallurgical and materials transactions A*. 2005, **36**, pp.1263-1271.
230. Barsuk, D. *Metallurgical Design of New Nanoporous Structures*. thesis, Universidade federal de São Carlos, 2017.
231. Brandes, E.A. and Brook, G. *Smithells metals reference book.* Elsevier, 2013.
232. Wagner, M. *Thermal analysis in practice: fundamental aspects.* Carl Hanser Verlag GmbH Co KG, 2017.
233. Buehler. *Buehler SumMet - A Guide to Materials Preparation and Analysis.* 4 ed. Lake Bluff, IL, USA: Buehler, 2007.
234. Brodusch, N., Brahimi, S.V., Barbosa De Melo, E., Song, J., Yue, S., Piché, N. and Gauvin, R. Scanning Electron Microscopy versus Transmission Electron Microscopy for Material Characterization: A Comparative Study on High-Strength Steels. *Scanning*. 2021, **2021**(1), p.5511618.
235. Badami, A.S. Morphological and Structure-Property Analyses of Poly (arylene ether sulfone)-Based Random and Multiblock Copolymers for Fuel Cells. 2007.
236. Vernon-Parry, K.D. Scanning electron microscopy: an introduction. *III-Vs review*. 2000, **13**(4), pp.40-44.
237. Mohammed, A. and Abdullah, A. Scanning electron microscopy (SEM): A review. In: *Proceedings of the 2018 International Conference on Hydraulics and Pneumatics—HERVEX, Băile Govora, Romania*, 2018, pp.7-9.
238. Wang, Z.L. and Lee, J.L. Electron microscopy techniques for imaging and analysis of nanoparticles. In: *Developments in Surface Contamination and Cleaning*. Elsevier, 2008, pp.531-584.
239. Girão, A.V., Caputo, G. and Ferro, M.C. Application of scanning electron microscopy–energy dispersive X-ray spectroscopy (SEM-EDS). In: *Comprehensive analytical chemistry*. Elsevier, 2017, pp.153-168.

240. Hutchison, J. and Kirkland, A. *Nanocharacterisation.* Royal Society of Chemistry, 2007.
241. Reyntjens, S. and Puers, R. A review of focused ion beam applications in microsystem technology. *Journal of micromechanics and microengineering*. 2001, **11**(4), p.287.
242. Kannan, M. Transmission electron microscope—Principle, components and applications. *A textbook on fundamentals and applications of nanotechnology*. 2018, pp.93-102.
243. Hawkes, P.W. and Spence, J.C. *Springer handbook of microscopy.* Springer Nature, 2019.
244. Krishnan, K.M. *Principles of materials characterization and metrology.* Oxford University Press, 2021.
245. Zhang, F., Chan, S.-W., Spanier, J.E., Apak, E., Jin, Q., Robinson, R.D. and Herman, I.P. Cerium oxide nanoparticles: Size-selective formation and structure analysis. *Applied Physics Letters*. 2002, **80**(1), pp.127-129.
246. Mugnaioli, E., Capitani, G., Nieto, F. and Mellini, M. Accurate and precise lattice parameters by selected-area electron diffraction in the transmission electron microscope. *American Mineralogist*. 2009, **94**(5-6), pp.793-800.
247. Lee, E.-S. and Ahn, S. Solidification progress and heat transfer analysis of gas-atomized alloy droplets during spray forming. *Acta metallurgica et materialia*. 1994, **42**(9), pp.3231-3243.
248. Ranz, W. and Marshall, W. Evaporation from droplets. *Chem. Eng. Prog*. 1952, **48**(3), pp.141-146.
249. Chai, T. and Draxler, R.R. Root mean square error (RMSE) or mean absolute error (MAE). *Geoscientific model development discussions*. 2014, **7**(1), pp.1525-1534.
250. Bahadur, R.R. Some approximations to the binomial distribution function. *The Annals of Mathematical Statistics*. 1960, pp.43-54.
251. Lukas, H., Fries, S.G. and Sundman, B. *Computational thermodynamics: the Calphad method.* Cambridge university press, 2007.
252. Eleno, L.T. and Schön, C.G. Ternary interaction parameters in calphad solution models. *Brazilian Journal of Physics*. 2014, **44**, pp.208-214.
253. Gallagher, C., Kerr, E. and McFadden, S. Stereologically corrected particle size distributions for polymer-mounted additive manufacturing powders. *Powder Technology*. 2024, **444**, p.120022.
254. Franco Jr, A.R., Pintaúde, G., Sinatora, A., Pinedo, C.E. and Tschiptschin, A.P. The use of a Vickers indenter in depth sensing indentation for measuring elastic modulus and Vickers hardness. *Materials Research*. 2004, **7**, pp.483-491.
255. Guo, S., Ng, C., Lu, J. and Liu, C. Effect of valence electron concentration on stability of fcc or bcc phase in high entropy alloys. *Journal of Applied Physics*. 2011, **109**(10).
256. Zhang, Y., Chen, Z., Cao, D., Zhang, J., Zhang, P., Tao, Q. and Yang, X. Concurrence of spinodal decomposition and nano-phase precipitation in a multi-component AlCoCrCuFeNi high-entropy alloy. *Journal of Materials Research and Technology*. 2019, **8**(1), pp.726-736.
257. Xu, X., Liu, P., Guo, S., Hirata, A., Fujita, T., Nieh, T., Liu, C. and Chen, M. Nanoscale phase separation in a fcc-based CoCrCuFeNiAl0. 5 high-entropy alloy. *Acta materialia*. 2015, **84**, pp.145-152.
258. Bonnell, D., Treverton, J., Valerga, A. and Margrave, J. *The emissivities of liquid metals at their fusion temperatures.* 1972.

259. Mullis, A.M., Jegede, O.E., Bigg, T.D. and Cochrane, R.F. Dynamics of core–shell particle formation in drop-tube processed metastable monotectic alloys. *Acta materialia*. 2020, **188**, pp.591-598.
260. Nan, W. and Bing-Bo, W. Droplet undercooling during containerless processing in a drop tube. *Chinese Physics Letters*. 2004, **21**(6), p.1120.
261. Kreischer, C. and Volkmann, T. Transformation kinetics of the metastable bcc phase during rapid solidification of undercooled Fe-Co alloy melts. *Materialia*. 2021, **20**, p.101211.
262. Zhang, J., Zhang, Y., Zhang, F., Cui, D., Zhao, Y., Wu, H., Wang, X., Zhou, Q. and Wang, H. Dendrite growth and grain “coarsening” in an undercooled CoNi equiatomic alloy. *Journal of alloys and compounds*. 2020, **816**, p.152529.
263. Zhang, J., Li, X., Zhang, Y., Zhang, F., Wu, H., Wang, X.-z., Zhou, Q. and Wang, H. Sluggish dendrite growth in an undercooled high entropy alloy. *Intermetallics*. 2020, **119**, p.106714.
264. Rahul, M. and Phanikumar, G. Solidification behaviour of undercooled equiatomic FeCuNi alloy. *Journal of alloys and compounds*. 2020, **815**, p.152334.
265. Jeon, S., Sansoucie, M.P. and Matson, D.M. Hyper-cooling limit, heat of fusion, and temperature-dependent specific heat of Fe-Cr-Ni melts. *The Journal of chemical thermodynamics*. 2019, **138**, pp.51-58.
266. Fopp, P., Kolbe, M., Kargl, F., Kobold, R., Hornfeck, W. and Buslaps, T. Phase selection in hypercooled alloys. *Journal of alloys and compounds*. 2020, **834**, p.154439.
267. Inoue, A. Stabilization of metallic supercooled liquid and bulk amorphous alloys. *Acta materialia*. 2000, **48**(1), pp.279-306.
268. Kashchiev, D. *Nucleation.* Elsevier, 2000.
269. Wagner, R., Kampmann, R. and Voorhees, P.W. Homogeneous second-phase precipitation. *Phase transformations in materials*. 2001, pp.309-407.
270. Binder, K. and Fratzl, P. Spinodal decomposition. *Phase transformations in materials*. 2001, pp.409-480.
271. Cahn, J.W. Phase separation by spinodal decomposition in isotropic systems. *The Journal of chemical physics*. 1965, **42**(1), pp.93-99.
272. Stauffer, D. and Aharony, A. *Introduction to percolation theory.* CRC press, 2018.
273. Seol, D., Hu, S., Li, Y., Shen, J., Oh, K. and Chen, L. Computer simulation of spinodal decomposition in constrained films. *Acta materialia*. 2003, **51**(17), pp.5173-5185.
274. Nishimori, H. and Onuki, A. Pattern formation in phase-separating alloys with cubic symmetry. *Physical Review B*. 1990, **42**(1), p.980.
275. Zhu, F., Haasen, P. and Wagner, R. An atom probe study of the decomposition of Fe-Cr-Co permanent magnet alloys. *Acta metallurgica*. 1986, **34**(3), pp.457-463.
276. Wang, W., Gong, D., Wang, H., Ke, Y., Qi, L., Li, S., Yang, R. and Hao, Y. Spinodal decomposition coupled with a continuous crystal ordering in a titanium alloy. *Acta materialia*. 2022, **233**, p.117969.
277. Lipton, J., Glicksman, M. and Kurz, W. Dendritic growth into undercooled alloy metals. *Materials Science and Engineering*. 1984, **65**(1), pp.57-63.
278. Lipton, J., Kurz, W. and Trivedi, R. Rapid dendrite growth in undercooled alloys. *Acta metallurgica*. 1987, **35**(4), pp.957-964.

279. Langer, J. and Müller-Krumbhaar, J. Stability effects in dendritic crystal growth. *Journal of crystal growth*. 1977, **42**, pp.11-14.
280. Alexandrov, D.V. and Galenko, P.K. A review on the theory of stable dendritic growth. *Philosophical Transactions of the Royal Society A*. 2021, **379**(2205), p.20200325.
281. Ben-Jacob, E., Goldenfeld, N., Langer, J. and Schön, G. Dynamics of interfacial pattern formation. *Physical review letters*. 1983, **51**(21), p.1930.
282. Karma, A. and Kotliar, B.G. Pattern selection in a boundary-layer model of dendritic growth in the presence of impurities. *Physical Review A*. 1985, **31**(5), p.3266.
283. Amar, M.B. and Pelcé, P. Impurity effect on dendritic growth. *Physical Review A*. 1989, **39**(8), p.4263.
284. Kurz, W., Fisher, D.J. and Trivedi, R. Progress in modelling solidification microstructures in metals and alloys: dendrites and cells from 1700 to 2000. *International Materials Reviews*. 2019, **64**(6), pp.311-354.
285. Alexandrov, D., Danilov, D. and Galenko, P. Selection criterion of a stable dendrite growth in rapid solidification. *International Journal of Heat and Mass Transfer*. 2016, **101**, pp.789-799.
286. Ivantsov, G. Temperature field around a spherical, cylindrical, and needle-shaped crystal, growing in a pre-cooled melt. *Temperature field around a spherical*. 1985, **58**, pp.567-569.
287. Glicksman, M., Koss, M. and Winsa, E. Dendritic growth velocities in microgravity. *Physical review letters*. 1994, **73**(4), p.573.
288. Wilthan, B., Schützenhöfer, W. and Pottlacher, G. Thermal diffusivity and thermal conductivity of five different steel alloys in the solid and liquid phases. *International Journal of Thermophysics*. 2015, **36**, pp.2259-2272.
289. Quested, P., Brooks, R., Chapman, L., Morrell, R., Youssef, Y. and Mills, K. Measurement and estimation of thermophysical properties of nickel based superalloys. *Materials Science and Technology*. 2009, **25**(2), pp.154-162.
290. Uporov, S., Bykov, V., Pryanichnikov, S., Shubin, A. and Uporova, N. Effect of synthesis route on structure and properties of AlCoCrFeNi high-entropy alloy. *Intermetallics*. 2017, **83**, pp.1-8.
291. Du, Y., Chang, Y., Huang, B., Gong, W., Jin, Z., Xu, H., Yuan, Z., Liu, Y., He, Y. and Xie, F.-Y. Diffusion coefficients of some solutes in fcc and liquid Al: critical evaluation and correlation. *Materials Science and Engineering: A*. 2003, **363**(1-2), pp.140-151.
292. Cao, C., Herlach, D., Kolbe, M., Görler, G. and Wei, B. Rapid solidification of Cu84Co16 alloy undercooled into the metastable miscibility gap under different conditions. *Scripta materialia*. 2003, **48**(1), pp.5-9.
293. Xia, Z., Wang, W., Luo, S. and Wei, B. Liquid phase separation and rapid dendritic growth of highly undercooled ternary Fe62. 5Cu27. 5Sn10 alloy. *Journal of Applied Physics*. 2015, **117**(5).
294. Nishizawa, T. and Ishida, K. The Co− Cu (Cobalt-Copper) system. *Bulletin of Alloy Phase Diagrams*. 1984, **5**(2), pp.161-165.
295. Chakrabarti, D. and Laughlin, D. The Cr-Cu (chromium-copper) system. *Bulletin of Alloy Phase Diagrams*. 1984, **5**(1), pp.59-68.

296. Turchanin, M., Agraval, P. and Nikolaenko, I. Thermodynamics of alloys and phase equilibria in the copper-iron system. *Journal of phase equilibria*. 2003, **24**, pp.307-319.
297. Davies, R., Dinsdale, A., Gisby, J., Robinson, J. and Martin, a.M. MTDATA-thermodynamic and phase equilibrium software from the national physical laboratory. *Calphad*. 2002, **26**(2), pp.229-271.

Chapter 9 – Appendices

Appendix 1

Table A1 Expressions for Gibbs free energies for constituent elements of $CoCrCuFeNi_{0.8}$ at varying temperatures from SGSOL solutions database 2024 (SGTE)

	Element Gibbs Free Energy $(G_i^0 = G_i - H_{SER})$
Co	$737.832 + 132.750562T - 25.0861 * Tlog(T) - 2.654739 * 10^{-3}T^2 - 1.7348 * 10^{-7}T^3 + 72527/T$
Cr	$-1572.94 + 157.643T - 26.908 * Tlog(T) + 1.89435 * 10^{-3}T^2 - 1.47721 * 10^{-6}T^3 + 139250/T$
Cu	$-7770.458 + 130.4835T - 24.112392 * Tlog(T) - 2.65684 * 10^{-3}T^2 - 1.29223 * 10^{-7}T^3 + 52478/T$
Fe	$-236.7 + 132.416T - 24.6643 * Tlog(T) - 3.75752 * 10^{-3}T^2 - 5.8927 * 10^{-8}T^3 + 72359/T$
Ni	$-5179.159 + 117.854T - 22.096 * Tlog(T) - 4.8407 * 10^{-3}T^2$

Table A2 Binary Redlich-Kister interaction parameters for constituent elements of $CoCrCuFeNi_{0.8}$ in a solid FCC phase from SGSOL solutions database 2024 (SGTE)

Phase	Redlich-Kister Interaction Parameters
$CoCrCuFeNi_{(FCC)}$	${}^{0,FCC}L_{CoCr} = 1500.0 - 9.592T$
	${}^{0,FCC}L_{CoCu} = 49400.0 - 13.260T$
	${}^{1,FCC}L_{CoCu} = -3765.0 + 1.030T$
	${}^{0,FCC}L_{CoFe} = -8471.0 + 0.0T$
	${}^{1,FCC}L_{CoFe} = 1181.0 - 1.6544T$
	${}^{0,FCC}L_{CoNi} = -800.0 + 1.2629T$
	${}^{0,FCC}L_{CrCu} = 88112.0 - 30.38315T$
	${}^{0,FCC}L_{CrFe} = 10833.0 - 7.477T$
	${}^{1,FCC}L_{CrFe} = 1410.0 + 0.0T$
	${}^{0,FCC}L_{CrNi} = 8030.0 - 12.8801T$
	${}^{1,FCC}L_{CrNi} = 33080.0 - 16.0362T$
	${}^{0,FCC}L_{CuFe} = 48232.565 - 8.609542T$
	${}^{1,FCC}L_{CuFe} = 8861.882 - 5.289751T$
	${}^{0,FCC}L_{CuNi} = 8047.72 + 3.42217T$
	${}^{1,FCC}L_{CuNi} = -2041.3 + 0.99714T$
	${}^{0,FCC}L_{FeNi} = -12054.355 + 3.27413T$
	${}^{1,FCC}L_{FeNi} = 11082.131 - 4.45077T$
	${}^{2,FCC}L_{FeNi} = -725.805 + 0.0T$